# A novel transition metal dichalcogenide – reduced graphene oxide electrocatalyst family for hydrogen evolution reaction


**Jianan Jiang**

**Faculty of Science, Agriculture and Engineering**

**School of Engineering**

**Chemical Engineering**


**A thesis submitted for the degree of**

**Doctor of Philosophy**

# Abstract

The global energy crisis underscores the critical need for sustainable hydrogen production via efficient electrocatalysts. This study presents a novel family of transition metal dichalcogenide-reduced graphene oxide ($MoS_2$-rGO) hybrids and doped variants (V, W, Co) for the hydrogen evolution reaction (HER). Using orthogonal experimental design ($L9(3^3)$), we optimized synthesis parameters (rGO content, heating temperature, duration) to develop a $MoS_2$-rGO composite with 0.8 wt% rGO, synthesized at 200°C for 24 h. This optimized catalyst achieved superior HER performance in acidic media (0.5 M $H_2SO_4$), exhibiting a low overpotential ($\eta 10$ = -0.34 Vs RHE) and Tafel slope (98.2 mV/dec), significantly outperforming undoped $MoS_2$ ($\eta_{10}$ > 0.40 Vs RHE, Tafel slope 113.0 mV/dec).

While Pt/C remains the benchmark catalyst with ultra-low overpotential (~0.05 V vs. RHE) and a Tafel slope of ~30 mV/dec, its high cost and scarcity hinder widespread application. In contrast, our $MoS_2$-rGO catalysts offer a noble-metal-free alternative with enhanced conductivity and stability, facilitated by rGO integration. XRD and Raman spectroscopy confirmed structural improvements, while vanadium doping increased active site exposure, tungsten doping introduced sulfur vacancies to optimize hydrogen adsorption energy, and cobalt doping altered electronic structures.

Systematic characterization via XRD, XPS, BET, UV-vis, Raman spectroscopy, SEM and electrochemical techniques elucidated the structural and electronic contributions of each component. The synergistic effects of rGO and dopants were highlighted, with the $Co_{0.05}W_{0.05}S_2$/rGO heterostructure showing promising HER activity. This work establishes a rational framework for designing noble-metal-free HER catalysts, emphasizing the interplay between defect engineering, interfacial interactions, and scalable synthesis strategies. The integration of orthogonal optimization with multi-technique characterization provides a robust pathway for advancing green hydrogen technologies.

# Acknowledgements

I would like to express my deepest gratitude to my supervisor, Dr. Stevin Pramana, for his invaluable guidance, support, and encouragement throughout the course of my research. His insights and expertise have been instrumental in shaping this work, and I am truly fortunate to have had the opportunity to learn under his mentorship.

I would also like to thank my academic co-supervisory team members, Prof. Mohammed Mamlouk, and Dr. Evangelos Papaioannou, for their assistance, collaboration, and the many stimulating discussions that greatly contributed to the progress of this project. Their support and friendship have made this journey enjoyable and fulfilling.

I would like to give a special mention to Jian Huang for their assistance with electrochemistry in C320. I am also grateful to Dr. Yinxia Jin for her invaluable time and expertise in XPS measurements. Additionally, I extend my thanks to Miss Yanqi Wu and Dr. Jingtong Lu for their help with SEM and EDS testing. Finally, I appreciate Dr. Yuqi Jiang for providing valuable suggestions in XRD refinement.

Finally, I am grateful to my family and friends for their unwavering encouragement and understanding throughout this journey. Without their support, this work would not have been possible.

Thank you all for being a part of this journey.

## Table of contents

# List of figures

## Chapter 1.



## Chapter 2.



## Chapter 3.

## Chapter 4.



## Chapter 5.



## Chapter 6.

# Introduction

Transition metal dichalcogenides (TMDs), including molybdenum disulfide ($MoS_2$) and tungsten diselenide ($WSe_2$), have emerged as a distinct class of two-dimensional materials attracting intense scientific interest. Structurally, these compounds exhibit weakly bonded van der Waals layers, enabling facile isolation of atomically thin monolayers through mechanical or liquid-phase exfoliation. Notably, reducing material thickness to a single layer induces dramatic electronic transitions − bulk indirect bandgap semiconductors become direct bandgap monolayers, a dimensionality-driven phenomenon experimentally established in early 2010s studies. This thickness-dependent band structure modulation, coupled with strong spin-orbit interactions and tunable surface reactivity, positions TMDs as versatile platforms for next-generation technologies.[1–4]

The aim of this doctoral research project is to investigate transition metal dichalcogenide catalysts in absence of precious metals to advance the electrocatalytic activities tied to the hydrogen evolution reaction (HER) at the cathode within electrolyzer frameworks. Variations in catalytic efficacy are systematically examined by modifying the stoichiometric ratios, elemental composition, and microstructural characteristics of $Mo_xM_{1-x}S_2$ (where M represents V, W, and Co). This chapter elucidates the rationale behind the investigation of these materials by emphasizing the significance of the diverse energy systems in which they are employed.

## 1.1 The need for renewable energy

Fossil fuels, despite their historical significance in facilitating industrial expansion and contemporary amenities, entail a multitude of adverse effects that influence ecological integrity, public health, and economic resilience. These negative implications have catalyzed worldwide initiatives aimed at advancing the shift towards more sustainable energy alternatives. It is commonly accepted that fossil fuel combustion is the chief reason for the disturbing shifts in our climate pattern. As fossil fuels are burned, they discharge a remarkable volume of

## Introduction

greenhouse gases into the air, including carbon dioxide. Currently, over fifty percent of these gases that trap heat remain uncontained and linger in the atmosphere, significantly exacerbating the issue of climate change [5]. At this moment, our world is facing an unparalleled escalation in warmth, surpassing all prior moments in the timeline of humanity. Historically, beginning in the 1700s, the burning of fossil fuels has played a role in producing nearly 90% of carbon dioxide emissions, leading to over 75% of worldwide greenhouse gas emissions [6]. A thorough review executed by the Intergovernmental Panel on Climate Change has demonstrated that 89% of the $CO_2$ emissions documented around the globe in 2018 were linked to fossil fuel usage, with forecasts suggesting a potential increase in temperature of 1.5 ℃, likely to heighten the occurrence and intensity of various extreme weather and climatic phenomena [7]. When fossil fuels are combusted, numerous significant pollutants are discharged, which include fly ash, sulfur oxides, and nitrogen oxides. Recent findings from Harvard University, University of Birmingham, and University College London have disclosed that air pollution stemming from fossil fuels was linked to nearly 8 million fatalities in 2018; this statistic suggests that fossil fuel combustion was accountable for about 20% of the total deaths globally during that year[8]. Furthermore, these inorganic pollutants have severely compromised numerous natural habitats, thereby posing an increased threat to biodiversity and ecosystem integrity. A study by the World Wildlife Fund (WWF) reveals that various species have faced a significant reduction of 69% since 1970, a pattern linked to the growing dependence on fossil fuels [9]. The processes of extracting and combusting fossil fuels have also indirectly disrupted marine ecosystems, particularly through the mechanism of climate change. In the previous century, around 30% of carbon dioxide emissions attributable to fossil fuel usage have been taken up by the oceans, thereby causing significant changes in the chemical attributes of seawater, which has resulted in increased acidity and adverse effects on several marine species [9]. The aforementioned drawbacks compel us to seek more sustainable energy resources.

Hydrogen is progressively acknowledged as a feasible substitute for fossil fuels, presenting a multitude of benefits that correspond with international sustainability objectives.

The combustion of hydrogen yields water as the sole byproduct, thereby eradicating carbon dioxide emissions and markedly diminishing the environmental repercussions when juxtaposed with fossil fuels.[10,11] Moreover, hydrogen fuel cells facilitate the direct conversion of chemical energy into electrical energy, presenting greater efficiency relative to conventional combustion engines, which are subject to numerous energy transformation phases.[12] Furthermore, hydrogen possesses a substantial energy density per unit mass (141.9 MJ/kg for hydrogen. This value is nearly threefold greater than that of gasoline, which is estimated to be around 47 MJ/kg),[13] rendering it a more effective energy carrier in comparison to fossil fuels.[14] Thus, the transition towards hydrogen is paramount for the attainment of international sustainability objectives and for alleviating the grave repercussions associated with reliance on fossil fuels.

## 1.2 Water Splitting and the Hydrogen Evolution Reaction (HER)

There exist numerous methodologies for the generation of hydrogen fuel. Nonetheless, water constitutes one of the most naturally prevalent, hydrogen-rich, comparatively safe, and environmentally benign resources available on Earth. Hence, the approach of electrolysis, as it disassociates water into hydrogen and oxygen, marks a clear development toward the evolution of inventive sustainable technologies.[15]

One of the benefits of water splitting is water electrolysis that can be facilitated by sustainable energy sources, including solar, wind, and geothermal energy, thereby markedly diminishing the carbon emissions linked to hydrogen generation. As an example, employing solar energy in water splitting processes utilizing thermochemical cycles like the copper-chlorine (Cu-Cl) cycle is notable for its ability to generate hydrogen while emitting negligible greenhouse gases, leading to a global warming potential (GWP) as low as 0.91 kg $CO_2$ eq./kg $H_2$.[16]

At the heart of water splitting lies the Hydrogen Evolution Reaction (HER), a foundational element for the eco-conscious creation of hydrogen. HER encompasses the reduction of protons into hydrogen gas and constitutes one of the two half-reactions involved

in water electrolysis, with the Oxygen Evolution Reaction (OER) being the counterpart. The efficiency of HER exerts a significant influence on the overall efficacy of water electrolysis, thereby rendering it a critical area of focus in the advancement of electrocatalysts and the elucidation of reaction mechanisms.

The HER relies heavily on catalysts, serving as a core mechanism within the water electrolysis framework for generating hydrogen. Catalysts augment both the efficiency and kinetics of HER by facilitating alternative reaction mechanisms and minimizing the energy barriers associated with the reaction. However, the dependence on noble metals such as platinum for HER catalysts presents a considerable obstacle owing to their exorbitant price and restricted accessibility. Initiatives are underway to engineer non-noble metal catalysts that exhibit optimal performance in both acidic and alkaline media. Nonetheless, attaining the requisite activity and durability with non-noble metals continues to pose significant challenges [17]. The stability of catalysts represents another significant issue, especially within acidic environments where catalysts are susceptible to degradation. The advancement of robust catalysts capable of enduring extreme conditions without considerable performance deterioration is essential for sustained application [18]. While considerable advancements have been achieved in the formulation of catalysts for the HER, numerous obstacles persist concerning economic viability, durability, and catalytic activity. Dealing with these difficulties demands a comprehensive framework that unites progress in materials science, chemistry, and engineering areas. Thus, the work in this thesis is to aid in the understanding and knowledge of the scientific community in the study of electrocatalyst materials for the hydrogen evolution reaction.

## 1.3 Basic Principles of Electrocatalytic HER

Electrocatalytic water-splitting is a prominent method that enables the transformation of electrical energy into hydrogen fuel, utilizing water as the main substrate and producing oxygen and hydrogen as byproducts. This mechanism features two unique half-cell reactions: the oxygen evolution reaction happening at the anode and the hydrogen evolution reaction

taking place at the cathode. Collectively, these reactions facilitate the comprehensive process of water splitting, as illustrated in Figure 1-1(a).

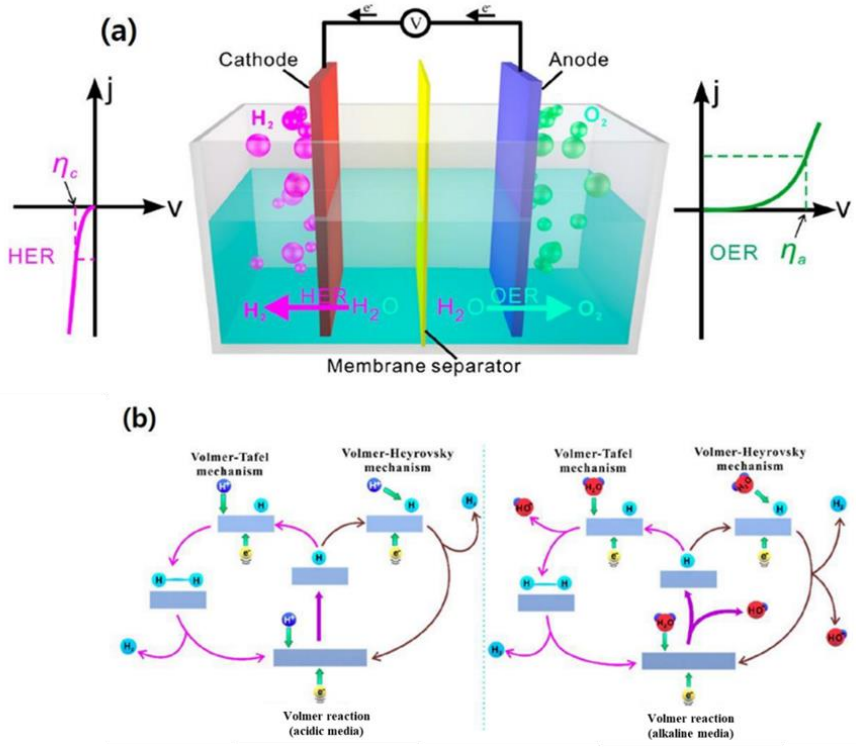


***Fig 1- 1 a) Schematic of the OER and HER mechanisms in the water-splitting process, illustrating the roles of the anode and cathode., (b) Basic principles of HER on electrocatalyst surfaces under acidic and alkaline conditions. In acidic environments, protons reduce to form hydrogen on the catalyst, while in alkaline settings, water molecules undergo reduction***[19]

The HER mechanism in acidic media proceeds through the initial electrochemical reduction of hydronium ions ($H_3O^+$), which is often simplified in equations as $H^+$ for brevity, resulting in the formation of adsorbed hydrogen atoms on the electrode surface. Subsequently, the production of molecular hydrogen occurs through two distinct pathways: either by the Tafel mechanism involving the recombination of two hydrogen adatoms ($H_{ads}$), or alternatively via the Heyrovsky mechanism, where an adsorbed hydrogen atom undergoes an electrochemical

reaction with a hydronium ion from the acidic electrolyte, as indicated in Figure 1-1(b).[19,20] The steps are as follows:

$$H^+ + e^- \rightarrow H_{ads}\,(Volmer) \quad eq\ 1\text{-}1$$

$$H_{ads} + H^+ + e^- \rightarrow H_2\,(Heyrovsky) \quad eq\ 1\text{-}2$$

$$2H_{ads} \rightarrow H_2\,(Tafel) \quad eq\ 1\text{-}3$$

In alkaline environments, the HER initiates via the electrocatalytic reduction of water molecules. This primary step generates adsorbed hydrogen intermediates ($H_{ads}$) on the electrode surface while liberating hydroxide ions ($OH^-$) into the surrounding electrolyte. Subsequent hydrogen formation proceeds through two divergent pathways: (1) direct chemical recombination of adjacent $H_{ads}$ species to yield molecular hydrogen ($H_2$), or (2) an electrochemical step where Hads interacts with an additional water molecule, simultaneously producing $H_2$ and regenerating $OH^-$ ions. The steps are as follows:[21]

$$H_2O + e^- \rightarrow H_{ads} + OH^-\,(Volmer) \quad eq\ 1\text{-}4$$

$$H_{ads} + H_2O + e^- \rightarrow H_2 + OH^-\,(Heyrovsky)\ eq\ 1\text{-}5$$

$$2H_{ads} \rightarrow H_2\,(Tafel) \quad eq\ 1\text{-}6$$

The Tafel slope ($b$) is an essential parameter that reveals the voltage change required to alter the current density by an order of magnitude, helping to clarify the HER mechanism. The slope value depends on the rate-limiting step of the reaction: [22]

- If the initial adsorption (Volmer) step proceeds quickly, but the combination reaction is slow, a Tafel slope of 29 mV $dec^{-1}$ is anticipated: $b = \frac{2.3RT}{2F} = 0.029$ V $dec^{-1}$ at 25 °C.
- If the discharge reaction is fast and the electrochemical desorption (Heyrovsky) is rate-limiting, the Tafel slope is 39 mV $dec^{-1}$: $b = \frac{4.6RT}{3F} = 0.039$ V $dec^{-1}$ at 25 °C.
- If the discharge reaction is slow, the Tafel slope is higher, at 116 mV $dec^{-1}$: $b = \frac{4.6RT}{F} = 0.116$ V $dec^{-1}$ at 25 °C.

### 1.3.1 Parameters Governing the Efficiency of Electrocatalytic HER

The efficacy of the HER within the realm of electrocatalysis is influenced by numerous critical factors. Each of these parameters provides insights into how well the catalyst

facilitates the reaction, influencing factors like energy input, reaction speed, and stability. By optimizing these parameters, researchers can develop more effective electrocatalysts to achieve highly efficient hydrogen production. [23]

#### 1.3.1.1 Overpotential (η)

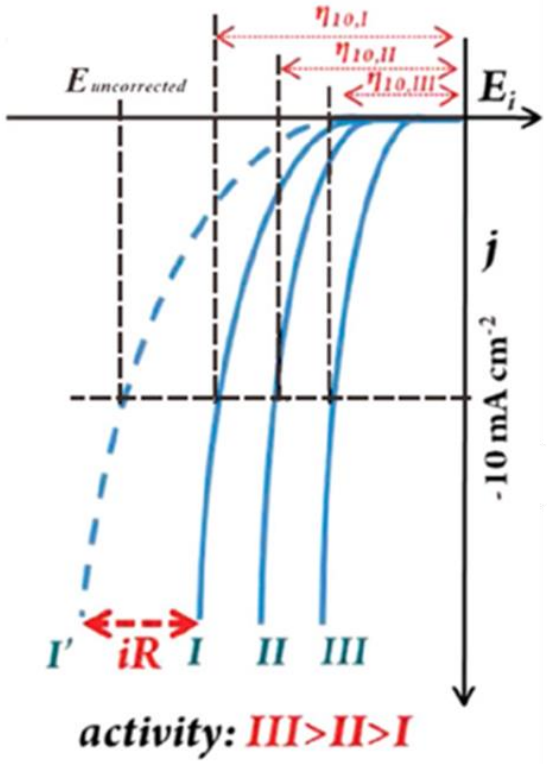


***Fig 1- 2. A diagram illustrating HER polarization curves across various electrocatalysts, with iR correction applied and overpotentials indicated.*** [24]

The overpotential is the additional voltage applied beyond the thermodynamic potential required to drive the HER. In the process of water electrolysis, the generation of hydrogen gas at the interface of the electrode establishes a hindrance to subsequent reactions, thereby decelerating the overall kinetics of the reaction. To overcome this, a supplementary potential, known as overpotential (η), is applied. [25]

Overpotential represents the difference between the thermodynamic potential for a specific HER and the actual applied potential at which the catalyst achieves a designated current density under certain operating conditions. The equation for the total electrolysis potential $\Delta E_{\text{electrolysis}}$ includes the reversible potential $\Delta E_{\text{irreversible}}$, overpotential, and the voltage drop from resistance $IR$:[25]

$$E_{electrolysis} \rightarrow E_{reversible} + \Delta E_{irreversible} + IR \quad eq\ 1\text{-}7$$

Where:

- $E_{electrolysis}$ refers to the actual potential applied across the electrolyzer to drive the water splitting process.
- $E_{reversible}$ represents the reversible thermodynamic potential for water electrolysis, which is the minimum potential required under standard conditions (typically 1.23 V for water splitting at 25°C and 1 atm).
- $\Delta E_{irreversible}$ accounts for the irreversible losses stemming from factors such as activation barriers at the electrode surface and mass transport limitations.
- $IR$ denotes the ohmic loss, which is the voltage drop caused by the resistances from electrical contacts, electrode materials, electrolyte solution, and any junctions within the system, where $I$ is the applied current and $R$ is the total system resistance.[25,26]

The effectiveness of the catalyst is evaluated through the quantification of the overpotential at a defined current density of 10 mA $cm^{-2}$, which is considered the standard for comparative analysis (Fig 1-2). Low overpotential values are desirable, as they indicate that the catalyst can drive HER efficiently with minimal additional energy input. Generally, electrocatalysts that achieve low overpotentials at high current densities are considered highly effective for HER. [25]

#### 1.3.1.2 Faradic Efficiency

Faradaic efficiency quantifies the effectiveness of electron transfer in the electrochemical reaction. [27] It indicates the proportion of electrons that contribute directly to the generation of hydrogen gas, as opposed to being lost to other reactions or inefficiencies.

This parameter is essential for assessing how much of the electrical energy applied is actually used for hydrogen production.

The Faradaic efficiency can be calculated by comparing the experimentally measured amount of hydrogen produced with the theoretically expected amount, as shown in the formula below: [19]

$$Faradaic\ Efficiency = \frac{H_{2\,produced_{experimental}}}{H_{2\,produced_{theoretical}}} \qquad eq\ 1\text{-}8$$

where:

- $H_{2\,produced_{experimental}}$ refers to the actual amount of molecular hydrogen collected during electrolysis, typically determined using gas chromatography or water displacement techniques.
- $H_{2\,produced_{theoretical}}$ denotes the amount of hydrogen theoretically expected based on the total charge passed through the system, according to Faraday's law.

A high Faradaic efficiency indicates that the majority of electrons supplied to the system are effectively used for hydrogen evolution, which is a hallmark of a selective and efficient electrocatalyst.

#### 1.3.1.3 Tafel Slope

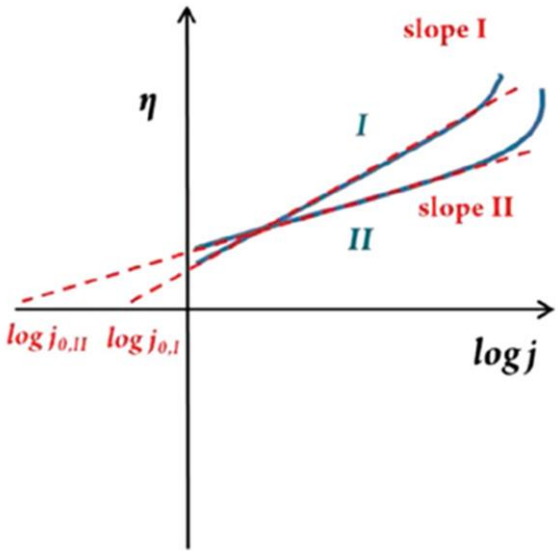


***Fig 1- 3. Schematic Tafel plots on different electrocatalysts with the Tafel slopes and exchange current densities indicated*** [24]

The Tafel slope is a critical parameter in electrocatalysis, as it represents the relationship between the steady-state current density and the overpotential applied. It provides insights into the reaction kinetics and the rate-limiting steps of HER on the catalyst surface. The Tafel slope can be determined using the Tafel equation: [28]

$$\eta = b \log j + a \qquad eq\ 1\text{-}9$$

where $\eta$ is the overpotential, $b$ represents the Tafel slope, $j$ is the current density, and $a$ is the intercept representing the logarithm of the exchange current (Fig 1-3). [24] A diminished Tafel slope signifies that a minimal elevation in overpotential yields a considerable escalation in current density, implying that the catalyst facilitates accelerated reaction kinetics and effective hydrogen evolution. Tafel slopes are often categorized based on the rate-limiting step: A slope of around 29 mV $dec^{-1}$ implies that the Volmer step is rate-limiting. A slope of 39 mV $dec^{-1}$ decade indicates that the Heyrovsky step is limiting. A higher slope, around 116 mV mV $dec^{-1}$, suggests slower initial discharge reactions. [22] Understanding the Tafel slope is

essential for determining the efficiency of a catalyst and the potential areas for performance enhancement.

#### 1.3.1.4 Turnover Frequency (TOF)

Turnover frequency (TOF) is an important activity indicator in electrocatalysis, quantifying the number of reactions (or the amount of product generated) per unit time per active site on the catalyst. It reflects the catalytic activity and efficiency of a given material, especially at the atomic or molecular level.[29] TOF is defined as:

$$TOF = \frac{jN_A}{Fn\tau} \quad eq\ 1\text{-}10$$

where:

- $j$ is the current density (A cm$^{-2}$),
- $N_A$ is Avogadro's number (6.022 × 10$^{23}$ mol$^{-1}$),
- $F$ is Faraday's constant (96,485 C mol$^{-1}$),
- $n$ is the number of electrons transferred per molecule of product, which equals 2 for the hydrogen evolution reaction (HER), according to:$2H^+ + 2e^- \rightarrow H_2$,
- $\tau$ represents the number of active sites (in moles) in the catalyst, which can be estimated from the electrochemically active surface area (ECSA) combined with an appropriate site density.

For solid-state catalysts, where directly counting the active sites is challenging, an alternative approach for calculating TOF is often used: [30,31]:

$$TOF = \frac{jA}{2nF} \quad eq\ 1\text{-}11$$

- $A$ is the surface area of the working electrode (cm$^2$),
- $n$ is the number of electrons required per molecule of molecular hydrogen formed, which equals 2 for HER,
- $F$ is Faraday's constant.

In practice, $A$ can be replaced with the electrochemically active surface area (ECSA) to normalize TOF to the actual active sites rather than the geometric area.[19]

#### 1.3.1.5 Gibbs Free Energy ($\Delta G_H$) of Hydrogen Adsorption

The Gibbs Free Energy of Hydrogen Adsorption ($\Delta \boldsymbol{G_H}$) is a critical parameter in evaluating the efficiency of an electrocatalyst for the hydrogen evolution reaction. This parameter represents the energy change associated with the adsorption of hydrogen atoms on the catalyst surface and plays a fundamental role in determining the reaction kinetics and overall HER efficiency. According to the Sabatier principle, an optimal catalyst should have a balanced binding strength with hydrogen: neither too weak nor too strong.[32] According to the Sabatier principle, an optimal catalyst should have a balanced binding strength with hydrogen: neither too weak nor too strong.[33]

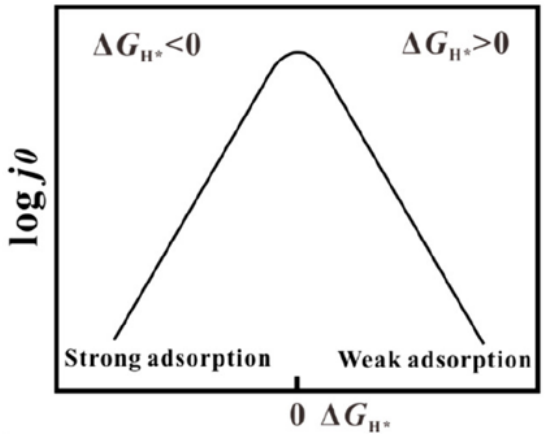


***Fig 1- 4. Correlation between $j_0$ and $\Delta G_H$ Based on the Langmuir Adsorption Model*** [34].

The value of $\Delta \boldsymbol{G_H}$ reflects how easily hydrogen atoms can adsorb onto and desorb from the catalyst's surface, which is essential for efficient HER (Fig 1-4). If $\Delta \boldsymbol{G_H}$ is too low (indicating weak adsorption), hydrogen atoms do not bind effectively to the catalyst surface, impacting the initial Volmer step where hydrogen is adsorbed. This weak interaction hinders the catalyst's ability to facilitate the initial step of HER, resulting in lower hydrogen production efficiency If $\Delta \boldsymbol{G_H}$ is too high (indicating strong adsorption), hydrogen binds too tightly to the surface, making it difficult for adsorbed hydrogen atoms to combine and release as molecular hydrogen ($H_2$) in the subsequent Heyrovsky or Tafel steps. [33] This strong interaction can slow

down the overall reaction rate, as the desorption step becomes the rate-limiting step. For optimal HER performance, the ideal $\Delta \boldsymbol{G_H}$ should be close to zero, allowing for efficient adsorption and desorption. This balance ensures that hydrogen atoms can readily attach to and detach from the catalyst, promoting a continuous and efficient HER process. [34]

The relationship between $\Delta \boldsymbol{G_H}$ and HER kinetics is often modeled using the Langmuir adsorption model, which assumes that (Fig 1-4): [34]

Adsorption occurs on a homogeneous surface with identical adsorption sites. Each site can hold only one hydrogen atom. There are no interactions between hydrogen atoms on adjacent sites.

Under these assumptions, the exchange current density ($j_0$), which is a measure of the intrinsic activity of the catalyst, can be correlated with $\Delta \boldsymbol{G_H}$. A "volcano-type" plot, often used in this context, illustrates how $logj_0$ varies with $\Delta \boldsymbol{G_H}$. The peak of this plot indicates the optimal $\Delta \boldsymbol{G_H}$, where the balance between adsorption and desorption is ideal, leading to maximum HER activity. Catalysts with $\Delta \boldsymbol{G_H}$ values near this optimal point are considered highly effective for HER. The Langmuir isotherm is mathematically expressed as $q_e = \frac{q_m K C_e}{1+KC_e}$, where $q_e$ is the amount of adsorbate adsorbed per unit mass of adsorbent at equilibrium. This reflects how much of the adsorbate (e.g., hydrogen atoms in HER) has been adsorbed by the catalyst or adsorbent at a given equilibrium concentration; $q_m$ is the maximum adsorption capacity, which represents the maximum amount of adsorbate that the adsorbent can hold under ideal conditions. This parameter provides insight into the theoretical saturation point of the adsorbent; $K$ is yhe Langmuir constant, which relates to the affinity of the binding sites for the adsorbate. A higher $K$ value suggests stronger interactions between the adsorbate and the adsorbent, meaning that even at lower equilibrium concentrations ($C_e$), a significant amount of adsorption will occur; $C_e$ is the equilibrium concentration of the adsorbate in the solution or gas phase, representing the remaining concentration after adsorption equilibrium is reached. [35]

In summary, $\Delta G_H$ is a pivotal parameter that defines the catalytic performance in HER, with optimal values enabling both efficient hydrogen adsorption and desorption, resulting in enhanced hydrogen production.

#### 1.3.1.6 Electrochemical Active Surface Area (ECSA)

The electrochemical active surface area (ECSA) represents the number of active sites on a catalyst available for the reaction. A larger ECSA indicates more sites on which HER can occur, typically leading to higher catalytic performance. ECSA can be determined by measuring the electrochemical double-layer capacitance ($C_{dl}$), which correlates with the surface area accessible for reactions. The ECSA can be calculated as: [36,37]

$$ECSA = \frac{C_{dl}}{C_s} \quad eq\ 1\text{-}12$$

where $C_{dl}$ is the double-layer capacitance and $C_s$ the specific capacitance. In an alkaline medium, for example, the typical specific capacitance value ($C_s$) is around 40 μF/cm$^2$. Higher ECSA values suggest that the catalyst has more exposed active sites, which can enhance the overall reaction rate and efficiency of HER.[38] Through meticulous examination and enhancement of these parameters, scholars are able to assess the efficacy of electrocatalysts and discern potential avenues for enhancement. This process ultimately contributes to the development of more efficient and sustainable catalysts for hydrogen production through HER.

### 1.3.2 Importance of Developing Noble-Metal-Free Catalysts for HER

In order to promote hydrogen as a viable sustainable fuel alternative, it is imperative to focus on the enhancement of effective catalysts alongside the identification of appropriate electrolytes, which are crucial for improving the kinetics of HER. Currently, electrocatalysts often rely on noble metals like platinum due to their remarkable properties, including low overpotentials and fast reaction kinetics, which make them highly effective for HER. However, the high cost and scarcity of noble metals like platinum present limitations for their broad application, driving the search for alternative catalysts that are more economical and sustainable.[39] The limited availability and high expense of noble metals have spurred efforts

to replace platinum-based catalysts with noble-metal-free alternatives that can match or approach their efficiency.[40,41] Researchers are actively investigating catalysts that not only exhibit superior catalytic efficiency but also ensure enduring stability, wide accessibility, non-toxic properties, excellent conductivity, and overall economic feasibility. These attributes are imperative for the establishment of a sustainable, mass hydrogen production system. As a result, studies in the present day have illustrated hopeful advancements in the crafting of electrocatalysts composed of non-noble metals, in both theoretical insights and practical findings, which might reach hydrogen evolution reaction efficiency levels that rival those of platinum systems.[42]

The choice of catalyst and electrolyte is crucial in HER, as they determine the reaction kinetics and efficiency.[21] Effective catalysts help lower the activation energy required for the reaction, which in turn reduces overpotential and enhances HER performance. In developing these catalysts, several key factors must be taken into account, including:

- **Material Cost and Abundance:** The catalyst should use materials that are affordable and readily available to ensure economic feasibility and scalability. Catalytic Efficiency: High intrinsic activity, reflected in reduced overpotential, is essential for an effective HER catalyst. [43]
- **Robustness and Stability:** The catalyst should maintain performance over long operational periods, even under harsh conditions.[44]
- **Ease of Synthesis:** Scalable, environmentally friendly synthesis methods are important for practical and large-scale applications. Key Performance Parameters: Exchange Current Density and Tafel Slope.[43]
    - In evaluating HER catalysts, exchange current density ($j_0$) and Tafel slope are two pivotal metrics:
- **Exchange Current Density**: measures the intrinsic catalytic activity of the material. A higher $j_0$ value indicates a more active catalyst.

- **Tafel Slope**: represents the rate at which the reaction rate increases with overpotential. A low Tafel slope is desirable, as it means the catalyst requires less additional energy to drive the reaction, indicating high catalytic efficiency.[45]

Both of these parameters are crucial in assessing non-noble metal catalysts and comparing their performance to that of platinum, which remains the gold standard in HER due to its exceptional activity.

Platinum is currently unparalleled in HER performance due to its optimal hydrogen adsorption energy, making it an ideal catalyst for both hydrogen evolution and oxidation reactions. However, given its cost and scarcity, replacing platinum with noble-metal-free alternatives is essential for large-scale hydrogen production.

Recent advances, particularly in TMDs like $MoS_2$, have shown potential as noble-metal-free catalysts. Through doping with multivalent elements, researchers have enhanced the catalytic properties of $MoS_2$, achieving improvements in both HER activity and stability. [46] These materials are promising because they allow for fine-tuning of hydrogen adsorption and desorption properties, similar to platinum, and their structure lends itself to further modification.

The push for noble-metal-free catalysts in HER is progressing rapidly, with a strong focus on materials that can achieve comparable catalytic performance to platinum while being more accessible and cost-effective. Ongoing progress in materials such as doped transition TMDs is anticipated to significantly contribute to the attainment of reduced overpotentials, elevated exchange current densities, and improved stability. The future of hydrogen production technology is contingent upon the advancement of these noble-metal-free electrocatalysts, which not only promise enhanced efficiency but also align with principles of environmental sustainability and economic viability for extensive applications.

## 1.4 Aims and Objectives

This study aims to advance noble-metal-free electrocatalyst development for the hydrogen evolution reaction (HER) through systematic engineering of $MoS_2$-based materials and their composites. The work focuses on three interconnected pillars:

## Introduction

1 Synthesis Optimization Develop an optimized protocol for $MoS_2$-rGO composites by interrogating critical parameters (rGO loading, hydrothermal temperature, reaction time) to balance crystallinity, conductivity, and catalytic activity.

2 Dopant Engineering Investigate how vanadium (V) and tungsten (W) doping alter $MoS_2$'s structural and electronic properties, focusing on interlayer expansion, sulfur vacancy generation, and active site modulation. Explore preliminary cobalt (Co) doping effects on band structure modification.

3 Hybrid Catalyst Design Assess the potential of W/Co co-doping strategies to create synergistic effects, leveraging interfacial interactions between dopants and the rGO matrix for enhanced charge transfer kinetics.

4 Systematic Characterization Employ a multi-technique approach:

- 4.1 Structural: XRD, Raman for crystallinity and defect analysis
- 4.2 Electronic: XPS, UV-Vis for chemical state and bandgap evaluation
- 4.3 Electrochemical: CV, EIS, Tafel analysis for activity/stability assessment
- 4.4 Surface: BET, SEM for porosity and morphology characterization

5 Performance Benchmarking Establish performance metrics (overpotential, Tafel slope, durability) under acidic conditions (0.5 M $H_2SO_4$), identifying critical factors governing HER efficiency.

6 Mechanistic Insights Derive structure-activity relationships by correlating dopant-induced modifications (layer spacing, vacancy density, electronic states) with catalytic performance, providing guidelines for rational catalyst design.

7 Scalability Assessment Evaluate synthesis reproducibility, material stability, and cost-effectiveness to bridge laboratory-scale innovation with industrial hydrogen production requirements.

By integrating materials engineering with fundamental mechanistic studies, this work seeks to deliver a blueprint for developing high-performance, non-precious HER catalysts while advancing the scientific understanding of TMD-based electrocatalysis.

# Literature Review

This chapter provides an overview of catalysts used for the hydrogen evolution reaction, focusing specifically on molybdenum disulfide-based catalysts, which are central to this thesis. Building on the prior chapter's discussion of HER catalysis mechanisms on acidic electrolyzer cathodes, this section emphasizes the importance of selecting effective catalytic materials to enhance cathode performance. It covers the development of HER catalysts over time, exploring both traditional and modern options, along with the different classes of materials applied in HER catalysis.

## 2.1 Noble Metals

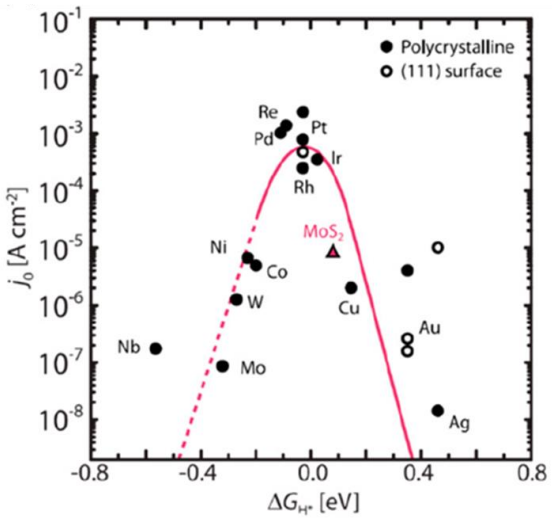


***Fig 2- 1. The correlation between $j_0$ and $\Delta G_{H^*}$ for HER occurring on the surfaces of diverse metallic substrates within an acidic environment. The Sabatier volcano relationship illustrates the optimal balance between hydrogen adsorption strength and catalytic activity, with the peak indicating the most favorable adsorption energy for efficient HER performance. The position of $MoS_2$ is highlighted for comparison.[34]***

Figure 2-1's volcano curve elucidates that platinum group metals (PGMs) (comprising Pt, Pd, Ru, Ir, and Rh) are situated near the apex, signifying their enhanced catalytic efficacy for the HER. With a nearly zero free energy of hydrogen adsorption, these

metals excel as HER electrocatalysts. Platinum, at the top of the curve, is particularly effective, with minimal onset overpotential and Tafel slope.[47] Following the Sabatier principle, Pt's balanced metal-hydrogen bond strength optimizes hydrogen adsorption and desorption, which drives its exceptional HER efficiency.

Regarding the deployment of platinum nanoparticles (Pt NPs) as electrocatalysts in the hydrogen evolution reaction (HER), three fundamental components—size, morphology, and crystallographic face arrangement-markedly influence their catalytic functionality. In general, the catalytic efficacy is predominantly determined by the dimensions of the nanoparticles. As the dimensions of the nanoparticle decrease, the surface area-to-volume ratio experiences an increase, thereby revealing a greater number of platinum atoms at the surface that serve as active catalytic sites. Notably, however, platinum nanoparticles within the dimensional range of 1 to 3 nm display an inverse correlation to this trend. Specifically, the specific mass activity of the platinum nanoparticles diminishes as their size falls within that range. Numerous investigations have been undertaken to elucidate this phenomenon, and a series of theoretical models have yielded persuasive rationales. It has been revealed that the planar sites on platinum single crystals possess lower activation energies and, as such, exhibit greater catalytic activity compared to their edge counterparts. Consequently, the augmentation of the edge-to-face site ratio as size diminishes results in a decline in the catalytic efficacy of platinum nanoparticles within the 1-3 nm range. For example, Tan and collaborators identified that the nearest-neighbor bridge site pairs located on the (100) facets account for approximately 75% of the nanoparticle's catalytic activity; conversely, the edge sites contribute no activity. By extrapolating the relative contributions to larger nanoparticles, wherein the ratio of face-to-edge sites increases, the deleterious size effect of platinum nanoparticles in relation to HER is instigated when their dimensions are less than 2 nm.[48]

The morphology of nanoparticles exerts a considerable influence on their surface characteristics and catalytic efficacy, as varying geometries unveil distinct crystallographic planes featuring unique atomic configurations. Elementary geometrical forms such as spheres and cubes expose (100) and (111) planes, whereas more intricate architectures, such as

ultrathin films, [49–52] nanoframes, [53–55] and branched or concave geometries, [56–58] provide an expanded surface area and improved accessibility to active sites, thereby enhancing catalytic performance. Advanced synthesis techniques, such as seed-mediated growth using surfactants, halide ions, or reducing agents, enable precise control over nanoparticle morphology. By tailoring these shapes, researchers can optimize catalytic properties for a range of applications, leveraging the specific electronic and geometric features that different planes provide. In essence, morphology design is a powerful tool in enhancing nanoparticle-based catalysis.[59]

Electrocatalysts made from abundant elements, including transition-metal nitrides, sulfides, and phosphides, have shown significant potential for the HER.[60] Nevertheless, electrocatalysts based on platinum continue to be regarded as the benchmark due to their unmatched catalytic activity for HER. Unfortunately, platinum's high cost and limited availability pose serious challenges to its widespread adoption. This has driven ongoing efforts to explore alternative materials that can deliver comparable catalytic performance at a lower cost.

## 2.2 Transition Metal Dichalcogenides (TMDs)

Transition metal dichalcogenides (TMDs) have emerged as a prominent category of materials in electrocatalysis, widely studied for their role in reactions related to environmental and energy applications, including the hydrogen evolution reaction, oxygen evolution reaction, oxygen reduction reaction (ORR), and carbon dioxide reduction reaction (CRR). Their unique electronic structure and crystalline structural characteristics make them highly suitable for these catalytic processes.[31,60–63] TMD catalysts, denoted chemically as $MX_2$ (where M represents Mo, Ta, Nb; and X signifies S, Se), are posited to be highly advantageous materials for hydrogen evolution owing to their relatively lower economic expenditure and elevated catalytic efficacy at their edges.[64–66] Despite the fact that bulk TMDs demonstrate subpar catalytic efficiency in hydrogen evolution reactions, shown by a Tafel slope of 692 mV $dec^{-1}$ and an onset potential of about 0.09 V vs RHE for bulk $MoS_2$ (Tafel slope of 18–24 mV $dec^{-1}$,

0 V vs RHE onset potential for Pt),[67] these materials exhibit adjustable band gaps, and the exfoliated monolayers can show metallic attributes under particular phases.

### 2.2.1 Molybdenum Sulfide

Among the various transition metal dichalcogenides, $MoS_2$ or molybdenum sulfide is extensively explored for its strong relationship with the HER. Extensive research over several decades has produced important revelations regarding its catalytic characteristics. $MoS_2$ can exist in three primary polymorphs based on the arrangement of S-Mo-S layers: hexagonal (2H), trigonal (1T), and rhombohedral (3R) forms.[68] In the 2H $MoS_2$ structure, $MoS_6$ units form edge-sharing trigonal prisms, with each unit cell containing two layers. The 3R phase, similar in single-layer coordination to the 2H form, consists of three layers per unit cell. The 1T phase, which is metastable, has a single layer per unit cell where molybdenum atoms exhibit octahedral coordination. Of these phases, the 2H and 1T forms are most commonly used in HER applications due to their superior catalytic performance.[19] Since crystal structures of $MoS_2$ (Fig 6) significantly influence the catalytic effect for HER, having rGO as a substrate will affect how the $MX_2$ grows and directly linked to the HER activitiy. The characteristics of these structures are elaborated below:

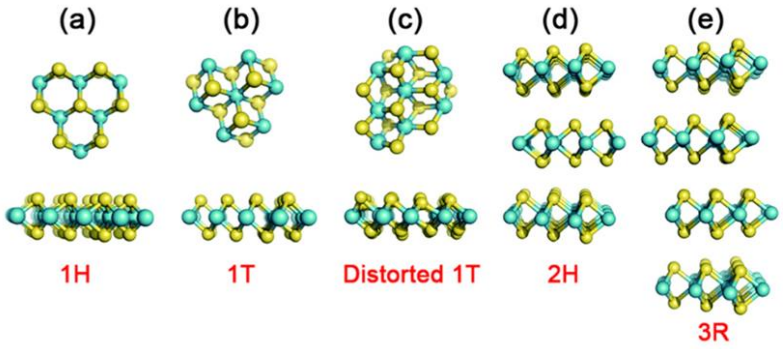


***Fig 2- 2. Structural polytypes of pristine $MoS_2$ layers (a) 1H, (b) 1T, (c) distorted 1T, or 1T', (d) 2H, (e) 3R phase. Chalcogen atoms are represented in yellow, and transition metal atoms are represented in blue.*** [68]

- The trigonal prismatic phase, typically semiconducting, is often denoted as 1H when referring to monolayers (see Fig. 2-2(a)).;
- The metallic phase with octahedral prismatic coordination is represented by the 1T structure (see Fig. 2-2(b)).
- In some instances, the 1T phase is thermodynamically unstable, leading to a structurally distorted variant known as the 1T' phase (see Fig. 2-2(c)).
- When $MoS_2$ crystals consist of multiple Sulfur-Molybdenum-Sulfur (S-Mo-S) layers in the 1H phase, held together by van der Waals (vdW) forces, additional polytypes emerge, reflecting different stacking arrangements (see Fig. 2-2(d)).
- Alternative stacking configurations can result in a rhombohedral 3R phase (see Fig 2-2(e)). [68,69]

In 2005, molybdenum disulfide ($MoS_2$) was first identified as a promising material for HER electrocatalysis, attributed to the catalytic properties of its edge sites. Initial theoretical calculations revealed that the Gibbs free energy change ($\Delta G_H$) at the Mo (1 0 $\bar{1}$ 0) edge site of $MoS_2$ is approximately 0.08 eV under conditions of 50% hydrogen coverage, nearly matching the ideal $\Delta G_H \approx 0$ value of platinum (Pt), which is close to zero (see Fig. 2-3(a)). Indicating that $MoS_2$ edge sites can effectively bind and release hydrogen, thereby facilitating efficient HER.[70]

Following these predictions, Jaramillo and colleagues conducted experiments that confirmed the HER activity of $MoS_2$'s edges. By analyzing the relationship between HER activity (exchange current density) and both perimeter length and surface area of $MoS_2$, measured with scanning tunneling microscopy (STM), they demonstrated that the HER rate correlates strongly with perimeter length rather than overall surface area. This finding emphasized the importance of edge sites as active sites in HER.[71] Since these insights, research has increasingly focused on enhancing the catalytic activity of $MoS_2$ by improving the ratio of edge sites to basal planes and modifying the material's structure. Common strategies include: (1) increasing the density of active edge sites, (2) creating defects and applying strain, (3) introducing heteroatom dopants, (4) adjusting phase structures, and (5) constructing $MoS_2$-based heterostructures. These approaches collectively aim to boost

$MoS_2$'s catalytic performance for HER applications by maximizing active sites and tuning surface properties.

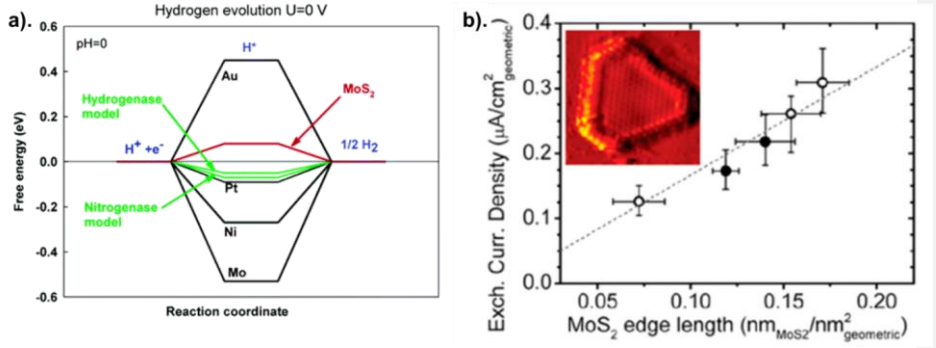


***Fig 2- 3. (a) The calculated free energy diagram for the HER on $MoS_2$ compared to various metals.*** [70] ***(b) Correlation between exchange current density and the edge length of $MoS_2$ nanoplatelets, as measured from the scanning tunneling microscopy (STM) image shown in the inset..*** [71]

#### 2.2.1.1 Increasing the Density of Active Edge Sites

In light of the remarkable catalytic efficacy exhibited at the edge sites of $MoS_2$, increasing the density of these sites has emerged as a primary objective for the enhancement of HER catalytic performance. This methodology is predicated on the notion that edge sites possess an intrinsic activity that surpasses that of basal planes, thus rendering their exposure pivotal for the optimization of catalytic efficiency. By maximizing the specific surface area, a greater quantity of edge sites per unit area becomes accessible, achievable through the engineering of $MoS_2$ in diverse nanoscale morphologies, including nanoparticles, nanowires, nanosheets, vertical nano-flakes, and mesoporous architectures. Each of these configurations offers a distinct pathway for accessing the active sites located at the edges, thereby converting $MoS_2$ into a highly effieciency electrocatalyst.[19]

For example, Kibsgaard and his team leveraged a double-gyroid (DG) silica template to fabricate interconnected thin $MoS_2$ films. This innovative structure features a bicontinuous network with nanopores and a highly curved surface, maximizing the exposure of active edge sites. By designing $MoS_2$ with a continuous and nanoporous network, they achieved a configuration that supports a large number of catalytic sites, which translates into superior

HER performance. This methodology emphasizes not just the presence of edge sites but also their accessibility and stability within a structured network, pushing the limits of HER efficiency.[72] In another study, Hu and colleagues developed vertical arrays of $MoS_2$ nanosheets with a distinctive stepped surface structure on carbon fiber paper. Using a microwave-assisted hydrothermal method, they achieved a highly ordered, vertically aligned $MoS_2$ structure that enhances edge site exposure. This arrangement offers optimal hydrogen adsorption characteristics, reaching an ideal $\Delta G_H = 0.02$ eV, very close to the thermoneutral point. Consequently, this structure exhibited outstanding HER performance, as demonstrated by an overpotential of only 104 mV at 10 mA $cm^{-2}$, an exchange current density of 0.2 mA $cm^{-2}$, and remarkable stability.[73]

These advancements highlight how crucial it is not only to increase the number of active sites but also to fine-tune their spatial arrangement and exposure. By designing specific structures that emphasize edge sites, researchers can tap into the full catalytic potential of $MoS_2$, offering a pathway toward cost-effective and high-performance electrocatalysis.

#### 2.2.1.2 Creating Defects and Applying Strain

Compared to the edge sites, the basal plane of $MoS_2$, with its robust stability and semiconducting nature, is generally considered thermodynamically favorable and largely inert to the hydrogen evolution reaction (HER) in its original form. This basal plane, which makes up a substantial portion of $MoS_2$'s surface, does not actively participate in HER, primarily due to its lack of reactive sites. In contrast, theoretical studies suggest that catalytic activity at $MoS_2$'s edges is driven by unsaturated sulfur atoms present at these sites. Therefore, edge sites and their associated activity can be introduced by creating structural defects within the basal plane of 2H $MoS_2$. [19] Introducing defects in the basal plane not only generates new edge-like sites but also alters the local electronic structure by adding energy levels between the valence and conduction bands. This adjustment helps to optimize the Gibbs free energy for hydrogen adsorption ($\Delta G_H$), making these modified basal sites more catalytically active. Common strategies for activating basal plane sites in $MoS_2$ include creating sulfur vacancies

and applying strain, both of which increase the density of active sites and improve HER performance.[74–76]

To achieve this, Xie and his team used a high concentration of precursor materials along with an excess of thiourea to produce $MoS_2$ nanosheets rich in defects. Thiourea played a dual role in this process, acting as a reducing agent to convert $Mo^{6+}$ to $Mo^{4+}$ and as a stabilizer for the ultrathin nanosheet structure. These defect-laden $MoS_2$ nanosheets demonstrated excellent HER performance, with an onset potential of just 120 mV in 0.5 M $H_2SO_4$ - a significant improvement over defect-free $MoS_2$ nanosheets. Inspired by Xie's approach, subsequent studies have explored the controlled introduction of sulfur vacancies during hydrothermal synthesis to further enhance catalytic efficiency.[77–79]

While $MoS_2$'s basal plane is inherently stable and inactive in its original form, introducing defects can unlock catalytic activity by creating reactive edge-like sites and modifying electronic states. Techniques such as sulfur vacancy creation and structural strain application have proven effective, with defect-rich $MoS_2$ nanosheets achieving impressive HER performance.

#### 2.2.1.3 Introducing Heteroatom Dopants

Doping represents a significant methodology for the alteration of the structural attributes and hydrogen evolution reaction catalytic efficiency of $MoS_2$. Without a doubt, cutting-edge density functional theory (DFT) evaluations have confirmed that the integration of cobalt (Co) dopants at the $MoS_2$ edges can reduce $\Delta G_H$ of the sulfur edges from 0.18 to 0.10 eV, while no variations have been observed for the molybdenum (Mo) edges, indicating that Co's introduction helps activate S edges as catalytic sites for HER. This assertion is corroborated by empirical findings that indicate Co-doped $MoS_2$ exhibits substantially improved performance in HER applications.[80] Building on these findings, researchers have been exploring different ways to boost $MoS_2$'s hydrogen evolution performance by adding various elements to its edges or basal plane. This encompasses precious metals such as platinum, gold, palladium, and ruthenium,[75,81–83] alongside more economical metals such as cobalt, iron, nickel, copper, vanadium, and zinc.[84–90] Additionally, nonmetals including oxygen,

nitrogen, phosphorus, and boron have been employed.[91–94] Each of these additions can bring something valuable to $MoS_2$'s catalytic abilities (whether it's better conductivity, altered electronic properties, or extra active sites) helping to make $MoS_2$ an even more effective catalyst for hydrogen production.

#### 2.2.1.4 Adjusting Phase Structures

As previously highlighted, the 2H $MoS_2$ exhibits semiconducting properties, which constrains the flow of electrons within its structure. The metallic 1T and disordered 1T′ phases of $MoS_2$ present significant advantages over the semiconducting 2H phase, primarily due to their superior electron conduction, which accelerates hydrogen evolution reaction (HER) kinetics. Computational studies reveal a stark contrast in band gaps: metallic 1T′ $MoS_2$ has an extremely narrow band gap of 0.006 eV, compared to the 2H phase's much wider band gap of 1.74 eV, underscoring its semiconducting nature. This enhanced conductivity, combined with a greater density of active edge sites, positions 1T $MoS_2$ as a highly promising material for efficient HER catalysis.[95] Supporting these findings, Lukowski et al. empirically demonstrated increased HER activity in 1T $MoS_2$ nanosheets, derived from 2H $MoS_2$ synthesized on graphite and exfoliated through n-butyl lithium intercalation. Structural analyses and electrochemical tests confirmed that these metallic nanosheets featured accelerated electrode kinetics, reduced transport losses, and a higher density of catalytic active sites, all of which contributed to enhanced intrinsic catalytic performance.[96] Additionally, theoretical insights suggest that HER on 1T $MoS_2$ follows the Volmer–Heyrovsky pathway, with the Heyrovsky step as the rate-limiting factor. The molybdenum edges in the 1T phase display similar HER activity to those in the 2H phase but with superior charge transfer kinetics, further solidifying 1T $MoS_2$'s potential as an effective HER catalyst.[97]

In summary, adjusting the phase structure of $MoS_2$ from the semiconducting 2H phase to the metallic 1T or 1T′ phases offers several key advantages for catalytic applications, particularly in HER. These benefits include enhanced electrical conductivity, optimized electronic structure with a nearly zero band gap, increased density of active edge sites, and improved hydrogen adsorption characteristics. Together, these features contribute to faster

reaction kinetics and lower overpotential requirements, making the 1T and 1T′ phases of $MoS_2$ highly promising for efficient and stable HER catalysis

#### 2.2.1.5 Constructing $MoS_2$-based Heterostructures

The incorporation of $MoS_2$ alongside conductive materials has been demonstrated as a particularly efficacious strategy for improving electrocatalytic efficacy in hydrogen evolution reactions. In a foundational 2011 study, Li et al. demonstrated this strategy by synthesizing $MoS_2$ nanoparticles on reduced graphene oxide (rGO), using $(NH_4)_2MoS_4$ as a precursor and GO as the substrate. This setup created numerous accessible edge sites on the $MoS_2$ nanoparticles while ensuring strong electrical connectivity to rGO, significantly boosting electron conductivity.[98]

Further theoretical studies reinforced the benefits of this approach, showing that conductive materials not only improve electron transport but also help tune the $\Delta G_H$ value, increasing HER efficiency.[99,100] As a case in point, Lee and associates (2021) succeeded in improving the hydrogen evolution reaction by implementing vertically aligned $MoS_2$/$WS_2$ heterostructures, a formation that promotes electron flow via distinctive shapes and greater interlayer gaps, thereby enhancing edge site accessibility.[101] Sharma and co-authors have also indicated that the implementation of thin-sheet $MoSe_2$/$MoS_2$ heterostructures considerably facilitates the HER across a spectrum of pH values, where the interaction between $MoSe_2$ and $MoS_2$ enhances charge dynamics and broadens hydrogen adsorption sites, thereby optimizing catalytic effectiveness.[102]

Overall, these studies underscore the importance of integrating $MoS_2$ with conductive phases, such as rGO or other transition metal dichalcogenides, to enhance HER performance. By improving electron transport, increasing the density of active edge sites, and optimizing $\Delta G_H$ , these modifications significantly elevate $MoS_2$'s catalytic efficiency, establishing conductive integration as a crucial strategy in the advancement of $MoS_2$-based HER catalysts.

### 2.2.2 Other TMDs.

$MoS_2$ is often considered a top contender due to its abundance and catalytic abilities, but alternative transition metal dichalcogenides are now being studied to optimize HER effectiveness.

Among molybdenum-based dichalcogenides, $MoSe_2$ has drawn comparatively less research interest than $MoS_2$, despite its notably higher intrinsic conductivity (approximately $10^{-1}$ S $cm^{-1}$ compared to $MoS_2$'s $10^{-2}$ S $cm^{-1}$).[103] Recently, Yin and colleagues developed a modified hydrothermal method to synthesize $MoSe_2$ nanosheets featuring both 1T and 2H phases. By adjusting the amount of $NaBH_4$ reducing agent and the reaction temperature, they tailored the phase ratio, achieving an optimal structure that supported a current density of 10 mA $cm^{-2}$ at an overpotential of 152 mV, with a Tafel slope of 52 mV $dec^{-1}$.[104]

Explorations into other TMDs have also revealed promising HER properties. Structurally akin to $MoS_2$, tungsten sulfide ($WS_2$) offers similar HER capabilities. Voiry and team employed lithium intercalation and exfoliation to create atomic-scale $WS_2$ nanosheets, observing that a higher concentration of the strained metallic 1T phase enhanced catalytic activity. This improvement was marked by a significant increase in exchange current density, directly linked to the concentration of active 1T phase sites.[65]

The compounds featuring the pyrite structure ($FeS_2$, $CoS_2$, $NiS_2$, and their respective alloys) have undergone analysis for their capabilities in electrocatalytic applications. A comprehensive evaluation highlighted a correlation between their electrocatalytic performance and their unique compositional and morphological features. Of these, $CoS_2$ exhibited the most promising HER kinetics, with cobalt playing a key role in accelerating the reaction rate, outperforming other metal pyrites in catalytic activity.[105]

Additionally, first-row transition metal dichalcogenides, including Fe, Co, and Ni paired with S or Se, have shown potential as HER catalysts. Kong and colleagues identified $Fe_{0.43}Co_{0.57}S_2$ and $CoSe_2$ as highly effective HER catalysts under acidic conditions. This

performance is attributed to the partially filled $e_g$-bands in their d-orbitals, which facilitate electron transfer, further boosting their catalytic efficiency. [106]

These findings illustrate the potential of various TMD-based materials in enhancing HER performance. By optimizing phase compositions, manipulating structural elements, and strategically selecting compositions, researchers have succeeded in improving conductivity, active site density, and catalytic rates. This strategic diversification across TMDs, such as $MoSe_2$, $WS_2$, and pyrite-phase alloys, positions these materials as strong candidates for efficient hydrogen evolution applications.

***Table 2-1. Performance of Various TMD Electrocatalysts for HER Under Different Reaction Conditions*** [19]

| Catalyst | Substrate | Electrolyte | Overpotential | | Tafel slope | Mass loading |
|---|---|---|---|---|---|---|
| | | | $\eta_{10}$ (mV) | $\eta_{100}$ (mV) | (mV dec$^{-1}$) | (mg cm$^{-2}$) |
| **$MoS_2$-based catalysts** | | | | | | |
| Ni-Co/1T $MoS_2$ [85] | GCE | 0.5 M $H_2SO_4$ | 70 | - | 38.1 | 0.14 |
| single-layer $MoS_2$ [107] | GCE | 0.5 M $H_2SO_4$ | 185 | - | 45 | - |
| porous 1T $MoS_2$ [108] | GCE | 0.5 M $H_2SO_4$ | 153 | - | 43 | 0.14 |
| P-$MoS_2$ NSs [109] | GCE | 0.5 M $H_2SO_4$ | 43 | ~90 | 34 | 0.32 |
| 1T' Pt-$MoS_2$ [81] | GCE | 0.5 M $H_2SO_4$ | 35 | - | 25 | 0.07 |
| $MoSSe_2$ nanodots [110] | GCE | 0.5 M $H_2SO_4$ | 140 | - | 80 | 1.0 |
| $MoS_2$@C [111] | CFP | 0.5 M $H_2SO_4$ | 136 | ~210 | 78 | 1.0 |
| | | 1.0 M KOH | 155 | ~290 | 99 | |
| SE-$MoS_2$ film [73] | CFP | 0.5 M $H_2SO_4$ | 104 | - | 59 | 3.2 |
| $MoS_2/Ni_3S_2$ [112] | NF | 0.5 M $H_2SO_4$ | 98 | ~190 | 61 | - |
| reduced $MoS_2$ [113] | NF | 1.0 M KOH | 71 | - | 100 | 0.8 |
| monolayer $MoS_2$ [74] | NPG | 0.5 M $H_2SO_4$ | 226 | - | 98 | - |
| monolayer 2H-$MoS_2$ [114] | Si | 0.5 M $H_2SO_4$ (pH 0.2) | 170 | - | 60 | - |
| porous $MoS_2$ film [72] | ITO | 0.5 M $H_2SO_4$ | 150 | - | 50 | - |
| **$MoSe_2$-Based catalysts** | | | | | | |
| 1T $MoSe_2$ [104] | GCE | 0.5 M $H_2SO_4$ | 152 | - | 52 | 5.0 |
| $MoSe_2$/SMCNT [115] | GCE | 0.5 M $H_2SO_4$ | 100 | 170 | 63 | - |
| b-$MoSe_2$ NSs [116] | CC | 0.5 M $H_2SO_4$ | 84 | - | 39 | 0.07 |

| | | | | | | |
|---|---|---|---|---|---|---|
| **Transition mental sulfides & phoshides** | | | | | | |
| CoSlP/CNT[117] | CFP | 0.5 M $H_2SO_4$ | 48 | 109 | 55 | 13 |
| $CoS_2$@Co@CNT[118] | GCE | 1.0 M KOH | 112 | ~250 | 106.9 | 1.6 |
| $CoMoS_3$ NRs[119] | GCE | 0.5 M $H_2SO_4$ | 143 | ~300 | 78 | 0.5 |
| | | 1.0 M KOH | 133 | ~300 | 105 | |
| Co-$WS_2$/$W_{18}O_{49}$[120] | FTO | 0.5 M $H_2SO_4$ | 201 | - | 49 | - |
| 1T $WS_2$ NSs[121] | Graphite | 0.5 M $H_2SO_4$ | 142 | - | 70 | - |
| $Ni_xCo_{3-x}S_4$/$Ni_3S_2$[122] | NF | 1.0 M KOH | 136 | 258 | 107 | - |
| Ni-Mo-S[123] | CC | 0.5 M $H_2SO_4$ | 200 | - | 85.3 | 0.56 |
| **Other HER catalysts** | | | | | | |
| $FeS_2$-rGO film[124] | - | 0.5 M $H_2SO_4$ | 139 | ~230 | 66 | - |
| FeS NSs[125] | CC | 1.0 M KOH | 142 | - | 36.9 | 0.2 |
| $(Fe_xNi_{1-x})_9S_8$[126] | GCE | 0.5 M $H_2SO_4$ | 138 | ~220 | 82 | 0.5 |
| | | 0.5 M $H_2SO_4$ | 143 | ~300 | 78 | |
| | | 0.5 M $H_2SO_4$ | 70 | ~150 | 53 | |
| $FePSe_3$/NC[127] | GCE | PBS (pH 7) | 140.1 | ~450 | 167 | 0.212 |
| | | 1.0 M KOH | 118.4 | ~230 | 88 | |

"SE, stepped edge surface; NSs, nanosheets; NWs, nanowires; NRs, nanorods; GCE, glassy carbon electrode; PA, 3D nanoporous gold; NF, nickle foam; CEP, carbon file paper; CC, carbon cloth."

As indicated in Table 2-1, catalysts derived from $MoS_2$ continue to demonstrate significant advantages in terms of their HER catalytic performance and the breadth of research conducted. In light of this, materials based on $MoS_2$ constitute the primary focus of investigation in this thesis.

## 2.3 The Impact of Graphene Oxide on the Properties of $MoS_2$

Graphene exhibits a substantial surface area and superior electrical conductivity, which facilitates additional active sites and enhances electron transfer during the hydrogen evolution reaction. In contrast, while multi-wall nanotubes (MWNTs) present a notable surface area conducive to the growth of $MoS_2$, their catalytic effectiveness is insufficient because of suboptimal electron transfer within the inner $MoS_2$ layers.[128,129] Compared to graphene, GO has oxygen functional groups which make it easier to get dissolved in solution and bind other

functional groups than graphene, however the conductivity of GO is worse than graphene. $MX_2$-GO can be reduced to $MX_2$-rGO (reduced graphene oxide), which increases the stability of the hybrid catalysts.

### 2.3.1 $MoS_2$/rGO Heterostructure

As previously articulated, the $MoS_2$/rGO heterostructure manifests as an exceptionally proficient electrocatalyst for promoting the hydrogen evolution reaction. [98] The interaction between $MoS_2$ and rGO creates a heterostructure that enhances the overall electrocatalytic performance. This synergy is attributed to the complementary properties of $MoS_2$ and rGO, where $MoS_2$ provides active sites for HER, and rGO enhances the structural stability and electron mobility.[130] Futhurmore, the formation of a 2D/2D hybrid heterostructure between $MoS_2$ and rGO further optimizes the catalytic performance by increasing the surface area and providing more active sites for the HER reaction.[131]

In addition to facilitating the generation of heterostructures with $MoS_2$, reduced graphene oxide can significantly augment catalytic efficacy by enhance electron mobility. The underlying mechanism that contributes to this benefit is elucidated in the following section.

### 2.3.2 Electron Transfer at The $MoS_2$ Layers and $MoS_2$-rGO Interface

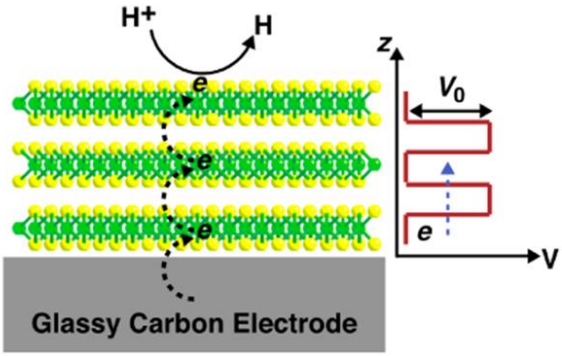


***Fig 2- 4. The vertical electron hopping (z-axis) within the layers of $MoS_2$ is a critical aspect of the hydrogen evolution reaction (HER) mechanism. Distribution of potential across the multilayer film (right), as well as the electron hopping phenomenon through the potential barrier present in the interlayer spacing (left).***[132]

It is established that the process of electron transfer occurring in a direction orthogonal to the basal plane of $MoS_2$ materials transpires via a hopping mechanism, attributable to the presence of potential barriers within the interlayer gap (Fig 2-4)[132]. This characteristic of electron transport is expected to be analogous in other $MX_2$ compounds, given their analogous X-M-X architecture and the fact that they are all interconnected by van der Waals (vdW) forces across the layers.[133] Such a transport mechanism suggests that the edge sites of $MX_2$ exhibit enhanced HER activities, resulting from a more energetically favorable pathway for electron hopping in comparison to the basal plane. Moreover, in addition to the incorporation of metallic dopants into $MX_2$, the $MX_2$/graphene composite is postulated to exhibit superior efficacy in enhancing electron transport efficiency.[132,134]

Figs. 2-5(a)-(b) show the comparative evaluation of charge transfer characteristics between clean $MoS_2$ and the $MoS_2$/graphene composite, with yellow markings representing areas of charge accumulation and blue markings illustrating charge depletion. The charge transfer in pristine $MoS_2$ predominantly transpires between the first and second layers; however, in the third layer, a conspicuous charge transfer is not evidently discernible. In $MoS_2$ and graphene composites, the delicate van der Waals (vdW) attractions in pristine $MoS_2$ support enhanced charge transfer, allowing for more flexible interactions. In contrast to pure $MoS_2$, which predominantly depends on vdW forces, the $MoS_2$/graphene heterostructure exhibits substantial charge transfer throughout all layers, with a significant ionic interaction occurring between the initial $MoS_2$ layer and graphene. This ionic interaction surpasses the typical strength of vdW forces, thereby facilitating enhanced conductivity. As demonstrated in Figs. 2-5(c)-(d), the variation in charge density along the z-direction on the (110) surface reveals regions of positive charge accumulation and regions of negative charge depletion, thereby supporting prior observations. This comparative analysis corroborates the findings deduced from Figs. 2-5(a)-(b). Fig. 2-5(e) shows averaged charge redistributions in the (x-y) plane for both pristine $MoS_2$ and the composite structure, mapped along the z-direction. In pristine $MoS_2$, the charge density difference approaches zero by the third layer (highlighted in pink), while the $MoS_2$/graphene composite exhibits varying charge density up to the graphene

layer, reflecting active $MoS_2$-graphene interactions. Fig. 2-5(f) further shows the average electrostatic potential, where pristine $MoS_2$ has an average energy of -5.47 eV compared to a more negative -5.91 eV in the $MoS_2$/graphene composite. This more negative value suggests that electron transfer from the electrode to $MoS_2$ along the z-direction is easier in the composite structure.[133]

In the $MoS_2$/graphene heterostructure, electron flow occurs from $MoS_2$ to graphene, attributed to graphene's slightly higher work function (4.57 ± 0.05 eV) compared to bulk $MoS_2$ (4.5 eV). [135] This difference creates a charge imbalance, leaving $MoS_2$ positively charged and graphene negatively charged. As the two materials' Fermi levels equalize, a built-in electric field forms from $MoS_2$ to graphene, promoting electron transfer. This coupling effect facilitates electron movement from the electrode through rGO to $MoS_2$, resulting in a higher negative charge density, which enhances catalytic performance for hydrogen evolution reactions (HER).[133,136]

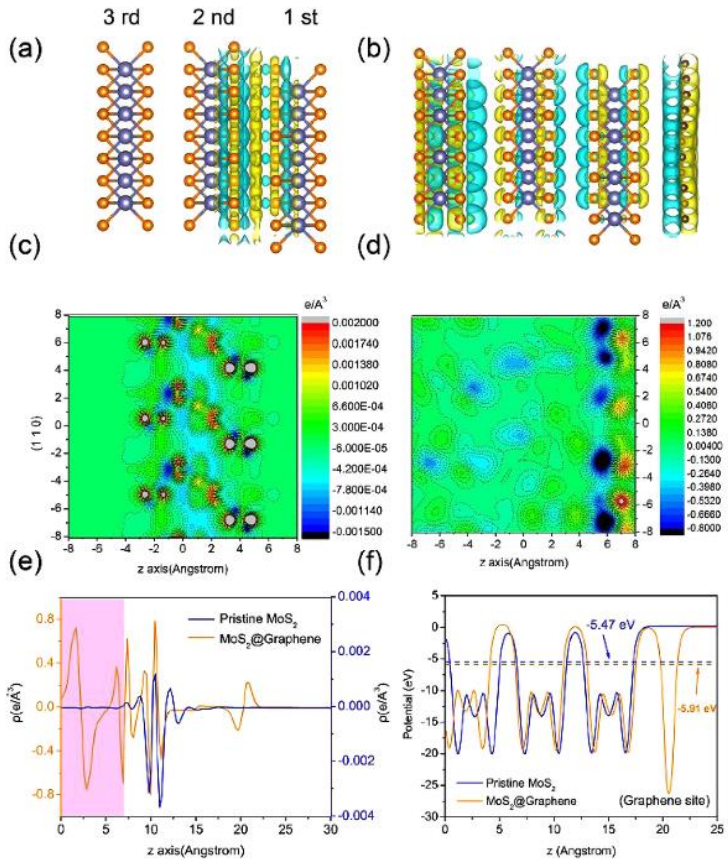


***Fig 2- 5. (a, b) Charge density differences for pristine $MoS_2$ (a) and $MoS_2$graphene composite (b). Blue regions indicate charge depletion, while yellow regions represent charge accumulation.***

***(c, d) Contour maps of charge density differences on the (110) plane for pristine $MoS_2$(c) and $MoS_2$/graphene (d).***

***(e) Charge density differences averaged in the x–y plane along the z-direction, comparing pristine $MoS_2$ (blue curve) and $MoS_2$/graphene (orange curve); the y-axis shows the charge density (ρ, e/Å$^3$), and the x-axis shows the distance along the z-direction (Å).***

***(f) Average electrostatic potential along the z-direction for pristine $MoS_2$ and $MoS_2$/graphene, with vacuum level set to zero; the respective work functions are indicated.***[133]

In summary, the $MoS_2$/graphene composite demonstrates significantly improved charge transfer compared to pristine $MoS_2$, primarily due to an ionic interaction that enhances conductivity beyond the typical van der Waals forces. This composite structure promotes

easier electron flow, driven by the higher work function of graphene relative to $MoS_2$, which establishes a built-in electric field from $MoS_2$ to graphene. This internal field facilitates electron movement through rGO to $MoS_2$, resulting in a higher negative charge density that enhances catalytic performance in HER.

# Experimental and Characterisation Techniques

This chapter investigates the various methodologies utilized in the synthesis, structural characterization, and performance assessment of transition metal dichalcogenides (TMDs), with a particular focus on $MoS_2$ and its significance in hydrogen evolution reaction (HER) applications. These methodologies yield essential insights into the crystalline structure, phase composition, surface morphology, hydrogen content, electrocatalytic efficacy, and electronic characteristics of TMDs, facilitating a thorough comprehension of their functional capabilities and optimization potential.

The assessment of HER performance in $MoS_2$ materials generally involves two primary analytical categories: structural and electrochemical analysis. Structural analysis serves a pivotal function in clarifying the mechanisms that govern the disparities in electrocatalytic performance. Non-destructive methodologies, including powder X-ray diffraction (XRD) and X-ray photoelectron spectroscopy (XPS), are utilized to examine the structural and compositional characteristics of the material, while Raman spectroscopy contributes to the comprehension of vibrational modes and variations in chemical bonding, thereby providing a comprehensive perspective on the architecture of $MoS_2$.

Nevertheless, these structural techniques are generally restricted to ex-situ conditions, which may not accurately replicate the operational environment of an electrolyzer. This limitation assumes that material properties remain constant between analytical and operational contexts, potentially introducing inaccuracies. To bridge this gap, in-situ analyses are conducted when feasible, with conditions adjusted to closely approximate real-world parameters. Ideally, in-operando analysis, which involves characterization under true operational conditions, would provide the most accurate data, though this remains challenging for many applications.

Conversely, the process of electrochemical characterization utilizes in-situ approaches that clarify important characteristics of the catalyst's behavior in the hydrogen

evolution reaction (HER). Practices such as electrochemical impedance spectroscopy (EIS) for appraising electrical impedance, cyclic voltammetry (CV) undertaken in the non-Faradaic domain to establish the electrochemically active surface area (ECSA), and linear sweep voltammetry (LSV) for reviewing overpotential and Tafel slope, are key for analyzing HER performance. These methods, as introduced in Chapter 1, section 3, form the basis for refining HER performance through structural and chemical modifications.

In summary, this chapter details the instrumental and methodological framework applied to the study of $MoS_2$-based HER catalysts. It begins with a discussion on hydrothermal synthesis methods for bulk $MoS_2$, followed by sections dedicated to ex-situ X-ray techniques and the analytical methods employed for data interpretation. These approaches collectively contribute to advancing our understanding of $MoS_2$'s electrocatalytic properties and optimizing its performance in HER applications.

## 3.1 Hydrothermal Synthesis

Hydrothermal processing relies on chemical reactions occurring in aqueous solvents or with mineralizers, facilitated by high-temperature and high-pressure conditions. These unique conditions allow typically insoluble or unreactive materials to dissolve and subsequently recrystallize or undergo structural transformations. [137] This method provides a controlled means to synthesize and modify materials, enabling the formation of specific crystal structures or morphologies that are challenging to obtain through conventional approaches

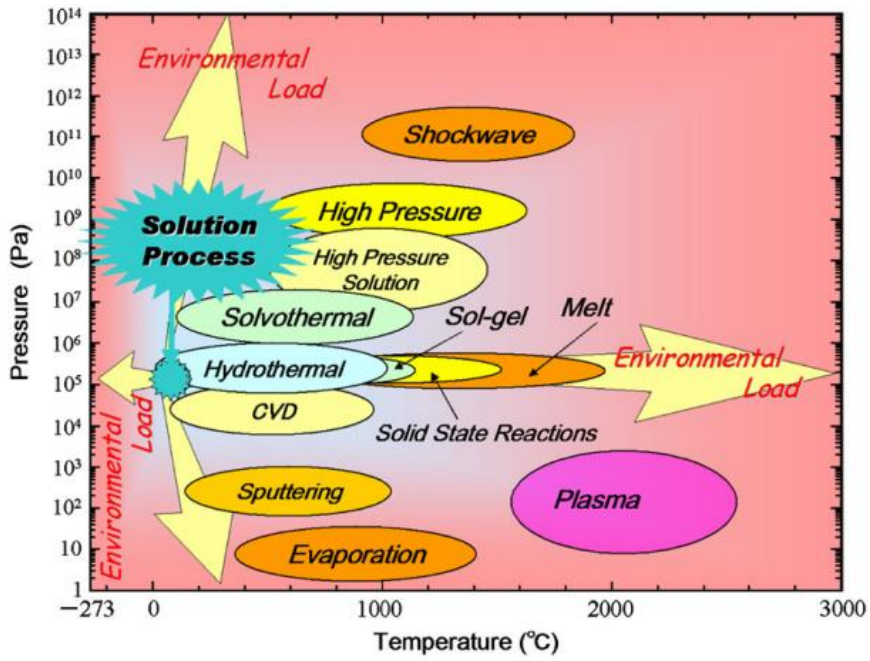


***Fig 3- 1. Pressure-Temperature Diagram of Various Material Processing Techniques and Environmental Loads.***[137]

The hydrothermal processing of materials constitutes a subset of solution processing, characterized as the manipulation of superheated aqueous solutions.[138] Figure 3-1 illustrates the phase transition map pertaining to various materials processing methodologies. In accordance with this framework, the hydrothermal processing of advanced materials can be regarded as environmentally sustainable, wherein hydrothermal synthesis utilizes water as the principal solvent, which is plentiful, non-toxic, and ecologically safe. This stands in stark contrast to conventional synthesis methodologies that frequently depend on hazardous organic solvents, thereby mitigating the environmental repercussions and health hazards linked with chemical synthesis. Furthermore, when it comes to the fabrication of nanomaterials, the hydrothermal approach presents distinct advantages due to the highly regulated diffusivity within a robust solvent medium in a closed system. The successful application of nanomaterials as functional entities necessitates meticulous control over their

physicochemical properties. As the dimensions are diminished to the nanoscale, these materials exhibit distinctive and remarkable mechanical and physical properties, including enhanced strength, greater diffusivity, and increased specific heat and electrical resistance, compared to their conventional large-grain counterparts, due to the effects of quantization.[139]

### 3.1.1 Instrumentation in hydrothermal processing of nanomaterials

Hydrothermal material processing requires specialized pressure vessels designed to endure highly corrosive solvents under extreme temperature and pressure conditions. Researchers rely on these vessels (commonly known as autoclaves, reactors, or high-pressure bombs) to maintain stable performance in demanding environments. Crafting the ideal hydrothermal setup is challenging, as each research project has unique requirements, but some essential features of an effective autoclave include:[137]

- **Chemical Resistance:** The vessel must withstand aggressive chemicals, including strong acids, bases, and oxidizing agents, to prevent degradation.
- **Ease of Use:** It should be easy to assemble and disassemble, facilitating straightforward sample loading and maintenance;
- **Temperature Control:** A sufficient length is needed to establish the desired temperature gradient, ensuring precise thermal conditions;
- **Leak-Proof Design:** The vessel should be tightly sealed to safely contain high pressures and temperatures, meeting specified experimental ranges;
- **Durability:** Robust construction is essential for withstanding prolonged high-pressure and high-temperature exposure without frequent repairs or maintenance.

In addition to the structural and functional features of an effective autoclave, several safety issues must be carefully addressed during hydrothermal synthesis operations:

- **Pressure Build-Up Risks:** Improper sealing or overfilling of the autoclave can lead to dangerous pressure build-up. It is essential to leave sufficient headspace in the vessel and to avoid exceeding the manufacturer’s recommended limits.

Thermal Shock: Sudden temperature changes, especially during cooling, can cause thermal shock and vessel rupture. Gradual heating and controlled cooling are necessary to maintain vessel integrity.

- **Chemical Reactivity:** Reactive or volatile substances used under hydrothermal conditions may produce unexpected by-products or pressure surges. Therefore, chemical compatibility and possible reaction pathways should be evaluated beforehand.
- **Maintenance and Inspection:** Regular maintenance and pre-use inspection of sealing components and rupture disks are crucial to identify wear or defects that could compromise safety.

By combining well-designed autoclave features with rigorous operational safety protocols, the risks associated with hydrothermal synthesis can be significantly minimized, ensuring both experimental success and laboratory safety.

To ensure these qualities, autoclaves are usually fabricated from robust alloys, particularly the 300 series of austenitic stainless steel, which grants both structural integrity and resistance to oxidation. When reactions transpire directly within the containment vessel, it is imperative to select materials that exhibit superior corrosion resistance. In certain scenarios, additional linings may be unnecessary. Nevertheless, for reactions that occur in highly corrosive conditions, such as those involving aqueous phosphoric acid or extreme pH levels, a Teflon lining is frequently indispensable to safeguard the vessel and ensure its durability.[137]

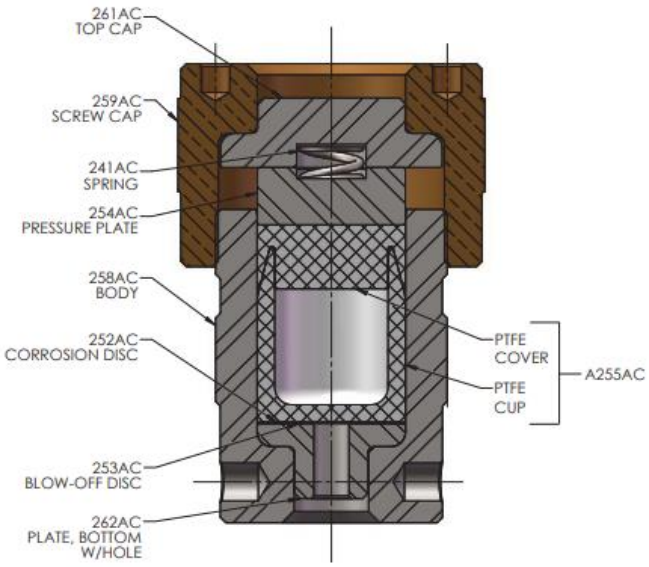


***Fig 3- 2. 4746 High Strength Acid Digestion Vessel***

Figure 3-2 illustrates the predominant designs of autoclaves. In this particular autoclave, the pressure can be determined employing the PVT relationships for water as delineated by Kennedy.[140] Figure 3-3 shows the PVT relations in the $SiO_2$-$H_2O$ system.

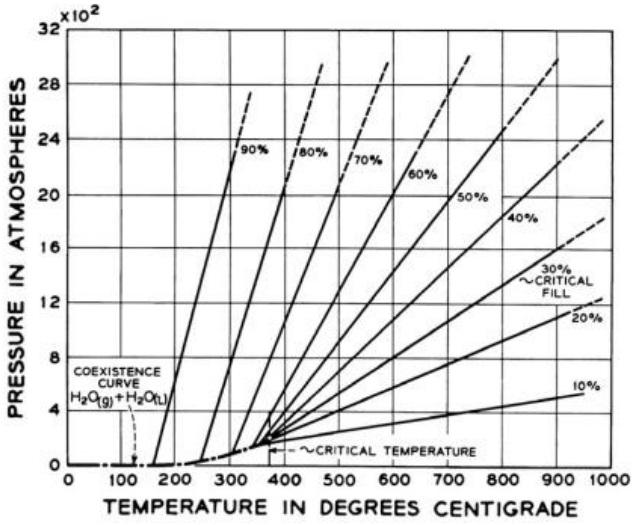


***Fig 3- 3. Kennedy's Pressure-Volume-Temperature (PVT) Diagram for the $SiO_2$-$H_2O$ System***[140]

### 3.1.2 Hydrothermal processing of molybdenum disulfide ($MoS_2$)

The fabrication of $MoS_2$ through hydrothermal processing is a thoroughly investigated technique attributed to its straightforwardness, economic viability, and capacity to yield high-quality nanostructures. This procedure necessitates the employment of particular precursors, regulated thermal conditions, and reaction durations to attain the targeted morphology and characteristics of $MoS_2$.[141]

$(NH_4)_6Mo_7O_{24}\cdot 4H_2O$ is recognized for its exceptional purity, which is essential for the synthesis of $MoS_2$ with minimal contamination. This guarantees that the resultant $MoS_2$ retains its requisite characteristics, including electrical conductivity and catalytic efficacy.[142] For the hydrothermal system, $(NH_4)_6Mo_7O_{24}\cdot 4H_2O$ must be initially dissolved in deionized water (resistivity of 18 MΩ cm). During this procedure, an ionization equilibrium is established. $(NH_4)_6Mo_7O_{24}\cdot 4H_2O$ tends to form molybdic acid ($Mo_7O_{24}^{6-} \leftrightarrow MoO_4^{2-} \leftrightarrow H_2MoO_4$).[143] This process is completed in a relatively short duration at ambient temperature. Mo (VI) preferentially exists in a 6-coordination compound,[144] indicating that molybdic acid exhibits a 6-coordinate structural configuration. In this study, three distinct geometries of molybdic acid are delineated, namely $Mo(OH)_6$, $MoO(OH)_4\cdot H_2O$, and $MoO_2(OH)_2\cdot 2H_2O$. These structural forms are capable of interconversion through hydrogen transfer, with $MoO(OH)_4\cdot H_2O$ possessing the lowest energy among the three geometries. In other terms, $MoO(OH)_4\cdot H_2O$ is regarded as the most stable configuration in the aqueous solution.[145] As the temperature and pressure undergo elevation, $\mathrm{MoO(OH)_4}$decomposition occurs, and subsequently, a product $\mathrm{MoO_3}$ is generated (eq 3-1 and eq 3-2).

$$(NH_4)_6Mo_7O_{24}\cdot 4H_2O + 7H_2O \rightarrow 6NH_3 + 7MoO(OH)_4 \quad eq\ 3\text{-}1$$

$$MoO(OH)_4 \rightarrow MoO_3 + 2H_2O \quad eq\ 3\text{-}2$$

Subsequently, based on the utilization of thiourea ($CSN_2H_4$) or thioacetamide ($CH_3CSNH_2$) as the sulfur precursor, the reactions delineated in Equations (3-3) and (3-4) were executed correspondingly. The principal product resulting from these reactions (as presented in Eqs. (3-3) and (3-4)) is hydrogen sulfide ($H_2S$), which plays a pivotal role in the

synthesis of $MoS_2$. Thereafter, hydrogen sulfide facilitates the reduction and sulfurization of $MoO_3$, culminating in the formation of $MoS_2$ nuclei as the ultimate product.[146]

$$CSN_2H_4 + 2H_2O \rightarrow 2NH_3 + CO_2 + H_2S \quad eq\ 3\text{-}3$$

$$CH_3CSNH_2 + 2H_2O \rightarrow CH_3CONH_2 + H_2S \quad eq\ 3\text{-}4$$

A significant distinction between thiourea and thioacetamide as sulfur sources lies in the kinetics of their thermal decomposition at elevated temperatures.[147] Thioacetamide decomposes rapidly and completely at the beginning of the reaction, resulting in an initial burst of sulfur. This leads to the formation of numerous $MoS_2$ nuclei early on, with limited sulfur available for further growth, producing randomly oriented nanosheets (Fig. 3-4a). In contrast, thiourea decomposes more gradually at elevated temperatures, providing a steady sulfur supply. This slower release means fewer $MoS_2$ nuclei form initially, while ample sulfur remains available throughout the growth phase, encouraging the nanosheets to adopt a spherical arrangement to minimize surface energy. As a result, this process yields larger nanoflowers (Fig. 3-4b). [146] In crafting hierarchical $MoS_2$ microspheres, polyethylene glycol (PEG 20000, MW = 16000 - 24000) serves as a soft templating agent, guiding the self-assembly of layered and porous structures during hydrothermal synthesis. This promotes improved structural uniformity and enhances the mechanical integrity of the resulting microspheres.[148]

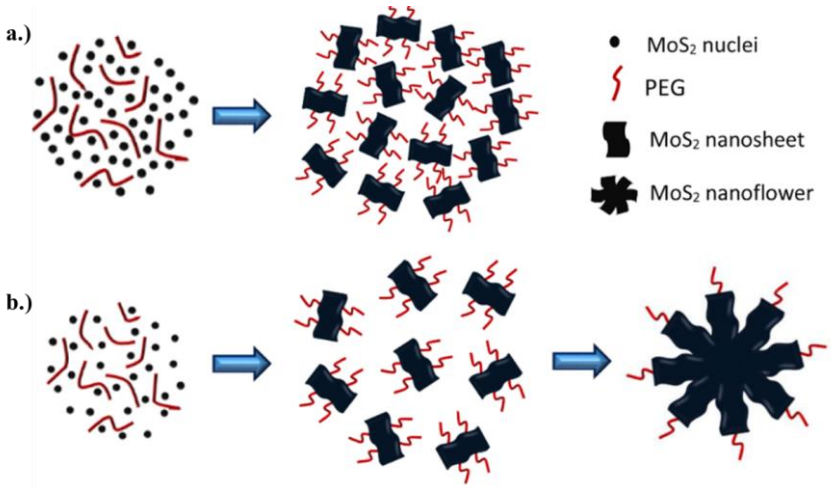


***Fig 3- 4. Schematic illustration of synthesis mechanism of a.) $MoS_2$ nanosheets and b.) $MoS_2$ nanoflower.***[146]

$$MoO_3 + 3H_2S + H_2O \rightarrow MoO_2 + SO_4^{2-} + 2H^+ \quad eq\ 3\text{-}5$$

$$MoO_2 + 2H_2S \rightarrow MoS_2 + 2H_2O \quad eq\ 3\text{-}6$$

As the reaction moves forward, $MoO_3$ reacts with $H_2S$ and $H_2O$, thereby yielding $MoO_2$, $SO_4^{2-}$, and protons. Throughout this procedure, molybdenum undergoes reduction (moving from $Mo^{6+}$ to $Mo^{4+}$), in contrast, sulfur goes through oxidation (moving from $S^{2-}$ to $S^{6+}$). Then, $MoO_2$ combines with remanent $H_2S$ resulting in $MoS_2$ and $H_2O$ (Equation 3-5 and 3-6).

## 3.2 X-ray Diffraction (XRD)

As a vital method, X-ray diffraction (XRD) allows researchers to explore the structural attributes of crystalline compounds. Initially unveiled through the groundbreaking endeavors of Wilhelm Conrad Röntgen in 1885, [149] and subsequently refined by Max von Laue in 1912, [150] XRD has emerged as an essential analytical approach, particularly following Laue's Nobel Prize-winning revelation regarding the scattering of X-rays within crystalline substances.[151–153] From the time Laue conducted his innovative studies, X-ray diffraction (XRD) has risen as a key and significant approach for understanding the structural attributes of crystalline compounds. The technique's unique ability to provide atomic-level structural insights stems from the wavelength of X-rays, typically between 0.5 and 2.5 Å, [149] which aligns closely with

atomic distances in solids. XRD has profoundly impacted numerous fields, including polymer science, metallurgy, [149] structural biology, pharmaceutical science, [154–158] geology, [159,160] and catalysis. [150,161–163] Its influence is evident from the numerous Nobel Prizes awarded, including three to physicists who advanced XRD as a technique and twenty-two to researchers who used it to reveal the structures of biological molecules. [149]

At its essence, XRD serves as a comprehensive characterization method that reavels the atomic and molecular architecture of crystalline solids through the examination of how incoming X-rays are scattered by the material. By investigating the angles and intensities of the scattered beams, researchers can create a three-dimensional representation of electron density within the crystal, enabling them to find out the typical atomic placements This ability to precisely describe atomic arrangements makes XRD invaluable in fields such as catalyst development, where it aids in understanding the bulk structure and composition of materials like metal oxides, perovskites, and zeolites. In the sections that follow, the fundamental principles of XRD are outlined, with additional resources recommended for readers seeking deeper insights into the physics and data analysis associated with the technique. [163]

### 3.2.1 Sources of X-Rays

The chief origin of X-rays lies within an X-ray tube, featuring a vacuum-sealed configuration comprising a cathode and an anode. As rapid electrons are emitted from the cathode (frequently crafted from tungsten filament), they strike a metallic anode, typically composed of copper, molybdenum, or aluminum. This collision produces X-rays along with thermal energy.

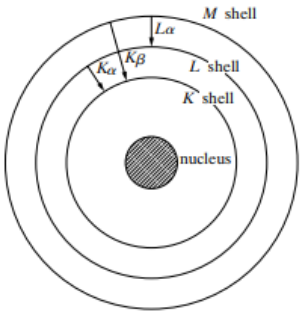


***Fig 3- 5. Schematic of electronic transitions in an atom with emission processes indicated by arrows.***[164]

As illustrated in Fig. 3-5, when a high-velocity electron strikes the anode, it ejects an electron from one of the inner shells of the metal atom, typically the K shell. This vacancy is quickly filled by an electron moving down from a higher-energy shell (such as the L or M shell), which releases an X-ray photon corresponding to the energy gap between the shells. The emitted radiation is categorized based on the shell transition. If the transition is from the L shell to the K shell (an adjacent shell transition), it's known as $K_\alpha$ radiation. For a transition from the M shell to the K shell (non-adjacent shells), the emission is termed $K_\beta$ radiation. Because the energy difference is greater for the $K_\beta$ transition, its wavelength ($\lambda_{K\beta}$) is shorter than that of Kα ($\lambda_{K\alpha}$). [164,165] Further distinctions exist within the Kα line, specifically $K_{\alpha1}$ and $K_{\alpha2}$, which result from transitions within different L subshells to the K shell. $K_{\alpha1}$ arises when an electron moves from the $L_3$ subshell ($2p_{3/2}$) to the K shell (1s), while $K_{\alpha2}$ corresponds to an electron moving from the $L_2$ subshell ($2p_{1/2}$) to the K shell (1s). $K_{\alpha1}$ has a slightly shorter wavelength and higher energy than $K_{\alpha2}$ due to the $L_3$ subshell being closer to the nucleus than $L_2$, creating a larger energy gap. The L shell, which is the second principal energy level, includes three subshells: $L_1$ (2s), $L_2$ ($2p_{1/2}$), and $L_3$ ($2p_{3/2}$). The energy differences between these L levels and the K shell lead to X-ray emission whenever an electron transitions from an L level down to the K shell. [164]

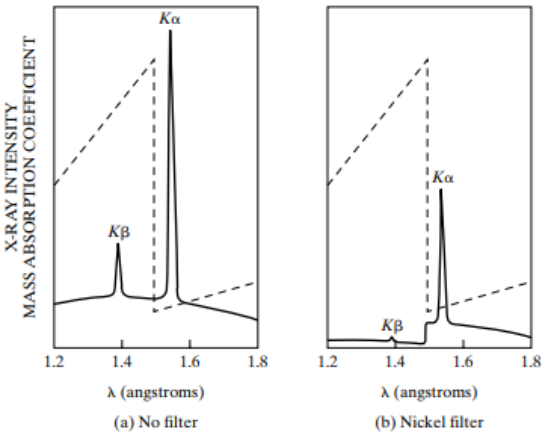


***Fig 3- 6. Schematic comparison of copper radiation spectra: (a) without and (b) with nickel filter***

***The dashed line represents nickel's mass absorption coefficient.***[164]

Traditionally, X-ray filters were used to remove unwanted radiation; for example, a nickel (Ni) filter can selectively reduce Cu-$K_\beta$ radiation (illustrated in Fig. 3-6).[164] However, filters have limitations: they cannot effectively minimize high background radiation and tend to allow a wide range of wavelengths to pass through, making them less precise for isolating specific wavelengths. [165]

To address these issues, modern X-ray systems primarily rely on monochromators (particularly single-crystal monochromators) which provide more refined wavelength selection. These monochromators are typically made from materials like pyrolytic graphite, which offers broader wavelength selection, or silicon, which is more selective. By exploiting the crystal structure of these materials, monochromators allow precise isolation of the desired wavelength range ($\lambda_{K\beta}$ or $\lambda_{K\alpha}$) from the emitted radiation, enhancing the clarity and accuracy of X-ray measurements. [165]

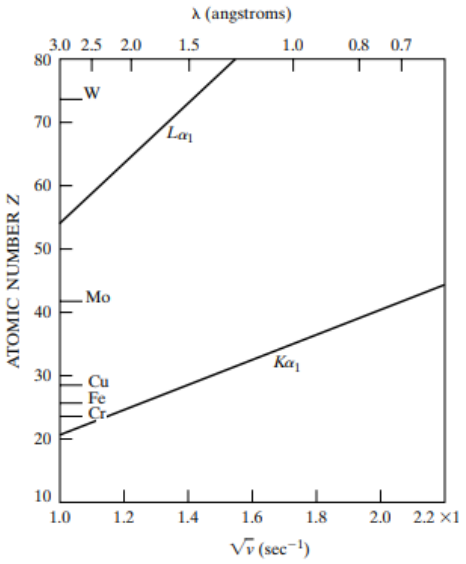


***Fig 3- 7. Moseley's relation between, and Z for two characteristic lines.*** [164]

The anode composition, potentially featuring chromium, iron, cobalt, copper, molybdenum, silver, and magnesium, directly influences the wavelength of the X-rays emitted, but options are restricted because of the rigorous demands for choosing the right anodic metals, which must have high melting points and exceptional thermal conductivity. Following Moseley's law ($\sqrt{\nu} = C(Z - \sigma)$ where $\nu$ denotes the frequency associated with the emitted X-ray radiation. $Z$ represents the atomic number corresponding to the specific element in question. $\sigma$ signifies the shielding constant, which reflects the extent of nuclear charge screening by inner-shell electrons. $C$ is a constant that is contingent upon the transition between energy levels as well as the intrinsic properties of the atom.[166] raising the atomic number of the anode material results in a shorter wavelength of Kα, designated as $\lambda_{K\alpha}$. For instance, the Kα wavelengths pertaining to often used anode metals are listed as: chromium, 2.29 Å; iron, 1.94 Å; cobalt, 1.79 Å; copper, 1.54 Å; molybdenum, 0.71 Å; and silver, 0.56 Å (shown in Fig 3-7). It's noteworthy that copper and molybdenum are primarily employed as anodes in standard lab XRD equipment. The choice of anode material (and consequently the

wavelength $\lambda_{K\alpha}$) is essential for successful XRD characterization, as the selected wavelength directly impacts the energy of the X-rays. This energy level determines the penetration depth (or mean free path length) of the X-rays as they interact with the material's surface and internal structure Furthermore, the wavelength that is selected plays an essential part in affecting multiple aspects of the resulting diffractogram, which includes peak intensity, the amount of identifiable peaks, and the degree of background noise found in the XRD data collected. Careful selection of the anode material and wavelength is therefore crucial to optimizing the clarity and detail of the XRD results.[164,165]

### 3.2.2 Crystalline Solids and XRD

Diffraction constitutes an elastic scattering phenomenon that X-rays undergo upon their interaction with the atomic structure of a crystalline solid. This scattering happens when a plane wave encounters an obstacle or opening with dimensions similar to the X-ray wavelength (around 0.5-2.5 Å).[150] In the most basic X-ray scattering experiment, an X-ray beam interacts with the sample, and the intensity of scattered radiation is measured as it varies with the scattering angle. In a typical X-ray scattering experiment, an X-ray beam is directed at the sample, and the scattered radiation intensity is measured at different angles. The scattering, caused by multiple atomic planes within the crystal, results in both constructive and destructive interference. Constructive interference enhances the scattered intensity, while destructive interference diminishes it.

The condition for constructive interference, captured by Bragg's Law, [152,167] was defined in 1913 by Sir W.H. Bragg and his son Sir W.L. Bragg. [167–169] According to Bragg's Law:

$$n\lambda = 2d\,sin\,\theta \quad eq\,3\text{-}7$$

Where $n$ is an integer representing the order of reflection, $\lambda$ is the X-ray wavelength, $d$ is the distance between the scattering planes in the crystal, and $\theta$ is the angle of incidence. This principle is fundamental to understanding diffraction patterns: when the conditions of

Bragg's Law are met, scattered waves align constructively, allowing the internal structure of the crystal to be mapped based on the intensities and angles of the diffracted beams.

A crystalline solid is characterized by a systematic organization of particles (atoms, molecules, or ions) in stable locations, forming a lattice structure. [170] One can envision a lattice as a repeating grid of points in space, where every point shares an identical neighboring environment.[150] The classification of the crystalline structure is dictated by the particles and forces at play: ionic (e.g., NaCl), covalent (e.g., diamond), molecular (e.g., ice), or metallic (e.g., gold), with each category showcasing unique structural and physicochemical properties. Regardless of type, every crystalline solid possesses a unit cell (the smallest repeating unit) that builds the entire lattice through three-dimensional translation, forming the overall crystal structure. [170] Through the exploration of X-ray diffraction patterns, scientists can unveil intricate details regarding the atomic organization, distances, and bonding characteristics present within a crystal. This technique is invaluable in fields ranging from materials science to biology, where the precise atomic structure often determines a material's or molecule's properties and function.

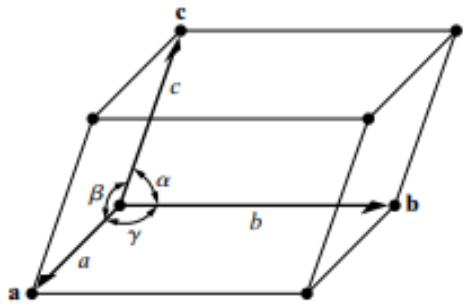


***Fig 3- 8. Depiction of Lattice Vectors and Designated Interaxial Angles*** [164]

A Bravais lattice, named after August Bravais, is an infinite array of points that represents a crystalline structure in three-dimensional space through translation.[171–173] Each of the 14 unique Bravais lattices has specific properties defined by six lattice parameters (Fig. 3-8):

- The lengths of the unit cell along the $x$, $y$, and $z$ axes, labeled as a, b, and c, respectively.

- The angles between these lengths: α (between b and c), β (between a and c), and γ (between a and b).

The values of these parameters vary based on the type of lattice. [171] For example, in an orthorhombic lattice, a ≠ b ≠ c and α = β = γ = 90°. [171] In a tetragonal lattice a = b ≠ c, and all angles are α = β = γ = 90°. [171] In a triclinic lattice, both side lengths and angles differ (a ≠ b ≠ c, and α ≠ β ≠ γ). Although in simple cubic, tetragonal, and orthorhombic unit cells, the axes a, b, and c align directly with the Cartesian coordinates $x$, $y$, and $z$. However, this alignment does not apply to all crystal structures, as many other lattices feature axes and angles that deviate from the orthogonal arrangement found in these specific unit cells Therefore, the Cartesian axes should be viewed as general indicators of three-dimensionality rather than strict orthogonality.

The 14 Bravais lattices are categorized into seven crystal systems, which are further classified into 32 crystallographic point groups. A crystallographic point group defines the set of symmetry operations (like rotation) that preserve the position of a point within the lattice. Point groups maintain the lattice's three-dimensional translational symmetry, characteristic of crystalline solids. Together with additional symmetry operations, a point group forms a space group (the complete set of transformations that leave the lattice invariant). In three-dimensional space, there are 230 unique space groups. [171]

Within the crystal lattice, the spatial arrangement of particles creates planes, identified by their intersections with the three axes. These planes can be described in reciprocal space using Miller indices, a notation system widely used in crystallography to define lattice planes. Miller indices $(h, k, l)$ - $(h, k, l)$ represent the reciprocals of the fractional intercepts that the plane makes with the crystallographic axes. [150] For example, as illustrated in Fig. 3-9, a plane parallel to an axis (intersecting it at infinity) has Miller indices that reflect this alignment. In Fig. 3-9(a) the fractional coordinates of a plane intersecting only the x-axis are $(\frac{a}{a}, \frac{\infty}{b}, \frac{\infty}{c})$, resulting in Miller indices of $(h,k,l) = \left(\frac{x}{a}, \frac{y}{b}, \frac{z}{c}\right)^{-1} = (\frac{a}{a}, \frac{b}{\infty}, \frac{c}{\infty}) = (1,0,0)$. In Fig 3-

9 (b), a plane with fractional coordinates $(\frac{0.5a}{a}, \frac{0.5b}{b}, \frac{0.5c}{c})$ has Miller indices of $(h, k, l) = (2,2,2)$. [165]

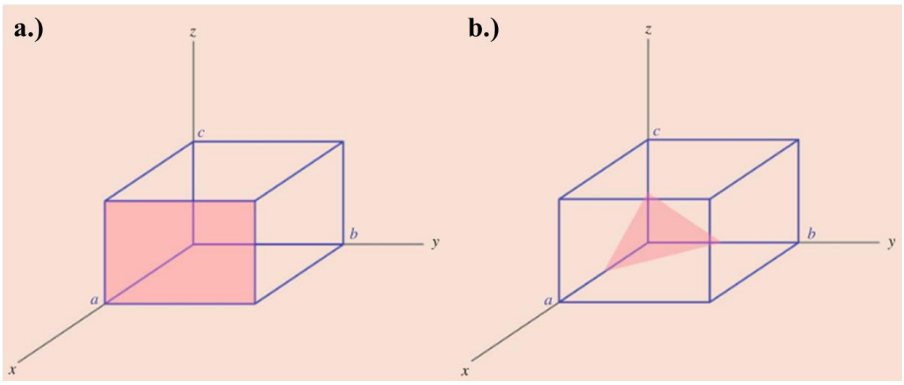


***Fig 3- 9. Three-Dimensional Representation of an Orthorhombic Unit Cell with Relative Lengths Labeled as a (x), b ( y), and c (z). a.) the shaded region indicates the (100) plane; b.) the shaded region indicates the (222) plane.[165]***

With a basic understanding of Miller indices and planes established, we can now explore how Miller indices relate to the planes observed in X-ray diffraction peaks. s illustrated in Figure 3-9(b), atomic planes are identified by specific Miller indices, such as (222). In practice, a single (222) plane does not exist independently; rather, there is a full set of parallel planes equivalent to (222) plane, collectively denoted as <222>. The spacing between these parallel planes is known as the interplanar spacing, represented by '$d$' - the same spacing variable used in Bragg's equation (eq 3-7).

n conventional notation, the interplanar spacing for any given set of planes is designated with the Miller indices as a subscript. Thus, for the <222> planes, the interplanar spacing is expressed as $d_{222}$. Numerous formulas exist that link interplanar spacing to lattice constants a, b, and c for different unit cell systems, allowing for precise calculations of crystal geometry and corresponding diffraction patterns. These relationships are essential for interpreting X-ray diffraction data and understanding the structural details of crystalline materials. [164]

- $Cubic\ Lattice\ Structure$: $\frac{1}{d_{hkl}^2} = \frac{h^2+k^2+l^2}{a^2}$ $eq\ 3\text{-}8$

In a cubic system, all three lattice parameters are equal ($a = b = c$), and all angles are 90°.

- $Tetragonal\ Lattice\ Structure$: $\frac{1}{d_{hkl}^2} = \frac{h^2+k^2}{a^2} + \frac{l^2}{c^2}$ *eq 3-9*

  In a tetragonal system, $a = b \neq c$, and all angles are 90°.

- $Orthorhombic\ Lattice\ Structure$: $\frac{1}{d_{hkl}^2} = \frac{h^2}{a^2} + \frac{k^2}{b^2} + \frac{l^2}{c^2}$ *eq 3-10*

  In an orthorhombic system, $a \neq b \neq c$, and all angles are 90°

- $Hexagonal\ Lattice\ Structure$: $\frac{1}{d_{hkl}^2} = \frac{4}{3} \cdot \frac{h^2+hk+k^2}{a^2} + \frac{l^2}{c^2}$ *eq 3-11*

  In a hexagonal system, $a = b \neq c$, and the angles are 90°, 90°, 120°.

- $Rhombohedral\ (Trigonal)\ Lattice\ Structure$: $\frac{1}{d_{hkl}^2} = \frac{h^2+k^2+l^2}{a^2} sin^2\alpha + \frac{2(hk+kl+hl)}{a^2}(cos^2\alpha - cos\alpha)$ *eq 3-12*

  In a rhombohedral (or trigonal) system, $a = b = c$, but the angles are $\alpha = \beta = \gamma \neq 90°$.

- $Monoclinic\ Lattice\ Structure$: $\frac{1}{d_{hkl}^2} = \frac{1}{\sin^2\beta}\left(\frac{h^2}{a^2} + \frac{k^2\sin^2\beta}{b^2} + \frac{l^2}{c^2} - \frac{2hl\cos\beta}{ac}\right)$ *eq 3-13*

  In a monoclinic system, $a \neq b \neq c$, with angles $\alpha = \gamma = 90°$ and $\beta \neq 90°$.

- $Triclinic\ Lattice\ Structure$: $\frac{1}{d_{hkl}^2} = \frac{1}{V^2}(S_{11}h^2 + S_{22}k^2 + S_{33}l^2 + 2S_{12}hk + 2S_{23}kl + 2S_{31}hl)$ *eq 3-14*

  In a triclinic system, $a \neq b \neq c$ and all angles are $\alpha \neq \beta \neq \gamma \neq 90°$. The lattice parameter formula is more complex due to the asymmetry. In this system, $V$ is the unit cell volume and The constants $S_{11}, S_{22}, S_{33}, S_{12}, S_{23}, S_{31}$ are related to the lattice parameters and the angles between the axes. Where $S_{11} = b^2c^2\sin^2\alpha, S_{22} = a^2c^2\sin^2\beta, S_{33} = a^2b^2\sin^2\gamma, S_{12} = abc^2(\cos\alpha\cdot\cos\beta - \cos\gamma), S_{12} = abc^2(\cos\alpha\cdot\cos\beta - \cos\gamma), S_{23} = a^2bc(\cos\beta\cdot\cos\gamma - \cos\alpha), S_{31} = ab^2c(\cos\gamma\cdot\cos\alpha - \cos\beta)\ and\ V^2 = a^2b^2c^2(1 - \cos^2\alpha - \cos^2\beta - \cos^2\gamma + 2\cos\alpha\cdot\cos\beta\cdot\cos\gamma)$.

The bulk structure of a crystalline solid can be determined using X-ray diffraction through the following three main steps:[165]

- **Determining unit cell geometry and dimensions:** The geometric configuration and size of the unit cell are established by analyzing the angular positions of the XRD reflections (lines). This process begins by hypothesizing the lattice type, then assigning Miller indices to each reflection, which corresponds to distinct crystallographic planes.
- **Calculating atomic density:** Using the unit cell parameters determined in the first step, the number of atoms within the volume of the unit cell (referred to as atomic density) is calculated.
- **Determining atomic arrangement:** The spatial arrangement of atoms within the unit cell is inferred by examining the intensities of the X-ray diffraction peaks.

As the analysis progresses from the first to the second step, the refinement of the structural model becomes essential, particularly to achieve an accurate representation in the third step. For this purpose, the 'Rietveld refinement technique' (developed in the 1960s) has become the standard approach for refining crystal structures derived from XRD data.[174] IThis technique relies on an initial crystal structure model as a foundation and does not independently derive such a model from the data. However, it is invaluable for revealing additional structural details that may be missing from an incomplete model or for extracting new insights from experimental data.

The Rietveld refinement involves a nonlinear least squares fitting procedure, in which a calculated profile, based on an assumed structural model, is matched with the experimental data. This process requires careful adjustment and approximation of both structural and instrumental parameters to achieve optimal alignment between the theoretical model and observed data, often involving iterative refinement and hypothesis testing. [165]

### 3.2.3 XRD quantification method (Rietveld methods)

The whole pattern method, a variant of X-ray diffraction (XRD) quantification techniques, enables the analysis of all XRD reflection intensities in a crystalline sample by fitting them to parameters derived from standard crystallographic data or pre-established pure sample data. Two widely used whole pattern methods are the Rietveld method, which relies

on calibrated crystallographic data, and the full pattern summation method, which utilizes pure standard data.[175] This section focuses on the Rietveld method, the primary tool used for quantitative analysis of XRD data in this study.

As a comprehensive analysis technique, the Rietveld method models all diffraction reflections using standardized crystallographic parameters.[174,176,177] This method facilitates a profound comprehension of crystalline formations, shedding light on the spatial configuration of atoms, the arrangement of cations within octahedral and tetrahedral locations, and the positions of interchangeable cations. [177] Unlike techniques relying on single reflections, the Rietveld approach employs a meticulous point-by-point refinement strategy that reduces the differences between observed and predicted XRD intensities across the entire dataset, yielding an exceptionally precise model The method aims to reduce the weighted residual $R$, calculated as: [177]

$$R = \sum_i w_i |y_i(obs) - y_i(calc)|^2 \quad eq\ 3\text{-}15$$

where $y_i(obs)$ and $y_i(calc)$ represent the observed and calculated intensities at point $i$, and $w_i$ denotethe weight for each measurement. $y_i(calc)$ is determined by summing the contributions from background and Bragg reflections:

$$y_i(calc) = S \sum_k (p_k L_k |F_k| G(\Delta\theta_{ik}) P_k) + y_i(bkg) \quad eq\ 3\text{-}16$$

Here, $S$ is a scaling factor, $p_k$ is the multiplicity, $L_k$ signifies the Lorentz and polarization factor applicable to the $k^{th}$ Bragg reflection, $F_k$ is the structure factor, $G(\Delta\theta_{ik})$ represents the reflection profile, $P_k$ is the preferred orientation function, and $y_i(bkg)$ is the refined background. By fine-tuning these parameters, specific theoretical XRD patterns for each crystalline material are generated. [174,178–180]

Originally developed for powder diffraction data, the Rietveld method has evolved for quantitative phase analysis, with the refined scale factor $S$ indicating the relative proportions of different crystalline phases within a sample. [177] This capability has made the Rietveld method invaluable for quantitative analysis in multi-phase systems, where it accurately reflects complex structures, compositions, and orientations. However, certain materials, such as $MX_2$

compounds, exhibit unique characteristics like structural variability and preferred orientations that require careful consideration in Rietveld analysis. [181] For example, Viani et al. (2002) introduced a model for Ca-montmorillonite to improve structural refinement using the $R_p$ factor, where: [182]

$$R_p = \frac{\sum|y_i(obs) - y_i(calc)|}{\sum y_i(obs)} \quad eq\ 3\text{-}17$$

A lower $R_p$ value signifies better alignment between observed and calculated patterns, making this model effective for refining multi-phase materials. [182] Nonetheless, it is essential to highlight that insufficient reflections are requisite to effectively calibrate such models, and on certain occasions, a vector representing preferred orientation along with pertinent parameters associated with the extent of preferred orientation must be provided.[175]

The Rietveld method is also applicable to analyzing chemical compositions through intensity ratios of characteristic reflections. [183,184] Ban and Okada (1992) found a strong correlation between chemical composition and these intensity ratios, enabling the detection of chemical variations. [184] To support the complex refinement required in quantitative Rietveld analysis, various software programs have been developed, including SIROQUANT, [185] BGMN, [186] GSAS, [187] WYRIET, [187] BRENDA, [188] Highscore, and TOPAS. [189] Of these, BGMN, TOPAS, and SIROQUANT are particularly known for producing reliable results in quantitative phase analysis.

The General Structure Analysis System II (GSAS-II) constitutes a sophisticated, open-source software suite tailored for the analysis of crystallographic data. It presents an extensive array of functionalities applicable to both X-ray and neutron diffraction datasets, rendering it an invaluable instrument for researchers engaged in this domain. The benefits of GSAS-II are manifold, highlighting its user-centric interface, extensive scripting functionalities, and robust analytical capabilities. GSAS-II is architected around a cohesive graphical user interface (GUI), which facilitates the data analysis procedure for its users. This interface affords intuitive access to the comprehensive features of the software, thereby making it accessible even to individuals possessing minimal programming proficiency.[190] Moreover, the

scripting functionalities inherent in GSAS-II render it highly adaptable, enabling users to tailor and augment the software's capabilities to address particular research requirements.[190] Furthermore, GSAS-II utilizes sophisticated algorithms, such as the Levenberg-Marquardt minimization technique, for the refinement of structures. These algorithms guarantee rapid convergence and substantial stability, even in scenarios involving a considerable number of parameters.[191] Additionally, the software encompasses modules dedicated to the analysis of small-angle X-ray scattering data, offering tools for the modeling and refinement of scattering data across diverse experimental conditions.[192]

## 3.3 X-ray photoelectron spectroscopy (XPS)

X-ray photoelectron spectroscopy (XPS) is a highly surface-sensitive analytical technique that provides valuable information on the elemental composition and chemical states present on the surface of materials. In XPS, a focused X-ray beam is directed at the sample's surface, causing the emission of electrons whose kinetic energies are measured. This process enables the determination of the binding energies specific to elements within the sample, excluding only hydrogen and helium due to their unique properties. XPS is widely used across various fields, including materials science, polymers, semiconductor analysis, and environmental science, as surface characteristics significantly influence adhesion, corrosion, catalytic activity, and other critical material properties.[193]

XPS is based on the photoelectric effect, first observed by Heinrich Hertz in 1887 and theoretically explained by Albert Einstein in 1905 - a breakthrough that earned him the Nobel Prize. The first recorded X-ray-induced photoemission was documented by Robinson and Rawlinson in 1914, while significant advancements that shaped XPS into a powerful analytical tool were led by Kai Siegbahn during the 1950s and 1960s.[194–197] Siegbahn's contributions in high-resolution electron spectroscopy earned him the Nobel Prize in 1981.

### 3.3.1 Generation of photoelectrons

The core mechanism behind XPS relies on the photoelectric effect. When the sample surface is irradiated with soft X-rays (with energies typically below 6 keV), it absorbs this

energy, leading to the ejection of photoelectrons from core atomic levels, as demonstrated in Figure 3-10.

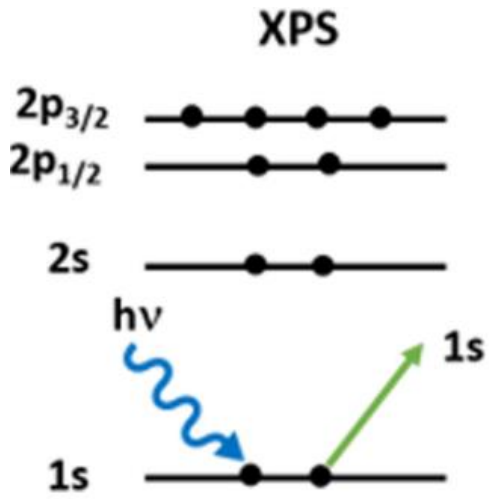


***Fig 3- 10. Processes resulting from X-ray bombardment of a surface: photoelectron emission***[193]

This energy transfer can be described by the equation:

$$h\nu = BE + KE + \Phi_{spec} \quad eq\ 3\text{-}18$$

where $h\nu$ is the photon energy, $BE$ represents the electron's binding energy, in conjunction with the kinetic energy, $KE$ is the kinetic energy of the emitted photoelectron, and $\Phi_{spec}$, is the work function specific to the spectrometer. By rearranging the equation, we isolate the binding energy, giving:

$$BE = h\nu - KE - \Phi_{spec} \quad eq\ 3\text{-}19$$

This principle is also visually represented in Fig. 3-11. It is important to note that the This binding energy is characteristic of the element and orbital from which the electron is ejected, acting as an elemental "fingerprint." Each electron's binding energy remains consistent regardless of the X-ray source used, though the kinetic energy may vary according to the photon energy ($h\nu$). Figure 3-11 provides a schematic overview of this relationship in XPS. [193]

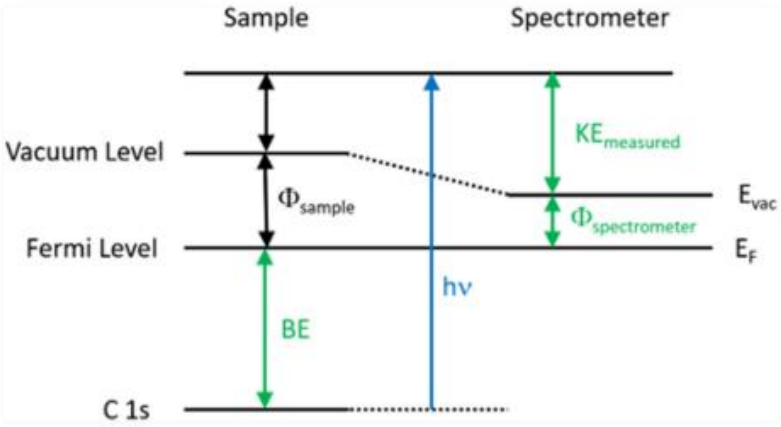


*Fig 3- 11. Schematic energy level diagram depicting the basic XPS equation*[193]

### 3.3.2 Auger electrons

When an electron is removed from a core level, a vacancy or "hole" is created, putting the atom in an ionized and excited state. To return to stability, an electron from a higher energy level may fill this vacancy, releasing the energy as an X-ray photon or as an Auger electron. Auger electron emission, depicted in Figure 3-12, occurs when the relaxation energy is sufficient to eject another electron from the atom, resulting in a second emission. [193]

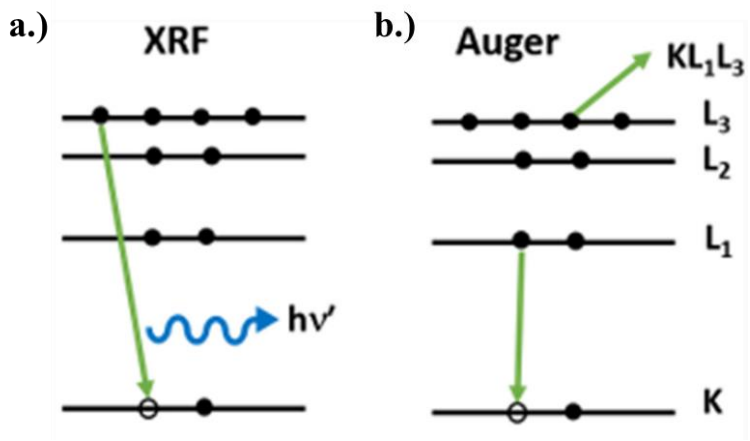


*Fig 3- 12. Processes resulting from X-ray bombardment of a surface: (a) X-ray fluorescence, and (b) Auger electron emission*[193]

Auger peaks are labeled with orbital designations, such as "KLL," indicating the origin and transition path of the electrons involved in the emission. This three-step transition process gives Auger electrons a distinct kinetic energy that is independent of the X-ray source, calculated as: [193]

$$KE_{Auger} \sim BE(K) - BE(L_1) - BE(L_2) \quad eq\ 3\text{-}20$$

This property is especially useful for resolving overlapping spectra. By varying the X-ray source, researchers can differentiate Auger and photoelectron peaks, as illustrated by the shift in the Auger peak of silver from 902 eV with magnesium excitation to 1135 eV with aluminum.

### 3.3.3 Chemical environment

One of XPS's distinguishing strengths is its ability to reveal details about the chemical environment of atoms within a sample, including oxidation states and neighboring atomic interactions. As shown in the high-resolution C 1s spectrum for polyethylene terephthalate (PET) in Figure 3-13, the binding energy of core electrons depends on factors such as the electronegativity of surrounding atoms. For example, the C 1s peak varies based on the presence of different chemical bonds (e.g., C-C, C-O, C=O), with higher electronegativity leading to increased binding energy. This chemical sensitivity allows XPS to distinguish between various bonding environments, with peak areas reflecting the quantity of atoms in each state. [193]

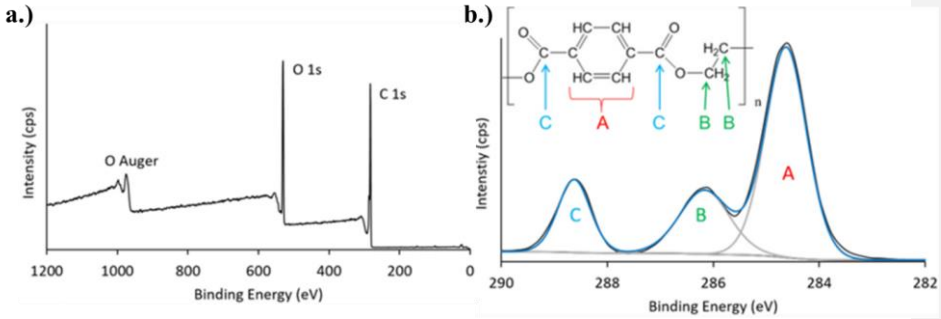


***Fig 3- 13. XPS survey spectrum a). and high-resolution C 1s spectrum b). of PET. The inset of (b) shows the chemical structure of PET and the assignments of the three peaks in the C 1s spectrum.*** [193]

When the electronegativity of a neighboring atom increases, the binding energy of the C 1s electron also rises, as shown in Table 3-1. XPS is capable of accurately distinguishing between various carbon environments (such as C-C, C-O, C=O, and C–$F_2$), based on this core trend of electronegativity. [198]

*Table 3-1. Binding energies of different carbon chemical environments[198]*

| Chemical state | Binding energy (eV) |
|---|---|
| C-C or C=C | 285 |
| C-N | 286 |
| C-O | 286.5 |
| C=O | 288 |
| O-C=O | 289 |
| $CF_2$ | 292 |
| $CF_3$ | 293–294 |

For the majority of transition metals, the binding energy is predominantly influenced by the oxidation state of the metal species. In instances where an atom has already experienced a loss of electron density and possesses a positive charge, the removal of an electron from that atom becomes increasingly challenging, thereby resulting in an elevated binding energy. Table 3-2 presents binding energies corresponding to various oxidation states of titanium, effectively demonstrating the correlation between the augmentation of binding energy and the increase in oxidation state.

*Table 3-2. Binding energies for several titanium chemical states for the Ti $2p_{3/2}$ orbital[199]*

| Chemical state | Oxidation state | Binding energy (eV) |
|---|---|---|
| Ti | Ti(0) | 453.9 |
| TiO | Ti(II) | 455.2 |
| $TiO_2$ | Ti(IV) | 458.7 |

Molybdenum, as a transition metal, exhibits varying binding energies that are significantly affected by its oxidation states and the chemical environment surrounding the Mo atom. Table 3-3 delineates the binding energies associated with different oxidation states of molybdenum and its corresponding chemical states.[200–208]

*Table 3-3. Binding energies for several molybdenum chemical states.*

| Chemical state | Binding energy (eV) |
|---|---|
| Mo | 227.6–228.8 |
| $Mo_2C$ | 227.5–228 |
| $MoO_2$ | 228.6–230.7 |
| $MoCl_3$ | 229.7–230.0 |
| $MoO_3$ | 229–229.7 |
| $MoS_2$ | 229–229.5 |
| $MoCl_4$ | 230.3–230.9 |
| $MoCl_5$ | 230.7–231.3 |
| $Mo^{5+}$ | 231.3–231.9 |
| $(NH_4)_2MoO_4$ | 231.9–232.4 |
| $MoO_3$ | 232.3–233.15 |

### 3.3.4 Surface sensitivity

XPS's high surface sensitivity is attributed to the limited escape depth of electrons. While X-rays can penetrate deeply into a sample, only electrons generated within the first few nanometers can escape without significant energy loss. Electrons originating from deeper within the material undergo inelastic collisions that dissipate their energy, contributing to background noise rather than distinct spectral peaks. Figure 3-14 illustrates the three categories of emitted electrons: those escaping without scattering (A), those experiencing inelastic scattering (B), and those from deeper layers that do not escape (C). [193]

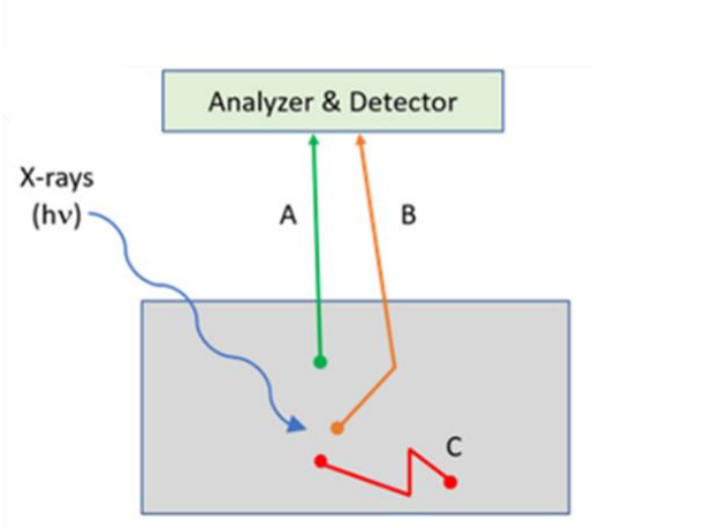


***Fig 3- 14. Interactions of emitted electrons with the sample at varying depths: Electrons emitted from different depths within the sample interact uniquely: those emitted without any interaction (labeled A) produce XPS photoelectron and Auger peaks; those experiencing at least one inelastic collision (labeled B) contribute to the background signal; and electrons undergoing multiple collisions that do not escape the sample are labeled C.***[193]

The XPS spectrum of polyethylene terephthalate (PET) shown in Figure 3-15 illustrates the main photoelectron and Auger peaks, with additional contributions from the background signal, primarily due to C 1s electrons. The shaded orange area highlights this background signal, arising from electrons that underwent inelastic scattering before reaching the detector. This background signal provides a clear visual of how scattered electrons can influence the overall spectral intensity, distinguishing the characteristic peaks from the inelastic scattering contributions. [193]

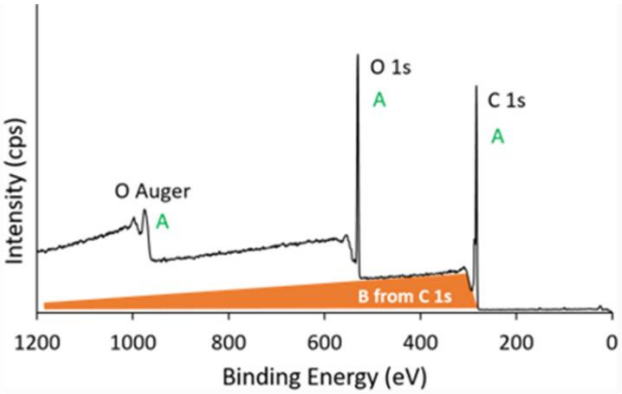


***Fig 3- 15. The XPS spectrum for PET with photoelectron and Auger peaks labeled. The orange shaded area shows the contribution to the background signal that results from C 1s electrons.***[193]

The intensity $I$ of electrons escaping from depth $d$ follows Beer's Law:

$$I = I_0 \, exp\left(-\frac{d}{\lambda}\right) \quad eq\ 3\text{-}21$$

where $\lambda$ represents the attenuation length, which depends on the electron's energy and the material's properties. This attenuation length is closely related to the inelastic mean free path (IMFP), which describes the average distance an electron travels before undergoing inelastic scattering. Using higher-energy X-ray sources increases the IMFP, enabling analysis at greater depths within the sample, as shown in Figure 3-16. [209] For example, the information depth for Si 2p electrons with an aluminum source is around 7 nm, while a chromium source increases this depth to approximately 22 nm. [210]

This flexibility in information depth allows XPS to examine both surface and near-surface layers, making it a powerful tool for comprehensive material analysis. The designation $\lambda$ refers to the attenuation length associated with an electron, which is contingent upon both the electron's energy and the specific material through which it traverses. The attenuation length bears resemblance to the inelastic mean free path (IMFP) of electrons (characterized as the mean distance an electron possessing a particular kinetic energy can traverse prior to undergoing inelastic scattering); however, the attenuation length also incorporates the influence of elastic scattering. A graphical representation of the universal curve depicting the inelastic mean free path as a function of electron kinetic energy is presented in Fig 3-16.[209]

Electrons exhibiting kinetic energies on the order of approximately 1000 eV possess an IMFP in the vicinity of several nanometers. By employing Beer's law, it can be demonstrated that approximately 95% of electrons will successfully escape from a depth of 10 nm or less, with 10 nm frequently referenced as the information depth pertinent to XPS. The information depth (often referred to as the sampling depth) is delineated as the maximum depth perpendicular to the surface from which pertinent information can be extracted.[210,211]

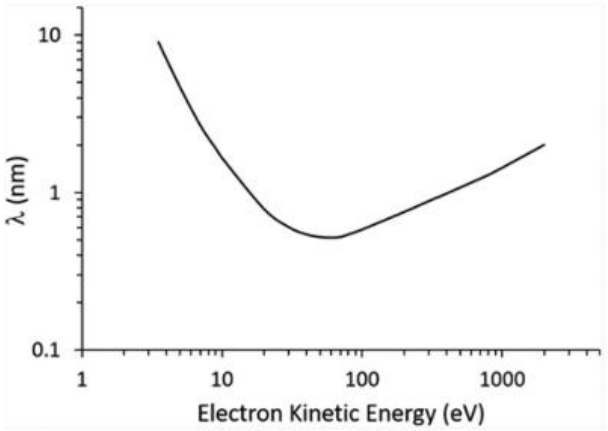


***Fig 3- 16. Inelastic mean free path (IMFP or λ) as a function of electron kinetic energy[209]***

This chapter provides an overview of X-ray Photoelectron Spectroscopy, focusing on its principles, mechanisms, and applications. XPS enables the precise analysis of surface composition and chemical states by measuring the energies of emitted electrons when a sample is exposed to X-rays. Key processes such as photoelectron and Auger electron emissions are explained, alongside their significance in identifying atomic environments and oxidation states. The chapter also highlights XPS's surface sensitivity, emphasizing its ability to probe shallow depths for insights into surface and near-surface material properties.

## 3.4 UV-Vis spectroscopy

UV-Vis spectroscopy is a powerful analytical technique that quantifies how much ultraviolet or visible light a sample absorbs or transmits relative to a reference or blank sample. Through the examination of distinct wavelengths that are absorbed, UV-Vis spectroscopy

unveils crucial insights into composition and concentration of different components within the sample.[212] Since this method depends on light, having a fundamental grasp of light's characteristics is vital.

The energy of light is inversely related to its wavelength: shorter wavelengths carry higher energy, while longer wavelengths have lower energy. This energy allows UV and visible light to excite electrons within materials, promoting them to higher energy states. The specific energy required for these transitions varies depending on the molecule's electronic structure, which is why different materials exhibit unique absorption patterns across particular wavelengths. Visible light spans wavelengths from approximately 380 nm (violet) to 780 nm (red), while ultraviolet (UV) light extends down to about 100 nm.[213] In UV-Vis spectroscopy, each wavelength corresponds to a specific electronic transition, enabling scientists to identify and quantify compounds by analyzing peaks in absorbance.

### 3.4.1 The working principle of UV-Vis spectrophotometer

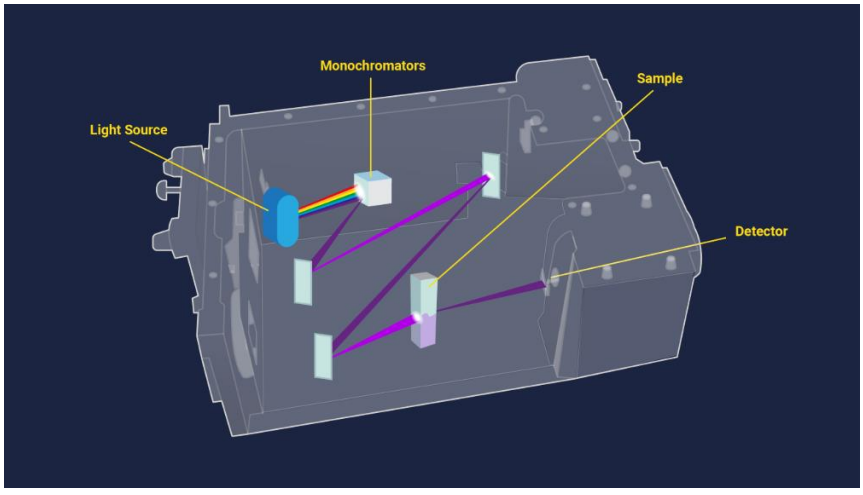


***Fig 3- 17. Illustration of a UV-Vis spectroscopy setup using a cuvette system***[212]

The structure and functionality of a typical UV-Vis spectrophotometer, as depicted in **Figure 3-17**, involve several critical components. A stable, broad-spectrum light source is essential, as it provides illumination across both the ultraviolet and visible ranges. The sample is placed in a transparent cuvette, which allows light to pass through without interference.

High-intensity xenon lamps are often used as the light source due to their broad wavelength coverage, although dual-lamp configurations are also common. In dual-lamp setups, a tungsten or halogen lamp supplies visible light, while a deuterium lamp provides ultraviolet light.[214] The spectrophotometer is designed to transition seamlessly between these sources during scanning, typically in the 300-350 nm range, where both lamps emit comparable wavelengths, ensuring a continuous spectrum across UV and visible light regions.[212]

Following illumination, specific wavelengths suited to the analyte must be isolated from the broad-spectrum light.[213,214] Monochromators perform this selection by isolating narrow bands of wavelengths through diffraction gratings. The groove density of these gratings determines the resolution and range; higher groove densities improve resolution but reduce range, while lower densities expand range at the expense of precision. Holographic diffraction gratings are generally preferred due to their low defect rates, yielding high-accuracy measurements. After passing through the monochromator, the selected wavelength of light traverses the sample in the cuvette, where the analyte absorbs certain wavelengths. A detector then converts the transmitted light into an electronic signal, which is processed to reveal the absorbance profile of the sample. [212,215]

### 3.4.2 Principles and theory

When ultraviolet or visible light encounters a sample, it can be absorbed, transmitted, or reflected, and may also induce photoluminescence, such as fluorescence or phosphorescence.[216] Absorption is the most relevant interaction for UV-Vis spectroscopy and occurs when the light's energy matches the energy gap for an electronic transition within the sample. This interaction can be explained through the Bohr model:

$$\Delta E = E_2 - E_1 = h\nu \rightarrow h\nu = hc\bar{\nu} = \frac{hc}{\lambda} \quad eq\ 3\text{-}22$$

where $E_1$ and $E_2$ are initial and final energy states; $h$ represents Planck's constant ($6.62 \times 10^{-34}$ Js); c is the speed of light in a vacuum ($2.99 \times 10^8$ m/s); $\nu$ is frequency; $\lambda$ is wavelength; and $\bar{\nu}$ refers to wavenumber. This equation links energy levels to the wavelength of the incident light, explaining why each material absorbs specific wavelengths. Once

absorbed, the light energy excites electrons to a higher energy state. However, this excited state is typically unstable, leading the molecule to return to its ground state through various "deactivation" pathways, such as heat dissipation, fluorescence, or other photochemical reactions. [212]

The Beer-Lambert Law elegantly articulates the way light absorption in a sample correlates with the concentration of the absorbing agents, the distance the light travels through the sample, and the substance's molar absorptivity. This connection is vital in UV-Vis spectroscopy, as it enables the calculation of concentration in a solution through the measurement of absorbance. [212] The Beer-Lambert Law is expressed as:

$$A = \varepsilon bc = -log\, T = log\left(\frac{1}{T}\right) = \log\left(\frac{I_0}{I}\right) \quad eq\ 3\text{-}23$$

where $A$ is the absorbance, a unitless value calculated as the logarithmic ratio of the incident light intensity ($I_0$) to the transmitted light intensity ($I$); $T$ is the transmittance, defined as $T = \frac{I}{I_0}$, the ratio of transmitted light to incident light; $\varepsilon$ is the molar absorptivity (also known as the molar extinction coefficient) in L mol$^{-1}$ cm$^{-1}$, indicating how strongly the analyte absorbs light at a specific wavelength; $b$ is the path length of light through the sample, typically the width of the cuvette, in centimeters (cm); $c$ is the concentration of the analyte in the solution, expressed in mol/L. In practice, the Beer-Lambert Law states that absorbance $A$ is directly proportional to both the concentration $c$ of the analyte and the path length $b$. This linear relationship allows researchers to determine the concentration of a substance in solution by measuring its absorbance at a specific wavelength, given that $\varepsilon$ is known.

### 3.4.3 Electronic transitions

In the ultraviolet-visible (UV-Vis) spectrum, electronic transitions within materials manifest as distinct absorption bands. These occur when an electron absorbs energy from light, matching the energy difference between its current state and an excited state, allowing it to transition between energy levels. The width of this energy gap is shaped by the electronic framework of the substance and its surroundings. For an electronic transition to occur, specific conditions must be met, including charge redistribution and adherence to selection rules such

as the Laporte Selection Rule, Spin Multiplicity Rule, and interactions with neighboring atoms.[217]

Electronic transitions are classified by the types of molecular orbitals involved, which determine the probability and intensity of absorption bands. Key selection rules specify that transitions between states of the same spin multiplicity (parallel spins) are allowed, while transitions between states with differing spins are typically forbidden, leading to either intense spectral peaks or weak, sometimes absent, signals. [218]

Absorption bands in pigments are primarily due to Ligand-Field (LF), Charge Transfer (CT), and Valence-Conduction (VC) transitions. These transition types provide critical insights into material properties and are instrumental in identifying pigments, dyes, and other compounds. [216,217,219]

- **Ligand-Field (LF) Transitions:** Ligand-Field theory describes the behavior of metal ions with unpaired d or f electrons in their outer orbitals, especially transition metals like Ti, V, Cr, Mn, Fe, Co, Ni, and Cu. In these materials, the d-orbital electrons are directly involved in absorbing UV and visible light, with the resulting absorption spectra determined by factors such as the arrangement, symmetry, and type of surrounding ligands. [216,219] For example, $Cu^{2+}$ ions display unique spectral characteristics in minerals like azurite and malachite, where the LF transitions differ depending on the local chemical environment. Due to selection rule restrictions, LF transitions are only partially allowed, resulting in relatively low-intensity bands. However, these transitions still provide a clear signature that aids in material identification and analysis. [217]
- **Charge Transfer (CT) Transitions:** Charge Transfer (CT) transitions occur when an electron moves from one ion to another or from an ion to a ligand, resulting in intense absorption bands because these transitions fully satisfy selection rules. [216] In a common scenario like lead chromate ($PbCrO_4$) or “chrome yellow,” light absorption causes an electron shift from an oxygen atom to the chromium ion, a transition classified as ligand-to-metal charge transfer (LMCT). CT transitions can also resemble oxidation-reduction reactions in compounds with ions of different valence states, as seen in Prussian blue

($Fe_4[Fe(CN)_6]_3 \cdot nH_2O$), where charge transfer occurs between $Fe^{2+}$ and $Fe^{3+}$ ions. These transitions are highly sensitive to ion proximity and chemical environment, making CT transitions particularly useful for analyzing electronic structures in compounds with mixed oxidation states. [217]

- **Valence-Conduction (VC) Transitions:** Valence-Conduction (VC) transitions characterize metals and semiconductor-like inorganic pigments. In crystalline solids, distinct energy levels merge into broader bands known as the valence band (lower energy) and conduction band (higher energy), separated by a band gap where no electrons can exist. Electrons in the conduction band can move freely through the lattice, earning the term “conduction electrons.” Semiconductor pigments, such as cadmium yellow (CdS), vermilion (HgS), and red lead ($Pb_3O_4$), have a band gap that allows electrons to transition from the valence to the conduction band under UV-Vis light, creating prominent absorption bands. These transitions yield absorption spectra with a distinctive “S” shape, where the transition energies can be determined from inflection points on the curve, identified by analyzing the first derivative of reflectance spectra. VC transitions are central to understanding the optical properties of semiconductors, as the band gap size is directly related to a material’s light absorption range. [220]

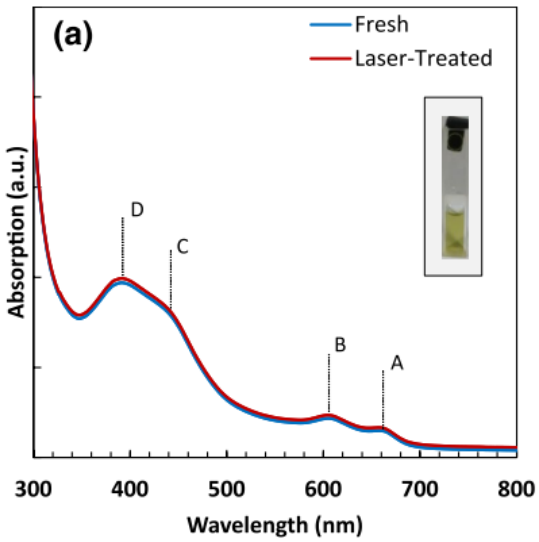


***Fig 3- 18. UV–Vis absorption profiles of fesh and lser-mdified $MoS_2$ dispersion (inset: green-yellow hue of $MoS_2$ Solution)***[221]

In the UV-Vis spectrum analysis of $MoS_2$, as illustrated in Figure 3-18, a significant peak located approximately at 650 nm is indicative of the A exciton, which denotes a direct optical transition occurring between the K and K' valleys within the Brillouin zone. This A exciton has an energy of approximately 1.9 eV, aligning with a wavelength around 650 nm in the visible spectrum. The B exciton, observed at around 610 nm, is associated with a slightly higher energy direct transition within the K valley but arises from the spin-orbit splitting of the valence band, which creates two closely spaced energy levels.[222,223]

Alongside the excitonic peaks, the absorption regions noted around 340 nm and 430 nm reflect $MoS_2$'s direct and indirect band gaps, respectively. The highest point seen at 340 nm is linked to the direct band gap shift, during which electrons shift directly from the valence band to the conduction band with no simultaneous change in momentum. Conversely, the peak located at 430 nm is representative of the indirect band gap transition, which necessitates a change in momentum, typically facilitated by phonons, as electrons transition from the apex of the valence band to the nadir of the conduction band.[224,225]

The A and B excitons' optical attributes in the system are heavily impacted by interlayer interactions and spin-orbit coupling, culminating in an excitonic splitting of roughly 65 nm, corresponding to 0.39 eV. Empirical research has demonstrated that the binding energy associated with the B exciton in $MoS_2$ exhibits variability contingent upon the number of layers and the surrounding dielectric medium. As reported by Park and others, the binding energy ($E_{b,exc}$) for monolayer $MoS_2$ on a sapphire substrate measured 240 meV, [226] whereas Jindal and his associates noted a binding energy increase associated with decreased layer thickness in few-layer $MoS_2$ films. [227]

To further analyze the optical characteristics, the band gap (representing the energy difference between the highest occupied molecular orbital, HOMO, and the lowest unoccupied molecular orbital, LUMO) was determined from the UV-visible absorption spectra. The calculation of the band gap was based on Equation 3-24: [225]

$$(\alpha dv)^n = A(hv - E_g) \quad eq3\text{-}24$$

In this equation: $\alpha$ the absorption coefficient, is derived from UV-visible spectroscopy using the Lambert-Beer law, $d$ represents the film thickness or path length through the material, $v$ is the frequency of the incident light, $hv$ represents the photon energy, $E_g$ denotes the band gap energy, and $A$ is a constant. The exponent nnn specifies the certain category of electronic transitions: $n$ = 2 directs attention to direct transitions, $n$ = 1/2 identifies indirect transitions, $n$ = 2/3 aligns with direct forbidden transitions, and $n$ =1/3 points to indirect forbidden transitions. This approach facilitates an accurate computation of the band gap contingent upon the transition type identified within each respective sample. [225]

## 3.5 Raman spectroscopy

Raman spectroscopy stands out as a remarkable analytical approach that enables the identification of chemical entities by exploring the interplay between light and matter. This technique specifically harnesses the effects of Stokes and Anti-Stokes scattering to investigate molecular configurations. When near-infrared (NIR) or visible light interacts with a molecule, various scattering phenomena take place, as depicted in Figure 3-19.[228,229]

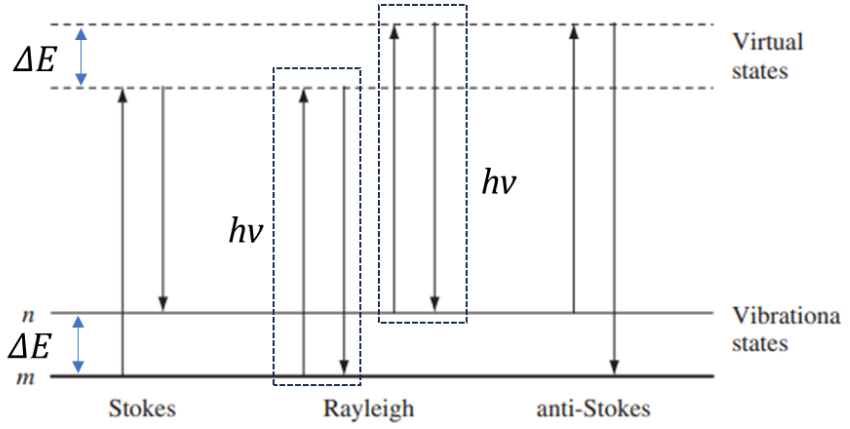


***Fig 3- 19. Diagram illustrating Rayleigh and Raman scattering processes: The ground vibrational state (m) is at the base, with Higher energy states above. the incident (upward arrows) and scattered (downward arrows) energies are significantly greater than the vibrational energy.***

Figure 3-19 showcases the trio of scattering types: Rayleigh, Stokes, and Anti-Stokes scattering. In Rayleigh scattering, the molecule gets excited to a transient virtual state before returning to its initial vibrational state, resulting in photons that scatter elastically, retaining the same energy as the incoming light. Conversely, Stokes scattering happens when the molecule settles into a higher vibrational state, producing inelastic scattering where the released photon carries less energy Anti-Stokes scattering, the least common, involves the molecule starting in an excited vibrational state and relaxing to a lower state, emitting a photon with more energy than the incident photon. [228]

Rayleigh scattering is the most prevalent form because it does not involve a change in the molecule's vibrational state. Anti-Stokes scattering, on the other hand, is rare due to its requirement for pre-existing vibrational excitation in the molecule. Consequently, Stokes scattering is primarily used in Raman measurements as it provides significant insights into molecular vibrations. [228,229] The relative intensities of Rayleigh, Stokes, and Anti-Stokes scattering are illustrated in Figure 3-20, where peak height and width represent their comparative strengths.

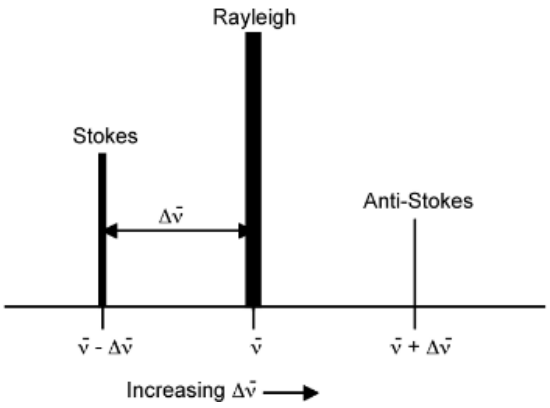


***Fig 3- 20. Relative position and intensity of Stokes and Anti-Stokes scattering peaks compared to Rayleigh scattering (Indicated by peak height and width)***[228]

In Raman spectroscopy, the spotlight shines on the energy disparity between incoming and reflected photons, illustrated by the Stokes and Anti-Stokes shifts. This energy variation is commonly represented in wavenumbers ($cm^{-1}$) in relation to the original light source. Although Raman measurements can be conducted using any light wavelength, near-infrared and visible sources are most common, as ultraviolet light can often cause sample decomposition. [228]

The vibrational states of a molecule are shaped by its degrees of freedom, with each degree reflecting a possible vibrational mode. A molecule consisting of $N$ atoms can possess $3N - 6$ vibrational modes if it is non-linear, or $3N - 5$ if it has a linear configuration. For instance, diatomic molecules have merely one vibrational mode, but triatomic molecules like water ($H_2O$) and carbon dioxide ($CO_2$) unveil three distinct vibrational modes: symmetric stretching, bending (deformation), and asymmetric stretching. These vibrational modes are illustrated in Figure 3-21, where a "spring and ball" model represents atoms as balls and bonds as springs, with bond strength directly influencing vibrational frequency. [229]

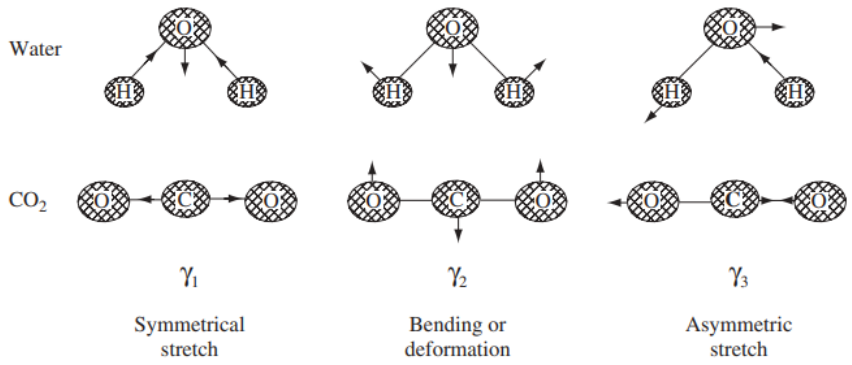


*Fig 3- 21. Spring-and-Ball model depicting three vibrational modes in $H_2O$ and $CO_2$ molecules.*[229]

Figure 3-22 provides a simplified electron cloud model of $CO_2$, illustrating both infrared (IR) and Raman active vibrations. A variation in the vibrational state of a molecule could lead to alternative in its dipole moment, which can be revealed by IR spectroscopy, or its polarizability, noticeable via Raman spectroscopy. Symmetric stretching, for instance, significantly alters polarizability, generating a strong Raman signal with minimal change in dipole moment, resulting in weak IR absorption. Conversely, bending modes tend to affect dipole moment more than polarizability, leading to stronger IR absorption and weaker Raman scattering. [229]

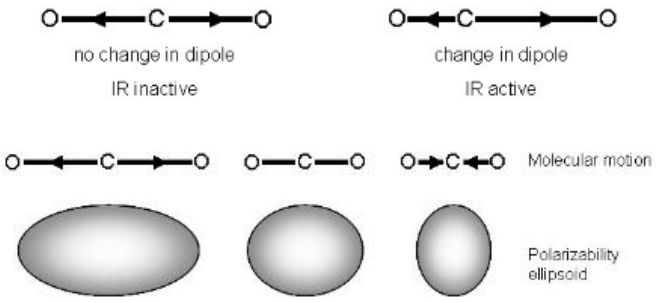


*Fig 3- 22. Electron cloud representation of carbon dioxide, illustrating IR-Active and Raman-Active vibrational modes*[228]

In Raman spectroscopy, the observed Raman activity depends on a bond's polarizability, which is essentially the bond's susceptibility to deformation within an electric

field. High polarizability, often due to loosely bound electrons, produces strong Raman signals. Thus, Raman spectroscopy is more sensitive to a molecule's overall structure than to specific functional groups, differentiating it from IR spectroscopy, which is more responsive to polar molecules. Polar molecules generally exhibit weaker Raman signals because strongly electronegative atoms hold their electrons tightly, reducing polarizability.[228]

Raman spectroscopy is applicable to both organic and inorganic compounds. For instance, metals in coordination complexes, with their abundance of loosely bound electrons, exhibit high Raman activity. This enables the technique to analyze metal-ligand bonds, providing insight into the composition, stability, and structure of metal complexes, especially those with low vibrational frequencies in the IR spectrum. Additionally, Raman spectroscopy excels at identifying molecular fingerprints of organic compounds. Raman spectra often reflect vibrations across the entire molecule rather than localized bonds, making it a valuable tool for characterizing complex molecular structures with unique vibrational patterns.[228]

## 3.6 Brunauer–Emmett–Teller (BET) method

The BET (Brunauer-Emmett-Teller) theory offers a detailed framework for understanding gas adsorption on solid surfaces, particularly important for studying porous materials.[230–232] This adsorption process arises due to van der Waals interactions between gas molecules and the solid surface, and can be classified as either physical adsorption (physisorption), where weak van der Waals forces are involved, or chemical adsorption (chemisorption), where stronger chemical bonds are formed between the adsorbate and the surface.[233–236]

TThe BET theory is a significant extension of the Langmuir theory, which describes only monolayer adsorption. In contrast, BET extends this model to account for multilayer adsorption. This multilayer phenomenon becomes especially relevant at temperatures below the critical point of the gas, where condensation can occur, leading to the formation of adsorbate layers beyond the first, which may not be in direct contact with the adsorbent surface. By applying Langmuir’s equation to each layer individually and assuming equilibrium,

the BET theory provides a more complete description of how gas molecules accumulate on surfaces, which is critical for determining surface area in materials science.[237] The BET equation mathematically relates the volume of gas adsorbed to the relative pressure. This relationship is central to estimating the surface area of materials and is expressed as:[238]

$$\frac{P/P_0}{n(1-P/P_0)} = \frac{1}{n_m C} + \frac{C-1}{n_m C}\left(\frac{P}{P_0}\right) \quad \textit{eq 3-25}$$

where $P$ is the equilibrium pressure of the adsorbate gas, $P_0$ is the saturation pressure of the adsorbate gas, $n$ is the amount of gas adsorbed at a given pressure $\frac{P}{P_0}$, $n_m$ is the monolayer capacity, representing the volume of gas needed to form a single monolayer over the surface, $C$ is a constant related to the adsorption energy of the first layer compared to subsequent layers. This equation describes the linear relationship between $\frac{P/P_0}{n(1-P/P_0)}$ and $\frac{P}{P_0}$. A BET plot, constructed by plotting $\frac{P/P_0}{n(1-P/P_0)}$ versus $\frac{P}{P_0}$, yields a straight line within a specific relative pressure range (typically 0.05 to 0.30). [238] From this line, the monolayer capacity $n_m$ and the constant $C$ can be determined, allowing for the calculation of the specific surface area of the material.

It needs to acknowledge that the BET methodology entails the conversion of a BET isotherm, which subsequently facilitates the derivation of a BET plot. Figure 3-23 illustrates six distinct categories of BET isotherms.[237]

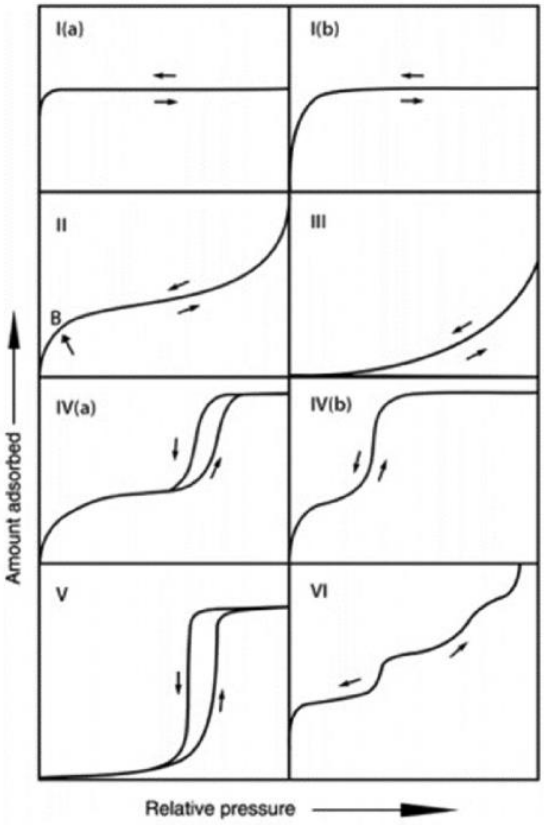


***Fig 3- 23. Classification of BET adsorption isotherms by the International Union of Pure and Applied Chemistry (IUPAC)*** [238]

BET isotherms can be delineated in the following manner:

**Type I (Langmuir Isotherm)**: Associated with microporous materials (pores < 2 nm), showing a sharp rise at low relative pressures. Type I(a) observed in materials with very narrow micropores, where adsorption primarily occurs in these ultra-small spaces. These materials have very limited multilayer adsorption due to the restricted pore sizes. Type I(b) is in materials with slightly larger micropores or narrow mesopores, adsorption capacity is higher, and there may be more indication of multilayer formation as the pore size approaches mesoporous dimensions.

**Type II (Non-Porous or Macroporous Materials)**: typically observed in non-porous or macroporous materials that do not have significant micropores to restrict gas adsorption. This category of isotherm exhibits a pronounced initial escalation at low pressures attributed to monolayer adsorption, subsequently followed by a more gradual increase as supplementary layers of adsorbate accumulate, signifying the occurrence of multilayer adsorption. At a specific point, referred to as point B, the adsorption process transitions from monolayer to multilayer coverage.

**Type III (Weak Adsorbent-Adsorbate Interactions)**: Indicate situations where adsorbate-adsorbent interactions are weaker than adsorbate-adsorbate interactions. The adsorption curve here is concave to the pressure axis and lacks a distinct monolayer formation point. This particular classification of isotherm implies that the molecules of the adsorbate tend to aggregate rather than bond directly with the surface, since the interactions among adsorbate molecules exhibit greater strength compared to those with the surface. Type III isotherms are less common and can be seen in materials that poorly adsorb gases, such as certain graphitic carbons or nonpolar materials with low surface reactivity.

**Type IV (Mesoporous Materials)**: Characteristic of mesoporous materials, which have pore sizes between 2 nm and 50 nm. The isotherm initially resembles the Type II isotherm, with a steep rise at low pressures corresponding to monolayer and multilayer adsorption. Nonetheless, as the applied pressure increases, a hysteresis loop emerges as a consequence of capillary condensation occurring within the mesoporous structures. This hysteresis loop, seen at higher pressures, is a distinguishing feature of Type IV isotherms and provides insights into the pore size and shape of the material. In Type IV(a) subtype, adsorption occurs in materials with relatively wide mesopores. The hysteresis loop is more obvious attributable to the phenomenon of capillary condensation that takes place within larger mesopores, and the configuration of the loop may fluctuate in accordance with the specific pore architecture of the material. Type IV(b) is observed in materials with narrower mesopores. The hysteresis loop here is narrower and may differ in shape, reflecting the influence of

narrower pore sizes on adsorption-desorption behavior. Type V Isotherm (Weak Interactions with Hysteresis)

**Type V:** Type V isotherms are similar to Type III at lower pressures but display hysteresis at higher pressures due to clustering and capillary condensation. This type of isotherm occurs in mesoporous or macroporous materials where adsorbate-adsorbent interactions are weak, similar to Type III. Nevertheless, under increased pressure conditions, capillary condensation induces hysteresis, signifying that the adsorbate molecules are commencing to occupy the mesopores or larger pore regions. This type of isotherm is less common and is usually seen in materials that exhibit weak adsorptive interactions but possess pore structures that allow for clustering and condensation.

**The type VI (Stepwise Multilayer Adsorption):** Type VI isotherms depict stepwise adsorption, where each step corresponds to the formation of a complete adsorbate layer. This isotherm is typically seen in nonporous surfaces with highly uniform sites for adsorption, where the adsorbate molecules build up in layers one at a time. Each horizontal step in the isotherm represents the addition of a new molecular layer. Materials that exhibit Type VI isotherms include certain metal oxides and highly ordered, nonporous surfaces. This type of adsorption behavior is rare and generally observed under specific conditions with highly uniform surfaces.

To determine the surface area using the BET method, the linear portion of the BET plot (often at relative pressures between 0.05 and 0.30) is used to calculate the monolayer capacity $n_m$. The surface area may subsequently be determined by utilizing the established surface area of the adsorbate molecules in conjunction with the monolayer capacity, thereby facilitating an accurate evaluation of the surface area of the material. [238]

The BET method remains a cornerstone in materials science for evaluating the surface area and porosity of solids. This analysis is especially valuable for porous catalysts, adsorbents, and materials used in environmental and industrial applications, as it provides critical insights into surface interactions and material efficiency.

## 3.7 Scanning electron microscopy (SEM)

Scanning Electron Microscopy (SEM) is a powerful technique employed for detailed surface characterization of both organic and inorganic materials across diverse scientific fields. It enables visualization of surface features at exceptionally high resolutions, typically up to 300,000x, with advanced instruments reaching magnifications of 1,000,000x. This capacity to resolve fine details at the nanometer to micrometer scale makes SEM indispensable for fields ranging from materials science and biology to industrial quality control. Combined with Energy Dispersive X-ray Spectroscopy (EDS), SEM extends beyond imaging to provide compositional analysis of a sample.[239] EDS allows researchers to obtain qualitative and semi-quantitative information on the elemental makeup of a material, which is crucial for understanding material properties and behavior. SEM chambers can accommodate a range of sample sizes, often up to 200 mm in diameter and 80 mm in height, which broadens the applicability to various types of specimens, including biological tissues, polymers, metals, ceramics, and complex composites.[240]

### 3.7.1 Components and Working System of SEM

As shown in Figure 3-24, SEM's core components include:

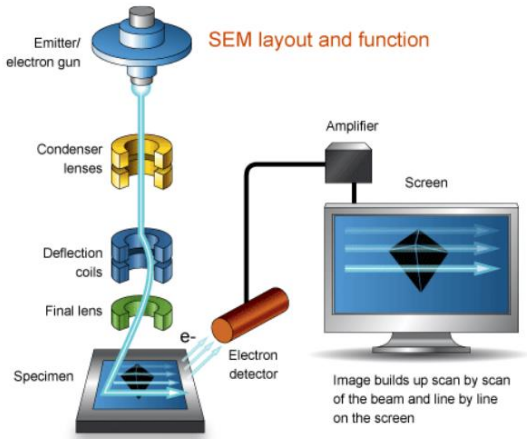


***Fig 3- 24. All SEM components***[241]

**Electron gun:** The electron gun, located at the top of the SEM column, generates a focused electron beam. This beam can reach energy levels of 100-30,000 eV, depending on the acceleration voltage;

**Electromagnetic lenses:** The electron beam is directed and focused by electromagnetic lenses. The final spot size, typically less than 10 nm, is achieved through the action of condenser and objective lenses, determining the resolution and quality of the image;

**Scanning System (Deflection System)**: Scan coils deflect the beam to raster it over the sample surface systematically, allowing point-by-point data collection across the target area;

**Detectors**: SEM typically employs secondary electron (SE) detectors and backscattered electron (BSE) detectors. SEs provide high-resolution surface morphology details, while BSEs deliver atomic contrast by responding to differences in atomic number, useful for distinguishing areas of varied composition; [241]

**Sample Chamber and Holder**: This part stabilizes the sample and controls its orientation, distance from the electron beam, and temperature if cryogenic conditions are required;

**Control and Imaging System**: Computers manage beam alignment, focus, magnification, and image generation. Specialized software processes the collected data into real-time images and supports analysis functions.

In operation, the high-energy electron beam is directed onto the specimen's surface, penetrating to various depths based on the accelerating voltage and sample composition. Low accelerating voltages (<5 kV) emphasize surface features by generating more secondary electrons near the surface, while higher voltages (15-30 kV) allow deeper penetration into the sample, [242] facilitating internal structural analysis. [243] Figure 3-25 typically illustrates electron interaction depths, underscoring the capacity to capture both surface and subsurface features depending on beam energy.

SEM images are created by raster-scanning the focused electron beam over the specimen's surface. The point-by-point signal gathered from secondary and backscattered electrons forms the image. Secondary electrons, generated from inelastic scattering near the surface, yield topographical details by highlighting the fine surface texture. In contrast,

backscattered electrons provide information on composition, as elements with higher atomic numbers backscatter electrons more effectively, producing areas of higher brightness in the image.[244]

The working distance, spot size, and accelerating voltage are adjusted to tailor the imaging conditions to the material's characteristics. By optimizing these parameters, researchers can capture high-contrast, high-resolution images that reveal complex surface features and compositional variations.

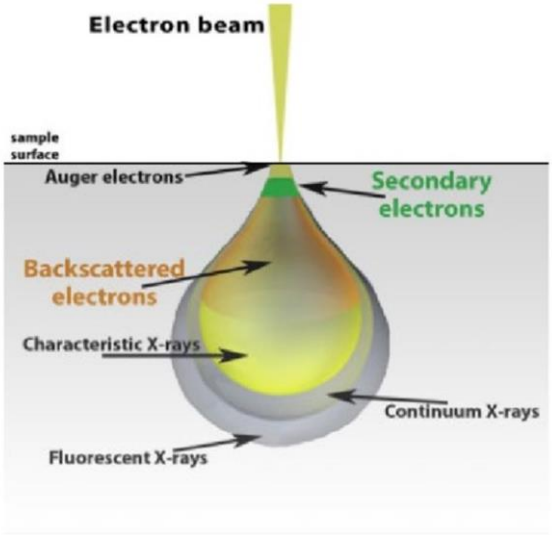


***Fig 3- 25. Different penetration level of electron through the sample[242]***

### 3.7.2 Energy Dispersive X-Ray Spectroscopy (EDS)

EDS enhances SEM by allowing elemental analysis of the sample's surface layers. When the high-energy electron beam interacts with atoms beneath the surface, it can displace core electrons, leading to the emission of characteristic X-rays as other electrons fill the resulting vacancies. These emitted X-rays possess energy levels unique to each element, enabling their identification within the sample,[243] as illustrated in Fig. 3-25.

Heinrich's foundational work in 1968 established the principles for quantitative microanalysis using EDS, introducing necessary correction factors to account for electron

scattering, X-ray absorption, and other influences that impact accuracy.[244] In modern SEM-EDS setups, software systems interpret the energy signals into data, mapping the distribution of elements across the sample. [245]

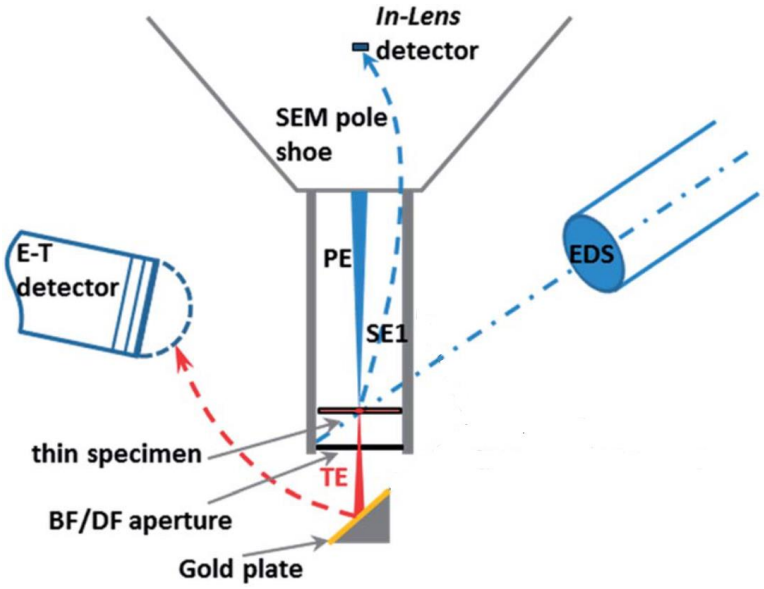


***Fig 3- 26. A schematic diagram of a scanning electron microscopy/energy-dispersive X-ray spectroscopy (SEM/EDS) system operating in transmission mode, featuring the Zeiss integrated transmission configuration. Key components are denoted as: primary electrons (PE); SE1 secondary electrons generated at the PE-sample interaction point; transmitted electrons (TE); bright-field (BF) and dark-field (DF) imaging modes; and the Everhart-Thornley detector (E-T) for signal collection.*** [246]

The EDS process typically follows these steps: [243]

**Goal Definition**: Establishing specific objectives, such as identifying elemental composition or distribution patterns;

**Qualitative Analysis**: Conducting an initial scan to identify the presence of elements;

**Sample Preparation**: Polishing the sample to a thickness under 0.1 μm and ensuring it remains clean and dry;

**Quantitative Measurement**: Using X-ray intensity to determine element concentrations.

The refinement process in EDS data analysis adjusts for various factors to provide accurate quantitative data on elemental concentrations. The calculated data from EDS is

adjusted through corrections that take into account electron penetration depth and X-ray interactions within the sample, ensuring accurate representation of the material's composition.[244]

In summary, SEM, when coupled with EDS, serves as a versatile tool in fields like nanotechnology, materials science, geology, and biomedical research. In materials science, SEM-EDS assists in evaluating material failures, surface coatings, and corrosion layers, while in biology, it aids in examining cell structures, tissues, and biofilms. In quality control, SEM-EDS is invaluable for characterizing products at the microstructural level, ensuring adherence to precise specifications.

By offering both high-resolution imaging and elemental analysis, SEM-EDS enables scientists and engineers to gain detailed insights into materials' structural and compositional properties, bridging the gap between surface morphology and elemental distribution.

# Electronic conductivity enhancement through graphene oxide (GO)-$MoS_2$-heterostructure

## 4.1 Introduction

Reduced graphene oxide (rGO) has a crucial role in enhancing the catalytic activity and stability of molybdenum disulfide ($MoS_2$), directed for HER reaction, by employing various synergistic mechanisms through the creation of heterostructures.

Firstly, the exceptional electrical conductivity of rGO promotes electron transfer within the $MoS_2$-rGO composite, which is indispensable for the efficacy of catalytic processes. The increased electron mobility significantly boosts the HER performance by diminishing the energy obstacles linked with hydrogen evolution [247,248]. Secondly, $MoS_2$ with rGO composites generate fresh defect sites and elevates the number of active edge sites accessible for the HER. These active sites play a pivotal role in the adsorption and reduction of hydrogen ions[249]. Thirdly, the integration of rGO into $MoS_2$ structures not only enhances the dispersion of $MoS_2$ but also amplifies the charge transfer capability. This culminates in a more effective separation of photo-induced charge carriers, which proves advantageous for photocatalytic HER[250], which is beyond the scope of this work. Another aspect to consider is the stability and durability attained through the structural support of rGO[251]. In conclusion, the incorporation of rGO with $MoS_2$ not only overcomes the conductivity restrictions of $MoS_2$ but also introduces advantageous structural and electronic characteristics. These improvements collectively contribute to the exceptional HER performance of $MoS_2$-rGO composites[252].

Although $MoS_2$-rGO has demonstrated numerous benefits in the hydrogen evolution reaction (HER), the specific conditions required for the synthesis of uniformly dispersed $MoS_2$-rGO using the hydrothermal method in order to achieve the most efficient HER performance remain unresolved within the current literature. Consequently, to address this research gap, a three-factor, three-level orthogonal experimental design was employed to

optimize the synthesis conditions of $MoS_2$–rGO composites. The experimental design followed the Taguchi method using orthogonal arrays, which allows for the identification of statistically significant factors and the determination of optimal conditions that maximize catalytic performance. Based on the results of the orthogonal array analysis, a series of $MoS_2$–rGO composites were subsequently synthesized to experimentally validate the identified optimal parameters

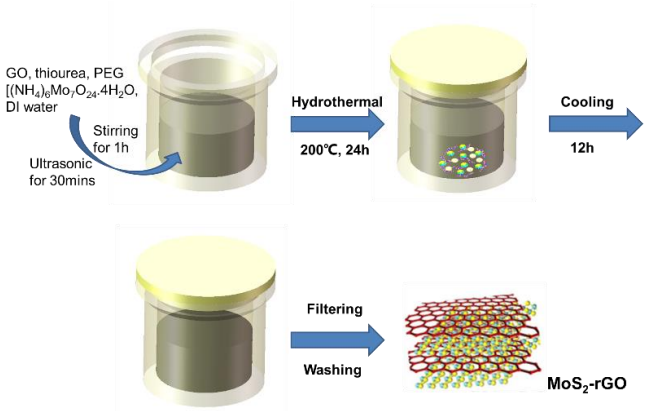


***Scheme 4-1. Schematic illustration of $MoS_2$-rGO synthesis process***

In this work, $MoS_2$ was prepared by the hydrothermal method at 160 - 220 °C for 12 – 36 h with the starting chemicals of GO, thiourea, and polyethylene glycol (PEG). $(NH_4)_6Mo_7O_{24}.4H_2O$ dissolved in deionized (DI) water. The specific process of synthesis is shown in Scheme 4-1.

## 4.2 Orthogonal experiment analysis

The orthogonal experiment, a methodology employed within the realm of orthogonal experimental design (OED), serves as a valuable tool for examining the impacts of numerous variables on a particular outcome.[253] This approach proves especially beneficial in elucidating the interplay among different factors within a system, all the while streamlining the requisite number of experiments. The concept of orthogonality, fundamental to this experimental technique, denotes the inherent characteristic of the design that facilitates the

isolation of individual factor effects from those of the other variables. Within an orthogonal experiment, the structure of the study guarantees that data analysis can proceed unhindered by the fluctuating levels of other factors under consideration. The experiments encompass a range of "factors," which represent the variables under scrutiny, each with distinct "levels" denoting the specific values at which the factor is assessed. Originating from the pioneering work of Genichi Taguchi,[254] these methodologies leverage orthogonal arrays to systematically arrange factors and levels in a manner that strikes a balance between comprehensive data collection and operational efficiency. Central to this approach is the emphasis on robust design principles and quality engineering standards. By employing Orthogonal Arrays as a key organizational tool, researchers can effectively navigate the complexities inherent in multifactor experiments, enabling a more structured and insightful analysis of the interrelationships among variables. This methodological framework not only aids in unraveling the intricate interactions between various factors but also paves the way for enhanced experimental design strategies that prioritize efficiency and statistical rigor. Through the systematic application of orthogonal experiment techniques, researchers can gain a deeper understanding of the underlying mechanisms influencing outcomes, leading to more informed decision-making processes in diverse fields ranging from industrial manufacturing to scientific research [254].

***Table 4-1. Detailed orthogonal experimental design (OED) for optimizing the feature extraction parameters.***

| Sample | Factor | | |
|---|---|---|---|
| | rGO Weight Percentage (wt%) | Heating Temperature (℃) | Heating Time (h) |
| S1 | A1 (0.8) | B1( 160) | C1 (12) |
| S2 | A1 (0.8) | B2 (180) | C2 (24) |
| S3 | A1 (0.8) | B3 (200) | C3 (36) |
| S4 | A2 (1.6) | B1 (160) | C2 (24) |
| S5 | A2 (1.6) | B1 (180) | C3 (36) |
| S6 | A2 (1.6) | B2 (200) | C1 (12) |
| S7 | A2 (2.4) | B3 (160) | C3 (36) |
| S8 | A2 (2.4) | B4 (180) | C1 (12) |
| S9 | A3 (2.4) | B1 (200) | C2 (24) |

## Electronic conductivity enhancement through graphene oxide (GO)-$MoS_2$-heterostructure

Taguchi orthogonal arrays (OAs) are structured in a balanced manner to ensure equal consideration of all levels of factors. Consequently, the evaluation of factors can be done independently of one another despite the fractional nature of the design. In the Taguchi OA setup, the focus is primarily on main effects and two-factor interactions, with higher-order interactions being assumed to be nonexistent [255]. Prior to conducting the experiment, designers are required to identify potentially significant interactions based on their subject matter expertise. The full factorial design comprising three factors (rGO weight percentage, hydrothermal heating temperature, and heating Time) with three levels entailed 27 runs, while an L9($3^3$) OED arrangement was selected following the OED guidelines. The varying levels of rGO weight percentage, heating temperature, and heating time parameters were determined based on prior studies [256]. Detailed information on the L9($3^3$) arrangement is presented in Table 4-1 and visually represented in Figure 4-1. Additionally, to assess the influence of different factors on the enhancement of the material's HER catalytic performance overpotential at a benchmark current density of 10 mA/cm$^2$ ($\eta_{10}$) was determined as pivotal variables in our study.

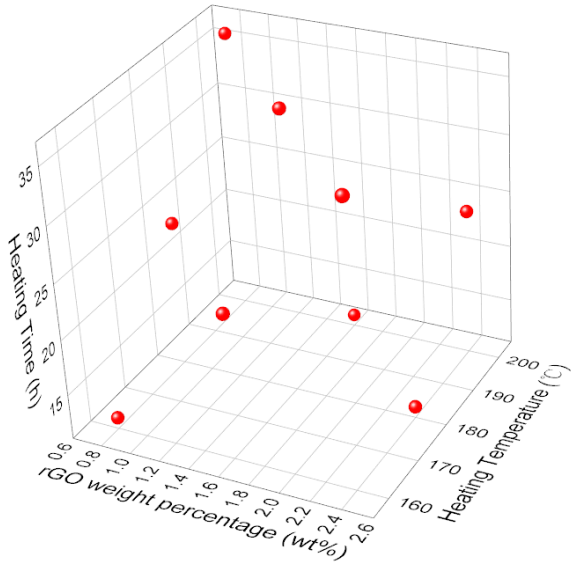


*Fig 4- 1. L9($3^3$) orthogonal experimental design (OED).*

### 4.2.1 Electrochemistry test of orthogonal experiment

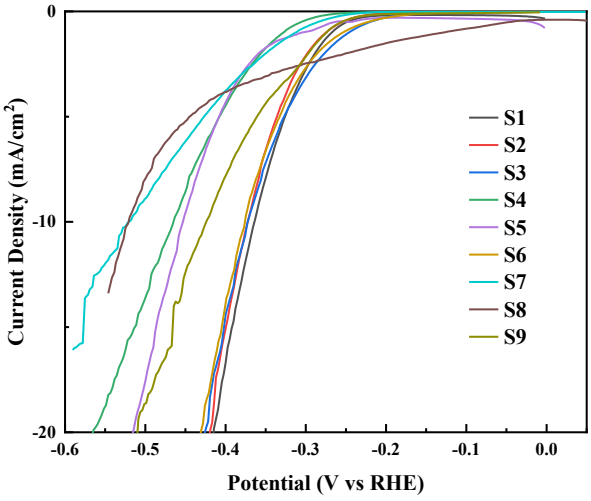


*Fig 4- 2. LSV curves of catalysts from S1-S9*

*Table 4-2. $\eta_{10}$ of $MoS_2$-rGO samples*

| Sample | S1 | S2 | S3 | S4 | S5 | S6 | S7 | S8 | S9 |
|---|---|---|---|---|---|---|---|---|---|
| $\eta_{10}$ (V) | 0.366 | 0.373 | 0.373 | 0.468 | 0.454 | 0.376 | 0.518 | 0.521 | 0.425 |

The following specimens were subsequently utilized as electrocatalysts for the hydrogen evolution reaction (HER). Evaluation of the electrochemical performance was conducted in a 0.5 M $H_2SO_4$ solution utilizing a glassy carbon electrode as the working electrode. For electrode preparation, 10 mg of the sample was dispersed in a mixture of 10 µL Nafion (Nafion™ 117 containing solution, Sigma-Aldrich) and 1000 µL deionized water, followed by ultrasonic treatment for 30 minutes to ensure uniform dispersion. A volume of 8 µL of the suspension, containing approximately 0.08 mg of the sample, was drop-cast onto the surface of a 3 mm diameter GC electrode. The electrode was dried under a white incandescent lamp for 15 minutes to ensure proper adhesion of the sample. An examination was carried out on the impact of the rGO weight percentage on the HER efficiencies. Visualization of polarization curves for the 9 specimens is presented in Fig. 4-2. At a current density of 10 mA/cm$^2$, the overpotential of the $MoS_2$-rGO samples under various synthesis conditions is clearly presented in Table 4-2, providing a comprehensive overview of the electrochemical performance at this specific operating condition.

### 4.2.2 Statistics analysis for orthogonal experiment results

The overall mean in an orthogonal design plays a vital role as a statistical metric that denotes the mean response observed in all experimental trials, serving as a reference point for assessing the impacts of various factors.

$$\bar{Y} = \frac{1}{N}\sum_{i=1}^{N} Y_i \quad \text{eq 4-1}$$

where $N$ is the number of experiments, and $Y_i$ is the response value of the $i^{\text{th}}$ experiment [257].

The mean of factor levels plays a pivotal role in enhancing comprehension regarding the impacts of various factors on the dependent variable, for a factor $A$ at level $k$, the average response value is:

$$\overline{Y_{A_k}} = \frac{1}{n_k}\sum_{j=1}^{n_k} Y_{A_k j} \quad eq\ 4\text{-}2$$

where $n_k$ is the number of experiments at level $k$ for factor $A$, and $Y_{A_k}$ is the response value of the $j^{th}$ experiment at level $k$ for factor $A$.

The term "Range" within this particular framework denotes the disparity between the highest and least values of a dependent variable, which is impacted by a multitude of factors. For a factor $A$, the range $R_A$ is showed below:

$$R_A = max\left(\overline{Y_{A_1}}, \overline{Y_{A_2}}, \dots, \overline{Y_{A_k}}\right) - min\left(\overline{Y_{A_1}}, \overline{Y_{A_2}}, \dots, \overline{Y_{A_k}}\right) \quad eq\ 4\text{-}3$$

where $\overline{Y_{A_k}}$ is the average response value at different levels of factor $A$ [257].

***Table 4-3. L9($3^3$) orthogonal experimental design and results analysis***

| Sample | Factor | | | Results ($\eta_{10}$) (V) |
|---|---|---|---|---|
| | rGO Weight Percentage (wt%) | Heating Temperature (℃) | Heating Time (h) | |
| S1 | A1 (0.8) | B1( 160) | C1 (12) | 0.373 |
| S2 | A1 (0.8) | B2 (180) | C2 (24) | 0.366 |
| S3 | A1 (0.8) | B3 (200) | C3 (36) | 0.373 |
| S4 | A2 (1.6) | B1 (160) | C3 (36) | 0.454 |
| S5 | A2 (1.6) | B1 (180) | C2 (12) | 0.468 |
| S6 | A2 (1.6) | B2 (200) | C1 (24) | 0.376 |
| S7 | A2 (2.4) | B3 (160) | C4 (24) | 0.518 |
| S8 | A2 (2.4) | B4 (180) | C3 (36) | 0.521 |
| S9 | A3 (2.4) | B1 (200) | C3 (12) | 0.425 |
| I | 1.112 | 1.345 | 1.266 | |
| II | 1.298 | 1.355 | 1.260 | |
| III | 1.464 | 1.174 | 1.348 | |
| $K_1$ | 0.371 | 0.448 | 0.422 | |
| $K_2$ | 0.433 | 0.452 | 0.420 | |
| $K_3$ | 0.488 | 0.391 | 0.449 | |
| R | 0.117 | 0.060 | 0.029 | |
| S | 0.021 | 0.007 | 0.002 | |

## Electronic conductivity enhancement through graphene oxide (GO)-$MoS_2$-heterostructure

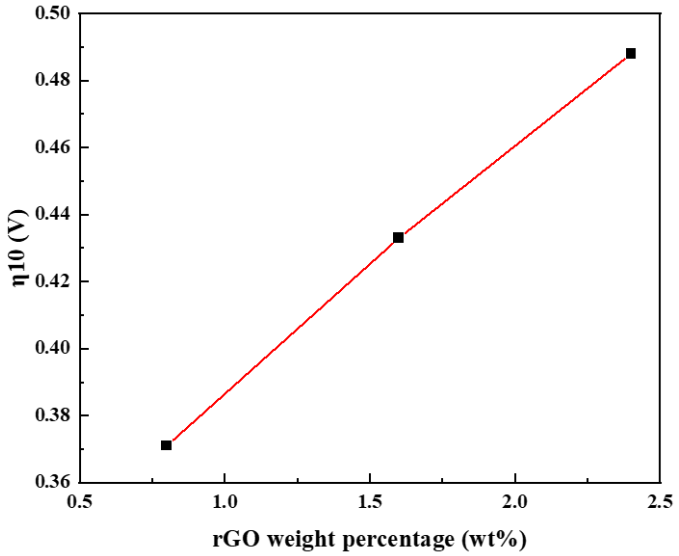


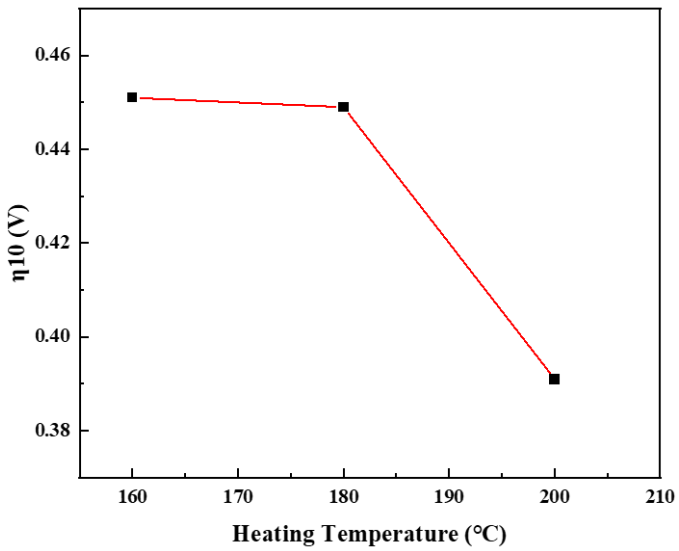

## Electronic conductivity enhancement through graphene oxide (GO)-$MoS_2$-heterostructure

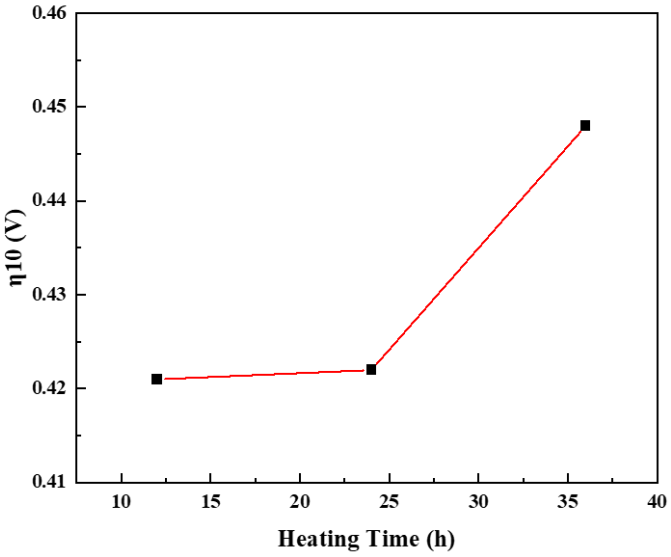


***Fig 4- 3. Main effect on the parameters a). rGO weight percentage, b.) Heating Temperature, and c). Heating time.***

Range analysis is a method of data processing in orthogonal experiments allowing for the assessment of each factor's level of influence on a specific indicator, as well as the identification of the optimal combination of factors for said indicator. The tables utilized for data analysis, namely Tables 4-3, use $Y_i$ to denote the sum of experimental outcomes linked to the $i^{th}$ level of a particular factor, with $\overline{Y}_i$ in parentheses representing the average value of $Y_i$. The optimal level of a factor is reached when $\overline{Y}_i$ attains its minmum value. Once the optimal levels of all factors are established, the optimal combination can be directly determined.[258] A higher $R$ value signifies a greater impact of a factor's variation on the experimental outcomes. Consequently, the hierarchy of factors influencing a specific indicator can be ascertained. Examination of Table 4-3 reveals that $MoS_2$-rGO exerts the most significant influence on rGO weight percentage ($R = 0.117$), followed by heating temperature ($R = 0.059$) and heating time ($R = 0.027$). Attaining a $\eta_{10}$ minimum requires GO weight percentage, heating temperature and heating time to be at 0.8 (wt%), 200 ℃ and 12

h respectively, as shown in Fig 4-3 These conditions signify that A1B3C1 represents the most optimum combination to achieve the best performing catalyst.

The determination of the impact of different factors on the catalytic performance of HER in the experimental setting can be ascertained by conducting an analysis of variance. In the examination of variance, the sum of squares $SST$ represents the total square deviation, which is derived through the utilization of (eq 4-4). The mean square (MS) is a statistical measure calculated through the application of (eq 4-7) and (eq 4-8) [259].

Total Sum of Squares ($SST$):

$$SST = \sum_{i=1}^{N}(Y_i - \bar{Y})^2 \quad eq\ 4\text{-}4$$

Sum of Squares for Factor $A$ ($SSA$) (could be any factor, such as $B$ or $C$),

where $m$ is the number of levels of factor $A$

$$SSA = \sum_{k=1}^{m} n_k\left(\overline{Y_{A_k}} - \bar{Y}\right)^2 \quad eq\ 4\text{-}5$$

Sum of Squares for Error ($SSE$)

$$SSE = SST - SSA \quad eq\ 4\text{-}6$$

Variance for Factor $A$, $\sigma_A^2$

$$\sigma_A^2 = \frac{SSA}{m-1} \quad eq\ 4\text{-}7$$

Error Variance, $\sigma_e^2$

$$\sigma_e^2 = \frac{SSE}{N-m-degree\ of\ freedom\ for\ other\ factors} \quad eq\ 4\text{-}8$$

$F$ -value

$$F_A = \frac{\sigma_A^2}{\sigma_e^2} \quad eq\ 4\text{-}9$$

The $F$ -value in the analysis of variance serves to indicate the relative importance of different factors on the volume of rock that is broken. A larger $F$ -value suggests a higher level of importance associated with the specific factor under consideration. On the other hand, the $p$ -value is utilized to assess the significance of each factor in relation to the $\eta_{10}$. A lower $p$ -value is indicative of a higher level of significance associated with the factor being analyzed.

A factor is deemed to be significant when its $p$ -value is equal to or less than 0.1. Conversely, if the $p$ -value exceeds 0.1, the factor is considered not significant.[260]

*Table 4-4. Variance analysis of $\eta_{10}$.*

| Factors | $df_A$ | *SSA* | $\sigma^2$ | *F-value* | *p-value* |
|---|---|---|---|---|---|
| **rGO Weight Percentage** | 2 | 0.0207 | 0.0103 | 8.0203 | 0.1109 |
| **Heating Temperature** | 2 | 0.0069 | 0.0034 | 2.6716 | 0.2724 |
| **Heating Time** | 2 | 0.0014 | 0.0007 | 0.5593 | 0.6413 |
| **Error** | 2 | 0.0026 | 0.0013 | | |
| **Total** | 8 | 0.0316 | | | |

The outcomes of the variance analysis regarding the overpotential at 10 mA/cm$^2$ can be observed in Table 4-4. The ordering of the $F$-value aligns with the range analysis findings. The $p$-values associated with rGO weight percentage, heating temperature and heating time are 0.1109, 0.2724 and 0.6413, respectively. While the current results of the orthogonal experiment indicate that none of the factors exhibit significance, it is anticipated that two specific factors, namely the rGO weight percentage and the heating temperature, may exhibit significance with an increase in the number of levels.

## 4.3 Verification of optimal levels of all factors

In order to ascertain the optimum combination of A1B3C1, a series of experiments were devised to authenticate its catalytic performance towards the HER. In this series of experiments, the rGO concentration was set at 0.8 wt%, while the duration of heating was 12 hours. The sole independent variable under investigation is the heating temperature, as it exerts the most significant influence on the crystal lattice of the substance.

### 4.3.1 Crystallography investigation

XRD is used for identifying crystal structures and calculating lattice parameters employing Bragg's law that shows the inverse relation of inter planar '$d_{hkl}$' spacing to the diffraction angle '2θ' and '*hkl*'s represent the Miller indices of a crystal [261] (eq 4-10)

$$2d_{hkl}\sin\theta = n\lambda \ (\lambda_{Cu,K\alpha} = 0.15406\ nm) \quad \textit{(eq 4-10)}$$

## Electronic conductivity enhancement through graphene oxide (GO)-$MoS_2$-heterostructure

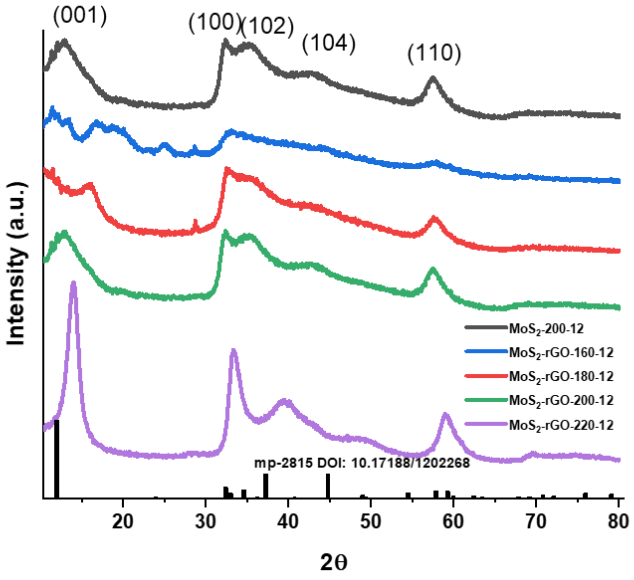


***Fig 4- 4. XRD patterns of $MoS_2$ and $MoS_2$-rGO at different synthesis conditions.***

In Figure 4-4, it is crucial to observe that as the synthesis temperature decreases, all peaks display notable broadening, indicating a decline in crystallinity. The decrease in intensity at lower synthesis temperatures also implies a short-range disordering feature present in samples synthesized under such conditions. The distinctive characteristics of samples prepared at low temperatures could potentially provide a greater number of active sites for the HER. Moreover, the occurrence of two widened peaks in the high-angle region (at 2θ of 32° and 57°) can be precisely linked to the (100) and (110) planes of the pristine 2H-$MoS_2$, demonstrating a uniform atomic configuration along the basal planes.[91]. An intriguing observation pertains to the prominent diffraction peak with a high index at 2θ = 12~13° (d=6.8~7.5 Å) evident in all samples, with the exception of $MoS_2$-rGO-160-12. This particular sample, synthesized at 160°C for 12 hours with a blend of 2.1 mg rGO, displays broader peaks falling within the 2θ = 10~21° range, thereby indicating its characterization as the most amorphous specimen within the group. Additionally, the analysis involving $MoS_2$-

200-12 (prepared at 160°C for 12 hours with a 2.1 mg rGO mixture), $MoS_2$-200-12 (synthesized at 160°C for 12 hours), and $MoS_2$-rGO-200-12 (fabricated at 200°C for 12 hours with a 2.1mg rGO mixture) illustrates that the presence of a 0.8 wt% rGO mixture does not exert a substantial influence on the structure of $MoS_2$. Moreover, it is worth mentioning that the XRD analysis fails to detect the 0.8 wt% rGO phase, given its absence of a distinct diffraction peak at approximately 2θ of 25°, a threshold beyond the detection capability of XRD assessment. [262]

### 4.3.2 Conductivity

The four-point probe test is a highly versatile and accurate approach utilized across various disciplines for the assessment of diverse parameters, with a primary emphasis on electrical characteristics and pressure evaluations. When it comes to electrical assessment, the four-point probe methodology is utilized for determining the resistivity and sheet resistance of different materials. [263,264]

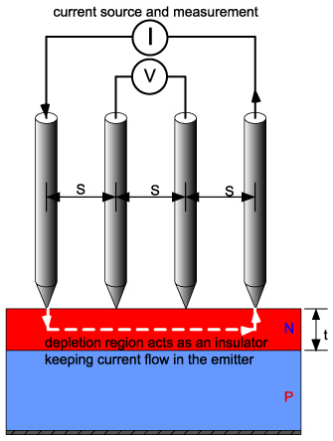


***Scheme 4-2 Schematic diagram of the four-point probe method.*** [264]

This process involves the utilization of four individual probes to establish contact with the material, where the two external probes administer current while the two internal probes gauge the voltage drop (Sheme 4-2). Consequently, this approach effectively

eliminates contact resistance inaccuracies and furnishes precise resistivity measurements.[263]

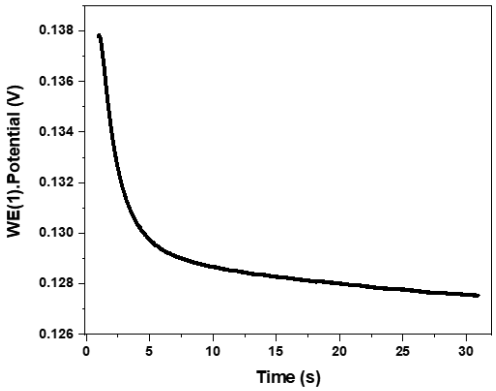


*Fig 4- 5. Chronopotentiometry showing the voltage drop after applying 0.3 A for 30 s.*

For the $MoS_2$ specimens, an electric current of 0.3 A was applied, and the corresponding voltage decline was recorded over a period of 30 seconds employing the chronopotentiometry methodology (Figure 4-5). This assessment was conducted five times across various regions of the specimen, and the mean voltage drop was computed to guarantee precision and uniformity in the findings.

The conductivity values calculated for the samples with rGO contents of 0.8 wt%, 1.7 wt%, 2.4 wt%, 3.2 wt%, as well as bulk $MoS_2$, are summarized in Table 4-5. This table provides a comprehensive reference for comparing the specific electrical properties of each sample.

*Table 4-5. The conductivity of different rGO wt% of $MoS_2$*

| Sample | $MoS_2$ | 0.8% rGO | 1.7% rGO | 2.5% rGO | 3.5 % rGO |
|---|---|---|---|---|---|
| Conductivity (S/m) | 69.966 | 118.957 | 51.004 | 169.546 | 203.405 |

As shown in the data, there is a clear trend of enhanced electrical conductivity with increasing rGO content, indicating the positive role of rGO in improving the charge transport characteristics of the $MoS_2$ matrix. An exception is observed at 1.7 wt% rGO, where a slight

deviation from the overall increasing trend occurs, possibly due to structural irregularities or agglomeration effects.

### 4.3.3 Raman Spectrum

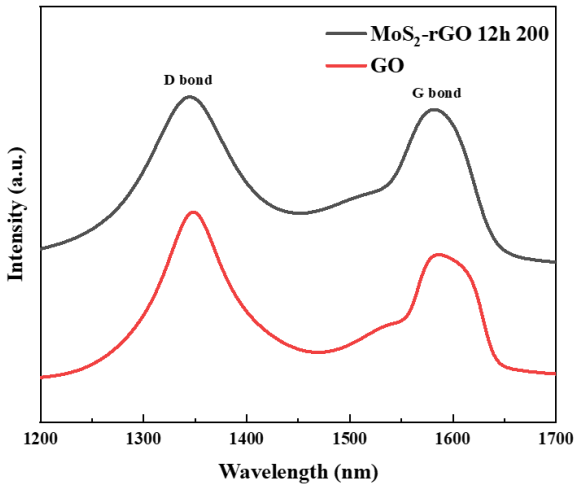


*Fig 4- 6. Raman spectra measured for $MoS_2$-rGO 12h 200 and GO*

rGO significantly boosts the conductivity of $MoS_2$ by various mechanisms. Initially, the $MoS_2$, structured in a hierarchical 3D flower-like manner and integrated with rGO nanosheets, creates sandwich heterostructures [265]. It establishes a conductive framework that promotes swift electron transfer to the active sites of the catalysts. Additionally, rGO exhibits elevated conductivity in comparison to GO as a result of the reduction procedure involving hydrazine hydrate, leading to the elimination of oxygen-based functional moieties present in GO.[266] This is confirmed by a lowering $I_D/I_G$ ratio in Raman analysis in Fig 4-6 (1.08 for $MoS_2$-rGO 12h 200 and 1.35 for GO). The presence of two distinctive bands, namely the D and G bands, in $MoS_2$-rGO 12h 200 is evident through their respective peaks at 1345 $cm^{-1}$ and 1581 $cm^{-1}$. The D band is indicative of the presence of $sp^3$ defects or disordered states, while the G peak signifies the vibrational motion of in-plane carbon atoms ($sp^2$) and is

associated with the $E_{2g}$ symmetry of the doubly degenerate phonon mode [267]. Similarly, characteristic peaks of GO are observed at D band ~1347 $cm^{-1}$ and G band ~1587 $cm^{-1}$.

### 4.3.4 Electrochemistry

In acidic media, the possible reactions are Volmer-Heyrovsky or Volmer-Tafel process [20,268]:

Chapter 1. discharge step (Volmer reaction):

$H_3O^+ + e^- \rightarrow H_{ads} + H_2O$(subscript$_{ads}$ means adsorbed to the catalyst)

$$b = 120\ mV\ (where\ b\ is\ Tafel\ slope)\ eq\ 4\text{-}11$$

Chapter 2. desorption step (Heyrovsky reaction):

$$H_{ads} + H_3O^+ + e^- \rightarrow H_2 + H_2O, b = 40mV\ eq\ 4\text{-}12$$

Chapter 3. recombination step (Tafel reaction):

$$H_{ads} + H_{ads} \rightarrow H_2, b = 30mV\ eq\ 4\text{-}13$$

The kinetics of the as-synthesized material for HER was investigated by measuring the Tafel slope. The Tafel slope analysis reveals the possible mechanism involved in the HER process. As shown in Figs. 4-7 (a) and 4-7 (b), the HER on a Pt surface is known to proceed through the Volmer-Tafel mechanism (equations 4-11 and 4-13), and the recombination step is the rate-limiting step at low overpotentials, given by the reported Tafel slope of 41 mV/dec [128].

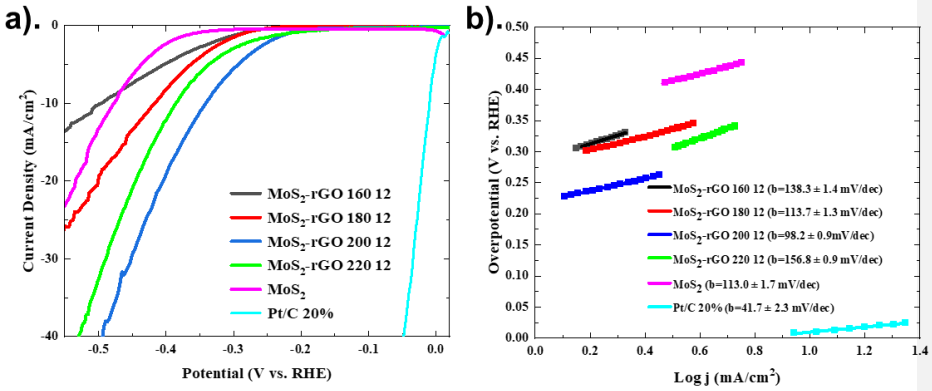


*Fig 4- 7. (a) Linear sweep voltammograms (LSV) in 0.5 M $H_2SO_4$ at sweep rate of 1mV/s. (b). Corresponding Tafel plot.*

### Electronic conductivity enhancement through graphene oxide (GO)-$MoS_2$-heterostructure

As illustrated in Figure 4-7 (a), the overpotential values for rGO/$MoS_2$ specimens at 10 A/cm$^2$ are $\eta_{10}$ = -0.50 V vs RHE ($MoS_2$-rGO 160 12), $\eta_{10}$ = -0.42 Vs RHE (MoS2-rGO 180 12), $\eta_{10}$ = -0.34 V vs RHE ($MoS_2$-rGO 200 12), and $\eta_{10}$ = -0.39 V vs RHE ($MoS_2$-rGO 220 12). The overpotential shows an upward trend with the rise in synthesis temperature, except upon reaching 220 °C. It is noteworthy to observe that only '$MoS_2$-rGO 200 12' exhibits a lower Tafel slope of 98.2 mV/dec compared to pure $MoS_2$ (Tafel slope = 113.0). In this scenario, the crystal structure of $MoS_2$ exerts a more significant influence on the HER performance than the 0.8% rGO. Nonetheless, the addition of rGO does contribute to the reduction of overpotential, attributed to the enhancement in $MoS_2$ conductivity as demonstrated in Table 4-5. The composite of $MoS_2$-rGO 200 12 exhibited superior catalytic performance for the HER at current densities of 10 mA/cm$^2$. These results provided evidence that the combination of $A_1B_3C_1$ was the most effective among the options tested in orthogonal experimental setups.

## 4.4 Conclusion

In the realm of orthogonal experiments, despite the absence of statistical significance in any of the factors attributed to inadequate levels, it is still viable to ascertain the comparative significance of individual factors by analyzing range and p-values. By performing the mean of factor levels, the optimal combination of HER catalytic properties was determined, and the validity of this combination was confirmed via electrochemical assessments.

By utilizing X-ray diffraction (XRD) analysis, it was discerned that with escalating temperature, there was a notable observation in the level of crystallinity observed in $MoS_2$-rGO. This phenomenon occurs due to the fact that an increase in temperature facilitates the growth of crystals.

By employing four-probe testing, it was determined that the rise in weight percentage (wt%) of rGO in $MoS_2$ led to an enhancement in conductivity. This enhancement can be largely attributed to the incorporation of rGO within the $MoS_2$ layer, resulting in the creation of a conductive framework that facilitates electron migration. Moreover, by utilizing

## Electronic conductivity enhancement through graphene oxide (GO)-$MoS_2$-heterostructure

Raman spectroscopy, it has been ascertained that the conductivity of rGO exhibits the potential for additional enhancement compared to GO as a result of a reduced number of defects.

# Effect of layer structure modification through vanadium dopant in $MoS_2$

## 5.1 Introduction

Transition metal dichalcogenides (TMDs) have risen as promising candidates for catalyzing the HER due to their distinct properties and benefits, which encompass cost-effectiveness, adjustable electronic characteristics, as well as structural and chemical versatility[269,270]. Among the myriad of TMDs available such as tungsten disulfide, molybdenum diselenide, and tin disulfide, molybdenum disulfide ($MoS_2$) holds a significant position due to its exceptional catalytic performance for the HER, along with its favorable mechanical and thermal stability, capacity for electronic property flexibility via structural adjustments (e.g., transitioning from 2H to 1T phase), as well as its abundance and economical nature relative to noble metals. The metastable 1T polymorph of molybdenum disulfide ($MoS_2$) has emerged as a promising functional material in electrochemical energy conversion technologies, owing to its metallic electronic structure and the presence of delocalized electrons. This phase demonstrates exceptional electronic conductivity (exceeding $10^3$ $S \cdot cm^{-1}$) and superior electrochemical activity compared to its semiconducting 2H phase, particularly in critical processes such as the hydrogen evolution reaction (HER) with onset potentials below 50 mV versus RHE. [271–274] Despite its benefits, the production of 1T-$MoS_2$ poses challenges. One common approach involves a lithium intercalation technique, which entails the insertion of lithium ions into the 2H-$MoS_2$ framework to form 1T-$MoS_2$. This process usually involves reacting 2H-$MoS_2$ with n-butyllithium in an unreactive environment. The lithium ions intercalate between the $MoS_2$ layers, causing a phase transition from 2H to 1T. Nonetheless, the complex process of removing residual lithium can be time-consuming and may introduce impurities. Moreover, the subsequent exfoliation process following lithium intercalation to produce single or few-layer 1T-$MoS_2$ nanosheets must be meticulously controlled to ensure uniform thickness

and size, a task that can be daunting and necessitates precise adjustment of conditions. In contrast to converting 2H-$MoS_2$ to 1T-$MoS_2$, doping offers a more straightforward method of altering the material's structural properties [275–278]. Doping with aliovalent ions such as $Ni^{2+}$ or isovalent ions $Co^{4+}$ into the $Mo^{4+}$ site can enhance the catalytic efficacy of 2H-$MoS_2$ for reactions like the HER by introducing active sites or modifying the material's surface characteristics. Thus, the potential for enhancing $MoS_2$'s HER capabilities through strategic doping is substantial.

Among various dopants, the inclusion of vanadium ions ($V^{2+}$, $V^{4+}$ and $V^{5+}$), a transition metal, into $MoS_2$ significantly enhances its HER performance. Research into the utilization of vanadium (V) doped $MoS_2$ for the hydrogen evolution reaction (HER) has exhibited encouraging outcomes in amplifying the electrocatalytic efficacy of $MoS_2$. The incorporation of vanadium into $MoS_2$ has been investigated using diverse synthesis methodologies, encompassing solvothermal approaches and electrospinning, to enhance the catalytic efficiency and endurance for HER[279–281]. V doping introduces distinct electronic configurations and generates numerous active sites, which aid in enhancing the HER performance by enabling efficient electron transfer and hydrogen adsorption/desorption processes. The fabrication of V-doped $MoS_2$-$Ni_xS_y$/NF (NF represent nanoflower) hollow nanospheres through an in situ one-pot technique illustrated that the electrocatalytic efficiency could be fine-tuned by regulating the quantity of vanadium doping. This adjustment resulted in a notable decrease in overpotential and improved endurance during HER [282]. Similarly, the co-doping of $V^{4+}$ and $N^{3-}$ in $MoS_2$ has been demonstrated to induce strain in the crystal lattice, reduce the optical band gaps, and shift the absorbance band towards lower energy levels, collectively improving the catalytic efficacy for HER[283]. Furthermore, the synthesis of V-doped $MoS_2$-rGO nanocomposites using a simple solvothermal approach demonstrated exceptional catalytic performance characterized by a low initiation potential, minimal Tafel slope, and robust stability under acidic conditions, emphasizing the collaborative influence of V-doping and the conductive rGO [284]. Nonetheless, it is crucial to recognize that not all doping techniques result

in enhanced catalytic efficacy. A particular investigation exploring the impact of different dopants, such as V, on $MoS_2$ and $WS_2$, revealed that while $Mn^{3+}$ and $Fe^{3+}$ dopants improved electrocatalytic efficiency towards the oxygen reduction reaction (ORR)[285]. These observations emphasize the intricate nature of doping approaches and their implications on the electrocatalytic characteristics of $MoS_2$. Although V doping has demonstrated potential in augmenting HER performance, the overall effectiveness is contingent on factors such as the synthesis process, doping level, and the interplay between the dopant and the $MoS_2$ framework [286–288].

In this research, a simple one-step hydrothermal method was employed to fabricate vanadium-doped $MoS_2$ at designated concentrations. To evaluate the influence of doping levels on HER activity within a 0.5 M $H_2SO_4$ electrolyte, $MoS_2$ samples were synthesized with 2%, 5%, and 10% vanadium doping. The $V^{4+}$ dopant has the capacity to substitute for $Mo^{4+}$ atoms, integrating itself into the transition metal lattice. The structural and compositional modifications introduced by vanadium doping and interlayer stacking contribute to the enhancement of HER activity. The $V^{4+}$ dopant is considered to substitute for $Mo^{4+}$ atoms within the $MoS_2$ lattice, rather than occupying interstitial positions. This assumption is supported by the absence of a significant shift to lower angles in the (002) peak of the XRD pattern, which would otherwise suggest interlayer expansion typical of interstitial doping. Moreover, XPS analysis confirms that vanadium exists predominantly in the +4 oxidation state, with no detectable signal corresponding to metallic $V^0$, which is often associated with unincorporated or interstitial species. These observations together indicate a substitutional doping mechanism, wherein $V^{4+}$ replaces $Mo^{4+}$ within the crystal lattice.[289] A detailed investigation was performed to analyze the effects of varying vanadium concentrations on the HER performance of the nanosheets. The 10% V-$MoS_2$ catalyst, containing a moderate amount of vanadium, exhibits the most favorable activity. Furthermore, the synergistic interactions of V-doping, interlayer contraction, and site-specific V substitution on the enhanced HER performance of $MoS_2$ nanosheets are examined in greater detail.

## Effect of layer structure modification through vanadium dopant in $MoS_2$

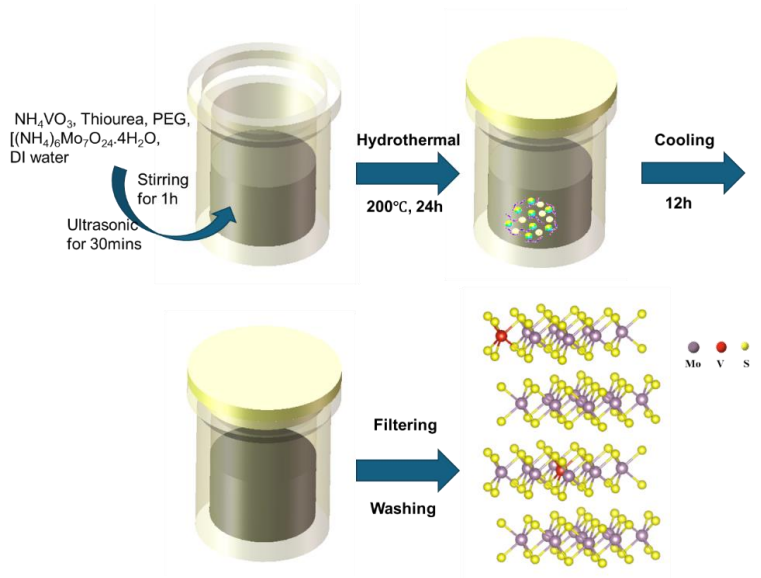


***Scheme 5-1. Schematic illustration of V-doped $MoS_2$ synthesis process***

In this work, $MoS_2$ was prepared by the hydrothermal method at 200 °C with the starting chemicals of thiourea, and polyethylene glycol (PEG). $(NH_4)_6Mo_7O_{24}.4H_2O$ dissolved in deionized (DI) water. Ammonium metavanadate ($NH_4VO_3$) was used as a vanadium precursor, and different concentrations of $NH_4VO_3$ were mixed into solutions to make certain dopant ratios (2%, 5% and 10% vanadium dopant). The synthesis procedure is illustrated in Scheme 5-1, while the quantities of starting materials are detailed in Table 5-1.

***Table 5-1 Compositions of the V-doped $MoS_2$ nanoflowers prepared with reactants of various V contents***

| Samples | Reactants | | | | |
|---|---|---|---|---|---|
| | $(NH4)_{6Mo7O24·4H2O}$ (mmol) | NH4VO3 (mmol) | CH4N2S (mmol) | Polyethylene glycol (g) | DI water (ml) |
| **MoS2** | 0.223 | 0 | 4.532 | 0.322 | 13.8 |
| **V0.02Mo0.98S2** | 0.219 | 0.031 | 4.532 | 0.322 | 13.8 |
| **V0.05Mo0.95S2** | 0.212 | 0.078 | 4.532 | 0.322 | 13.8 |
| **V0.1Mo0.9S2** | 0.201 | 0.156 | 4.532 | 0.322 | 13.8 |

## 5.2 Results and Discussion

### 5.2.1 Investigation of morphological characteristics

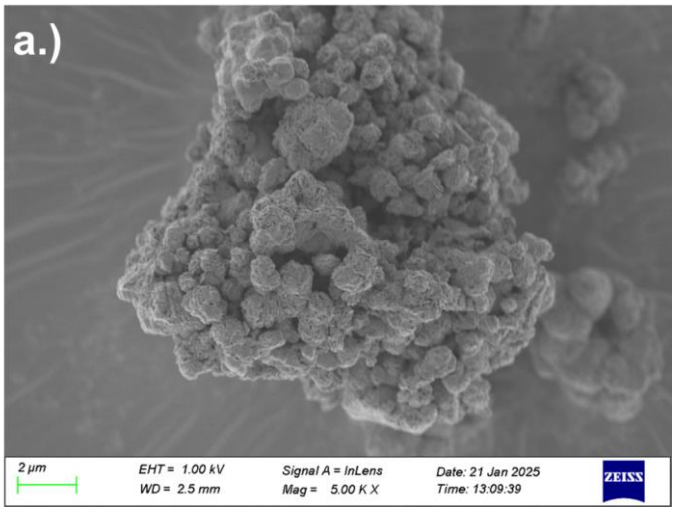


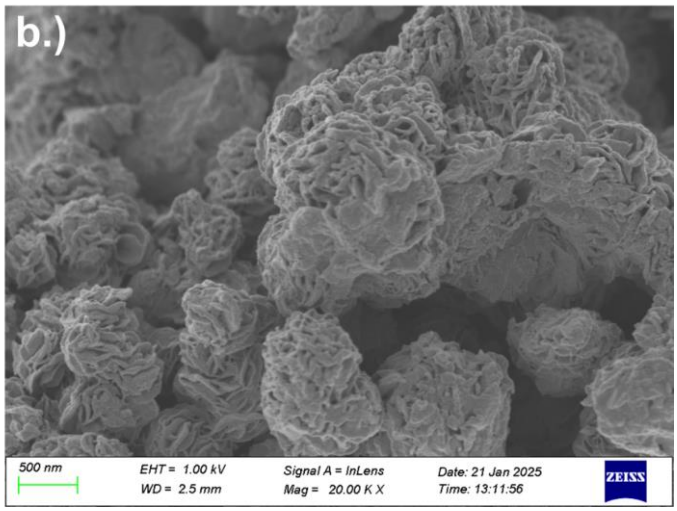

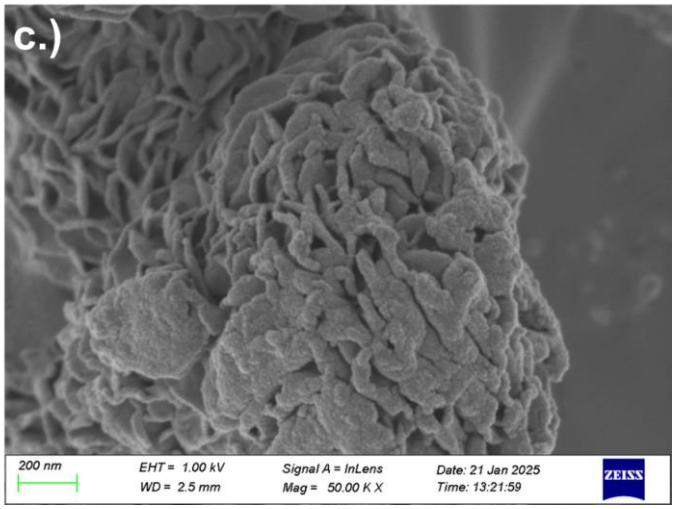
c.)
200 nm
EHT = 1.00 kV
WD = 2.5 mm
Signal A = InLens
Mag = 50.00 K X
Date: 21 Jan 2025
Time: 13:21:59
ZEISS

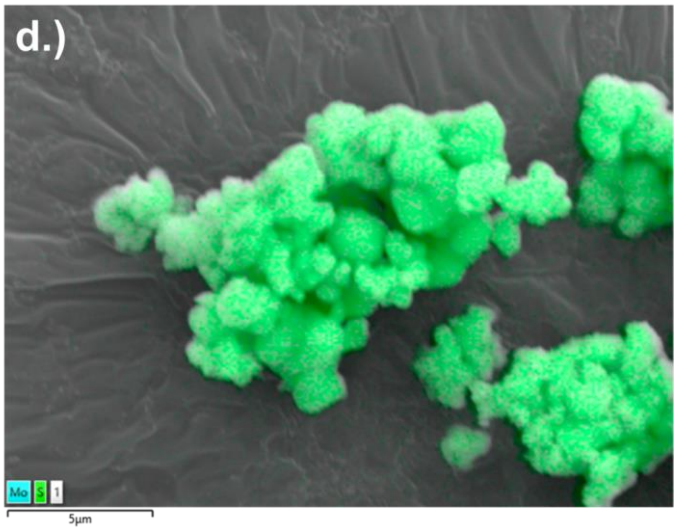
d.)
Mo
S
1
5µm

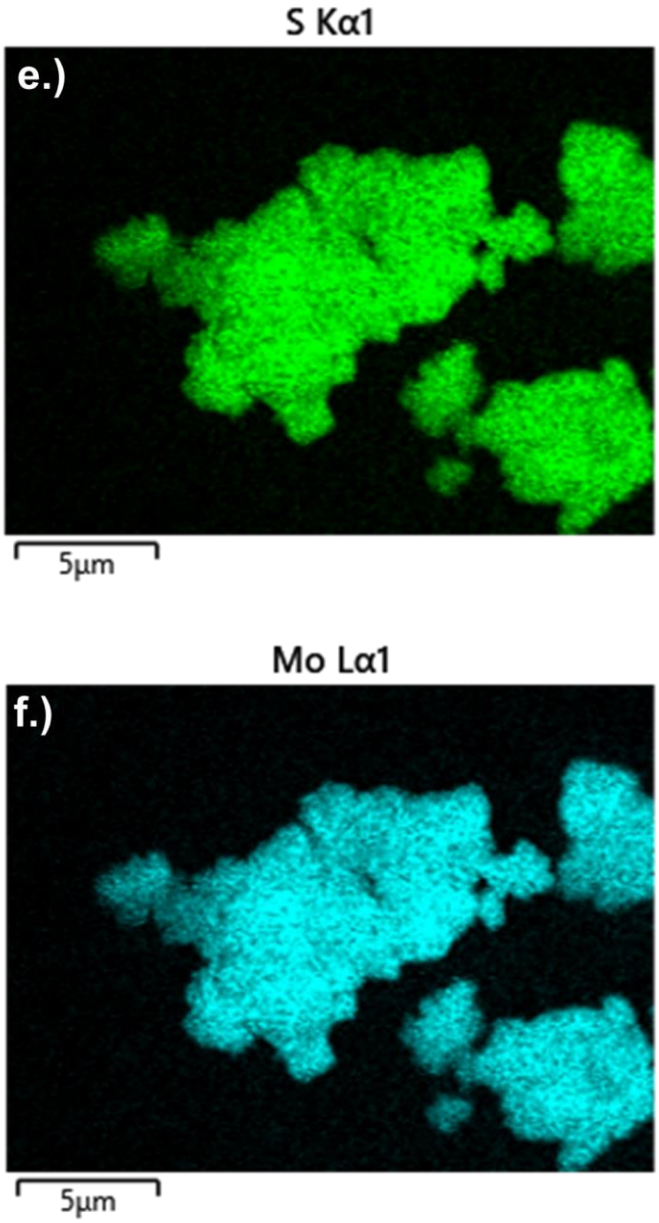


*Fig 5- 1. (a-c) Scanning electron microscope (SEM) images of $MoS_2$, (d-f) and corresponding elemental mapping*

## Effect of layer structure modification through vanadium dopant in $MoS_2$

Scanning electron microscope (SEM) images were collected in order to comprehend the crystal growth mechanism and the morphology of the produced materials. The surface morphologies of the synthesized $MoS_2$ are illustrated in Fig. 5-1. Detailed SEM images of $MoS_2$ revealed a flower-like architecture characterized by large petals converging at a central point of adhesion. This particular molecular configuration exposes active sites, thereby enhancing the hydrogen adsorption capacity [284]. The diameter of $MoS_2$ nano-flowers with ultra-thin petals was estimated to be approximately 200 nm (as shown in Fig. 5-1c). Further analysis unveiled that the petals of the nano-flowers exhibited a rough surface. Elemental mapping for $MoS_2$ was also conducted (depicted in Fig. 5-1 d~f), revealing the presence of Mo and S fabricated nanomaterials. The elemental mapping outcomes reveal the uniform dispersion of Mo and S atoms throughout $MoS_2$ specimens [290].

## Effect of layer structure modification through vanadium dopant in $MoS_2$

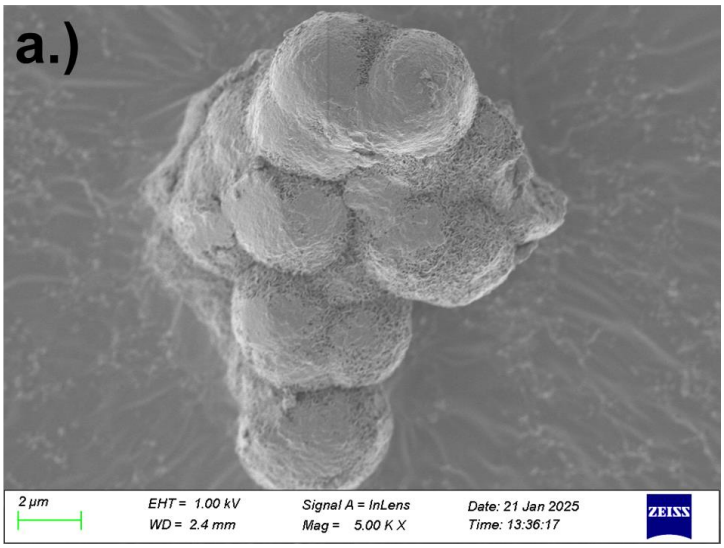


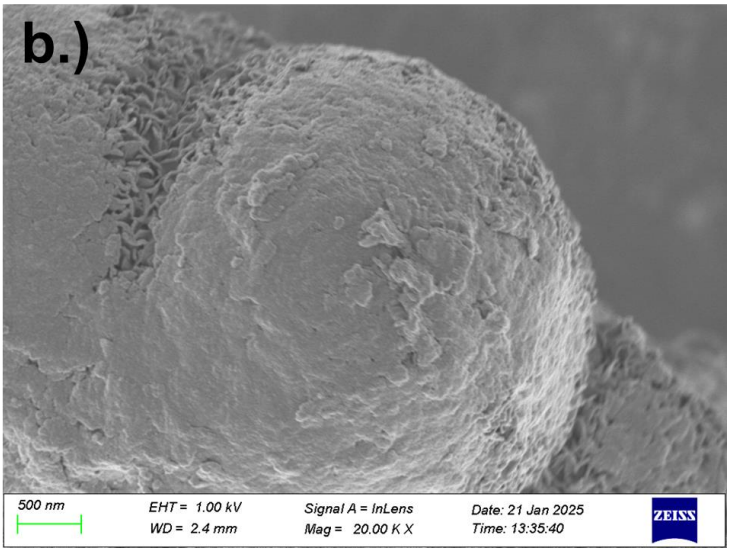

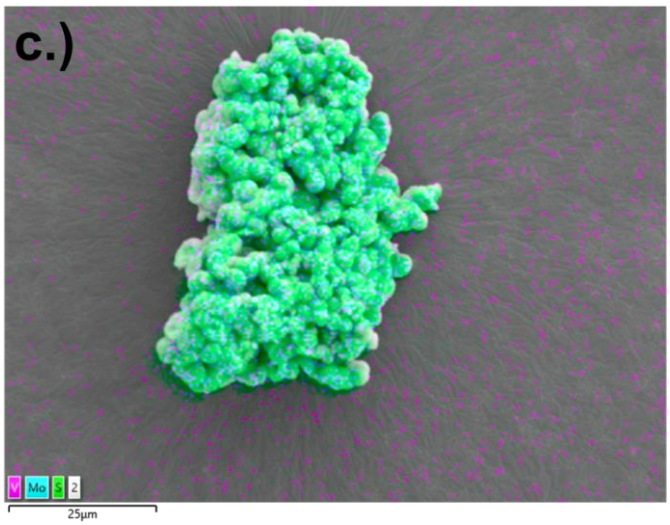
c.)
V
Mo
S
2
25µm

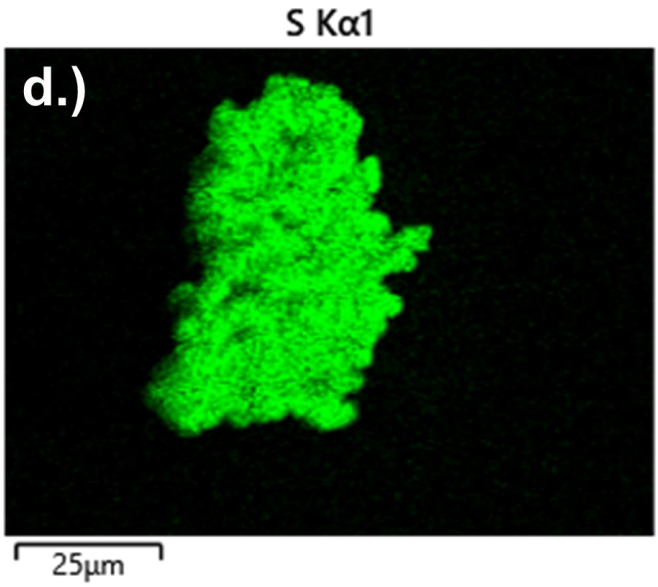
S Kα1
d.)
25µm

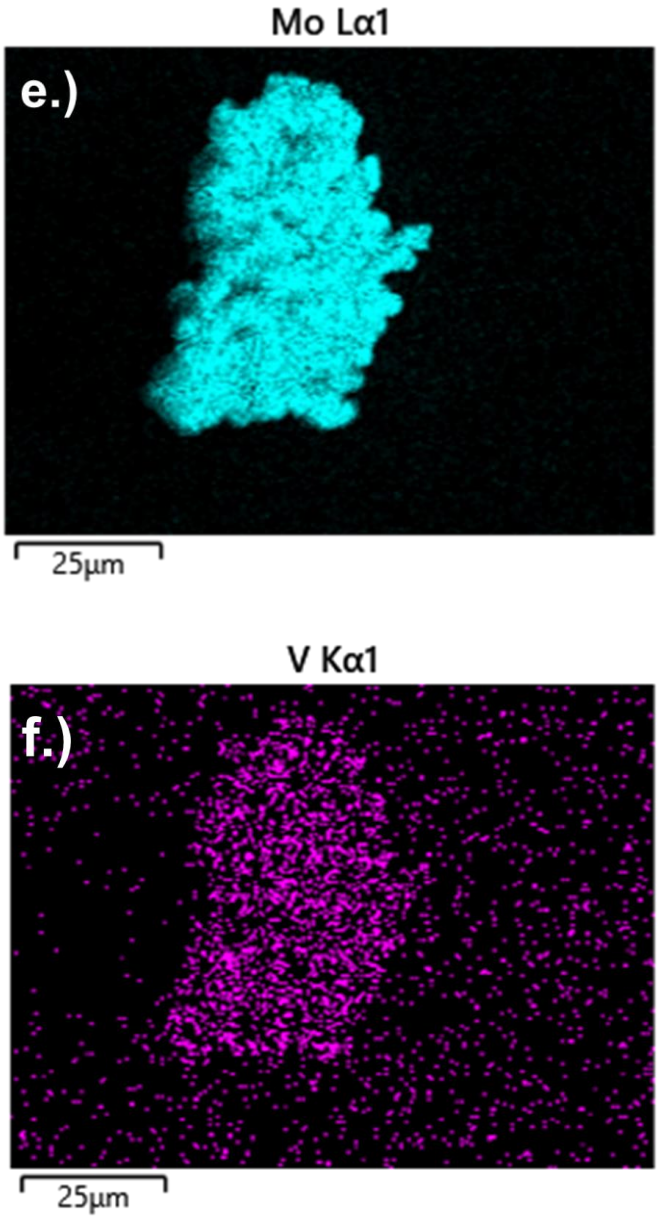


*Fig 5- 2. (a-b) SEM images of $V_{0.1}Mo_{0.9}S_2$, and (c-f) corresponding elemental mapping*

In comparison to $MoS_2$, the material's morphology underwent significant alterations following the addition of V (shown in Fig 5-2 a-c). It is important to note a distinct increase in smoothness, with the petal structure proving challenging to distinguish. This phenomenon arises due to the introduction of various defects, including vacant sites, alter the interlayer separation, and change of strain, during the process of doping. The doped V displaces the original Mo, prompting the migration of Mo and S atoms from their usual positions to create vacancies and alter the interlayer separation. Furthermore, V doping leads to a rise in the dislocation density within the material, thereby further disrupting the regularity of the crystal lattice. These imperfections and impurities (manifesting as an upsurge in the $S^{4+}$ quantity shown in Fig 5b.) contribute to the disorder within the material and facilitate the development of amorphous states. Mapping of Mo, V, S using Energy Dispersive X-ray Spectroscopy (EDS) was performed on the $V_{0.1}Mo_{0.9}S_2$ specimen. The spatial distribution of the three elements reveals a homogeneous distribution within the aggregates, providing additional evidence supporting the synthesis of V-doped $MoS_2$.

### 5.2.2 Crystallographic investigation

X-ray diffraction (XRD) analysis was conducted to investigate the crystal structure of $MoS_2$ nanoflowers doped with V, as illustrated in Figure 5-3. The XRD patterns obtained for all the samples closely matched the characteristic pattern of the hexagonal $MoS_2$ phase as documented in the Powder Diffraction File (PDF Card - 04-010-5047). The absence of any indication of the presence of $VS_2$ phase, coupled with the consistent observation of the hexagonal $MoS_2$ phase in all samples, strongly suggests that the doping of V in $MoS_2$ occurred through substitution, thereby maintaining the crystal structure of $MoS_2$ [291]. The outcomes of the Rietveld analysis demonstrated goodness-of-fit ($\chi^2$) values of 2.26, 1.93, 2.28, and 1.67 for $MoS_2$, $V_{0.02}Mo_{0.98}S_2$, $V_{0.05}Mo_{0.95}S_2$ and $V_{0.1}Mo_{0.9}S_2$ correspondingly, indicating the validity of the refinement outcomes (Table 5-2). The introduction of dopants at concentrations of 0%, 2%, 5% and 10% by weight results in an elevation of the (002) lattice plane to angles of 13.887, 14.067, 14.13 and 14.262 degrees, respectively (Table 5-3). The reduction in d-space with

higher dopant levels can be attributed to the substitution of some $V^{4+}$ with $Mo^{4+}$, which possesses a larger atomic size. [292] A peak corresponding to an angle of 2θ=7.3 is detectable in the diffraction pattern, indicating the presence of absorbed water molecules within the structure of $MoS_2$ nanoflower. It is noteworthy that the hydrophilic nature of 1T-$MoS_2$ and hydrophobic nature of 2H-$MoS_2$ dictate their interaction with water molecules, with 1T-$MoS_2$ showing an affinity for absorbing such molecules. This affinity is reflected in the appearance of a distinct peak at approximately 2θ=7.5 degree in the diffraction spectrum.[279]

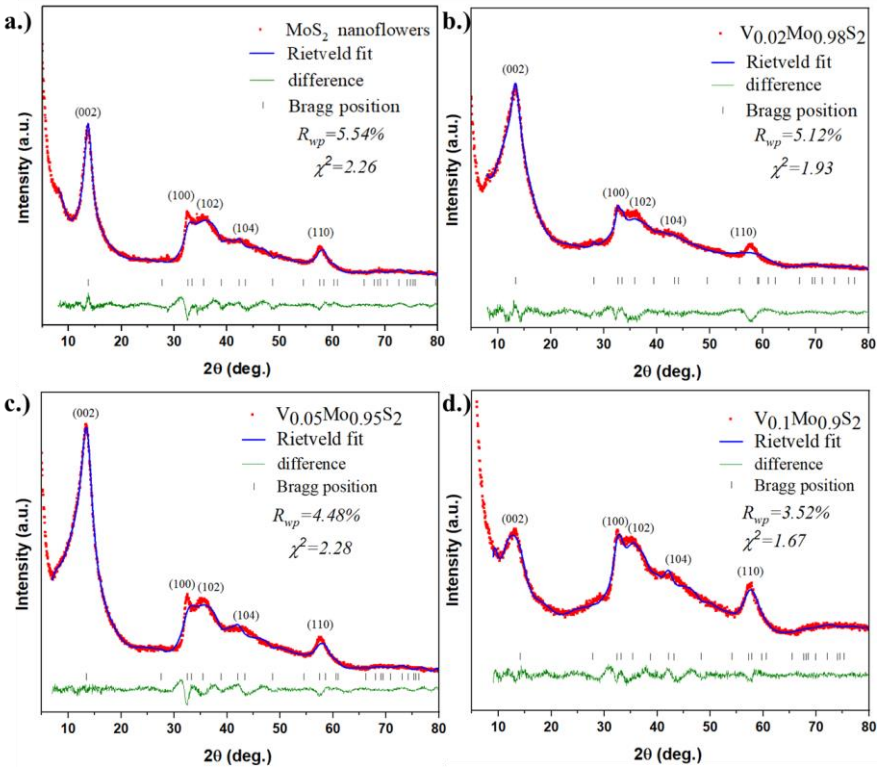


***Fig 5- 3. Powder XRD pattern with Rietveld refinement a). $MoS_2$ nanoflowers b). $V_{0.02}Mo_{0.98}S_2$ c). $V_{0.05}Mo_{0.95}S_2$ d). $V_{0.1}Mo_{0.9}S_2$.***

The absence of (103) and (105) peaks in the XRD pattern of $MoS_2$ indicates a specific crystallographic orientation or structural arrangement [293,294].

***Table 5-2. Parameters of $MoS_2$ nanoflower and V-doped $MoS_2$ As Obtained by Rietveld Refinement***

Effect of layer structure modification through vanadium dopant in $MoS_2$

| Parameters | $MoS_2$ | $V_{0.02}Mo0._{98}S_2$ | $V_{0.05}Mo0._{95}S_2$ | $V_{0.1}Mo0._9S_2$ |
|---|---|---|---|---|
| a(Å) | 3.143±0.0086 | 3.154±0.099 | 3.076±0.0089 | 3.081±0.0234 |
| b(Å) | 3.143±0.0086 | 3.154±0.099 | 3.076±0.0089 | 3.081±0.0234 |
| c(Å) | 12.744±0.0196 | 12.577±0.242 | 12.526±0.018 | 12.423±0.054 |
| V($Å^3$) | 109.072±0.493 | 108.386±0.616 | 102.67±0.484 | 102.129±0.135 |
| $\%R_{wp}$ | 5.37 | 5.11 | 4.48 | 3.52 |
| $\chi^2$ | 2.26 | 1.93 | 2.28 | 1.67 |

***Note: "a", "b", and "c" correspond to the lattice parameters along the crystallographic axes.***

***Table 5-3. 2θ values for $MoS_2$ nanoflower and V-doped $MoS_2$ nanoflower and V-doped $MoS_2$***

| (h k l) | 2 theta (degree) | | | |
|---|---|---|---|---|
| | $MoS_2$ | $V_{0.02}Mo0._{98}S_2$ | $V_{0.05}Mo0._{95}S_2$ | $V_{0.1}Mo0._9S_2$ |
| 0 0 2 | 13.887 | 14.067 | 14.13 | 14.262 |
| 1 0 0 | 32.632 | 32.672 | 32.546 | 32.443 |
| 1 1 0 | 58.437 | 59.046 | 57.46 | 57.838 |

## 5.2.3 XPS measurements

X-ray photoelectron spectroscopy (XPS) was used to examine the surface state, composition, and phase information of the different samples. The binding energy assignments are supported by relevant literature references:

1. Mo binding energy distributions are based on Table 3-3 [200–208]
2. S binding energy distributions are also referenced from published literature:[295–306]

*Table 5-4. XPS-S 2p Binding Energy Reference Table*

| XPS-S 2p Binding Energy Reference Table | | | |
|---|---|---|---|
| **Chemical State** | **Binding Energy Range (eV)** | **Chemical State** | **Binding Energy Range (eV)** |
| -C-S-S-C- (organic disulfide) | 163.3~164.6 | $AgS_2$ | 160.6~160.9 |
| C-S-C | 163.1~164.3 | SnS | 160.7~161.5 |
| C-S-H | 163.3~164.3 | FeS | 160.7~161.6 |
| $C_4S$-H | 163.6~164.4 | PbS | 160~161.2 |
| $R_2$-SO | 165~166 | ZnS | 161.2~161.9 |
| C-$SO_3$-H | 167.9~168.4 | FeAsS | 161.3~162.5 |
| $SO_2$-C | 167.4~167.8 | $CuFeS_2$ | 161.3~165.7 |
| | | MnS | 161.4~162.1 |
| | | $CuS_2$ | 161.5~162.4 |
| | | CuS | 161.5~162.7 |
| | | $MnS_2$ | 161.6~162.3 |
| | | $Ga_2S_3$ | 161.8~162.6 |
| | | $MoS_2$ | 161.8~163.1 |
| | | $WS_2$ | 162.1~163.1 |
| | | NiS | 162.4~162.8 |
| | | $Co_9S_8$ | 162.6~163.1 |
| | | $CoS_2$ | 162~162.9 |
| | | $FeS_2$ | 162~163 |
| | | S | 163.4~164.5 |
| | | PtS | 163~163.9 |
| | | $As_2S_3$ | 164.5~165.2 |
| | | $SO_3^{2-}$ | 166.2~169.6 |
| | | $SO_4^{2-}$ | 168.1~169.6 |

3. V binding energy distributions were similarly derived from reported studies:[307–316]

*Table 5-5. XPS-V $2p_{3/2}$ Binding Energy Reference Table*

| **Chemical State** | **V $2p_{3/2}$ Binding Energy (eV)** |
|---|---|
| V | 512~513.5 |
| $V^+/V^{2+}$ | 513.4~513.9 |
| $V_2O_3$ | 515~515.6 |
| $VO_2$ | 516~516.6 |
| $V_2O_5$ | 516.6~517.9 |
| $VB_2$ | 512.9~513.4 |
| VN | 514.2~514.6 |
| $VOCl_2$ | 516.2~516.7 |
| $VOSO_4$ | 515.7~516.2 |
| $K_4V(CN)_6$ | 513~513.4 |

## Effect of layer structure modification through vanadium dopant in $MoS_2$

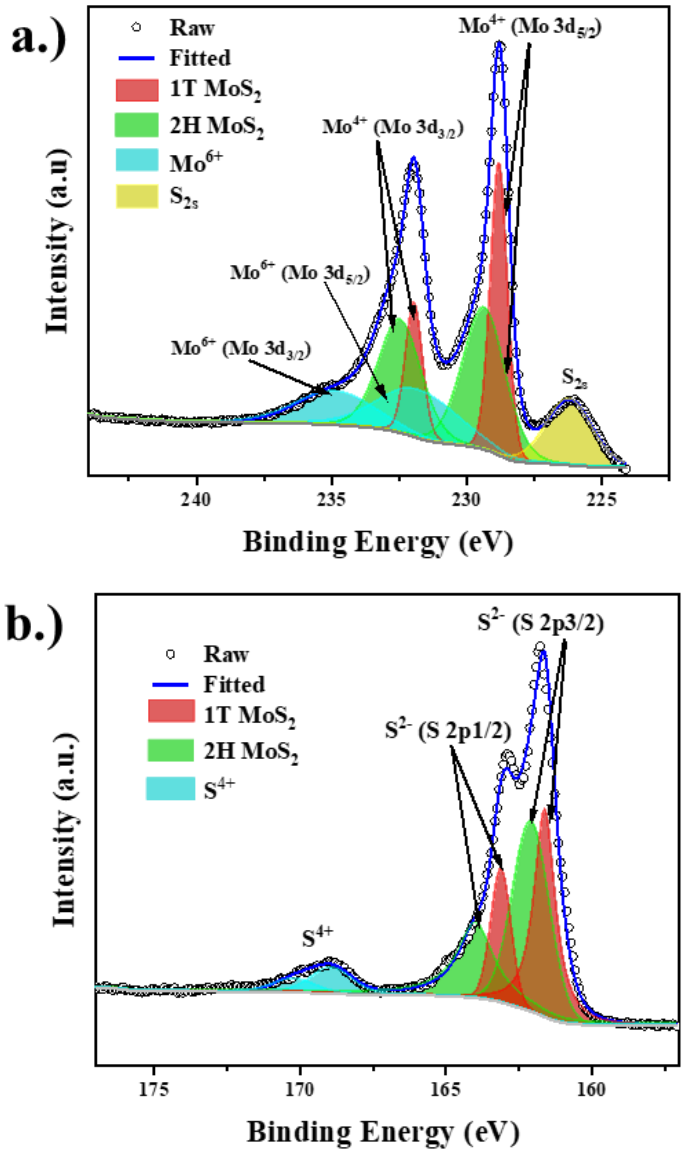


*Fig 5- 4. XPS spectra associated with a.) Mo (3d) and b). S (2p) of $MoS_2$*

As shown in Fig. 5-4a, the Mo (3d) core level spectra for the four samples reveal a consistent profile across all cases, where each spectrum is effectively fitted to two sets of doublet peaks. The first doublet set, positioned at lower binding energies of 228.8 and 231.9

eV, corresponds to $Mo^{4+}$ ($3d^{5/2}$) and $Mo^{4+}$ ($3d^{3/2}$) in the 1T-$MoS_2$ phase. In contrast, the second set, appearing at higher binding energies, represents Mo4+ ($3d^{5/2}$) and $Mo^{4+}$ ($3d^{3/2}$) associated with the 2H-$MoS_2$ phase. [96,317–319] This pattern suggests that the V-$MoS_2$ samples exist in a mixed-phase state, combining both 1T and 2H phases, with the 1T content estimated between 25.62% and 27.0%. Further examination in Fig. 5-4b identifies the $S^{2-}$ ($2p^{3/2}$) and $S^{2-}$ ($2p^{1/2}$) peaks for the 1T phase at 161.58 and 163.08 eV, respectively. Meanwhile, the $S^{2-}$ ($2p^{3/2}$) and $S^{2-}$ ($2p^{1/2}$) peaks for the 2H phase are detected at 162.05 and 163.95 eV.

Effect of layer structure modification through vanadium dopant in $MoS_2$

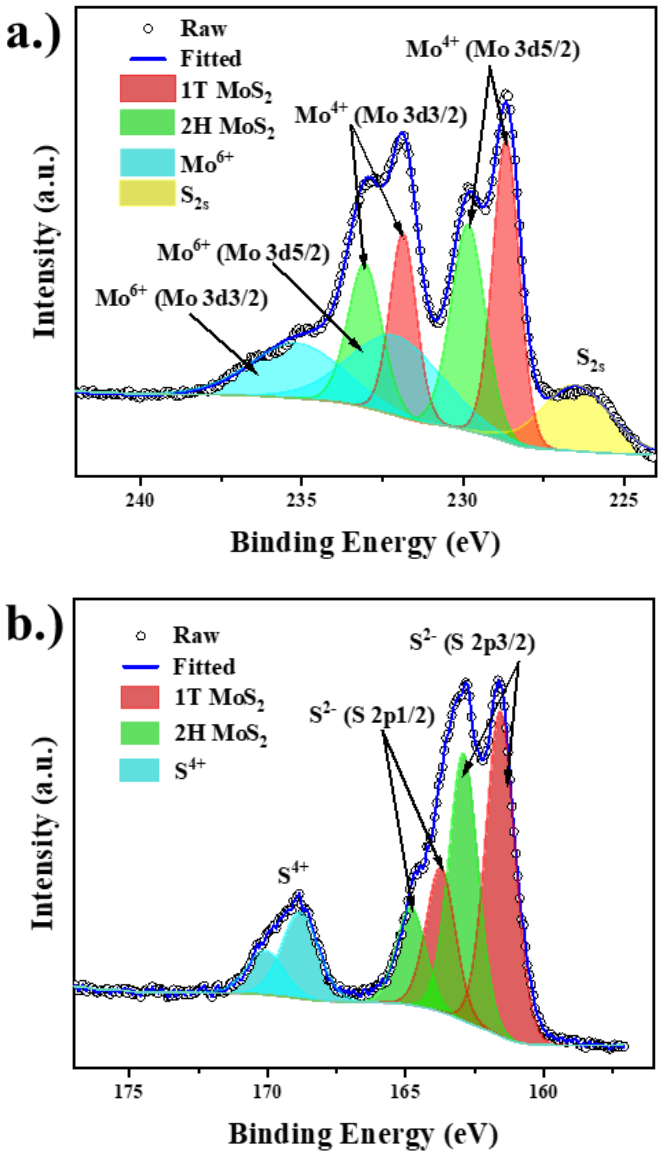

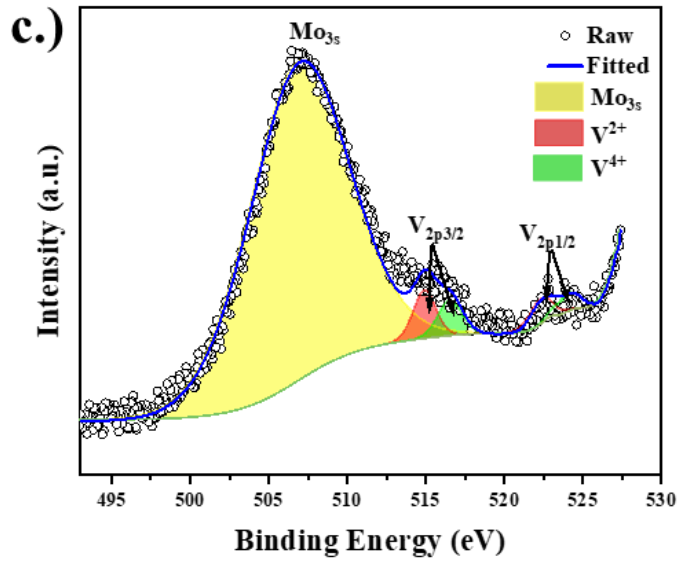


*Fig 5- 5. XPS spectra associated with a.) Mo (3d), b). S (2p) and c.) V (2p) of $V_{0.1}Mo_{0.9}S_2$*

For the $V_{0.1}Mo_{0.9}S_2$ sample, two main peaks appear at binding energies of 515 eV and 522.0 eV, which are attributed to $V^{2+}$ ($2p^{3/2}$) and $V^{2+}$ ($2p^{1/2}$) ions, respectively. Additionally, weaker peaks are observed at 516.6 eV and 524.2 eV, corresponding to $V^{4+}$ ($2p^{3/2}$) and $V^{4+}$ ($2p^{1/2}$) ions, indicating the presence of both $V^{2+}$ and $V^{4+}$ states within the $MoS_2$ structure. This dual presence of $V^{4+}$ and $V^{2+}$ ions signifies that V(IV) and V(II) have co-doped the $MoS_2$ framework, with $V^{4+}$ ions substituting $Mo^{4+}$ within the S-Mo-S monolayers and $V^{2+}$ ions positioned on the monolayer surfaces, creating Mo vacancies to maintain charge balance. Peak splitting in the Mo (3d) and S (2p) spectra further confirms the coexistence of the 1T and 2H phases in $V_{0.1}Mo_{0.9}S_2$, with approximately 56% of the material being in the 1T phase. This indicates that the prepared sample predominantly contains the 1T phase.[319] Additionally, around 55.6% of $Mo^{6+}$ ions are reduced to $Mo^{4+}$ within $MoS_2$, while the highly doped $V_{0.1}Mo_{0.9}S_2$ sample exhibits a lower reduction rate, with only 39.4% of $Mo^{6+}$ ions reduced to Mo4+. This discrepancy may be attributed to a limited and constant amount of reductant used during synthesis.[320–322] It is noteworthy that both molybdenum and vanadium are reduced by thiourea during the reaction; however, the redox potential for reducing $Mo^{6+}$ to $Mo^{4+}$ ($E_0$ = 0.65 V) is

lower than that required for the reduction of $V^{5+}$ to $V^{4+}$ or $V^{2+}$ (with $E_0 = 1.0$ V for $V^{4+}$ and 0.53 V for $V^{2+}$), explaining the differences in reduction tendencies between the two elements. [323]

### 5.2.4 Raman Spectrum

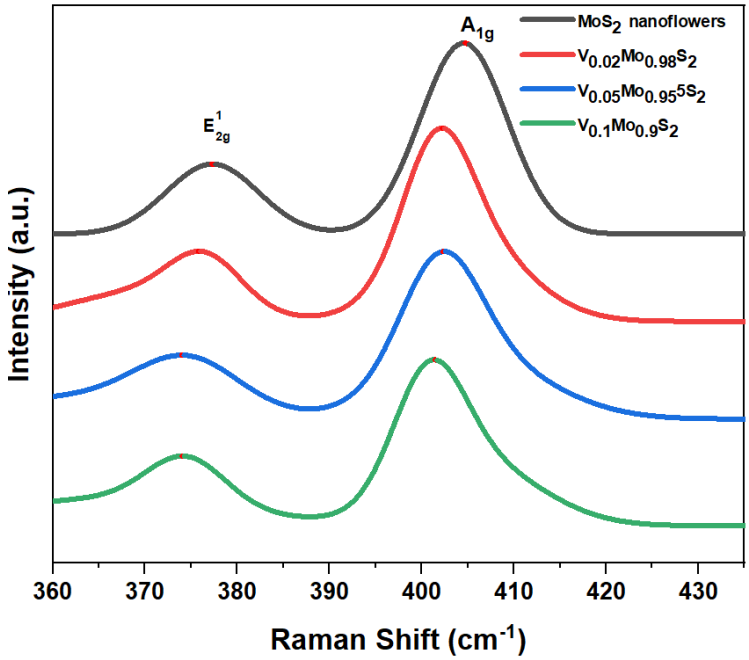


***Fig 5- 6. Raman spectra measured for different V doped level $MoS_2$ and $MoS_2$***

Fig 5-6 illustrates that as the vanadium content increases in the various V-doped $MoS_2$ samples, the band intensity of the V–S vibration correspondingly decreases. This trend provides additional evidence for the successful formation of V-doped $MoS_2$ with adjustable dopant levels.

## Effect of layer structure modification through vanadium dopant in $MoS_2$

*Table 5-6. Raman spectrum peak position of different V doped level MoS2 and MoS2,*

| Sample | $E^1_{2g}$ ($cm^{-1}$) | $A_{1g}$($cm^{-1}$) | Δk ($cm^{-1}$) |
|---|---|---|---|
| $MoS_2$ | 377.2 | 404.7 | 27.5 |
| $V_{0.02}Mo_{0.98}S_2$ | 375.8 | 402.2 | 26.4 |
| $V_{0.05}Mo_{0.95}S_2$ | 374.0 | 402.3 | 28.3 |
| $V_{0.1}Mo_{0.9}S_2$ | 374.0 | 401.4 | 27.4 |

According to the data presented in Table 5-6, there are two distinct peaks observed at 377.2 and 404.7 $cm^{-1}$, corresponding to the $E^1_{2g}$ and $A_{1g}$ vibration modes of Mo–S bonding. The difference in frequencies between the $E^1_{2g}$ and $A_{1g}$ vibrational modes does not exhibit a consistent pattern with the introduction of vanadium doping (2 wt% V dopant = -1.1 $cm^{-1}$ compared to $MoS_2$, 5% V dopant = 0.8 $cm^{-1}$ compared to $MoS_2$, and 10% V dopant = -0.1 $cm^{-1}$ compared to $MoS_2$). The addition of a 2 wt% V dopant to $MoS_2$ results in a reduction in the frequency difference between the $E^1_{2g}$ and $A_{1g}$ modes by more than 1 $cm^{-1}$, indicating a difference in the number of layers and their thickness compared to $MoS_2$ [47,324]. Additionally, a shift towards lower wave numbers is observed for both peaks following doping, accompanied by a decrease in intensity. This decrease in intensity is attributed to alterations in lattice symmetry, impacting the matrix elements and selection rules for Raman-active vibrational modes [325]. Furthermore, the shift in wave number is a result of the interaction between sulfur and vanadium atoms leading to a reduction in Mo–S vibration frequency. A higher V dopant level leads to a stronger reduction in Mo–S vibration frequency.

*Table 5-7. intensity comparison of different V doped level $MoS_2$ and $MoS_2$*

| Sample | $MoS_2$ | $V_{0.02}Mo_{0.98}S_2$ | $V_{0.05}Mo_{0.95}S_2$ | $V_{0.1}Mo_{0.9}S_2$ |
|---|---|---|---|---|
| $IE^1_{2g}/IA_{1g}$ | 0.387 | 0.439 | 0.550 | 0.638 |

With the increase of V doped level, the intensity ratio of $E^1_{2g}$ /$A_{1g}$ increases as well, indicating that V dopant level terminated structure[326]. The increase in the number of layers in $MoS_2$ has been shown to affect the Raman intensity ratio of the $E^1_{2g}$ , $A_{1g}$ modes. Specifically, as the number of layers increases, the Raman intensity area ratio of the $MoS_2$ $E^1_{2g}$ , $A_{1g}$ modes to that of the V substitution increases linearly, indicating a direct relationship between layer

stacking and Raman intensity ratios [327]. This suggests that layer stacking can indeed cause an increase in the intensity ratio in the Raman spectrum of $MoS_2$.

### 5.2.5 Electrocatalytic performance of V-doped $MoS_2$ nanosheets

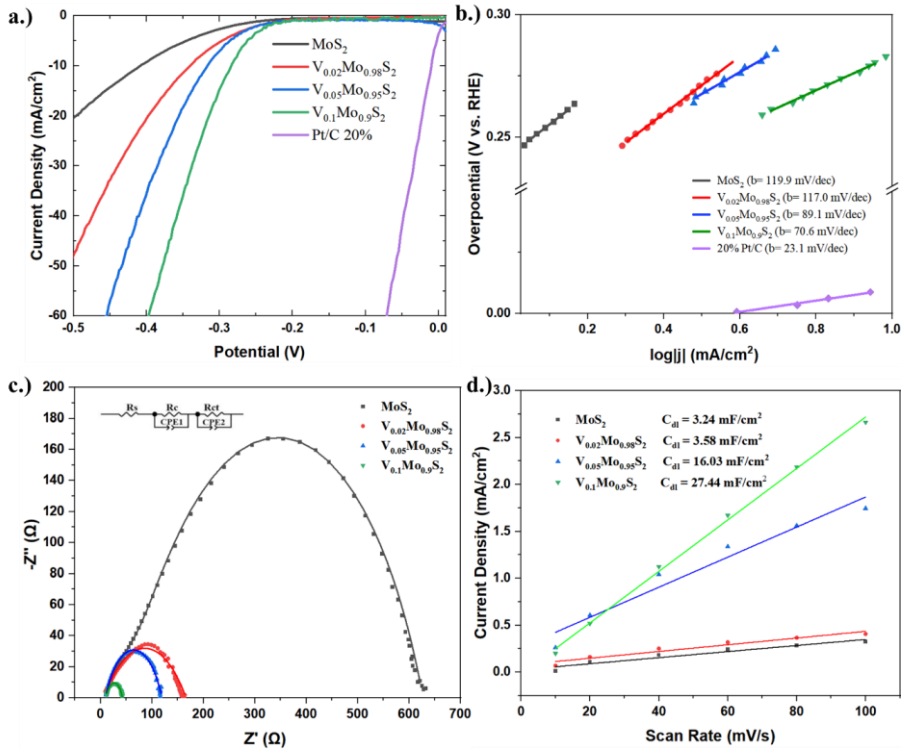


***Fig 5- 7. HER performance analysis of synthesized $MoS_2$ and V-Doped $MoS_2$ catalysts: (a) LSV curves illustrating catalyst activity, (b) Tafel plots derived from polarization curves for comparative evaluation, (c) EIS assessing charge transfer resistance in pure and V-Doped $MoS_2$ Samples, (d) ECSA measurements for $MoS_2$***

The prepared specimens served as electrocatalysts for the HER, with their electrochemical performance assessed in a 0.5 M $H_2SO_4$ solution. Using a glassy carbon electrode as the working electrode, the influence of different vanadium doping levels on HER efficiency was analyzed. As shown in Figure 5-7a, polarization curves illustrate that for undoped $MoS_2$, an overpotential (η) of approximately 410 mV is required to achieve a current density of 10 mA/cm$^2$. Notably, this overpotential decreases considerably in the V-doped $MoS_2$

samples, reaching 341 mV for 2%V-$MoS_2$, 317 mV for 5%V-$MoS_2$, and 285 mV for 10%V-$MoS_2$. Among the samples, 10%V-$MoS_2$ shows the lowest overpotential, indicating it facilitates current most effectively.

In Fig 5-7b, Tafel plots for the four electrocatalysts are fitted using the Tafel equation ($\eta = a + b\ logj$), with b denoting the Tafel slope. [319,328] The obtained Tafel slopes for the doped samples are 117 mV $dec^{-1}$ for the 2%V-$MoS_2$, 89.1 mV $dec^{-1}$ for the 5% V-$MoS_2$, and 70.6 mV $dec^{-1}$ for the 10%V-$MoS_2$, all of which are lower than the undoped $MoS_2$ slope of 119.9 mV $dec^{-1}$. The smallest Tafel slope, exhibited by 10%V-$MoS_2$, suggests faster reaction kinetics and greater catalytic efficiency.

The results align with known HER mechanisms, which involve two primary steps in an acidic environment.[328–330] The initial step, known as the Volmer reaction ($H^+ + e^- - H^*$ b = 120 mV $dec^{-1}$), forms an adsorbed hydrogen atom ($H^*$) on the catalyst's active site. This step may be followed by the Heyrovsky reaction ($H^+ + e^- + H^* - H_2$, b = 39 mV $dec^{-1}$) or the Tafel reaction ($H^* + H^* - H_2$, b = 29.5 mV $dec^{-1}$).[328] The Tafel slopes measured for the V-doped $MoS_2$ samples fall between the Volmer and Heyrovsky reaction values, indicating a Volmer–Heyrovsky mechanism, with the Volmer reaction as the rate-limiting step. The lowest Tafel slope observed for the 10%V-$MoS_2$ catalyst reflects enhanced hydrogen adsorption due to moderate V doping.

Additionally, electrical impedance spectroscopy (EIS) was employed to analyze the faradaic interfacial kinetics in HER.[319] The EIS data were modeled with an equivalent circuit (see Fig. 5-8), in which Rs represents the electrolyte resistance. The high-frequency component, $R_c$, relates to the material's surface pore structures and remains constant with overpotential variation, while the low-frequency component, $R_{ct}$, reflects charge transfer resistance and provides insights into the electron transfer efficiency within the HER process.

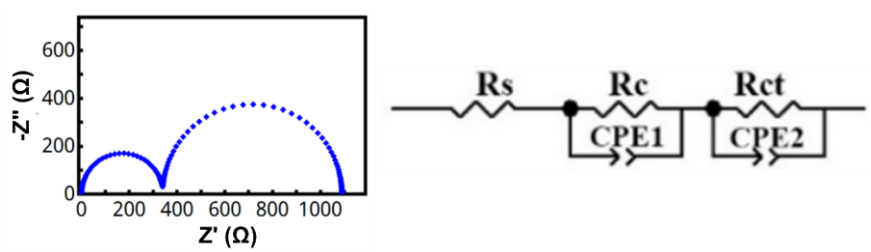


***Fig 5- 8. a.)Example Nyquist Plot and b). Corresponding equivalent circuit***

Fig 5-7c presents the Nyquist plots for the four electrocatalysts, highlighting the 10%V-$MoS_2$ catalyst as having the lowest charge transfer resistance ($R_{ct}$) at 31.6 Ω. This reduced $R_{ct}$ indicates a marked improvement in electron transfer efficiency at the catalyst-electrolyte interface, contributing to superior HER kinetics.[319] The performance of an electrocatalyst is highly dependent on the availability of active sites, making the electrochemically active surface area (ECSA) a crucial measure of its catalytic capability. Typically, the electrochemical double-layer capacitance ($C_{dl}$), directly proportional to the ECSA, is used to approximate the number of active sites.

To evaluate $C_{dl}$, we captured cyclic voltammetry (CV) profiles for every electrocatalyst in a non-faradaic potential range stretching from 0.15 to 0.3 V, applying sweep rates varying between 10 and 100 mV/s, with the resulting Cdl values illustrated in Fig 5-7d. [319] Relative to the non-altered $MoS_2$, every vanadium-doped specimen revealed a significantly elevated $C_{dl}$, with the 10% V-$MoS_2$ electrocatalyst hitting a Cdl high of 27.44 mF/cm$^2$, approximately nine times that of the non-modified $MoS_2$, measured at 3.24 mF/cm$^2$. These results highlight that the 10%V-$MoS_2$ sample, with an optimal vanadium content, possesses a significantly higher density of exposed active sites, enhancing its effectiveness as a catalyst for HER.

## 5.2.6 UV-vis spectrum

The UV–vis absorption spectra of $MoS_2$ samples were measured by dispersing 1 mg of the powder in 5 ml of deionized water, followed by ultrasonication for 15 minutes to obtain

a homogeneous suspension. The resulting dispersion was then subjected to UV–vis spectroscopic analysis.

As shown in Figure 5-9 (a), several distinct peaks appear at $\lambda_{max}$ values of 645, 612, 488, and 423 nm, highlighting the characteristic absorption bands of $MoS_2$ nanoflowers. The prominent peaks at 612 and 645 nm are attributed to the K point of the Brillouin zone, [222,223] while the peaks at 423 and 488 nm correspond to direct transitions from the inner valence band to the conduction band. [224,225] With 5% V-doping, these peak positions shift to 642, 615, 547, and 490 nm. For 10% V-doping, the peaks further shift to 642, 528, and 489 nm. Additionally, the reduction of the B exciton peak with increasing dopant concentration provides further evidence for the increased layer thickness.

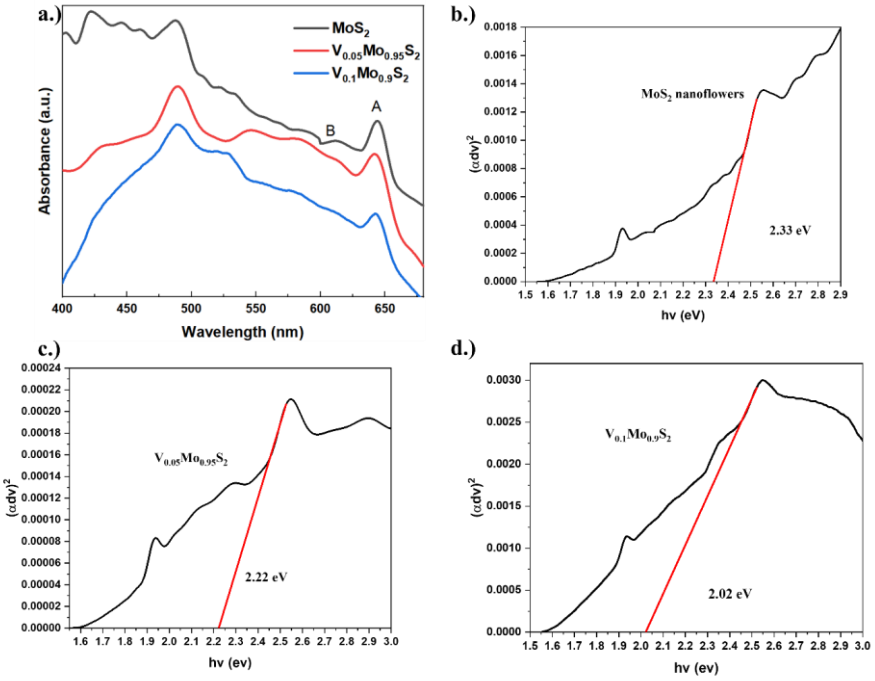


***Fig 5- 9. UV-Vis spectra of the $MoS_2$, $V_{0.05}Mo_{0.95}S_2$, and $V_{0.1}Mo_{0.9}S_2$ (a), direct transition ((αhu)² vs. hu) curves for $MoS_2$ (b), $V_{0.05}Mo_{0.95}S_2$ (c), and $V_{0.1}Mo_{0.9}S_2$ (d).***

From the perspective of direct band gap semiconductors, it is possible to determine the band gap of the materials that have been synthesized by analyzing the tangents of the Tauc plot [$(\alpha dv)^2\ vs\ hv$]. This analysis is carried out as strain is induced within the crystal lattice of $MoS_2$ through the introduction of a foreign element such as V, leading to modifications in the lattice parameter. The optical band gap derived from the Tauc plot, approximately 2.02 eV for $V_{0.1}Mo_{0.9}S_2$, was found to be lower than that of $MoS_2$ nanoflowers (around 2.33 eV) and $V_{0.05}Mo_{0.95}S_2$ (approximately 2.22 eV).

### 5.2.7 BET measurements

The BET surface area is determined using the Brunauer–Emmett–Teller (BET) method, widely utilized in fields such as drug development and material science, by measuring gas volume adsorbed on the material to calculate surface area [331–333]. This method applies the BET equation to calculate monolayer gas volume, crucial for understanding properties like reactivity and stability, essential for evaluating porous and nanomaterials in terms of regulatory compliance and performance [334,335].

Effect of layer structure modification through vanadium dopant in $MoS_2$

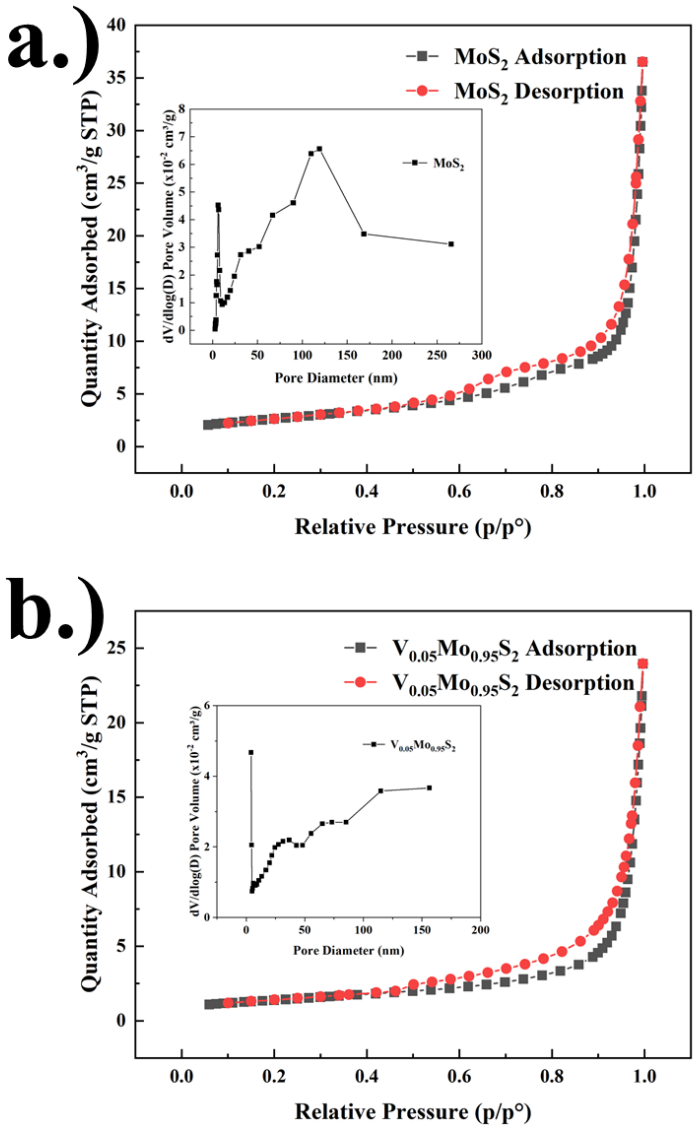

## Effect of layer structure modification through vanadium dopant in $MoS_2$

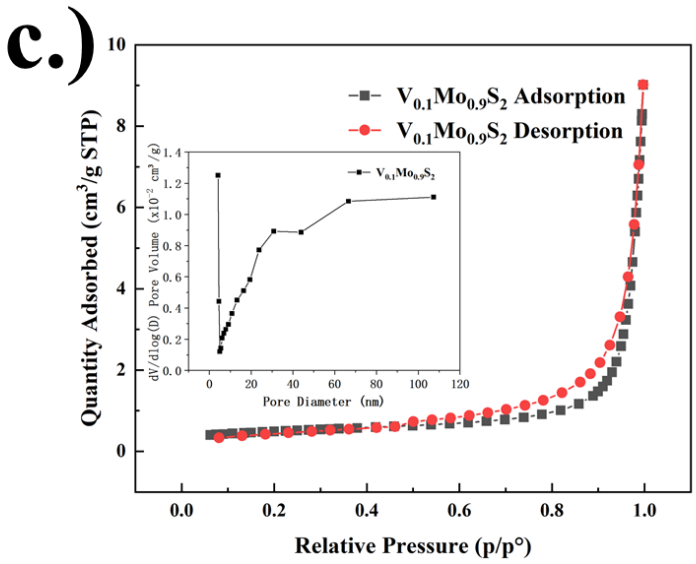


***Fig 5- 10. $N_2$ adsorption-desorption of (a) bare $MoS_2$, (b)$V_{0.05}Mo_{0.95}S_2$, (c) $V_{0.1}Mo_{0.9}S_2$***

As depicted in Fig. 5-10 a–c, the materials displayed type-V isotherms accompanied by type H3 hysteresis loops following the IUPAC categorization, which suggests the existence of mesopores within the materials. The BET specific surface areas of the materials were determined to be 9.3734, 4.9168, and 1.6663 $m^2$/g for $MoS_2$, $V_{0.05}Mo_{0.95}S_2$, and $V_{0.1}Mo_{0.9}S_2$, respectively.[336,337] The decreased BET surface area of $MoS_2$ materials may lead to a counterintuitive increase in hydrogen evolution reaction (HER) efficiency due to specific structural characteristics. Smaller $MoS_2$ nanosheets possessing a substantial electrochemical active surface area and edge sites demonstrate enhanced HER efficacy in comparison to larger counterparts, presenting reduced overpotentials and Tafel slopes[338]. The pore diameter measured corresponds to narrow openings created by the accumulation of nanosheets. The average pore diameters for $MoS_2$, $V_{0.05}Mo_{0.95}S_2$, and $V_{0.1}Mo_{0.9}S_2$ as determined by BJH adsorption were 23.23 nm, 30.91 nm, and 45.45 nm, respectively. With the increase in the level of V-doping, there is a decrease in pore size, as depicted in Figure 5-10 a-c. This phenomenon is attributed to the close packing of $MoS_2$ nanosheets due to the presence of

vanadium and the formation of small slit holes. The higher pore diameter level suggests a sufficient contact between the active sites and electrolytes [339].

## 5.3 Conclusion

V-doped $MoS_2$ is responsible for inducing changes not onlyin the Mo site but also in the S position within the material structure. This substitution phenomenon results in a reduction in the spacing between the layers as the concentration of V doping rises. Consequently, this reduction in spacing leads to the accumulation of layers within the material. The buildup of layers further promotes the expansion of material layers, which in turn exposes a greater number of highly efficient hydrogen evolution reaction (HER) active sites.

Furthermore, the introduction of vanadium ($V^{4+}$) doping into $MoS_2$ also induces alterations in the crystal lattice parameters, resulting in subsequent modifications in the strain experienced by the material. Such modifications in strain directly impact the intrinsic bandgap width of the $MoS_2$ structure, leading to a reduction in its bandgap width. Consequently, this reduction in bandgap width indirectly enhances the conductivity of the material and elevates the efficiency of electron transmission on the catalyst.

# Tungsten-Doped $MoS_2$ with Sulfur Vacancies for Enhanced HER Catalytic Performance

## 6.1 Introduction

Research into the incorporation of tungsten (W) into molybdenum disulfide ($MoS_2$) for the purpose of catalyzing the hydrogen evolution reaction (HER) has demonstrated significant progress, capitalizing on the distinctive characteristics of $MoS_2$ and the advantageous impacts of W addition. $MoS_2$ is recognized as a two-dimensional semiconductor with adjustable bandgap, superior electrical conductivity, and substantial light-matter interaction, useful for diverse catalytic uses, including HER [340]. Nevertheless, the unreactive nature of the basal plane of $MoS_2$ poses constraints on its electrochemical activity. Various doping methodologies, particularly involving metals like tungsten, have been investigated to activate the basal plane and improve the catalytic efficacy of $MoS_2$ [341]. Doping of tungsten (W) results in the introduction of sulfur defects and facilitates the generation of active sites, thereby leading to a substantial enhancement in the HER catalytic performance of $MoS_2$. This structure is achieved via a one-step hydrothermal process that not only induces sulfur defects but also expedites the separation and transfer of electron-hole pairs, consequently fostering a sustained high level of catalytic oxidation activity. Furthermore, the incorporation of W aids in decreasing the free energy of hydrogen adsorption and promoting charge transfer, both of which are essential for efficient HER. Theoretical and empirical investigations have indicated that the substitution of 50% of Mo with W in $MoS_2$ ($Mo_{0.5}W_{0.5}S_2$) produces the most favorable catalytic behavior, resulting in an onset potential of −37 mV and an overpotential of 138 mV to achieve 10 mA/cm$^2$ [342]. Additionally, W-doped $MoS_2$ displays remarkable stability and durability, maintaining a high level of catalytic efficacy over prolonged durations (last for 63 hours, 20 times loger than pure $MoS_2$). This stability is paramount for real-world applications, ensuring consistent performance across a variety of

operating conditions. The introduction of W also reinforces the material's resilience to water and sulfur, further bolstering its robustness and durability as a catalyst [343]. By deliberately adjusting the local chemical and atomic structure through doping, researchers can activate the typically inert basal plane of $MoS_2$. In conclusion, W-doped $MoS_2$ distinguishes itself for its capacity to significantly enhance HER activity by promoting enhanced separation of electron-hole pairs, reducing the free energy of hydrogen adsorption, and improving stability, positioning it as an exceedingly appealing option for sustainable hydrogen production [340–343].

In this study, a simple one-step solvothermal method to produce certain dopant level tungsten doped $MoS_2$. 5%, 10% and 20% tungsten doped $MoS_2$ were produced to investigate the influence of dopant level in HER activity in a 0.5 M $H_2SO_4$ electrolyzer. The incorporation of W dopants induces vacancies of S atoms within the crystal lattice of $MoS_2$, which is advantageous for improving the catalytic activity of HER. The effects of varying W content on the HER performance of the nanosheets were comprehensively examined. The 20% W-$MoS_2$ catalyst demonstrates optimal catalytic performance. Furthermore, the synergistic effects arising from W-doping, interlayer interactions, and the concentration of W substitutions at each site within the $MoS_2$ nanosheets on the enhanced HER performance are elaborated upon.

# Tungsten-Doped $MoS_2$ with Sulfur Vacancies for Enhanced HER Catalytic Performance

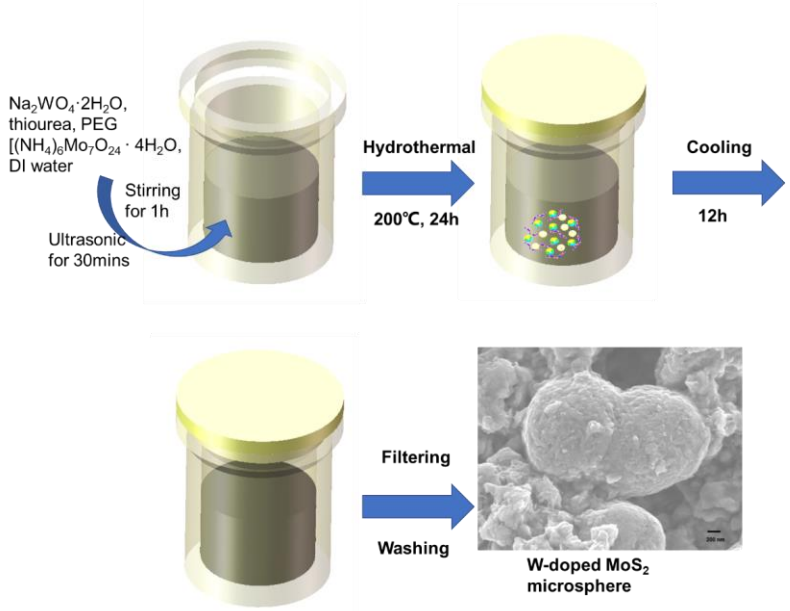


***Scheme 6-1. Schematic illustration of W-doped $MoS_2$ synthesis process***

In this work, $MoS_2$ was prepared by the hydrothermal method at 200 °C with the starting chemicals of thiourea, and polyethylene glycol (PEG). $(NH_4)_6Mo_7O_{24} \cdot 4H_2O$ was dissolved in deionized (DI) water. Sodium tungstate dihydrate ($Na_2WO_4 \cdot 2H_2O$) was used as a tungsten precursor, and certain amounts of $Na_2WO_4 \cdot 2H_2O$ were mixed into solutions to make certain dopant ratios (5%, 10% and 20% tungsten dopant respectively). The synthesis procedure is illustrated in Scheme 3, while the quantities of starting materials are detailed in Table 6-1.

***Table 6-1 Compositions of the W-doped MoS2 nanoflowers prepared with reactants of various W contents***

| Sample | Reactants | | | | |
|---|---|---|---|---|---|
| | $(NH_4)_6Mo_7O_{24} \cdot 4H_2O$ (mmol) | $Na_2WO_4 \cdot 2H_2O$ (mmol) | $CH_4N_2S$ (mmol) | Polyethylene glycol (g) | DI water (ml) |
| $MoS_2$ | 0.223 | 0 | 4.532 | 0.322 | 13.8 |
| $W_{0.05}Mo_{0.95}S_2$ | 0.212 | 0.078 | 4.532 | 0.322 | 13.8 |
| $W_{0.1}Mo_{0.9}S_2$ | 0.201 | 0.156 | 4.532 | 0.322 | 13.8 |
| $W_{0.2}Mo_{0.8}S_2$ | 0.179 | 0.312 | 4.532 | 0.322 | 13.8 |

## Results and Discussion

### 6.2.1 Investigation of morphological characteristics

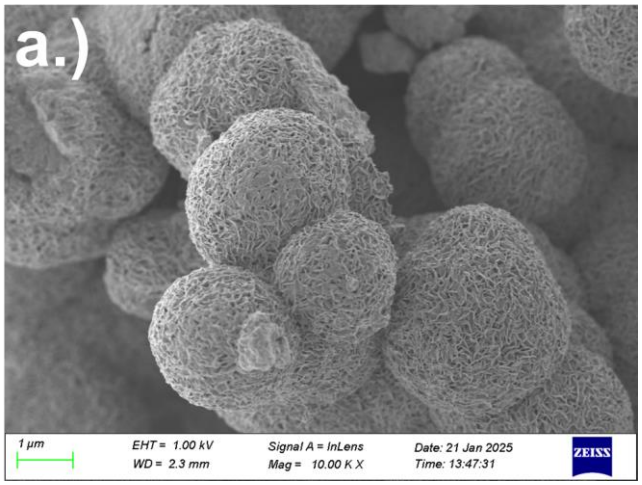


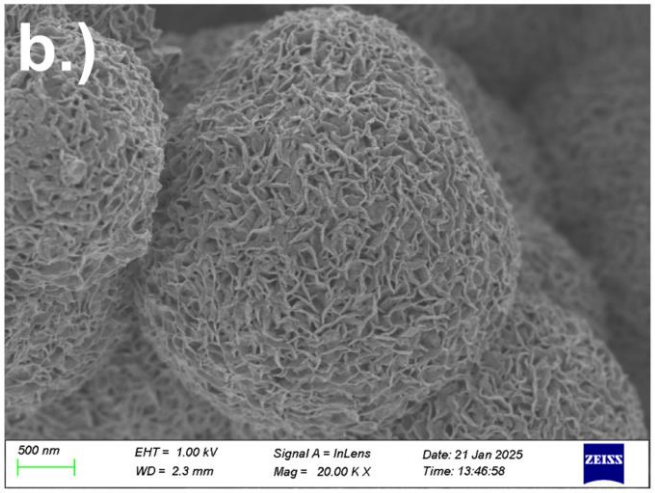

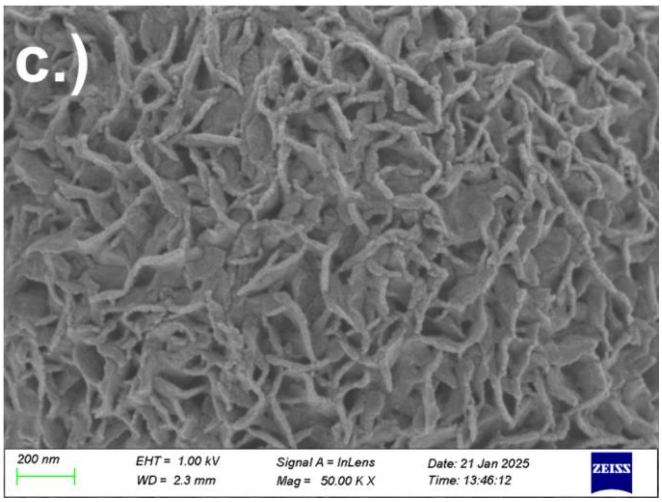
c.)
200 nm
EHT = 1.00 kV
WD = 2.3 mm
Signal A = InLens
Mag = 50.00 K X
Date: 21 Jan 2025
Time: 13:46:12
ZEISS

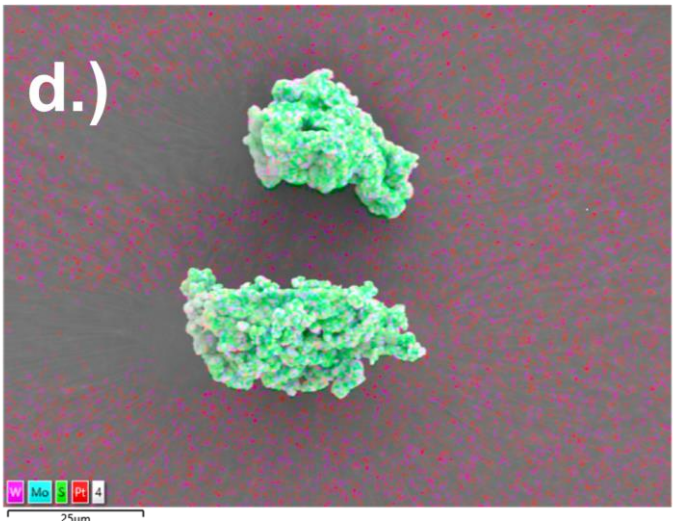
d.)
W
Mo
S
Pt
4

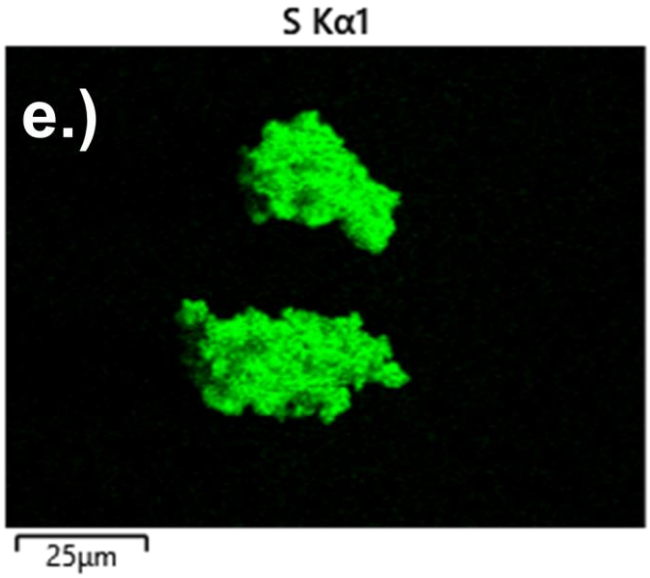
S Kα1
e.)
25µm

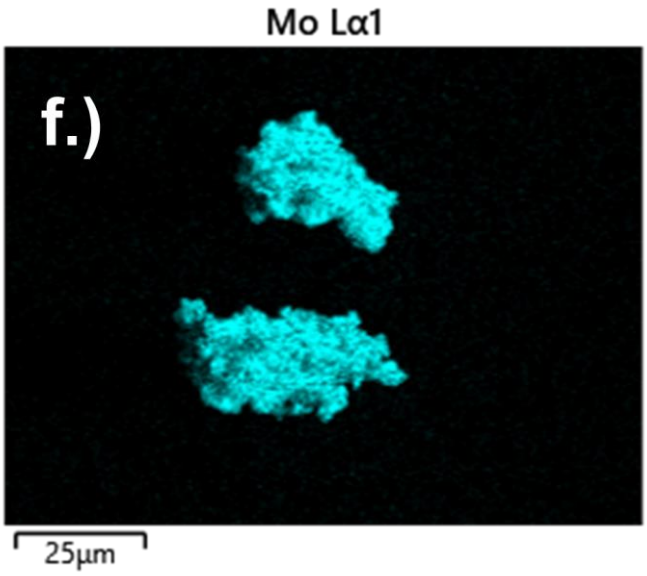
Mo Lα1
f.)
25µm

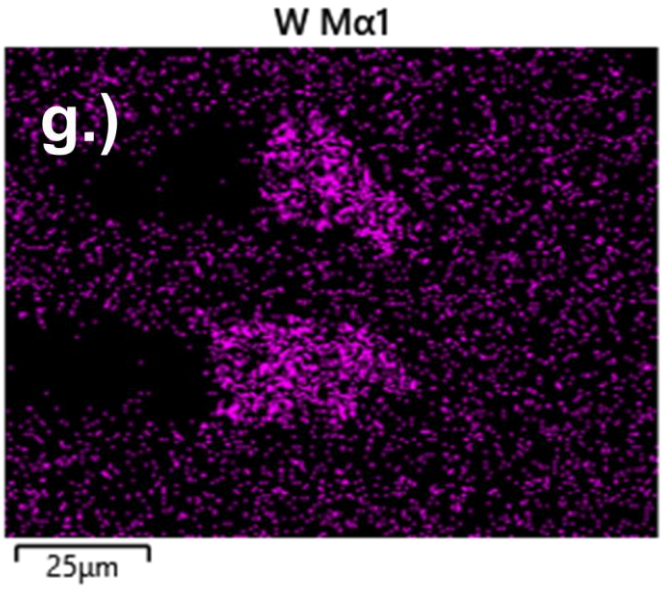


***Fig 6- 1. (a-c) SEM images of $W_{0.2}Mo_{0.8}S_2$, and (d-g) corresponding elemental mapping***

In this work, sulfur-defect-enriched $MoS_2$ was synthesized through the introduction of tungsten via a straightforward one-step hydrothermal method. The tungsten doping in this study was straight-forward to achieve, because its valence state and atomic radius (139 pm) are similar to molybdenum. As illustrated in Fig 6-1 a, W-$MoS_2$ specimen manifests as a nanosphere with an approximate average diameter of 800 nm. Regardless of this, the enlarged SEM images image (Fig. 6-1(b)) hints that the 3D flower-shaped nanospheres aren't readily apparent. This phenomenon may be attributed to the fact that the actual synthesis temperature lower than 200 ℃, which complicates the nucleation process of $WS_2$, while the $MoS_2$ phase exists concurrently with amouphus $WO_3$ [344]. The analysis of molybdenum (Mo), tungsten (W), and sulfur (S) utilizing Energy Dispersive X-ray Spectroscopy was conducted on the $W_{0.2}Mo_{0.8}S_2$ specimen. The spatial arrangement of the three aforementioned elements indicates a uniform distribution throughout the aggregates, thereby offering supplementary evidence that corroborates the synthesis of W-doped $MoS_2$.

### 6.2.2 Crystallographic investigation

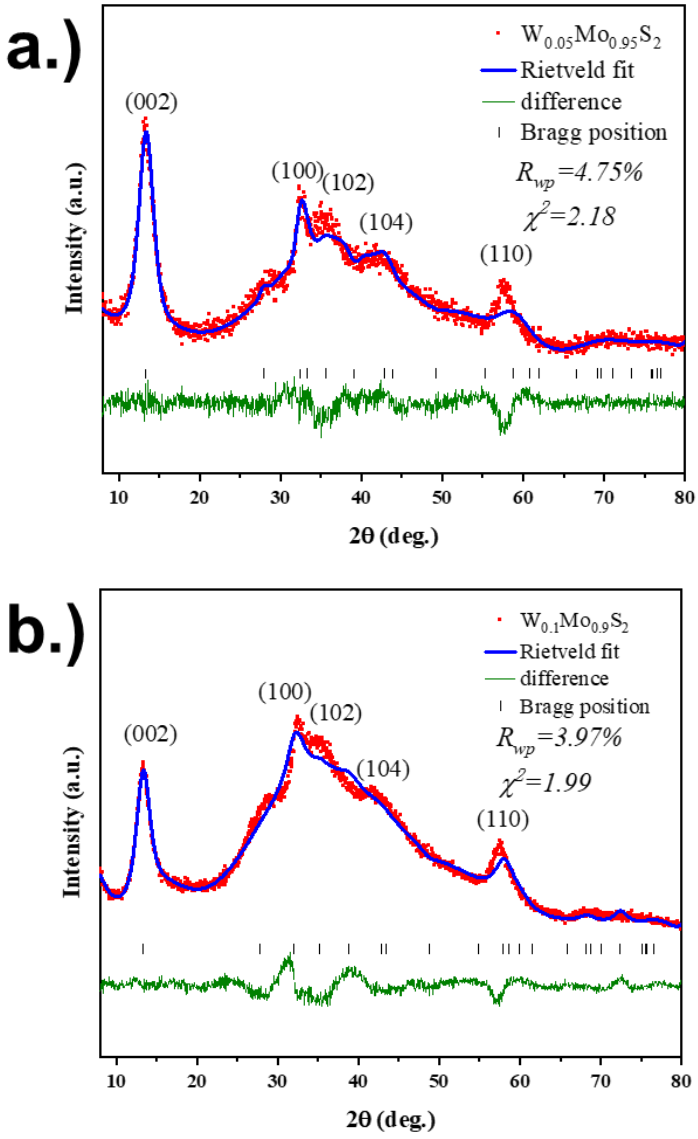

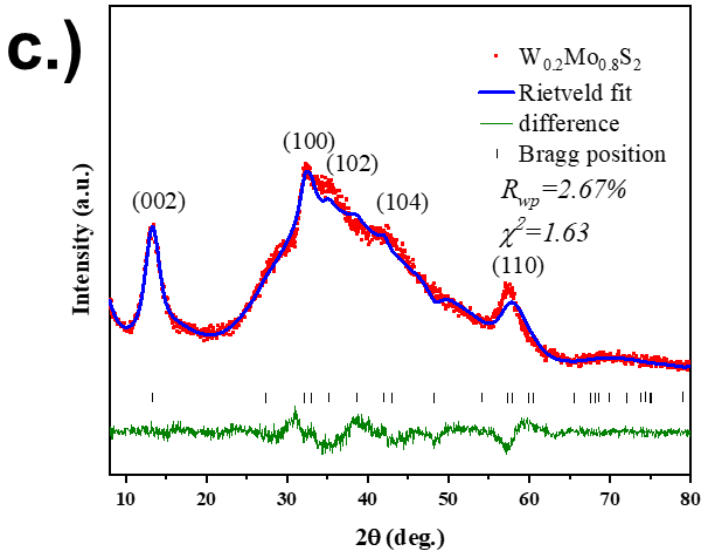


***Fig 6- 2. Powder XRD pattern with Rietveld refinement a). $W_{0.05}Mo_{0.95}S_2$ c). $W_{0.1}Mo_{0.9}S_2$ d). $W_{0.2}Mo_{0.8}S_2$.***

X-ray diffraction (XRD) analysis was performed to elucidate the crystalline architecture of $MoS_2$ nanoflowers that have been doped with tungsten, as represented in Figure 6-2. The XRD profiles acquired for all specimens exhibited a close correlation with the distinctive pattern characteristic of the hexagonal $MoS_2$ phase, as recorded in the Powder Diffraction File (PDF Card - 04-010-5047). The lack of any evidence suggesting the emergence of the $WS_2$ phase, in conjunction with the consistent manifestation of the hexagonal $MoS_2$ phase across all samples, provides compelling evidence that the incorporation of tungsten into $MoS_2$ transpired via a substitutional mechanism, thus preserving the crystalline integrity of $MoS_2$. The outcomes of the Rietveld analysis demonstrated goodness-of-fit ($\chi^2$) values of 2.18, 1.99, and 1.63 for $W_{0.05}Mo_{0.95}S_2$, $W_{0.1}Mo_{0.9}S_2$ and $W_{0.2}Mo_{0.8}S_2$ correspondingly, indicating the validity of the refinement outcomes (Table 6-2).

*Table 6-2. Parameters W-doped $MoS_2$ As Obtained by Rietveld Refinement*

| Parameters | $W_{0.5}Mo_{0.95}S_2$ | $W_{0.1}Mo_{0.9}S_2$ | $W_{0.2}Mo_{0.8}S_2$ |
|---|---|---|---|
| a(Å) | 3.106±0.0048 | 3.116±0.0049 | 3.152±0.0045 |
| b(Å) | 3.106±0.0048 | 3.116±0.0049 | 3.152±0.0045 |
| c(Å) | 12.45±0.0099 | 12.463±0.0123 | 12.739±0.012 |
| V($Å^3$) | 103.993±0.204 | 104.802±0.208 | 109.62±0.196 |
| $\%R_{wp}$ | 4.75 | 3.97 | 2.67 |
| $\chi^2$ | 2.18 | 1.99 | 1.63 |

More significantly, the observed diffraction peaks (002) of the aforementioned samples exhibit a shift towards a diminished diffraction angle concomitant with an increase in W dopant concentration, thereby indicating that the layered architecture of the synthesized samples possesses an expanded interlayer spacing and that interlayer strain is implicated, which aligns with the data depicted in Table 6-3. as presented. [345]. It is evident that the relative intensity ratio of (002) to (100) diminishes as the concentration of W dopants increases, and an amorphous grain cell is observed at approximately 2θ = 29 degrees [343]. This phenomenon may be attributed to the inability of $WS_2$ to effectively nucleate within $MoS_2$, where localized structural disorder constrains the growth of crystalline grains, thereby resulting in a crystal structure that demonstrates more amorphous characteristics. This situation is reflected in the XRD patterns by a weakening of the original crystalline plane diffraction peak's intensity, coupled with the rise of a distinct amorphous peak.

*Table 6-3. 2θ values for W-doped $MoS_2$*

| (h k l) | 2 theta (degree) | | |
|---|---|---|---|
| | $W_{0.05}Mo0._{95}S_2$ | $W_{0.1}Mo_{0.9}S_2$ | $W_{0.2}Mo_{0.8}S_2$ |
| 0 0 2 | 14.217 | 14.201 | 13.89 |
| 1 0 0 | 32.484 | 32.061 | 32.204 |
| 1 1 0 | 58.742 | 57.954 | 57.937 |

Through an analysis utilizing fractional coordinates of refined W-doped $MoS_2$ (Table 6-4), it was discerned that the occupancy of sulfur decreased in parallel with an elevation in the concentration of tungsten doping. This finding suggests that the introduction of tungsten

doping facilitates the emergence of defects at the sulfur sites of $MoS_2$, with vacant sites being the primary type of defect identified.

*Table 6-4. Refined site occupancies of Mo, S, and W atoms in W-doped $MoS_2$ (from Rietveld refinement)*

| Samples | Atoms | Expected occupancy | Refined occupancy |
|---|---|---|---|
| $W_{0.05}Mo_{0.95}S_2$ | Mo | 0.95 | 0.95±0.039 |
| | W | 0.05 | 0.043±0.0018 |
| | S | 1 | 1.068±0.044 |
| $W_{0.1}Mo_{0.9}S_2$ | Mo | 0.9 | 0.901±0.037 |
| | W | 0.1 | 0.103±0.0043 |
| | S | 1 | 0.98±0.041 |
| $W_{0.2}Mo_{0.8}S_2$ | Mo | 0.8 | 0.804±0.033 |
| | W | 0.2 | 0.195±0.008 |
| | S | 1 | 0.923±0.038 |

### 6.2.3 XPS measurement

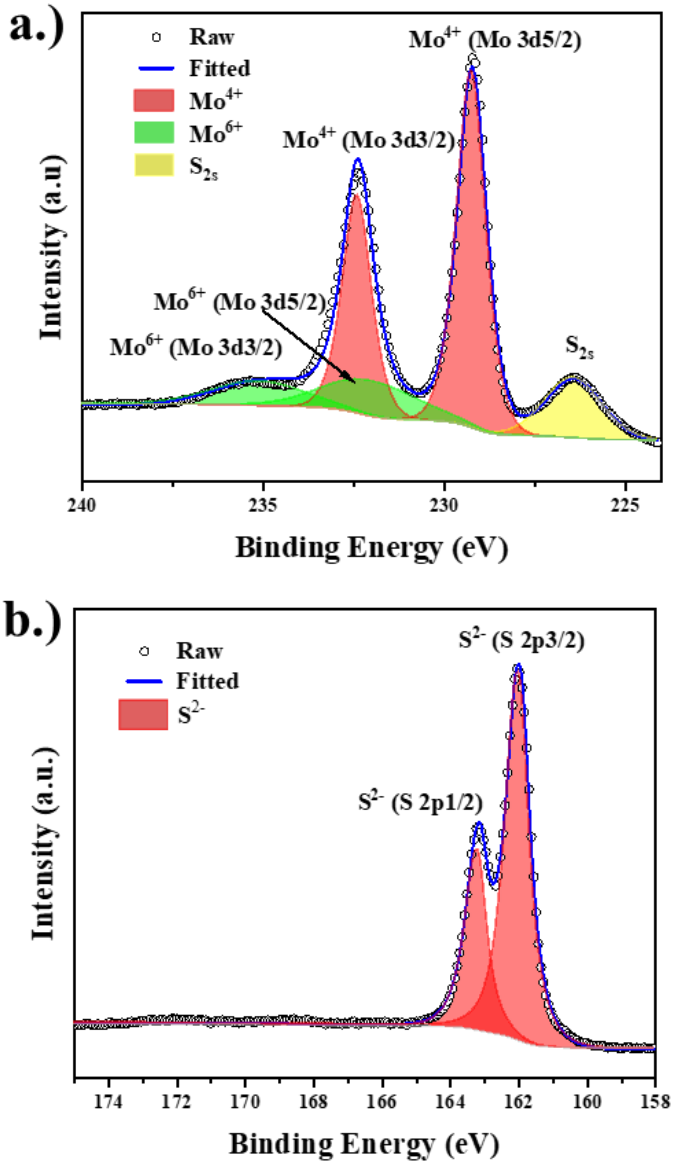

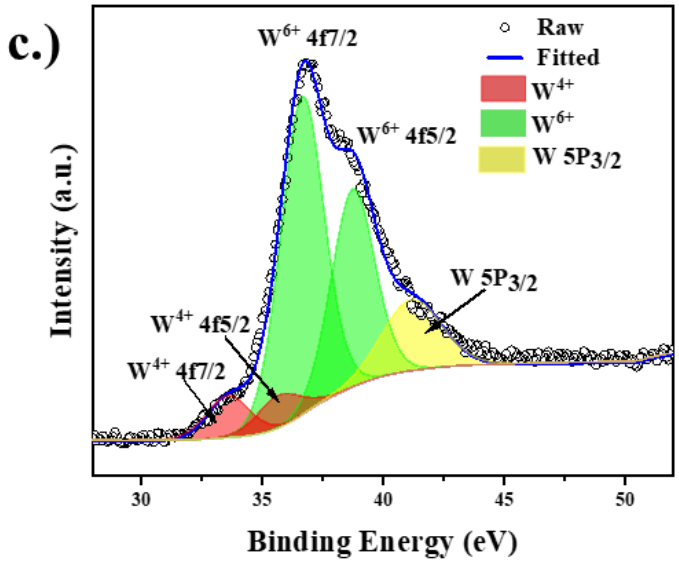


*Fig 6- 3. XPS spectra associated with a.) Mo (3d), b). S (2p) and c.) W (4f) of $W_{0.2}Mo_{0.8}S_2$*

As illustrated in Figure 6-3 a, the high-resolution Mo (3d) spectrum of $W_{0.2}Mo_{0.8}S_2$ reveals two distinct peaks at 229.2 and 232.4 eV, which are associated with the binding energies of 3d3/2 and 3d5/2, respectively, for $Mo^{4+}$ species in 2H-$MoS_2$. Furthermore, an additional peak at 226.5 eV is evident in the Mo (3d) spectrum, corresponding to the S (2s) orbital of $MoS_2$. The Mo (3d) peaks in $W_{0.2}Mo_{0.8}S_2$ exhibit noticeable negative shifts of approximately 0.2 eV and a decrease in intensity compared to pure $MoS_2$ (Fig 5-4). This observation indicates that the introduction of W enhances the surface electron density of $MoS_2$, leading to the destabilization of the H-S bond and facilitating the release of H atoms on $MoS_2$, thereby enhancing the performance of the hydrogen evolution reaction through the optimization of hydrogen adsorption energy [346]. Figure 6-3b presents the S (2p) spectra of $MoS_2$ and $W_{0.2}Mo_{0.8}S_2$, which can be deconvoluted into peaks at 162.0 and 163.2 eV for $W_{0.2}Mo_{0.8}S_2$, corresponding to the (2p3/2) and (2p1/2) orbitals of $S^{2-}$ species. The shifts of the $S^{2-}$ (2p3/2) and $S^{2-}$ (2p1/2) peaks to lower binding energies in $W_{0.2}Mo_{0.8}S_2$, as reported in the literature, provide evidence for the presence of sulfur vacancies [347]. Additionally, The W (4f) region demonstrates the distinctive $W^{4+}$ doublets at 35.7 and 33.6 eV, in addition to the

$W^{6+}$ doublets (at 38.8 and 36.7 eV), leading to the $W^{4+}$ ($f_{5/2}$) and $W^{4+}$ ($f_{7/2}$) regions, respectively, shown in Figure 6-3 c, confirm the presence of $W^{4+}$ and $W^{6+}$ in $MoS_2$ [348,349]. In conclusion, the introduction of $W^{6+}$ into the $MoS_2$ structure results in the creation of sulfur vacancies that are positively charged. Such vacancies arise due to the $W^{6+}$ doping, which diminishes the overall electron density, consequently lowering the binding energy of the adjacent sulfur atoms, thus promoting the formation of sulfur vacancies. [343].

1. XRD refinement results, as shown in Table 6.4, indicate a deviation from the ideal stoichiometry, supporting the existence of sulfur vacancies in the W-doped $MoS_2$ structure.
2. EDS analysis in the corresponding image region provides further evidence, with a calculated atomic ratio of $W_{0.0298}Mo_{1.1412}S_{1.8294}$, indicating sulfur deficiency relative to the ideal Mo:S ratio of 1:2.

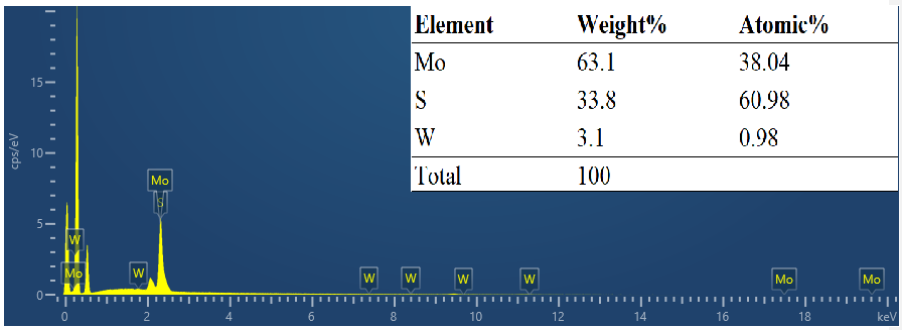


| Element | Weight% | Atomic% |
|---|---|---|
| Mo | 63.1 | 38.04 |
| S | 33.8 | 60.98 |
| W | 3.1 | 0.98 |
| Total | 100 | |

***Fig 6- 4. EDS spectrum and elemental composition of W-doped $MoS_2$ sample***

3. Based on the XPS quantitative analysis, the atomic percentages of S, Mo, and W are 60.83%, 35.26%, and 3.91%, respectively. Compared to the ideal stoichiometry of $MoS_2$(Mo:S = 1:2, i.e., 33.33% Mo and 66.67% S), the measured sulfur content is significantly lower. This deviation indicates a deficiency of sulfur atoms in the structure, suggesting the presence of sulfur vacancies.

*Table 6-4. XPS quantitative analysis of $W_{0.2}Mo_{0.8}S_2$.*

| Element | XPS Atomic % | Theoretical Atomic % ($MoS_2$) | Deviation |
|---|---|---|---|
| **S** | 60.83 | 66.67 | -5.84 |
| **Mo** | 35.26 | 26.66 | 8.6 |
| **W** | 3.91 | 6.67 | -2.76 |

Collectively, these complementary results from XRD, EDS, and XPS analyses suggest that the synthesized material is enriched with sulfur defects.

**Commented [SP1]:** Add these EDS and XPS to the thesis.

### 6.2.4 Raman Spectrum

The disparity in frequency between the in-plane $E_{2g}^1$ and out-of-plane $A_{1g}$ vibrational modes in $MoS_2$ constitutes a pivotal parameter that signifies the structural and electronic characteristics of the material. This disparity is modulated by several determinants, encompassing the number of layers, substrate interactions, and ambient conditions. Comprehending these determinants is crucial for the enhancement of $MoS_2$ for diverse applications, relevant for electrochemical processes.

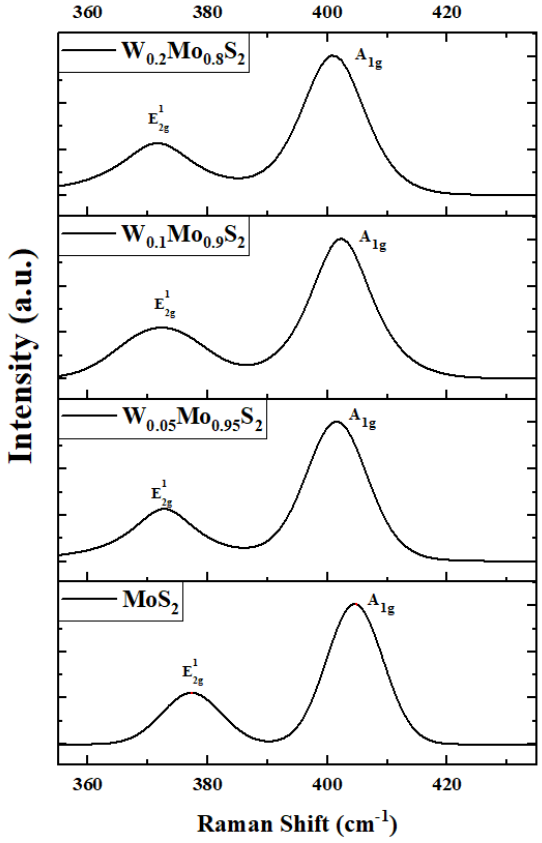


***Fig 6- 5. Raman spectra measured for different V doped level $MoS_2$ and $MoS_2$***

Figure 6-5 illustrates the Raman spectrum corresponding to varying concentrations of W-doped $MoS_2$ alongside pure $MoS_2$. It can be observed that the Raman peaks attributable to the in-plane vibrations of Mo and S atoms ($E^1_{2g}$ mode) for pure $MoS_2$ appear at roughly 372 $cm^{-1}$, while the out-of-plane vibrations of the S atoms ($A_{1g}$ mode) manifest at 401.5 (5% W-doped), 402.3 (10% W-doped), and 400.5 cm–1 (20% W-doped). In contrast to pure $MoS_2$, both vibrational modes exhibit a noticeable blue shift in the case of W-doped $MoS_2$. Typically, the blue shift observed in the Raman spectrum is significantly affected by both charge doping and mechanical strain [350,351]. During the phenomenon of grain growth in $MoS_2$, the occurrence of W-doping transpires, resulting in lattice distortion and the introduction of a substantial

number of holes. Subsequently, this will culminate in the induction of strain and the enhancement of electron-phonon scattering [340,352]. The distinction between the two vibrational modes was observed to augment in all samples infused with tungsten (W), suggesting that the incorporation of W contributes positively to the enhancement of layer stacking and interlayer distance (Table 6-5).

***Table 6-5. Raman spectrum peak position of different W doped level $MoS_2$ and $MoS_2$***

| Sample | $E^1_{2g}$ ($cm^{-1}$) | $A_{1g}$ ($cm^{-1}$) | Δk ($cm^{-1}$) |
|---|---|---|---|
| $W_{0.05}Mo_{0.95}S_2$ | 372.4 | 401.5 | 29.1 |
| $W_{0.1}Mo_{0.9}S_2$ | 372.3 | 402.3 | 30 |
| $W_{0.2}Mo_{0.8}S_2$ | 372 | 400.5 | 28.5 |
| $MoS_2$ | 377.2 | 404.7 | 27.5 |

### 6.2.5 Electrocatalytic performance of W-doped $MoS_2$ nanosheets

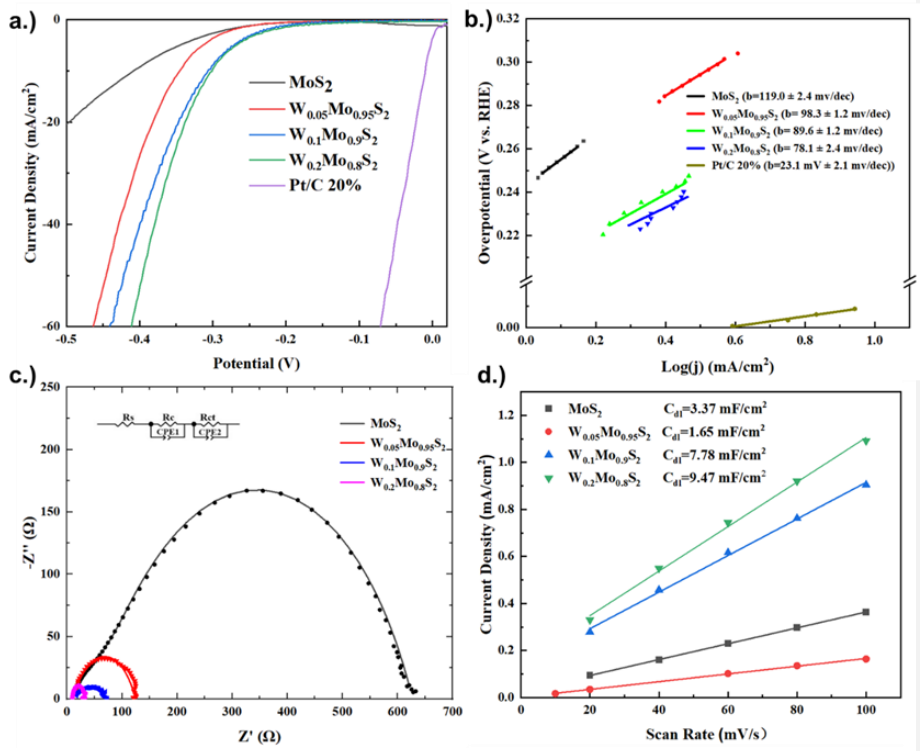


***Fig 6- 6. HER performance analysis of synthesized $MoS_2$ and W-Doped $MoS_2$ catalysts: (a) LSV curves illustrating catalyst activity, (b) Tafel plots derived from polarization curves for comparative evaluation, (c) EIS assessing charge transfer resistance in pure and W-Doped $MoS_2$ Samples, (d) ECSA measurements for W-Doped $MoS_2$.***

The synthesized $MoS_2$ and tungsten-doped $MoS_2$ samples were investigated as electrocatalysts for HER in an acidic environment. This study, conducted in a 0.5 M $H_2SO_4$ solution with a glassy carbon electrode as the working electrode, aimed to evaluate the effect of varying tungsten doping levels on HER efficiency, focusing on polarization behavior, Tafel slopes, impedance, and electrochemically active surface area.

The polarization curves for all four samples are shown in Figure 6-6(a). The pristine $MoS_2$ exhibited an overpotential (η) of 410 mV at a current density of 10 mA/cm$^2$. In contrast, the W-doped samples demonstrated a significant reduction in overpotential, with values

decreasing to: 345 mV for $W_{0.05}Mo_{0.95}S_2$, 306 mV for $W_{0.1}Mo_{0.9}S_2$ and 300 mV for $W_{0.2}Mo_{0.8}S_2$. $W_{0.2}Mo_{0.8}S_2$ catalyst exhibited the lowest overpotential, indicating the most efficient HER activity among the samples. This improvement in overpotential with increased W doping suggests that tungsten enhances the electron transfer capabilities and optimizes the electronic structure of $MoS_2$, making it more conducive for HER.

Figure 6-6(b) presents the Tafel plots for the four catalysts. The Tafel slopes, calculated for each sample, were as follows: 119.9 mV $dec^{-1}$ for pristine $MoS_2$, 98.3 mV $dec^{-1}$ for $W_{0.05}Mo_{0.95}S_2$, 89.6 mV $dec^{-1}$ for $W_{0.1}Mo_{0.9}S_2$, 78.1 mV $dec^{-1}$ for $W_{0.2}Mo_{0.8}S_2$. $W_{0.2}Mo_{0.8}S_2$ catalyst, with the lowest Tafel slope of 78.1 mV $dec^{-1}$, indicates the most favorable reaction kinetics. According to HER mechanisms, a Tafel slope between 120 and 39 mV $dec^{-1}$ typically suggests a Volmer–Heyrovsky reaction pathway. [328] The Tafel slopes of these samples indicate adherence to this pathway, with the Volmer reaction as the rate-determining step. The decreasing Tafel slope with increased W doping suggests enhanced hydrogen adsorption on $MoS_2$, particularly at higher dopant concentrations, leading to improved HER kinetics.

Nyquist plots (Figure 6-6(c)) reveal the charge transfer resistance ($R_{ct}$) of each catalyst, with values as follows: 113 Ω for $W_{0.05}Mo_{0.95}S_2$, 63.3 Ω for $W_{0.1}Mo_{0.9}S_2$, 21.6 Ω for $W_{0.2}Mo_{0.8}S_2$. The Rct progressively decreases with increased tungsten doping, with 20% W-$MoS_2$ showing the lowest resistance. A lower $R_{ct}$ suggests improved electron transport across the catalyst-electrolyte interface, which is crucial for HER efficiency. This trend confirms that tungsten doping enhances the electrical conductivity of $MoS_2$, facilitating faster charge transfer and thereby boosting HER kinetics.

The catalytic activity of electrocatalysts is highly dependent on the availability of active sites. ECSA, estimated through the electrochemical double-layer capacitance ($C_{dl}$), provides an indirect measure of active sites. Cyclic voltammetry was conducted within a non-faradaic potential range (0.33–0.53 V) at sweep rates spanning from 10 to 100 mV/s, and the $C_{dl}$ were extracted, as depicted in Figure 6-6(d). The Cdl values for the catalysts were:

3.24 mF/cm$^2$ for pristine $MoS_2$, 5.62 mF/cm$^2$ for $W_{0.05}Mo_{0.95}S_2$, 7.83 mF/cm$^2$, for $W_{0.1}Mo_{0.9}S_2$, 9.47 mF/cm$^2$ for $W_{0.2}Mo_{0.8}S_2$. The 20% W-$MoS_2$ sample displayed the highest $C_{dl}$, approximately three times that of pristine $MoS_2$, indicating a higher density of accessible active sites. This increase in active surface area correlates directly with enhanced HER performance, as a larger ECSA implies more catalytic sites available for hydrogen adsorption and reaction.

In conclusion, tungsten doping significantly enhances the HER activity of $MoS_2$, with 20% W- $MoS_2$ showing the best performance in terms of overpotential reduction, Tafel slope, charge transfer resistance, and active surface area. The study suggests that tungsten acts as an effective dopant by improving electron transfer, increasing active site availability, and enhancing hydrogen adsorption capabilities in $MoS_2$. The results of this investigation indicate that tungsten-doped $MoS_2$ catalysts, particularly at elevated doping concentrations, represent highly viable options for economically advantageous and effective HER electrocatalysis in acidic environments.

### 6.2.6 Uv-vis spectrum

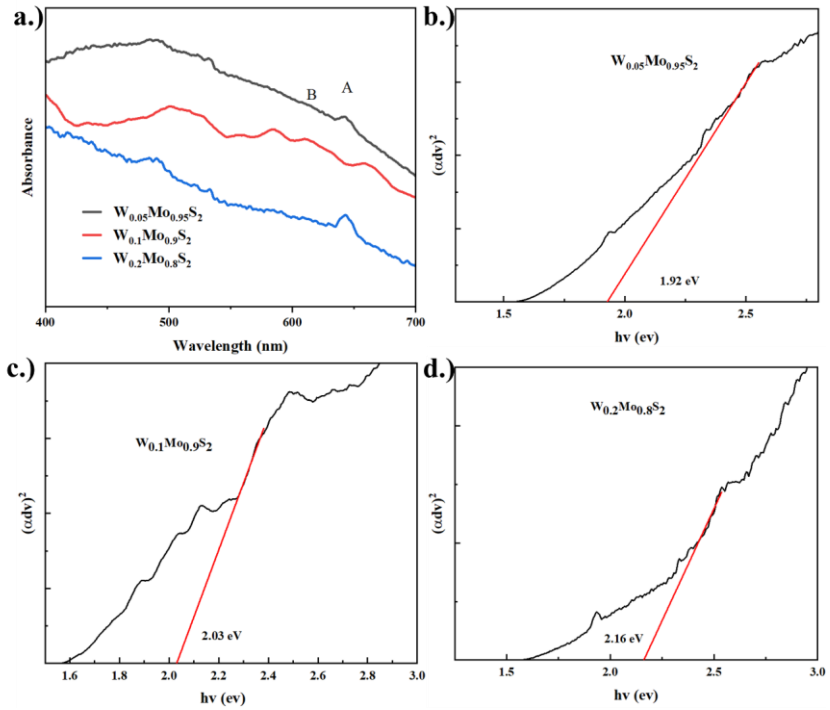


***Fig 6- 7. UV-Vis spectra of the $W_{0.05}Mo_{0.95}S_2$, $W_{0.1}Mo_{0.9}S_2$, and $W_{0.2}Mo_{0.8}S_2$ (a), direct transition ((αhu)² vs. hu) curves for $W_{0.05}Mo_{0.95}S_2$ (b), $W_{0.1}Mo_{0.9}S_2$ (c), and $W_{0.2}Mo_{0.8}S_2$ (d).***

As illustrated in Figures 5-9 (a) and 6-7 (a), multiple discrete spectral peaks are observed at $\lambda_{max}$ values of 645, 612, 488, and 423 nm, which highlight the unique absorption bands corresponding to $MoS_2$ nanoflowers. The prominent peaks identified at 612 and 645 nm are attributed to the K point within the Brillouin zone, [222,223] while the peaks situated at 423 and 488 nm are associated with direct electronic transitions from the inner valence band to the conduction band. [224,225] In the instance of $W_{0.05}Mo_{0.95}S_2$, these peak positions demonstrate a shift to 643, 532, and 492 nm. For $W_{0.1}Mo_{0.9}S_2$, the peaks undergo an additional displacement to 660, 613, 528, and 500 nm. In the case of $W_{0.2}Mo_{0.8}S_2$, the peaks encounter a further shift to 643, 533, and 490 nm.

# Tungsten-Doped $MoS_2$ with Sulfur Vacancies for Enhanced HER Catalytic Performance

From the viewpoint of direct band gap semiconductors, it is feasible to ascertain the band gap of synthesized materials by scrutinizing the tangential slopes of the Tauc plot [$(\alpha dv)^2$ $vs$ $hv$]. This examination is conducted as strain is introduced within the crystal lattice of $MoS_2$ via the incorporation of a foreign element such as vanadium, resulting in alterations to the lattice parameters. According to the Tauc plot, the optical band gap for $W_{0.5}Mo_{0.95}S_2$ is around 1.92 eV, which falls short compared to the values of $W_{0.1}Mo_{0.9}S_2$ at near 2.03 eV and $W_{0.2}Mo_{0.8}S_2$ at nearly 2.36 eV. An increase in the concentration of tungsten significantly correlated with a decrease in the bandgap. The findings indicate that the Fermi level shifts from the conduction band minimum (CBM). This phenomenon can be attributed to the presence of substitutional $W^{6+}$ ions, which exhibit a reduced number of valence electrons and a greater number of holes in comparison to the Mo ions (work function: W: 4.5 eV, Mo: 4.37 eV). [340,353,354]

### 6.2.7 BET measurements

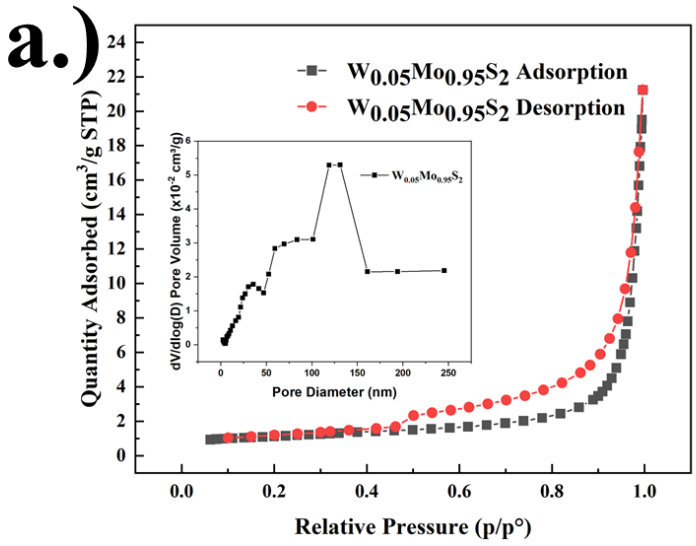


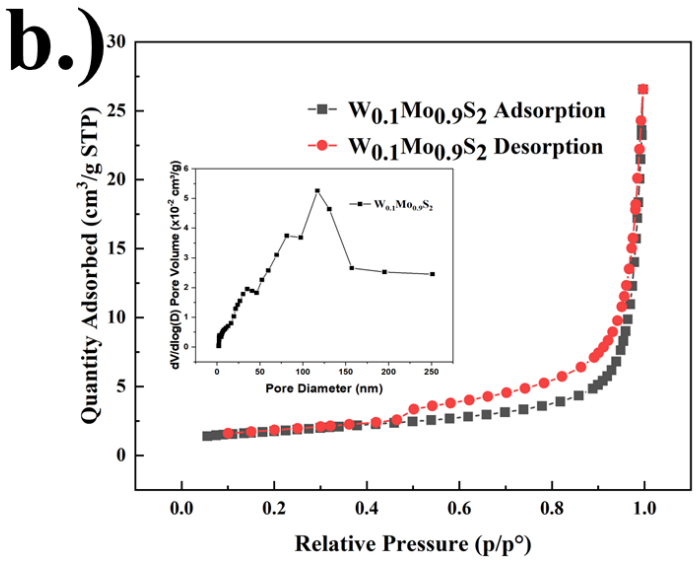

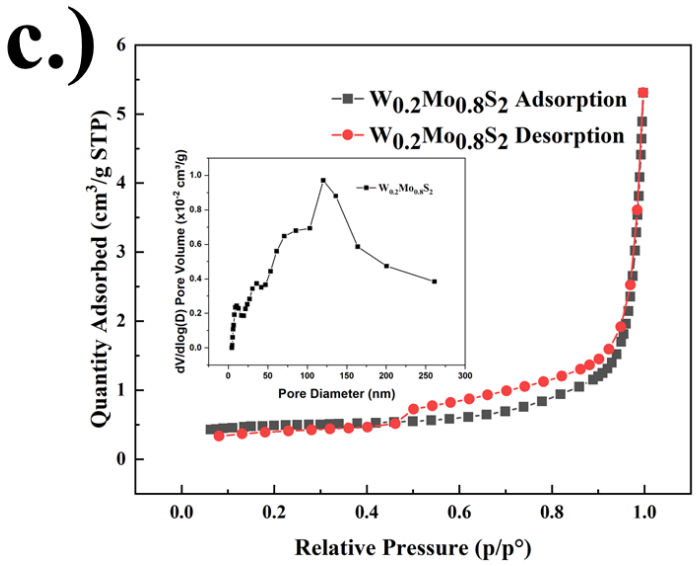


*Fig 6- 8. $N_2$ adsorption-desorption of (a) $W_{0.05}Mo_{0.95}S_2$, (b)$W_{0.1}Mo_{0.9}S_2$, (c) $W_{0.2}Mo_{0.8}S_2$*

$N_2$ adsorption/desorption isotherms (Fig. 6-8 a-c) were conducted on all the samples in the study. The isotherms displayed by these samples exhibit type V characteristics along with H3 hysteresis loops when the relative pressure ranges from 0 to 1.0. This observation indicates the presence of a mesoporous structure within the samples under investigation [349]. The calculated values were 6.16 $m^2$/g for 5% W-doped $MoS_2$, 1.54 $m^2$/g for 10% W-doped $MoS_2$ and 3.85 $m^2$/g for 20% W-doped $MoS_2$. Among these materials, it was observed that 5% W-doped molybdenum disulfide demonstrated the smallest average pore diameter of 29.87 nm alongside BET surface area. However, this material displayed the lowest catalytic activity for the HER. This analysis reveals that 20% W-doped $MoS_2$ exhibits a mesoporous configuration characterized by an average pore diameter of 41.14 nm. The substantial specific surface area featuring abundant mesopores promotes the efficient exposure of active sites and facilitates the diffusion of electrolyte within the material. Such attributes play a crucial role in enhancing the catalytic performance for hydrogen evolution reactions [355].

## 6.3 Conclusion

The infusion of tungsten into the $MoS_2$ structural design initiates the emergence of sulfur vacancies with a positive charge, attributable to the tungsten doping that effectively lessens the total electron density present in the material. This reduction in electron density leads to a consequential decrease in the binding energy associated with the neighboring sulfur atoms, thereby facilitating the emergence of sulfur vacancies as a notable and significant phenomenon. Additionally, the infusion of tungsten into the material causes the interlayer spacing to expand, producing a significant modification in structural traits as tungsten concentration rises. Hence, this modification in the spacing between layers fosters the buildup of supplementary layers within the material, a situation that is crucial for understanding the structural progression of the compound. The increse of the d-spacing not just optimizes the stacking of layers but also markedly heightens the thickness of the multi-layer $MoS_2$, leading to a higher presence of highly productive active sites for the hydrogen evolution reaction (HER), thus enhancing the overall catalytic effectiveness of the material in this regards.

# Enhanced Hydrogen Evolution in $MoS_2$ Enabled by Intermediate Bands through Co Doping

## 7.1 Introduction

Research into cobalt (Co) doped molybdenum disulfide showcases significant advancements across various fields including carbon capture, hydrogen generation processes, lithium-sulfur energy storage systems, and dye breakdown. The incorporation of Co into $MoS_2$ significantly improves its catalytic, electronic, and structural characteristics, rendering it a highly adaptable material for energy and environmental applications. This chapter examines the principal findings derived from the referenced research articles, emphasising the influence of Co doping on the performance of $MoS_2$ across various fields.

Liu and co-authors indicate that adding $MoS_2$ markedly hastens the catalytic reaction involving lithium polysulfides (LiPS), which contributes to better electron transfer and overall catalytic efficiency. This phenomenon resulted in remarkable capacity and cycling stability, achieving a capacity of 941 mAh $g^{-1}$ with minimal capacity degradation over 1000 cycles.[356] In the realm of environmental applications, Raza et al. demonstrated that Co-doped $MoS_2$ nanosheets exhibited superior dye degradation efficiency, particularly with respect to methylene blue, attributable to enhanced crystallinity and surface morphology. Such characteristics render them highly effective for the remediation of industrial pollutants. [357] Concerning the hydrogen evolution reaction (HER), Co-doped $MoS_2$ improves HER activity as a consequence of the incorporation of edge-rich, lattice-distorted configurations. The Co doping facilitates the exposure of active sites and enhances electron transport, thereby achieving low overpotentials of 67 mV and 155 mV in alkaline and acidic environments, respectively.[358] Pan et al. also established that the Co-O-Mo active centers further amplified HER and oxygen evolution reaction (OER) performance by promoting electron conductivity and charge transfer.[359]

## Enhanced Hydrogen Evolution in $MoS_2$ Enabled by Intermediate Bands through Co Doping

In this study, a simple one-step hydrothermal method to produce certain dopant level cobalt doped $MoS_2$. 5% and 10% cobalt doped $MoS_2$ were produced to investigate the influence of dopant level in HER activity in 0.5 M $H_2SO_4$ electrolyzer. The emergence of half-filled intermedia bands within the electronic band structure of 2H-$MoS_2$ induced by cobalt doping can be discerned from a contraction of the optical band gap. The effects of varying Co content on the HER performance of the nanosheets were comprehensively examined. The 10% Co-$MoS_2$ catalyst, characterized by a substantial Co content, demonstrates optimal catalytic performance.

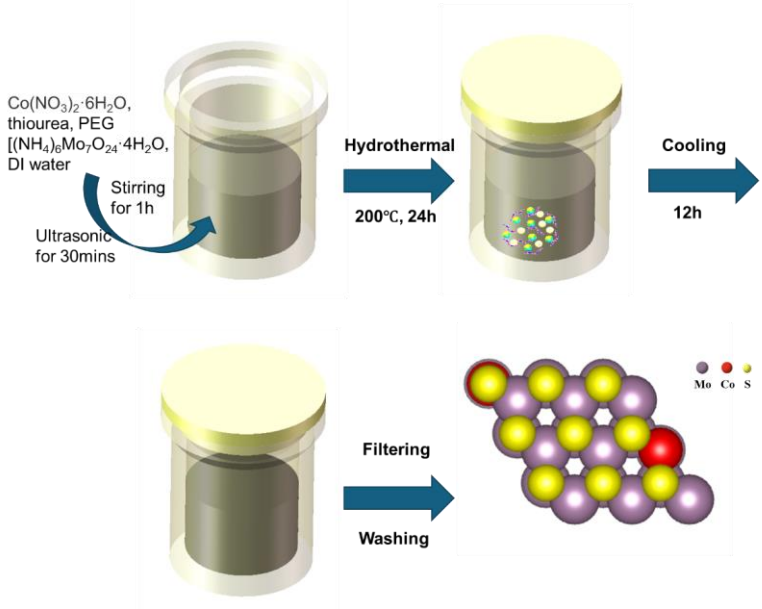


***Scheme 7-1. Schematic illustration of Co-doped $MoS_2$ synthesis process***

As illustrated in Scheme 7-1, $MoS_2$ was prepared by the hydrothermal method at 200 °C with the starting chemicals of thiourea, and polyethylene glycol (PEG). $(NH_4)_6Mo_7O_{24}·4H_2O$ dissolved in deionized (DI) water. Cobaltous nitrate hexahydrate ($Co(NO_3)_4·6H_2O$) was used as a Tungsten precursor, and certain amounts of $Co(NO_3)_4$ $6H_2O$ were mixed into solutions to make certain dopant ratios (5% and 10% cobalt dopant respectively. The synthesis procedure

is illustrated in Scheme 7-1, while the quantities of starting materials are detailed in Table 7-1.

***Table 7-1 Compositions of the Co-doped $MoS_2$ nanoflowers prepared with reactants of various Co contents***

| Samples | Reactants | | | | |
|---|---|---|---|---|---|
| | $(NH_4)_6Mo_7O_{24}\cdot 4H_2O$ (mmol) | $Co(NO_3)_4\cdot 6H_2O$ (mmol) | $CH_4N_2S$ (mmol) | Polyethylene glycol (g) | DI water (ml) |
| $MoS_2$ | 0.223 | 0 | 4.532 | 0.322 | 13.8 |
| $Co_{0.05}Mo_{0.95}S_2$ | 0.212 | 0.078 | 4.532 | 0.322 | 13.8 |
| $Co_{0.1}Mo_{0.9}S_2$ | 0.201 | 0.156 | 4.532 | 0.322 | 13.8 |

## 7.2 Results and Discussion

### 7.2.1 Investigation of morphological characteristics

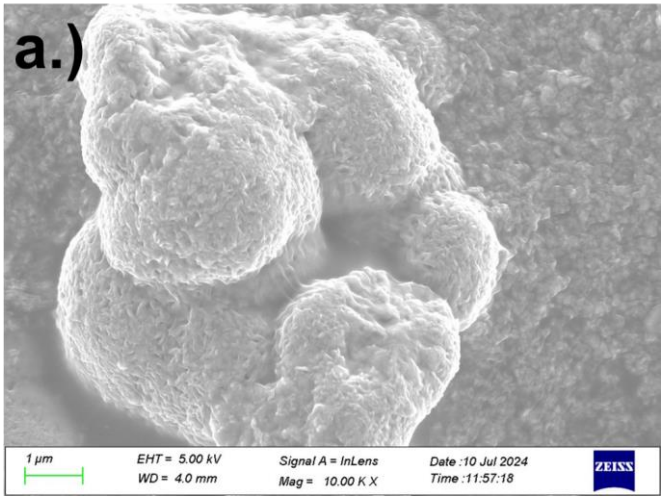


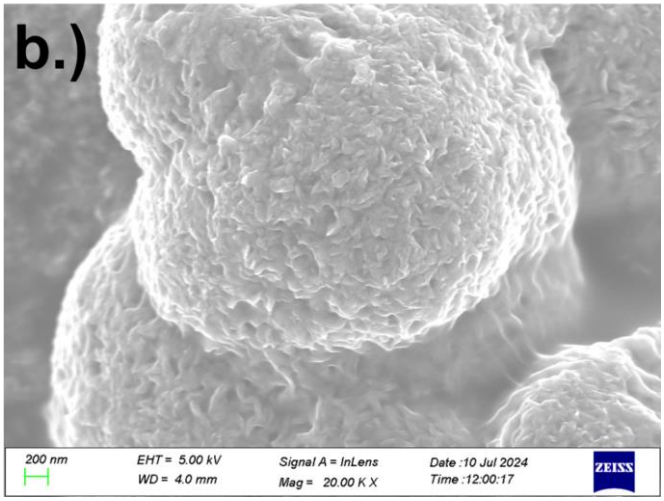

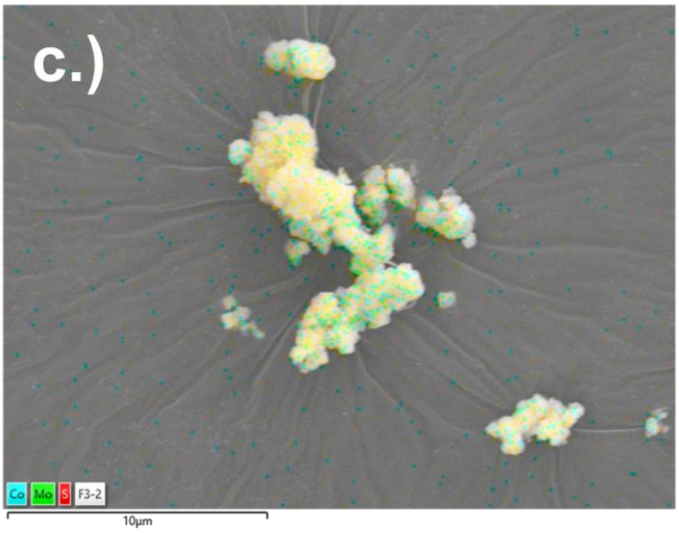
c.)
Co
Mo
S
F3-2
10µm

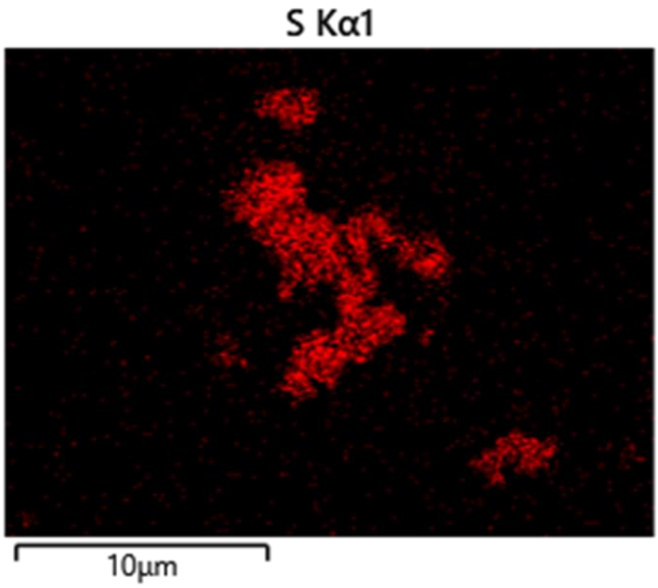
S Kα1
10µm

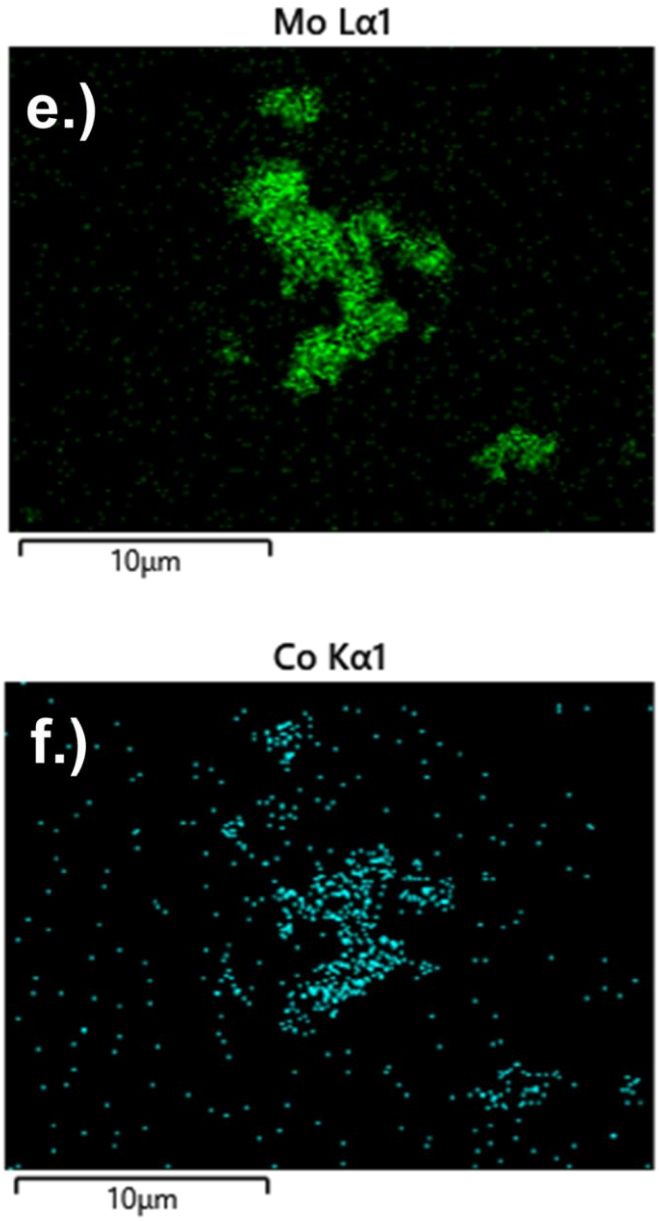


*Fig 7- 1. (a-b) SEM images of $Co_{0.1}Mo_{0.9}S_2$, and (c-f) corresponding elemental mapping*

As illustrated in Fig 7-1 a). Co-$MoS_2$ specimen manifests as a nanosphere with an approximate average diameter of 600 nm. Examining $Co_{0.1}Mo_{0.9}S_2$, Co-doping in $MoS_2$ suggests that the flower-like shape, featuring nanosheets, notably shows particulate aggregates, which are probably the result of $CoS_2$ deposition on the Co-$MoS_2$ nanosheets' surface.[360] The energy dispersive X-ray spectroscopy (EDS) spectrum image, alongside the corresponding elemental mapping images (Fig. 7-1d-g), substantiates the hypothesis that molybdenum (Mo), cobalt (Co), and sulfur (S) elements are uniformly distributed throughout the entire nanosheet, thereby further indicating the occurrence of doping of cobalt within the $MoS_2$.

### 7.2.2 Crystallographic investigation

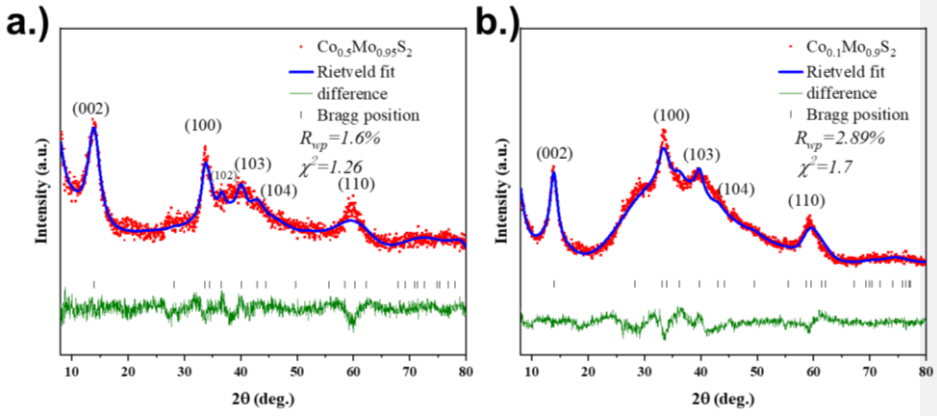


*Fig 7- 2. Powder XRD pattern with Rietveld refinement a). $Co_{0.05}Mo_{0.95}S_2$ b). $Co_{0.1}Mo_{0.9}S_2$*

X-ray diffraction analysis was executed to elucidate the crystalline structure of Co doped $MoS_2$ nanosheets (Figure 7-2). The XRD profiles obtained for all samples displayed a strong correlation with the characteristic pattern indicative of the hexagonal $MoS_2$ phase, as documented in the Powder Diffraction File (PDF Card - 04-010-5047). The absence of any characteristic peaks indications suggesting the formation of the $CoS_2$ phase, coupled with the persistent presence of the hexagonal $MoS_2$ phase across all specimens, constitutes substantial evidence that the incorporation of Cobalt into $MoS_2$ occurred through a

substitutional mechanism, thereby maintaining the crystalline integrity of $MoS_2$. Nevertheless, the presence of the amorphous phase emerges within the angular range of approximately 2theta = 20-55, which may imply the existence of $CoS_2$ within the $Co_{0.1}Mo_{0.9}S_2$ compound.[360] The results of the Rietveld analysis yielded goodness-of-fit values of 1.6 and 1.7 respectively, thereby affirming the reliability of the refinement results (Table 7-2).

***Table 7-2. Parameters Co-doped $MoS_2$ As Obtained by Rietveld Refinement***

| Parameters | $Co_{0.5}Mo_{0.95}S_2$ | $Co_{0.1}Mo_{0.9}S_2$ |
|---|---|---|
| a(Å) | 3.063±0.0112 | 3.092±0.0046 |
| b(Å) | 3.063±0.0112 | 3.092±0.0046 |
| c(Å) | 12.58±0.063 | 12.51±0.0131 |
| V($Å^3$) | 102.218±0.881 | 103.519±0.196 |
| $\%R_{wp}$ | 6.35 | 3.51 |
| $\chi^2$ | 1.6 | 1.7 |

Moreover, both samples subjected to investigation exhibited broadened (100) and (110) diffraction peaks attributed to $MoS_2$ (26.63 for $Co_{0.05}Mo_{0.95}S_2$ and 26.34 for $Co_{0.1}Mo_{0.9}S_2$, only 25.905 for pure $MoS_2$), indicating the emergence of defect-rich structures, correlated to enhanced performance in electrocatalysis.

***Table 7-3. 2θ values for Co-doped $MoS_2$***

| (h k l) | 2 theta (degree) | | |
|---|---|---|---|
| | $MoS_2$ | $Co_{0.05}Mo_{0.95}S_2$ | $Co_{0.1}Mo_{0.9}S_2$ |
| 0 0 2 | 13.887 | 14.069 | 14.152 |
| 1 0 0 | 32.632 | 33.61 | 33.15 |
| 1 1 0 | 58.437 | 60.24 | 59.49 |

### 7.2.3 XPS measurement

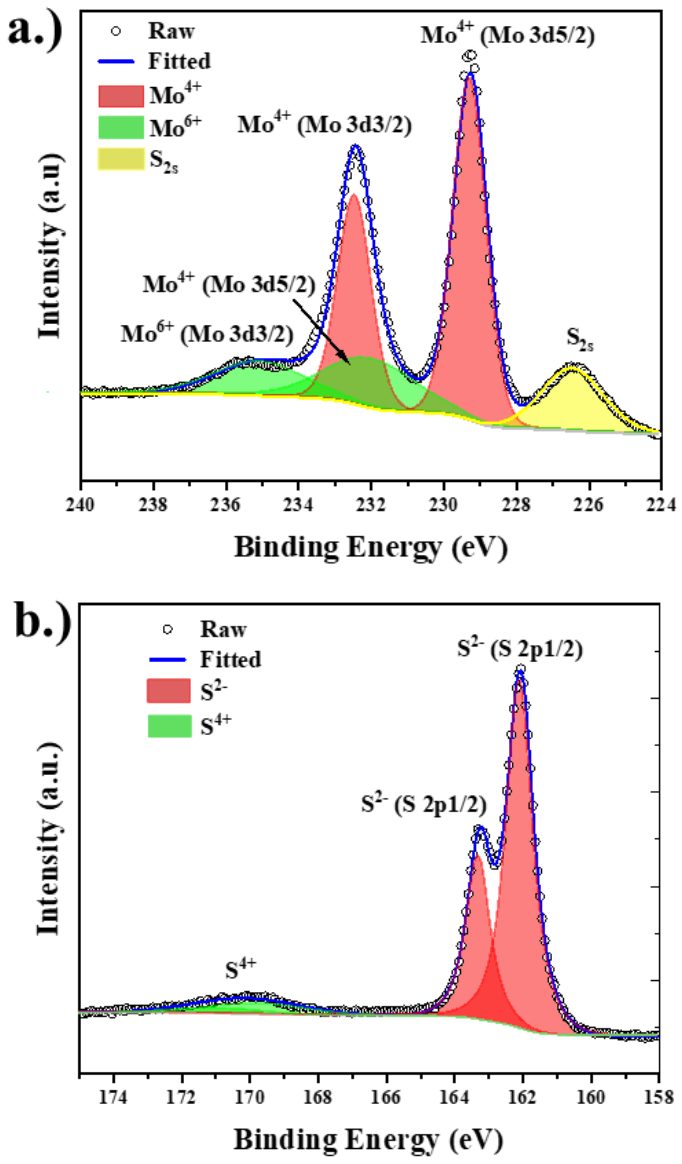


*Fig 7- 3. XPS spectra associated with a.) Mo (3d), b). S (2p)*

The characteristic Mo (3d5/2) and Mo (3d3/2) peaks of the 2H phase were observed at 229.3, 232.4 eV in the absence of doping and at 230.3, 233.6 eV in the presence of 10%

Cobalt doping in $MoS_2$. Additionally, two peaks were identified, shifted by approximately 1 eV Fig. 7-3(a) [96,317,318]. Similarly, the $S^{2-}$ (2p3/2) and S (2p1/2) peaks of the 2H phase were detected at 162.05, 164.0 eV without doping and at 162.06, 163.3 eV with 10% Co-doped $MoS_2$, depicted in Fig. 7-3(b). Two additional peaks, shifted by around 0.01 eV. The shifts of the $Mo^{4+}$ (3d5/2) and Mo (3d3/2) peaks towards higher binding energies were observed with increasing levels of Cobalt doping, as demonstrated in 10% Co-doped $MoS_2$. Cobalt doping in $MoS_2$ induces modifications in the electronic framework, specifically influencing the density of states (DOS) and the band structure. The incorporation of cobalt atoms leads to the emergence of intermediate energy states, predominantly derived from $Co^{2+}$ 3d orbitals, situated within the bandgap of $MoS_2$. These intermediate energy states significantly enhance the electrical conductivity and modify the electronic milieu, potentially resulting in upward shifts in the binding energies of $Mo^{4+}$ 3d and $S^{2-}$ 2p. [361]

### 7.2.4 Raman Spectrum

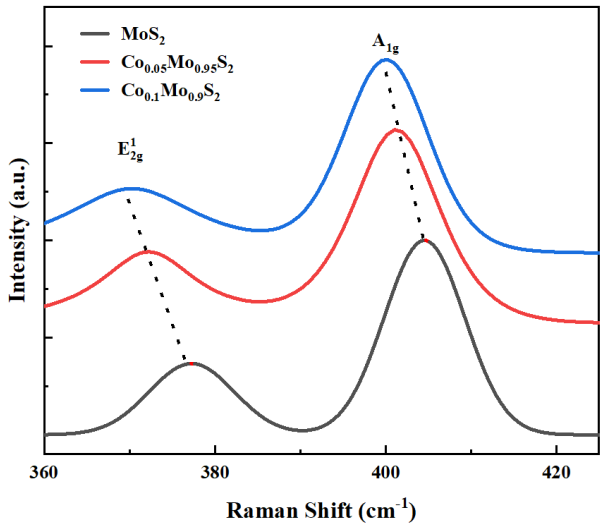


*Fig 7- 4. Raman spectra measured for different V doped level $MoS_2$ and $MoS_2$*

Figure 7-4 delineates the Raman spectra corresponding to diverse concentrations of Co-doped MoS2 in conjunction with pure $MoS_2$. It is discernible that the Raman peaks

associated with the in-plane vibrational modes of Mo and S atoms ($E^1_{2g}$ mode) for pure $MoS_2$ are observed at approximately 377.2 $cm^{-1}$, whereas a redshift is evident upon doping with Co (372.3 $cm^{-1}$ for 5% Co-doped and 370.2 $cm^{-1}$ for 10% Co-doped samples), while the out-of-plane vibrational modes of the S atoms ($A_{1g}$ mode) are manifested at 401.1 $cm^{-1}$ (5% Co-doped) and 400.2 $cm^{-1}$ (10% Co-doped).

***Table 7-4. Raman spectrum peak position of different Co doped level $MoS_2$ and $MoS_2$***

| Sample | $E^1_{2g}$ ($cm^{-1}$) | $A_{1g}$($cm^{-1}$) | Δk ($cm^{-1}$) |
|---|---|---|---|
| $Co_{0.05}Mo_{0.95}S_2$ | 372.3 | 401.1 | 28.8 |
| $Co_{0.1}Mo_{0.9}S_2$ | 370.2 | 400.2 | 30 |
| $MoS_2$ | 377.2 | 404.7 | 27.5 |

It is evident that as the concentration of Co increases, the $E^1_{2g}$ and $A_{1g}$ vibrational modes experience a gradual redshift, accompanied by a reduction in their peak intensities. This phenomenon can be attributed to the Co doping within $MoS_2$, which leads to a softening of the Mo–S vibrational modes, resulting in a decline in both their vibrational frequency and intensity.[362] The aforementioned findings suggest that $Co^{2+}$ can effectively substitute for Mo atoms, facilitating covalent doping in $MoS_2$ and thereby significantly modulating its electronic structure to enhance hydrogen evolution reaction activity.

***Table 7-5. intensity comparison of different V doped level $MoS_2$ and $MoS_2$***

| Sample | $Co_{0.05}Mo_{0.95}S_2$ | $Co_{0.1}Mo_{0.9}S_2$ | $MoS_2$ |
|---|---|---|---|
| $IE^1_{2g}/IA_{1g}$ | 0.3726 | 0.3360 | 0.3670 |

The distinction between the two vibrational modes was observed to increase in all samples infused with Cobalt (Co), suggesting that the incorporation of Co contributes positively to the enhancement of layer stacking and interlayer distance (Table 7-4)

## 7.2.5 Electrocatalytic performance of Co-doped $MoS_2$ nanosheets

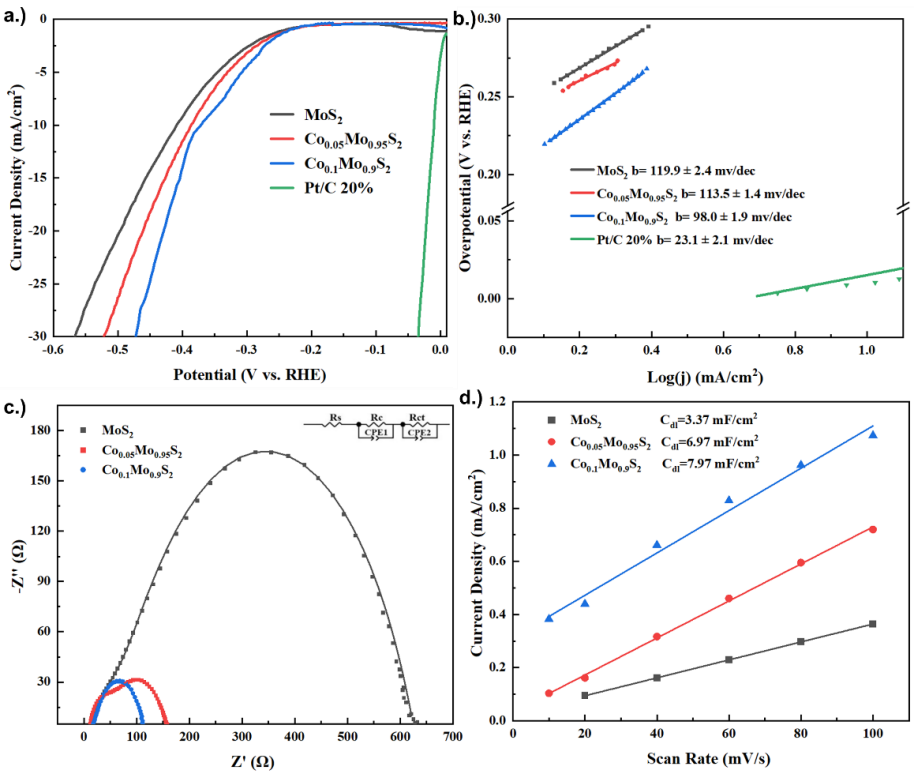


***Fig 7- 5. HER performance analysis of synthesized $MoS_2$ and Co-Doped $MoS_2$ catalysts: (a) LSV curves illustrating catalyst activity, (b) Tafel plots derived from polarization curves for comparative evaluation, (c) EIS assessing charge transfer resistance in pure and Co-Doped $MoS_2$ Samples, (d) ECSA measurements for Co-Doped $MoS_2$.***

The synthesized $MoS_2$ and cobalt-doped $MoS_2$ samples were evaluated as electrocatalysts for HER in acidic conditions. This study, conducted in a 0.5 M $H_2SO_4$ solution with a glassy carbon electrode as the working electrode, aimed to determine how varying cobalt doping levels affect HER efficiency. Key measurements included polarization behavior, Tafel slopes, impedance, and ECSA.

Figure 7-5(a) presents the polarization curves for each sample. The pristine $MoS_2$ exhibited an overpotential (η) of approximately 410 mV at a current density of 10 mA/cm$^2$.

The Co-doped samples showed a noticeable decrease in overpotential: 385 mV for $Co_{0.05}Mo_{0.95}S_2$, 356 mV for 10% $Co_{0.1}Mo_{0.9}S_2$. The 10% Co- $MoS_2$ catalyst displayed the lowest overpotential, indicating superior HER activity among the samples. This reduction in overpotential with increased cobalt doping suggests that cobalt enhances the electron transfer capabilities and optimizes the electronic structure of $MoS_2$, making it more suitable for HER.

The Tafel plots for the four catalysts, shown in Figure 7-5(b), were analyzed to determine the Tafel slope values: 119.9 mV $dec^{-1}$ for pristine $MoS_2$, 113 mV $dec^{-1}$ for $Co_{0.05}Mo_{0.95}S_2$, 98 mV $dec^{-1}$ for $Co_{0.1}Mo_{0.9}S_2$. The 10% Co-$MoS_2$ catalyst, with the lowest Tafel slope of 98 mV $dec^{-1}$, indicates improved reaction kinetics. The Tafel slopes of these samples fall between 120 mV $dec^{-1}$ (associated with the Volmer mechanism) and 39 mV $dec^{-1}$ (associated with the Heyrovsky mechanism), implying a Volmer–Heyrovsky reaction pathway, where the Volmer step (adsorption of hydrogen atoms onto the catalyst surface) is the rate-determining step. [328] The decreasing Tafel slope with increased cobalt doping suggests enhanced hydrogen adsorption capability in Co-$MoS_2$, especially at higher dopant concentrations, which in turn promotes efficient HER kinetics.

Nyquist plots (Figure 7-5(c)) were used to evaluate the charge transfer resistance ($R_{ct}$) of each catalyst: 101 Ω for $Co_{0.1}Mo_{0.9}S_2$, 123 Ω for $Co_{0.05}Mo_{0.95}S_2$. The reduced $R_{ct}$ values with increasing Co doping indicate enhanced electron transport across the catalyst-electrolyte interface. Notably, the 10% Co- $MoS_2$ catalyst exhibited the lowest $R_{ct}$, reflecting its superior conductivity and improved charge transfer characteristics, which are essential for efficient HER.

ECSA is a crucial indicator of an electrocatalyst's performance, as it reflects the availability of active sites. The ECSA was estimated through the electrochemical double-layer capacitance (Cdl), calculated from cyclic voltammetry (CV) in a non-faradaic potential range (0.33–0.53 V) at varying scan rates (10 to 100 mV/s). The Cdl values derived from these measurements (Figure 7-5(d)) were: 3.24 mF/$cm^2$ for pristine $MoS_2$, 5.42 mF/$cm^2$ for

$Co_{0.05}Mo_{0.95}S_2$, 7.97 mF/cm$^2$ for 10% $Co_{0.1}Mo_{0.9}S_2$. The 10% Co- $MoS_2$ sample demonstrated the highest $C_{dl}$, indicating a nearly threefold increase in active surface area compared to pristine $MoS_2$. This increase in ECSA correlates with a higher density of accessible active sites, which enhances the HER activity. The improved $C_{dl}$ values for Co-doped $MoS_2$ suggest that cobalt doping enhances electron transfer characteristics in an acidic environment.

In summary, cobalt doping significantly improves the HER activity of $MoS_2$, with 10% Co- $MoS_2$ showing the best performance across all key metrics, including overpotential, Tafel slope, charge transfer resistance, and ECSA. The study indicates that cobalt acts as an effective dopant, enhancing electron transfer and increasing active site density, ultimately promoting efficient hydrogen adsorption and reaction kinetics in $MoS_2$. These findings suggest that cobalt-doped $MoS_2$ catalysts, particularly at 10% doping, are promising candidates for cost-effective and comparatively high-performance HER electrocatalysis in acidic solutions.

### 7.2.6 UV-vis spectrum

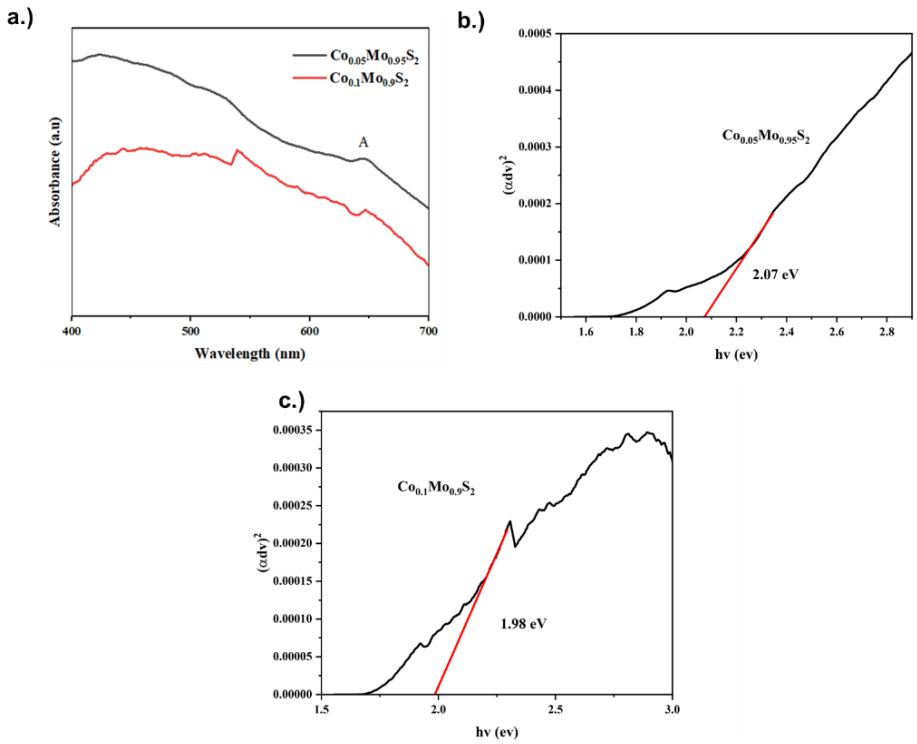


***Fig 7- 6. UV-Vis spectra of the $Co_{0.05}Mo_{0.95}S_2$ and $Co_{0.1}Mo_{0.9}S_2$(a), direct transition ((αhu)² vs. hu) curves for $Co_{0.05}Mo_{0.95}S_2$ (b) and $Co_{0.1}Mo_{0.9}S_2$ (c).***

As depicted in Figure 5-9 (a) and 7-6 (a), several distinct spectral peaks emerge at $\lambda_{max}$ values of 645, 612, 488, and 423 nm, which underscore the distinctive absorption bands associated with $MoS_2$ nanoflowers. The significant peaks observed at 612 and 645 nm are ascribed to the K point of the Brillouin zone, [222,223] whereas the peaks located at 423 and 488 nm are linked to direct electronic transitions from the inner valence band to the conduction band. [224,225] In the case of $Co_{0.05}Mo_{0.95}S_2$, t these peak positions exhibit a shift to 646, 621, 533, and 484 nm. For $Co_{0.1}Mo_{0.9}S_2$, the peaks experience an additional shift to 649, 629, 539 and 480 nm.

Cobalt doping in monolayer $MoS_2$ engenders the formation of half-filled intermediate electronic states within the band gap. These intermediate states facilitate additional electronic

transitions that are capable of photon absorption.[363] $MoS_2$ that has been doped with Co showcases a distinctly superior absorption spectrum, particularly for photons that lie within the energy spectrum of 2.26 eV to 2.46 eV. According to Figure 7-6 (b and c), the optical band gap reduces to 2.07 eV for $Co_{0.05}Mo_{0.95}S_2$ and further drops to 1.98 eV for $Co_{0.1}Mo_{0.9}S_2$, indicating that half-filled intermediate states are present.

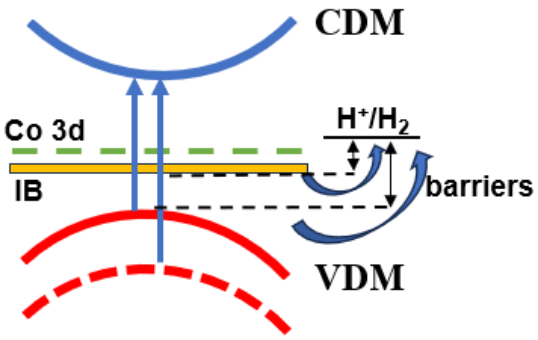


***Fig 7- 7. schematic of the band structure of $Co_xMo_{1-x}S_2$ and charge transfer during the HER.***

As shown in Fig 7-7, in the context of hydrogen adsorption, electrons situated within these half-filled IBs exhibit an enhanced capacity for rapid transfer into the hydrogen energy level, attributable to a diminished energy barrier.[361] This elucidation delineates that the incorporation of IBs plays a significant role in enhancing the HER through the mechanism of reduction $\Delta G_H$.

### 7.2.7 BET measurements

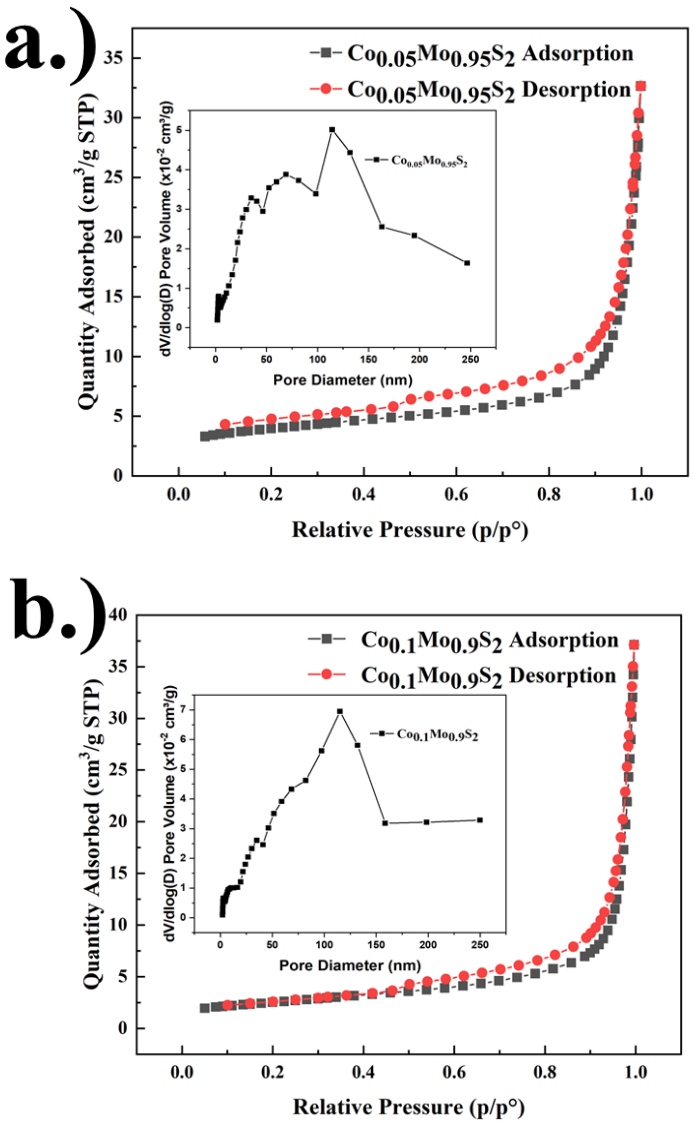


***Fig 7- 8. $N_2$ adsorption-desorption of (a) $Co_{0.05}Mo_{0.95}S_2$, and (b) $Co_{0.1}Mo_{0.9}S_2$. The insets show pore size distributions obtained using the BJH method.***

The BET surface areas of 5% Co-doped $MoS_2$ and 10% Co-doped MoS2 samples were measured to be 13.30 $m^2/g$ and 8.93 $m^2/g$, respectively. The corresponding pore

diameters were found to be 20.45 nm and 26.72 nm. Our study also observed a decline in surface area as the doping levels of Co increased. The decrease in BET surface area is believed to stem from the increased thickness and planarity of the nanosheets following higher Co doping, consequently diminishing the overall available surface area for adsorption. Furthermore, the alterations in structure induced by Co doping, such as heightened crystallinity and crystallite dimensions, further contribute to the decrease in surface area. [364,365]

## 7.3 Conclusion

This one-step hydrothermal synthesis not only facilitates the development of a defect-rich crystalline architecture in pristine $MoS_2$ but also engenders the introduction of intermediate bonds within the pristine $MoS_2$ bond framework. The existence of these intermediate bonds diminishes the energy barriers associated with electron transfer. This enhancement promotes swift electron migration from the intermediate bonds to the hydrogen energy levels, which is imperative for the hydrogen evolution reaction. Cobalt doping, in conjunction with the emergence of intermediate bonds, engenders an increase in active sites available for hydrogen adsorption and activate inert plane of $MoS_2$. This augmentation leads to an enhancement in the overall catalytic efficacy of the material.

# Conclusion and future work

## 8.1 Conclusion

In this research endeavor, the meticulously designed orthogonal experiments demonstrate the influence of three critical factors - namely heat time, heat temperature, and the weight percentage of reduced Graphene Oxide (rGO) on the catalytic efficacy of $MoS_2$. Subsequent investigations reveal that the rGO/$MoS_2$ heterostructure significantly enhances conductivity in comparison to bulk $MoS_2$. Furthermore, the optimal combination of these factors has been validated through the orthogonal experiment. Additional inquiries have focused on the incorporation of $V^{2+}$ and $V^{4+}$ ions into the $MoS_2$ matrix. The substitution of vanadium ions has been confirmed to modify the lattice strain of $MoS_2$ and adjust the interlayer separation, which has been substantiated to effectively enhance HER performance by increasing the availability of active sites. Additionally, tungsten ions in their 6+ and 4+ oxidation states have been investigated; the role of tungsten ions is posited to enhance HER performance by inducing vacancies at sulfur sites. The final topic of exploration pertains to cobalt ion doping. Although the valence state of cobalt ions has not been conclusively established through XPS measurements, it is highly plausible that $Co^{4+}$ exists within the $MoS_2$ structure. This dopant has been demonstrated to facilitate intermediate bonds, thereby enhancing the efficiency of charge transport between the layers.

***Table 8-1. Electrochemical comparison of $MoS_2$ with various dopants***

| Sample | $\eta_{10}$/mV | Tafel slope (mV/dec) | $R_s$/Ohm | $R_c$/Ohm | $R_{ct}$/Ohm |
|---|---|---|---|---|---|
| **$MoS_2$** | 0.41 | 119.9 | 10.3 | 60.8 | 556 |
| **$MoS_2$-rGO 12h 200℃** | 0.34 | 98.2 | - | - | - |
| **$V_{0.02}Mo_{0.98}S_2$** | 0.34 | 117 | 6.48 | - | 159 |
| **$V_{0.05}Mo_{0.95}S_2$** | 0.318 | 89.1 | 9.79 | - | 110 |
| **$V_{0.1}Mo_{0.9}S_2$** | 0.285 | 70.6 | 10.08 | - | 31.6 |
| **$W_{0.05}Mo_{0.95}S_2$** | 0.348 | 98.3 | 11.1 | - | 113 |
| **$W_{0.1}Mo_{0.9}S_2$** | 0.306 | 89.6 | 11.3 | - | 63.3 |
| **$W_{0.2}Mo_{0.8}S_2$** | 0.301 | 78.1 | 9.9 | - | 21.6 |
| **$Co_{0.05}Mo_{0.95}S_2$** | 0.385 | 113 | 9.91 | 29.7 | 123 |

| | | | | | |
|---|---|---|---|---|---|
| **$Co_{0.1}Mo_{0.9}S_2$** | 0.356 | 98 | 15.3 | - | 101 |
| **E-$MoS_2$**[366] | 0.398 | 175 | 7.1 | - | 25712 |
| **Commercial Pt/C** [366] | 0.045 | 27 | 7.01 | - | 6.682 |

As indicated in Table 8-1, the $V_{0.1}Mo_{0.9}S_2$ catalyst exhibits superior HER performance compared to other synthesized non-noble metal counterparts, achieving an overpotential ($\eta_{10}$) of 285 mV at 10 mA/cm$^2$ current density with a Tafel slope of 70.6 mV/dec. The significantly reduced charge transfer resistance ($R_{ct}$ = 31.6 Ω) further confirms enhanced interfacial charge transfer kinetics. These collective improvements demonstrate that controlled vanadium incorporation effectively enhances the intrinsic catalytic activity while optimizing electrode-electrolyte interface dynamics through optimized electronic structure modulation.

Other doped $MoS_2$ samples also display enhanced HER properties compared to pristine $MoS_2$ ($\eta_{10}$ = 410 mV, Tafel = 119.9 mV/dec, $R_{ct}$ = 556 Ω). For example:

- $V_{0.05}Mo_{0.95}S_2$: $\eta_{10}$ = 318 mV, Tafel = 89.1 mV/dec, $R_{ct}$ = 110 Ω
- $W_{0.2}Mo_{0.8}S_2$: $\eta_{10}$ = 301 mV, Tafel = 78.1 mV/dec, $R_{ct}$ = 21.6 Ω
- $Co_{0.05}Mo_{0.95}S_2$: $\eta_{10}$ = 385 mV, Tafel = 113 mV/dec, $R_{ct}$ = 123 Ω

These results emphasize the influence of dopant species and concentration on HER efficiency, with V and W doping at optimized levels leading to substantial kinetic improvements.

The $MoS_2$-rGO composite (prepared at 200 °C for 12 h) also achieves improved performance ($\eta_{10}$ = 340 mV, Tafel = 98.2 mV/dec), attributed to enhanced conductivity and better charge dispersion from the rGO matrix. However, it does not match the performance of the best V- or W-doped $MoS_2$ samples, indicating that electronic modulation through doping has a more pronounced effect than conductivity enhancement alone.

Electrochemically exfoliated $MoS_2$ nanosheets (E-$MoS_2$), by contrast, show significantly lower HER efficiency with an overpotential of 398 mV at 10 mA/cm$^2$, a Tafel slope of 175 mV/dec, and a $R_{ct}$ of 25,712 Ω. These metrics reveal the inherent limitations of unmodified $MoS_2$ basal planes, where neither exfoliation nor structural refinement compensates for the lack of active sites or optimized electronic configuration required for efficient hydrogen evolution.

## Conclusion and future work

The commercial Pt/C catalyst remains the benchmark HER material, with a minimal overpotential of 45 mV, a Tafel slope of 27 mV/dec, and $R_{ct}$ of only 6.682 Ω. Nevertheless, the $V_{0.1}Mo_{0.9}S_2$ and $W_{0.2}Mo_{0.8}S_2$ catalysts significantly narrow the activity gap with Pt/C, demonstrating the potential of doped $MoS_2$-based materials as highly promising, earth-abundant alternatives for hydrogen production.

## 8.2 Future work

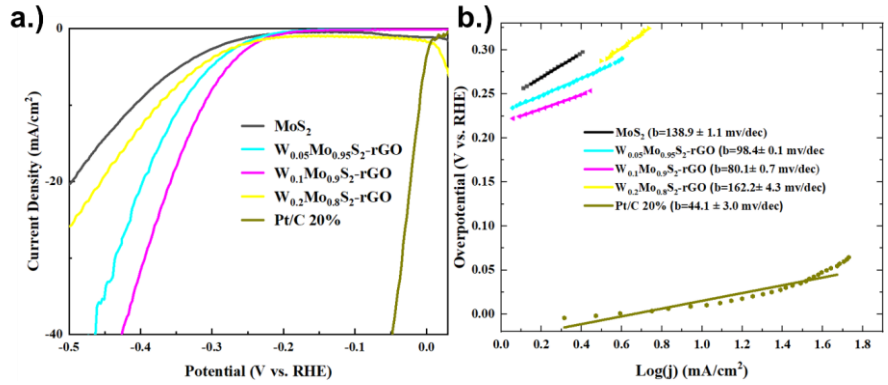


***Fig 8- 1. HER performance of the prepared $MoS_2$ and W-doped $MoS_2$-rGO catalysts. (a) LSV curves of catalysts. (b) Tafel plots of polarization curves of all samples studied.***

The overpotential ($\eta_{10}$) required to reach a current density of 10 mA/cm$^2$ is derived from polarization curves (Fig. 8-1 a). It is observed that $W_{0.1}Mo_{0.9}S_2$-rGO exhibits the most favorable $\eta_{10}$ of 0.312 mV and a Tafel slope of 80.1 mV/dec (Fig. 8-1b), significantly lower than that of $MoS_2$, which records 0.41 V and 138.9 mV/dec. This finding suggests an exceptional electrocatalytic performance and expedited HER kinetics for 10% W-doped $MoS_2$-rGO. The Tafel analysis indicates that the HER mechanism for 10% W-doped $MoS_2$-rGO follows the Volmer-Heyrovsky pathway, with the Heyrovsky step serving as the rate-determining step for the overall electrocatalytic process. However, it raises the question of why the 20% W dopant demonstrates inferior HER performance. Does the W-doped $MoS_2$/rGO heterostructure continue to exhibit enhancements in conductivity? What is the oxidation state of the W ion

present in the W-doped $MoS_2$-rGO? Does the presence of W still induce sulfur site vacancies? These inquiries necessitate further investigation.

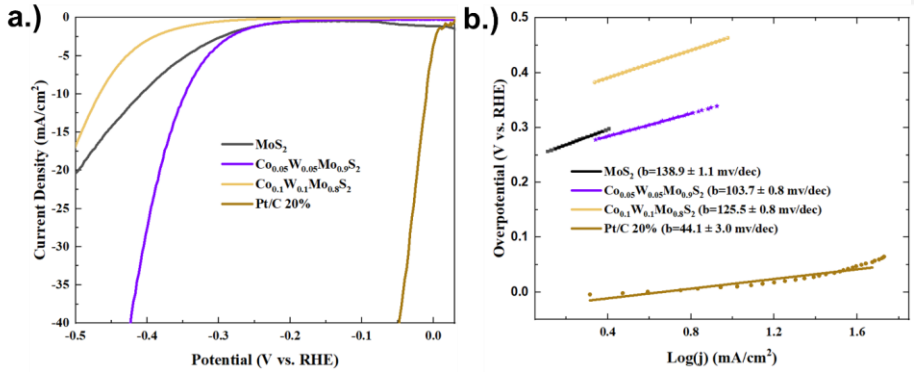


***Fig 8- 2. HER performance of the prepared $MoS_2$ and W and Co co-doped $MoS_2$ catalysts. (a) LSV curves of catalysts. (b) Tafel plots of polarization curves of all samples studied.***

Figure 8-2 illustrates the endeavors related to co-doped $MoS_2$. It has been noted that $W_{0.05}Co_{0.05}Mo_{0.9}S_2$ demonstrates the most advantageous η10 of 0.346 mV along with a Tafel slope of 103.7 mV/dec (refer to Fig. 8-1b). However, this outcome is only comparable to the singular 5% W-doped $MoS_2$. According to prior investigations, the doping of W and Co ions is expected to yield a synergistic effect where 1+1>2, as W creates sulfur vacancies while Co modifies the band-gap of $MoS_2$. Nonetheless, what accounts for the diminished efficacy of this composite? Could it potentially induce an unforeseen phase within the crystal structure? To elucidate this query, further investigations are imperative in this domain.

In forthcoming research endeavors, the investigation will concentrate on the influence of dopants on rGO/$MoS_2$ heterostructures. Concurrently, the incorporation of co-dopants and potentially triple-dopants will be considered to achieve enhanced efficiency in hydrogen evolution processes.

# References


1. Shaheen, S., Sadiq, I., Ali, S. A., & Ahmad, T. (2024). TMDs as Photocatalysts for Green Hydrogen Production. In *Towards Sustainable and Green Hydrogen Production by Photocatalysis: Insights into Design and Development of Efficient Materials (Volume 2)* (pp. 107-144). American Chemical Society.
2. Hannan, A., Khalil, A., Arshad, N., Tahir, M. B., Wattoo, A. G., & Shahzad, M. K. (2022). Transition Metal Dichalcogenides for Photo/Electrochemical Energy-Based Applications. *Energy Technology*, *10*(11), 2200546.
3. Yang, T., Wang, Z., Yuan, J., Zhou, J., & Yang, M. (2024). Emerging Electronic Properties of Polymorphic 2D-TMDs. *Two-Dimensional Transition-Metal Dichalcogenides: Phase Engineering and Applications in Electronics and Optoelectronics*, 127-179.
4. Kis, A. (2012). Graphene is not alone. *Nat. Nanotechnol*, *7*, 683.
5. Gao, Y. (2024). The Impacts of Combustion Reaction on the Environment. *Highlights in Science, Engineering and Technology*, *83*, 51-55.
6. Burning of Fossil Fuels. Understanding Global Change,. ugc.berkeley.edu/backgroundcontent/burning-of-fossil-fuels/. Accessed online on 16-5-2022.
7. Metz, B., Davidson, O., De Coninck, H. C., Loos, M., & Meyer, L. (2005). *IPCC special report on carbon dioxide capture and storage*. Cambridge: Cambridge University Press.
8. Vohra, K., Vodonos, A., Schwartz, J., Marais, E. A., Sulprizio, M. P., & Mickley, L. J. (2021). Global mortality from outdoor fine particle pollution generated by fossil fuel combustion: Results from GEOS-Chem. *Environmental research*, *195*, 110754.

## References


9. 69% average decline in wildlife populations since 1970, says new WWF report. https://www.worldwildlife.org/press-releases/69-average-decline-in-wildlife-populations-since-1970-says-new-wwf-report. Accessed online on 16-5-2022.
10. Salmani, F., Kesaeian, A., Saberi, N., Fereidooni, L., & Kim, H. D. (2024). Utilization of Hydrogen Energy for Power and Heat Generation. *Encyclopedia of Renewable Energy, Sustainability and the Environment*, 4, 195-208.
11. Cao, Y. (2024). Various Well-Designed Hydrogen Fuel Cells: Structure, Principle, and Advantages. *Highlights in Science, Engineering and Technology*, *88*, 860-864.
12. Hosseini, S. E. (2023). *Fundamentals of Hydrogen Production and Utilization in Fuel Cell Systems*. Elsevier, 283–329.
13. Goswami, D. Y., & Kreith, F. (Eds.). (2015). *Energy efficiency and renewable energy handbook*. CRC press.
14. Beschkov, V., & Ganev, E. (2023). Perspectives on the Development of Technologies for Hydrogen as a Carrier of Sustainable Energy. *Energies*, *16*(17), 6108.
15. Gómez, S. Y., & Hotza, D. (2016). Current developments in reversible solid oxide fuel cells. *Renewable and Sustainable Energy Reviews*, *61*, 155-174.
16. Sadeghi, S., & Ghandehariun, S. (2023). Environmental impacts of a standalone solar water splitting system for sustainable hydrogen production: a life cycle assessment. *International Journal of Hydrogen Energy*, *48*(50), 19326-19339.
17. Rao, K. K., Lai, Y., Zhou, L., Haber, J. A., Bajdich, M., & Gregoire, J. M. (2022). Overcoming hurdles in oxygen evolution catalyst discovery via codesign. *Chemistry of Materials*, *34*(3), 899-910.
18. Spöri, C., Kwan, J. T. H., Bonakdarpour, A., Wilkinson, D. P., & Strasser, P. (2017). The stability challenges of oxygen evolving catalysts: towards a common fundamental understanding and mitigation of catalyst degradation. *Angewandte Chemie International Edition*, *56*(22), 5994-6021.

## References


19. Zhu, J., Hu, L., Zhao, P., Lee, L. Y. S., & Wong, K. Y. (2019). Recent advances in electrocatalytic hydrogen evolution using nanoparticles. *Chemical reviews*, *120*(2), 851-918.
20. Conway, B. E., & Tilak, B. V. (2002). Interfacial processes involving electrocatalytic evolution and oxidation of $H_2$, and the role of chemisorbed H. *Electrochimica acta*, *47*(22-23), 3571-3594.
21. Zhang, S., Zhang, X., Rui, Y., Wang, R., & Li, X. (2021). Recent advances in non-precious metal electrocatalysts for pH-universal hydrogen evolution reaction. *Green Energy & Environment*, *6*(4), 458-478.
22. Eliaz, N., & Gileadi, E. (2019). *Physical electrochemistry: fundamentals, techniques, and applications*. John Wiley & Sons.
23. Karuppasamy, K., Nichelson, A., Vikraman, D., Choi, J. H., Hussain, S., et al. (2022). Recent Advancements in Two-Dimensional Layered Molybdenum and Tungsten Carbide-Based Materials for Efficient Hydrogen Evolution Reactions. *Nanomaterials*, *12*(21), 3884.
24. Gao, Q., Zhang, W., Shi, Z., Yang, L., & Tang, Y. (2019). Structural design and electronic modulation of transition-metal-carbide electrocatalysts toward efficient hydrogen evolution. *Advanced Materials*, *31*(2), 1802880.
25. Sahoo, P. K., Bisoi, S. R., Huang, Y. J., Tsai, D. S., & Lee, C. P. (2021). 2D-layered non-precious electrocatalysts for hydrogen evolution reaction: fundamentals to applications. *Catalysts*, *11*(6), 689.
26. Chen, Z., Qing, H., Zhou, K., Sun, D., & Wu, R. (2020). Metal-organic framework-derived nanocomposites for electrocatalytic hydrogen evolution reaction. *Progress in Materials Science*, *108*, 100618.
27. Ali, A., & Shen, P. K. (2020). Nonprecious metal's graphene-supported electrocatalysts for hydrogen evolution reaction: fundamentals to applications. *Carbon Energy*, *2*(1), 99-121.

## References


28. Anantharaj, S., Ede, S. R., Karthick, K., Sankar, S. S., Sangeetha, K., et al. (2018). Precision and correctness in the evaluation of electrocatalytic water splitting: revisiting activity parameters with a critical assessment. *Energy & Environmental Science*, *11*(4), 744-771.
29. Boudart, M. (1995). Turnover rates in heterogeneous catalysis. *Chemical reviews*, *95*(3), 661-666.
30. Trasatti, S., & Petrii, O. A. (1992). Real surface area measurements in electrochemistry. *Journal of electroanalytical chemistry*, *327*(1-2), 353-376.
31. Jin, H., Guo, C., Liu, X., Liu, J., Vasileff, A., et al. (2018). Emerging two-dimensional nanomaterials for electrocatalysis. *Chemical reviews*, *118*(13), 6337-6408.
32. Nørskov, J. K., Bligaard, T., Logadottir, A., Kitchin, J. R., Chen, J. G., Pandelov, S., & Stimming, U. (2005). Trends in the exchange current for hydrogen evolution. *Journal of The Electrochemical Society*, *152*(3), J23.
33. Trasatti, S. (1972). Work function, electronegativity, and electrochemical behaviour of metals: III. Electrolytic hydrogen evolution in acid solutions. *Journal of Electroanalytical Chemistry and Interfacial Electrochemistry*, *39*(1), 163-184.
34. Parsons, R. (1958). The rate of electrolytic hydrogen evolution and the heat of adsorption of hydrogen. *Transactions of the Faraday Society*, *54*, 1053-1063.
35. Ezzati, R. (2023). Rethinking the Use of Linear Forms of the Langmuir Isotherm in Adsorption Modeling to Calculate Langmuir Isotherm Parameters. *Preprints*.
36. Connor, P., Schuch, J., Kaiser, B., & Jaegermann, W. (2020). The determination of electrochemical active surface area and specific capacity revisited for the system MnOx as an oxygen evolution catalyst. *Zeitschrift für Physikalische Chemie*, *234*(5), 979-994.
37. Sahoo, P. K., Bisoi, S. R., Huang, Y. J., Tsai, D. S., & Lee, C. P. (2021). 2D-layered non-precious electrocatalysts for hydrogen evolution reaction: fundamentals to applications. *Catalysts*, *11*(6), 689.

## References


38. McCrory, C. C., Jung, S., Ferrer, I. M., Chatman, S. M., Peters, J. C., et al. (2015). Benchmarking hydrogen evolving reaction and oxygen evolving reaction electrocatalysts for solar water splitting devices. *Journal of the American Chemical Society*, *137*(13), 4347-4357.
39. Shao, R. Y., Chen, L. W., Yan, Q. Q., Zeng, W. J., Yin, P., et al. (2021). Is Pt/C more electrocatalytic than Ru/C for hydrogen evolution in alkaline electrolytes?. *ACS Applied Energy Materials*, *4*(5), 4284-4289.
40. Danilovic, N., Subbaraman, R., Strmcnik, D., Stamenkovic, V., & Markovic, N. (2013). Electrocatalysis of the HER in acid and alkaline media. *Journal of the Serbian Chemical Society*, 78(12), 2007-2015.
41. Sheng, W., Zhuang, Z., Gao, M., Zheng, J., Chen, J. G., & Yan, Y. (2015). Correlating hydrogen oxidation and evolution activity on platinum at different pH with measured hydrogen binding energy. *Nature communications*, *6*(1), 1-6.
42. Tian, X., Zhao, P., & Sheng, W. (2019). Hydrogen evolution and oxidation: mechanistic studies and material advances. *Advanced Materials*, *31*(31), 1808066.
43. Zheng, Y., Jiao, Y., Jaroniec, M., & Qiao, S. Z. (2015). Advancing the electrochemistry of the hydrogen-evolution reaction through combining experiment and theory. *Angewandte Chemie International Edition*, *54*(1), 52-65.
44. McKone, J. R., Sadtler, B. F., Werlang, C. A., Lewis, N. S., & Gray, H. B. (2013). Ni–Mo nanopowders for efficient electrochemical hydrogen evolution. *ACS catalysis*, *3*(2), 166-169.
45. Faber, M. S., & Jin, S. (2014). Earth-abundant inorganic electrocatalysts and their nanostructures for energy conversion applications. *Energy & Environmental Science*, *7*(11), 3519-3542.
46. Vesborg, P. C., Seger, B., & Chorkendorff, I. B. (2015). Recent development in hydrogen evolution reaction catalysts and their practical implementation. *The journal of physical chemistry letters*, *6*(6), 951-957.

## References


47. Greeley, J., Jaramillo, T. F., Bonde, J., Chorkendorff, I. B., & Nørskov, J. K. (2006). Computational high-throughput screening of electrocatalytic materials for hydrogen evolution. *Nature materials*, *5*(11), 909-913.
48. Tan, T. L., Wang, L. L., Zhang, J., Johnson, D. D., & Bai, K. (2015). Platinum nanoparticle during electrochemical hydrogen evolution: adsorbate distribution, active reaction species, and size effect. *ACS Catalysis*, *5*(4), 2376-2383.
49. Hsu, I. J., Kimmel, Y. C., Jiang, X., Willis, B. G., & Chen, J. G. (2012). Atomic layer deposition synthesis of platinum–tungsten carbide core–shell catalysts for the hydrogen evolution reaction. *Chemical Communications*, *48*(7), 1063-1065.
50. Yin, H., Zhao, S., Zhao, K., Muqsit, A., Tang, H., et al. (2015). Ultrathin platinum nanowires grown on single-layered nickel hydroxide with high hydrogen evolution activity. *Nature communications*, *6*(1), 6430.
51. Baker, L., Cavanagh, A. S., Yin, J., George, S. M., Kongkanand, A., et al. (2012). Growth of continuous and ultrathin platinum films on tungsten adhesion layers using atomic layer deposition techniques. *Applied Physics Letters*, *101*(11).
52. Zhu, E., Yan, X., Wang, S., Xu, M., Wang, C., et al. (2019). Peptide-assisted 2-D assembly toward free-floating ultrathin platinum nanoplates as effective electrocatalysts. *Nano letters*, *19*(6), 3730-3736.
53. Oh, A., Sa, Y. J., Hwang, H., Baik, H., Kim, J., et al. (2016). Rational design of Pt–Ni–Co ternary alloy nanoframe crystals as highly efficient catalysts toward the alkaline hydrogen evolution reaction. *Nanoscale*, *8*(36), 16379-16386.
54. Chen, C., Kang, Y., Huo, Z., Zhu, Z., Huang, W., et al. (2014). Highly crystalline multimetallic nanoframes with three-dimensional electrocatalytic surfaces. *Science*, *343*(6177), 1339-1343.
55. Jang, H. J., Hong, S., & Park, S. (2012). Shape-controlled synthesis of Pt nanoframes. *Journal of Materials Chemistry*, *22*(37), 19792-19797.

## References


56. He, D., Zhang, L., He, D., Zhou, G., Lin, Y., et al. (2016). Amorphous nickel boride membrane on a platinum–nickel alloy surface for enhanced oxygen reduction reaction. *Nature communications*, *7*(1), 12362.
57. Wang, S., Yang, G., & Yang, S. (2015). Pt-frame@ Ni quasi core–shell concave octahedral $PtNi_3$ bimetallic nanocrystals for electrocatalytic methanol oxidation and hydrogen evolution. *The Journal of Physical Chemistry C*, *119*(50), 27938-27945.
58. Cao, Z., Li, H., Zhan, C., Zhang, J., Wang, W., et al. (2018). Monocrystalline platinum–nickel branched nanocages with enhanced catalytic performance towards the hydrogen evolution reaction. *Nanoscale*, *10*(11), 5072-5077.
59. Jana, R., Bhim, A., Bothra, P., Pati, S. K., & Peter, S. C. (2016). Electrochemical dealloying of $PdCu_3$ nanoparticles to achieve pt-like activity for the hydrogen evolution reaction. *ChemSusChem*, *9*(20), 2922-2927.
60. Zou, X., & Zhang, Y. (2015). Noble metal-free hydrogen evolution catalysts for water splitting. *Chemical Society Reviews*, *44*(15), 5148-5180.
61. Voiry, D., Yang, J., & Chhowalla, M. (2016). Recent strategies for improving the catalytic activity of 2D TMD nanosheets toward the hydrogen evolution reaction. *Advanced materials*, 28(29), 6197-6206.
62. Ding, Q., Song, B., Xu, P., & Jin, S. (2016). Efficient electrocatalytic and photoelectrochemical hydrogen generation using $MoS_2$ and related compounds. *Chem*, *1*(5), 699-726.
63. Zhu, C. R., Gao, D., Ding, J., Chao, D., & Wang, J. (2018). TMD-based highly efficient electrocatalysts developed by combined computational and experimental approaches. *Chemical Society Reviews*, *47*(12), 4332-4356.
64. Mulla, R., & Dunnill, C. W. (2019). Powering the hydrogen economy from waste heat: A review of heat-to-hydrogen concepts. *ChemSusChem*, *12*(17), 3882-3895.
65. Voiry, D., Yamaguchi, H., Li, J., Silva, R., Alves, D. C., et al. (2013). Enhanced catalytic activity in strained chemically exfoliated $WS_2$ nanosheets for hydrogen evolution. *Nature materials*, *12*(9), 850-855.

## References


66. Chhowalla, M., Shin, H. S., Eda, G., Li, L. J., Loh, K. P., et al. (2013). The chemistry of two-dimensional layered transition metal dichalcogenide nanosheets. *Nature chemistry*, *5*(4), 263-275.
67. Yang, J., & Shin, H. S. (2014). Recent advances in layered transition metal dichalcogenides for hydrogen evolution reaction. *Journal of Materials Chemistry A*, *2*(17), 5979-5985.
68. Voiry, D., Mohite, A., & Chhowalla, M. (2015). Phase engineering of transition metal dichalcogenides. *Chemical Society Reviews*, *44*(9), 2702-2712.
69. Wilson, J. A., & Yoffe, A. D. (1969). The transition metal dichalcogenides discussion and interpretation of the observed optical, electrical and structural properties. *Advances in Physics*, *18*(73), 193-335.
70. Hinnemann, B., Moses, P. G., Bonde, J., Jørgensen, K. P., Nielsen, J. H., et al. (2005). Biomimetic hydrogen evolution: $MoS_2$ nanoparticles as catalyst for hydrogen evolution. *Journal of the American Chemical Society*, *127*(15), 5308-5309.
71. Skúlason, E., Karlberg, G. S., Rossmeisl, J., Bligaard, T., Greeley, J., et al. (2007). Density functional theory calculations for the hydrogen evolution reaction in an electrochemical double layer on the Pt (111) electrode. *Physical Chemistry Chemical Physics*, *9*(25), 3241-3250.
72. Kibsgaard, J., Chen, Z., Reinecke, B. N., & Jaramillo, T. F. (2012). Engineering the surface structure of $MoS_2$ to preferentially expose active edge sites for electrocatalysis. *Nature materials*, *11*(11), 963-969.
73. Hu, J., Huang, B., Zhang, C., Wang, Z., An, Y., et al. (2017). Engineering stepped edge surface structures of $MoS_2$ sheet stacks to accelerate the hydrogen evolution reaction. *Energy & Environmental Science*, *10*(2), 593-603.
74. Tan, Y., Liu, P., Chen, L., Cong, W., Ito, Y., et al. (2014). Monolayer $MoS_2$ films supported by 3D nanoporous metals for high-efficiency electrocatalytic hydrogen production. *Advanced Materials (Deerfield Beach, Fla.)*, *26*(47), 8023-8028.

# References


75. Deng, J., Li, H., Xiao, J., Tu, Y., Deng, D., et al. (2015). Triggering the electrocatalytic hydrogen evolution activity of the inert two-dimensional $MoS_2$ surface via single-atom metal doping. *Energy & environmental science*, *8*(5), 1594-1601.
76. Li, H., Tsai, C., Koh, A. L., Cai, L., Contryman, A. W., et al. (2016). Activating and optimizing $MoS_2$ basal planes for hydrogen evolution through the formation of strained sulphur vacancies. *Nature materials*, *15*(1), 48-53.
77. Guo, Y., Zhang, X., Zhang, X., & You, T. (2015). Defect-and S-rich ultrathin $MoS_2$ nanosheet embedded N-doped carbon nanofibers for efficient hydrogen evolution. *Journal of Materials Chemistry A*, *3*(31), 15927-15934.
78. Xu, Y., Wang, L., Liu, X., Zhang, S., Liu, C., et al. (2016). Monolayer $MoS_2$ with S vacancies from interlayer spacing expanded counterparts for highly efficient electrochemical hydrogen production. *Journal of Materials Chemistry A*, *4*(42), 16524-16530.
79. Zhang, J., Wang, Y., Cui, J., Wu, J., Li, Y., et al. (2019). Water-soluble defect-rich $MoS_2$ ultrathin nanosheets for enhanced hydrogen evolution. *The Journal of Physical Chemistry Letters*, *10*(12), 3282-3289.
80. Bonde, J., Moses, P. G., Jaramillo, T. F., Nørskov, J. K., & Chorkendorff, I. (2009). Hydrogen evolution on nano-particulate transition metal sulfides. *Faraday discussions*, *140*, 219-231.
81. Chen, Z., Leng, K., Zhao, X., Malkhandi, S., Tang, W., et al. (2017). Interface confined hydrogen evolution reaction in zero valent metal nanoparticles-intercalated molybdenum disulfide. *Nature communications*, *8*(1), 14548.
82. Qi, K., Yu, S., Wang, Q., Zhang, W., Fan, J., Zheng, W., et al. (2016). Decoration of the inert basal plane of defect-rich $MoS_2$ with Pd atoms for achieving Pt-similar HER activity. *Journal of Materials Chemistry A*, *4*(11), 4025-4031.

## References


83. Li, B. B., Qiao, S. Z., Zheng, X. R., Yang, X. J., Cui, Z. D., et al. (2015). Pd coated $MoS_2$ nanoflowers for highly efficient hydrogen evolution reaction under irradiation. *Journal of Power Sources*, *284*, 68-76.
84. Sun, X., Dai, J., Guo, Y., Wu, C., Hu, F., et al. (2014). Semimetallic molybdenum disulfide ultrathin nanosheets as an efficient electrocatalyst for hydrogen evolution. *Nanoscale*, *6*(14), 8359-8367.
85. Li, H., Chen, S., Jia, X., Xu, B., Lin, H., et al. (2017). Amorphous nickel-cobalt complexes hybridized with 1T-phase molybdenum disulfide via hydrazine-induced phase transformation for water splitting. *Nature Communications*, *8*(1), 15377.
86. Shi, Y., Zhou, Y., Yang, D. R., Xu, W. X., Wang, C., et al. (2017). Energy level engineering of $MoS_2$ by transition-metal doping for accelerating hydrogen evolution reaction. *Journal of the American Chemical Society*, *139*(43), 15479-15485.
87. Zhang, J., Wang, T., Liu, P., Liu, S., Dong, R., et al. (2016). Engineering water dissociation sites in $MoS_2$ nanosheets for accelerated electrocatalytic hydrogen production. *Energy & Environmental Science*, *9*(9), 2789-2793.
88. Wang, H., Tsai, C., Kong, D., Chan, K., Abild-Pedersen, F., et al. (2015). Transition-metal doped edge sites in vertically aligned $MoS_2$ catalysts for enhanced hydrogen evolution. *Nano Research*, *8*, 566-575.
89. Zhang, K., Kim, H. J., Lee, J. T., Chang, G. W., Shi, X., et al. (2014). Unconventional pore and defect generation in molybdenum disulfide: application in high-rate lithium-ion batteries and the hydrogen evolution reaction. *ChemSusChem*, *7*(9), 2489-2495.
90. Wang, H., Lu, Z., Xu, S., Kong, D., Cha, J. J., et al. (2013). Electrochemical tuning of vertically aligned $MoS_2$ nanofilms and its application in improving hydrogen evolution reaction. *Proceedings of the National Academy of Sciences*, *110*(49), 19701-19706.
91. Xie, J., Zhang, J., Li, S., Grote, F., Zhang, X., et al. (2013). Controllable disorder engineering in oxygen-incorporated $MoS_2$ ultrathin nanosheets for efficient

hydrogen evolution. *Journal of the American Chemical Society*, 135(47), 17881-17888.

92. Zhou, J., Fang, G., Pan, A., & Liang, S. (2016). Oxygen-incorporated $MoS_2$ nanosheets with expanded interlayers for hydrogen evolution reaction and pseudocapacitor applications. *ACS Applied Materials & Interfaces*, *8*(49), 33681-33689.
93. Xiao, W., Liu, P., Zhang, J., Song, W., Feng, Y. P., et al. (2017). Dual-functional N dopants in edges and basal plane of $MoS_2$ nanosheets toward efficient and durable hydrogen evolution. *Advanced Energy Materials*, *7*(7), 1602086.
94. Ye, R., Vicente, P. D. A., Liu, Y., Arellano-Jimenez, J., Peng, Z., et al. (2015). High-performance hydrogen evolution from $MoS_{2(1-x)}P_x$ solid solution. *Advanced Materials (Deerfield Beach, Fla.)*, *28*(7), 1427.
95. Gao, G., Jiao, Y., Ma, F., Jiao, Y., Waclawik, E., et al. (2015). Charge mediated semiconducting-to-metallic phase transition in molybdenum disulfide monolayer and hydrogen evolution reaction in new 1T′ phase. *The Journal of Physical Chemistry C*, *119*(23), 13124-13128.
96. Lukowski, M. A., Daniel, A. S., Meng, F., Forticaux, A., Li, L., et al. (2013). Enhanced hydrogen evolution catalysis from chemically exfoliated metallic $MoS_2$ nanosheets. *Journal of the American Chemical Society*, *135*(28), 10274-10277.
97. Tang, Q., & Jiang, D. E. (2016). Mechanism of hydrogen evolution reaction on 1T-$MoS_2$ from first principles. *Acs Catalysis*, *6*(8), 4953-4961.
98. Ha, E., Liu, W., Wang, L., Man, H. W., Hu, L., et al. (2017). $Cu_2ZnSnS_4/MoS_2$-reduced graphene oxide heterostructure: nanoscale interfacial contact and enhanced photocatalytic hydrogen generation. *Scientific reports*, *7*(1), 39411.
99. Chen, W., Santos, E. J., Zhu, W., Kaxiras, E., & Zhang, Z. (2013). Tuning the electronic and chemical properties of monolayer $MoS_2$ adsorbed on transition metal substrates. *Nano letters*, *13*(2), 509-514.

## References


100. Tsai, C., Abild-Pedersen, F., & Nørskov, J. K. (2014). Tuning the $MoS_2$ edge-site activity for hydrogen evolution via support interactions. *Nano letters*, *14*(3), 1381-1387.

101. Lee, H. J., Lee, S. W., Hwang, H., Yoon, S. I., Lee, Z., et al. (2021). Vertically oriented $MoS_2/WS_2$ heterostructures on reduced graphene oxide sheets as electrocatalysts for hydrogen evolution reaction. *Materials Chemistry Frontiers*, *5*(8), 3396-3403.

102. Sharma, M. D., Mahala, C., & Basu, M. (2020). 2D thin sheet heterostructures of $MoS_2$ on $MoSe_2$ as efficient electrocatalyst for hydrogen evolution reaction in wide pH range. *Inorganic Chemistry*, *59*(7), 4377-4388.

103. Najafi, L., Bellani, S., Oropesa-Nuñez, R., Ansaldo, A., Prato, M., et al. (2018). Engineered $MoSe_2$-based heterostructures for efficient electrochemical hydrogen evolution reaction. *Advanced Energy Materials*, *8*(16), 1703212.

104. Yin, Y., Zhang, Y., Gao, T., Yao, T., Zhang, X., et al. (2017). Synergistic phase and disorder engineering in 1T-$MoSe_2$ nanosheets for enhanced hydrogen-evolution reaction. *Advanced Materials*, *29*(28), 1700311.

105. Faber, M. S., Lukowski, M. A., Ding, Q., Kaiser, N. S., & Jin, S. (2014). Earth-abundant metal pyrites ($FeS_2$, $CoS_2$, $NiS_2$, and their alloys) for highly efficient hydrogen evolution and polysulfide reduction electrocatalysis. *The Journal of Physical Chemistry C*, *118*(37), 21347-21356.

106. Kong, D., Cha, J. J., Wang, H., Lee, H. R., & Cui, Y. (2013). First-row transition metal dichalcogenide catalysts for hydrogen evolution reaction. *Energy & Environmental Science*, *6*(12), 3553-3558.

107. Wan, Y., Zhang, Z., Xu, X., Zhang, Z., Li, P., et al. (2018). Engineering active edge sites of fractal-shaped single-layer $MoS_2$ catalysts for high-efficiency hydrogen evolution. *Nano Energy*, *51*, 786-792.

108. Yin, Y., Han, J., Zhang, Y., Zhang, X., Xu, P., et al. (2016). Contributions of phase, sulfur vacancies, and edges to the hydrogen evolution reaction catalytic activity of

porous molybdenum disulfide nanosheets. *Journal of the American Chemical Society*, *138*(25), 7965-7972.

109. Liu, P., Zhu, J., Zhang, J., Xi, P., Tao, K., et al. (2017). P dopants triggered new basal plane active sites and enlarged interlayer spacing in $MoS_2$ nanosheets toward electrocatalytic hydrogen evolution. *ACS Energy Letters*, *2*(4), 745-752.

110. Tan, C., Luo, Z., Chaturvedi, A., Cai, Y., Du, Y., et al. (2018). Preparation of high-percentage 1T-phase transition metal dichalcogenide nanodots for electrochemical hydrogen evolution. *Advanced Materials*, *30*(9), 1705509.

111. Xu, Q., Liu, Y., Jiang, H., Hu, Y., Liu, H., et al. (2019). Unsaturated sulfur edge engineering of strongly coupled $MoS_2$ nanosheet–carbon macroporous hybrid catalyst for enhanced hydrogen generation. *Advanced Energy Materials*, *9*(2), 1802553.

112. Yang, Y., Zhang, K., Lin, H., Li, X., Chan, H. C., et al. (2017). $MoS_2$–$Ni_3S_2$ heteronanorods as efficient and stable bifunctional electrocatalysts for overall water splitting. *Acs Catalysis*, *7*(4), 2357-2366.

113. Anjum, M. A. R., Jeong, H. Y., Lee, M. H., Shin, H. S., & Lee, J. S. (2018). Efficient hydrogen evolution reaction catalysis in alkaline media by all-in-one $MoS_2$ with multifunctional active sites. *Advanced Materials*, *30*(20), 1707105.

114. Li, H., Tsai, C., Koh, A. L., Cai, L., Contryman, A. W., et al. (2016). Activating and optimizing $MoS_2$ basal planes for hydrogen evolution through the formation of strained sulphur vacancies. *Nature materials*, *15*(1), 48-53.

115. Najafi, L., Bellani, S., Oropesa-Nuñez, R., Ansaldo, A., Prato, M., et al. (2018). Engineered $MoSe_2$-based heterostructures for efficient electrochemical hydrogen evolution reaction. *Advanced Energy Materials*, *8*(16), 1703212.

116. Gao, D., Xia, B., Zhu, C., Du, Y., Xi, P., et al. (2018). Activation of the $MoSe_2$ basal plane and Se-edge by B doping for enhanced hydrogen evolution. *Journal of Materials Chemistry A*, *6*(2), 510-515.

## References


117. Liu, W., Hu, E., Jiang, H., Xiang, Y., Weng, Z., et al. (2016). A highly active and stable hydrogen evolution catalyst based on pyrite-structured cobalt phosphosulfide. *Nature communications*, 7(1), 10771.

118. Wang, J. Y., Ouyang, T., Li, N., Ma, T., & Liu, Z. Q. (2018). S, N co-doped carbon nanotube-encapsulated core-shelled $CoS_2$@ Co nanoparticles: efficient and stable bifunctional catalysts for overall water splitting. *Science bulletin*, *63*(17), 1130-1140.

119. Guo, J., Zhang, X., Sun, Y., Tang, L., & Zhang, X. (2017). Self-template synthesis of hierarchical $CoMoS_3$ nanotubes constructed of ultrathin nanosheets for robust water electrolysis. *Journal of Materials Chemistry A*, *5*(22), 11309-11315.

120. Shi, X., Fields, M., Park, J., McEnaney, J. M., Yan, H., et al. (2018). Rapid flame doping of Co to $WS_2$ for efficient hydrogen evolution. *Energy & Environmental Science*, *11*(8), 2270-2277.

121. Lukowski, M. A., Daniel, A. S., English, C. R., Meng, F., Forticaux, A., et al. (2014). Highly active hydrogen evolution catalysis from metallic $WS_2$ nanosheets. *Energy & Environmental Science*, *7*(8), 2608-2613.

122. Wu, Y., Liu, Y., Li, G. D., Zou, X., Lian, X., et al. (2017). Efficient electrocatalysis of overall water splitting by ultrasmall $NixCo_3- xS_4$ coupled $Ni_3S_2$ nanosheet arrays. *Nano Energy*, *35*, 161-170.

123. Miao, J., Xiao, F. X., Yang, H. B., Khoo, S. Y., Chen, J., et al. (2015). Hierarchical Ni-Mo-S nanosheets on carbon fiber cloth: A flexible electrode for efficient hydrogen generation in neutral electrolyte. *Science advances*, *1*(7), e1500259.

124. Chen, Y., Xu, S., Li, Y., Jacob, R. J., Kuang, Y., et al. (2017). $FeS_2$ nanoparticles embedded in reduced graphene oxide toward robust, high-performance electrocatalysts. *Advanced Energy Materials*, *7*(19), 1700482.

125. Zhou, G., Shan, Y., Wang, L., Hu, Y., Guo, J., et al. (2019). Photoinduced semiconductor-metal transition in ultrathin troilite FeS nanosheets to trigger efficient hydrogen evolution. *Nature communications*, *10*(1), 399.

## References


126. Piontek, S., Andronescu, C., Zaichenko, A., Konkena, B., Junge Puring, K., et al. (2018). Influence of the Fe: Ni Ratio and Reaction Temperature on the Efficiency of $(Fe_xNi_{1-x})_9S_8$ Electrocatalysts Applied in the Hydrogen Evolution Reaction. *ACS catalysis*, *8*(2), 987-996.

127. Yu, J., Li, W. J., Zhang, H., Zhou, F., Li, R., et al. (2019). Metallic $FePSe_3$ nanoparticles anchored on N-doped carbon framework for All-pH hydrogen evolution reaction. *Nano Energy*, *57*, 222-229.

128. Li, Y., Wang, H., Xie, L., Liang, Y., Hong, G., et al. (2011). $MoS_2$ nanoparticles grown on graphene: an advanced catalyst for the hydrogen evolution reaction. *Journal of the American Chemical Society*, *133*(19), 7296-7299.

129. Laursen, A. B., Kegnæs, S., Dahl, S., & Chorkendorff, I. (2012). Molybdenum sulfides—efficient and viable materials for electro-and photoelectrocatalytic hydrogen evolution. *Energy & Environmental Science*, *5*(2), 5577-5591.

130. Mishra, S., Gupta, R. K., & Mishra, A. K. (2024). Efficient hydrogen evolution and high energy density solid state supercapacitors using rGO/$MoS_2$ heterostructure electrodes. *Materials Science and Engineering: B*, *300*, 117129.

131. Matsoso, J. B., Antonatos, N., Dekanovský, L., Lontio Fomekong, R., Elliot, J. D., Gianolio, D., et al. (2024). Enhancing Nitrogen Reduction Reaction through Formation of 2D/2D Hybrid Heterostructures of $MoS_2$@rGO. *ACS Applied Materials & Interfaces*, *16*(19), 24514-24524.

132. Yu, Y., Huang, S. Y., Li, Y., Steinmann, S. N., Yang, W., et al. (2014). Layer-dependent electrocatalysis of $MoS_2$ for hydrogen evolution. *Nano letters*, *14*(2), 553-558.

133. Li, H., Yu, K., Li, C., Tang, Z., Guo, B., et al. (2015). Charge-transfer induced high efficient hydrogen evolution of $MoS_2$/graphene cocatalyst. *Scientific reports*, *5*(1), 18730.

134. Tang, H., & Morrison, S. R. (1993). Optimization of the anisotropy of composite $MoS_2$ films. *Thin Solid Films*, *227*(1), 90-94.

## References


135. Ghatak, S., & Ghosh, A. (2013). Observation of trap-assisted space charge limited conductivity in short channel $MoS_2$ transistor. *Applied Physics Letters*, *103*(12).

136. Xing, J., Jiang, H. B., Chen, J. F., Li, Y. H., Wu, L., et al. (2013). Active sites on hydrogen evolution photocatalyst. *Journal of Materials Chemistry A*, *1*(48), 15258-15264.

137. Byrappa, K., & Adschiri, T. (2007). Hydrothermal technology for nanotechnology. *Progress in crystal growth and characterization of materials*, *53*(2), 117-166.

138. Suchanek, W., & Yoshimura, M. (1998). Processing and properties of hydroxyapatite-based biomaterials for use as hard tissue replacement implants. *Journal of materials research*, *13*(1), 94-117.

139. Krauss, W., Pabi, S. K., & Gleiter, H. (1989). On the mechanism of martensite nucleation. *Acta Metallurgica*, *37*(1), 25-30.

140. Kennedy, G. C. (1950). A portion of the system silica-water. *Economic geology*, *45*(7), 629-653.

141. Zhang, X., Suo, H., Zhang, R., Niu, S., qi Zhao, X., et al. (2018). Photocatalytic activity of 3D flower-like $MoS_2$ hemispheres. *Materials Research Bulletin*, 100, 249-253.

142. Cui, Y. R., He, J. S., Li, X. M., Zhao, J. X., Chen, A. L., et al. (2013). Preparation and characterization of $MoS_2$ microsphere by hydrothermal method. *Advanced Materials Research*, *631*, 306-309.

143. Spanos, N., & Lycourghiotis, A. (1994). Molybdenum-oxo species deposited on alumina by adsorption: III. Advances in the mechanism of Mo (VI) deposition. *Journal of Catalysis*, *147*(1), 57-71.

144. Cruywagen, J. J., & Rohwer, E. F. C. H. (1975). Coordination number of molybdenum (VI) in monomeric molybdic acid. *Inorganic Chemistry*, *14*(12), 3136-3137.

## References


145. Huang, H., Liu, N., Wang, X., Luo, Q., Huang, X., et al. (2020). DFT calculation of hydrothermal mechanism on preparation of $MoS_2$. *Journal of Molecular Modeling*, *26*, 1-6.
146. Salimi, M., Shokrgozar, M. A., Hamid, D. H., & Vossoughi, M. (2022). Photothermal properties of two-dimensional molybdenum disulfide ($MoS_2$) with nanoflower and nanosheet morphology. *Materials Research Bulletin*, *152*, 111837.
147. Bielewicz, T., Klein, E., & Klinke, C. (2016). New ways to synthesize lead sulfide nanosheets-substituted alkanes direct the growth of 2D nanostructures. *Nanotechnology*, *27*(35), 355602.
148. Qiao, X., Hu, F., Hou, D., & Li, D. (2016). PEG assisted hydrothermal synthesis of hierarchical $MoS_2$ microspheres with excellent adsorption behavior. *Materials Letters*, *169*, 241-245.
149. Cullity, B. D., & Smoluchowski, R. (1957). Elements of X-Ray Diffraction. *Physics Today, 10*(3), 50.
150. Coppens, P., & Penner-Hahn, J. (2001). Introduction: X-rays in chemistry. *Chemical Reviews*, *101*(6), 1567-1568.
151. Eckert, M. (2012). Disputed discovery: the beginnings of X-ray diffraction in crystals in 1912 and its repercussions. *Foundations of Crystallography*, *68*(1), 30-39.
152. Brooks-Bartlett, J. C., & Garman, E. F. (2015). The nobel science: One hundred years of crystallography. *Interdisciplinary Science Reviews*, *40*(3), 244-264.
153. Authier, A. (2013). *Early days of X-ray crystallography*. OUP Oxford.
154. Garman, E. F. (2014). Developments in x-ray crystallographic structure determination of biological macromolecules. *Science*, 343(6175), 1102-1108.
155. Shi, Y. (2014). A glimpse of structural biology through X-ray crystallography. *Cell*, *159*(5), 995-1014.
156. Parker, M. W. (2003). Protein structure from X-ray diffraction. *Journal of biological physics*, *29*(4), 341-362.

## References


157. Egli, M. (2016). Diffraction techniques in structural biology. *Current protocols in nucleic acid chemistry*, *65*(1), 7-13.

158. Meisburger, S. P., Thomas, W. C., Watkins, M. B., & Ando, N. (2017). X-ray scattering studies of protein structural dynamics. *Chemical reviews*, *117*(12), 7615-7672.

159. Bish, D. L., Blake, D. F., Vaniman, D. T., Chipera, S. J., Morris, R. V., et al. (2013). X-ray diffraction results from Mars Science Laboratory: Mineralogy of Rocknest at Gale crater. *science*, *341*(6153), 1238932.

160. Kahle, M., Kleber, M., & Jahn, R. (2002). Review of XRD-based quantitative analyses of clay minerals in soils: the suitability of mineral intensity factors. *Geoderma*, *109*(3-4), 191-205.

161. Newton, M. A., & van Beek, W. (2010). Combining synchrotron-based X-ray techniques with vibrational spectroscopies for the in situ study of heterogeneous catalysts: a view from a bridge. *Chemical Society Reviews*, *39*(12), 4845-4863.

162. Hargreaves*, J. S. J. (2005). Powder X-ray diffraction and heterogeneous catalysis. *Crystallography reviews*, *11*(1), 21-34.

163. Schloegl, R. (2009). X-Ray Diffraction: A Basic Tool for Characterization of Solid Catalysts in the Working State. *Advances in Catalysis*, *52*, 273-338.

164. Cullity, B.D., & Weymouth, J.W. (1957). Elements of X-ray diffraction.

165. Wachs, I. E., & Bañares, M. A. (Eds.). (2023). Springer handbook of advanced catalyst characterization. *Springer Nature*.

166. Egdell, R. G., & Bruton, E. (2020). Henry Moseley, X-ray spectroscopy and the periodic table. *Philosophical Transactions of the Royal Society A*, *378*(2180), 20190302.

167. Jauncey, G. E. M. (1929). Atomic Structure as Revealed by Crystal Reflection of X-Rays. *Chemical Reviews*, *5*(4), 437-449.

## References


168. Bragg, W. L. (1913). The structure of some crystals as indicated by their diffraction of X-rays. *Proceedings of the Royal Society of London. Series A, Containing papers of a mathematical and physical character*, *89*(610), 248-277.
169. Bragg, W. H., & Bragg, W. L. (1913). The reflection of X-rays by crystals. *Proceedings of the Royal Society of London. Series A, Containing Papers of a Mathematical and Physical Character*, *88*(605), 428-438.
170. Strinati, G. C. (2005). Hartree and Hartree–Fock methods in electronic structure. In F. Bassani, G. L. Liedl, & P. Wyder (Eds.), *Encyclopedia of condensed matter physics*, 311–318.
171. Kittel, C., & McEuen, P. (2018). Introduction to solid state physics. *John Wiley & Sons*.
172. Aroyo, M. I. (Ed.). (2021). International Tables for Crystallography: Crystallographic Symmetry. *John Wiley & Sons*.
173. Wondratschek, H., Müller, U., & Union internationale de cristallographie. (2004). International tables for crystallography (Vol. 1). *Kluwer Academic*.
174. Rietveld, H. M. (1969). A profile refinement method for nuclear and magnetic structures. *Applied Crystallography*, *2*(2), 65-71.
175. Zhou, X., Liu, D., Bu, H., Deng, L., Liu, H., et al. (2018). XRD-based quantitative analysis of clay minerals using reference intensity ratios, mineral intensity factors, Rietveld, and full pattern summation methods: A critical review. *Solid Earth Sciences*, *3*(1), 16-29.
176. Post, J. E., & Bish, D. L. (1989). Rietveld refinement of crystal structures using powder X-ray diffraction data. *Modern powder diffraction*, *20*, 277-308.
177. Bish, D. L., & Post, J. E. (1993). Quantitative mineralogical analysis using the Rietveld full-pattern fitting method. *American Mineralogist*, *78*(9-10), 932-940.
178. Tanaka, M., Fujishita, H., Shiozaki, Y., & Sawaguchi, E. (1980). X-Ray Diffraction Profile Analysis for the Determination of the Crystal Structure of $BaTiO_3$. *Japanese journal of applied physics*, *19*(9), 1757.

## References


179. Sleight, A. W., Chen, H. Y., Ferretti, A., & Cox, D. E. (1979). Crystal growth and structure of $BiVO_4$. *Materials Research Bulletin*, *14*(12), 1571-1581.

180. Kemper, G., Vos, A., & Rietveld, H. M. (1972). The Crystal Structure of Potassium Hydrogeniodate (V), $KIO_3$• $HIO_3$. *Canadian Journal of Chemistry*, *50*(8), 1134-1143.

181. Środoń, J., & McCarty, D. K. (2008). Surface area and layer charge of smectite from CEC and EGME/$H_2O$-retention measurements. *Clays and clay minerals*, *56*(2), 155-174.

182. Viani, A., Gualtieri, A. F., & Artioli, G. (2002). The nature of disorder in montmorillonite by simulation of X-ray powder patterns. *American Mineralogist*, *87*(7), 966-975.

183. Bish, D. L., Reynolds, R. C., & Post, J. E. (1989). Sample preparation for X-ray diffraction. *Modern powder diffraction*, *20*, 73-99.

184. Ban, T., & Okada, K. (1992). Structure refinement of mullite by the Rietveld method and a new method for estimation of chemical composition. *Journal of the American Ceramic Society*, *75*(1), 227-230.

185. Taylor, J. C. (1991). Computer programs for standardless quantitative analysis of minerals using the full powder diffraction profile. *Powder diffraction*, *6*(1), 2-9.

186. Bergmann, J., & Kleeberg, R. (1998). BGMN – A new fundamental parameters based Rietveld program for laboratory X-ray sources; its use in quantitative analysis and structure investigations. *CPD Newsletter, Commission on Powder Diffraction, International Union of Crystallography*.

187. Larson, A. C., & Von Dreele, R. B. (1994). Gsas. *Report lAUR*, 86-748.

188. Fuentes-Montero, L., Torres, E., Montero, M. E., & Fuentes, L. (2007). A simplified rietveld code for quantitative phase analysis: development, test and application to uranium mineral So. *Revista mexicana de física*, *53*, 108-112.

189. Kaminsky, H. A., Etsell, T. H., Ivey, D. G., & Omotoso, O. (2009). Distribution of clay minerals in the process streams produced by the extraction of bitumen from

Athabasca oil sands. *The Canadian Journal of Chemical Engineering*, *87*(1), 85-93.

190. O'Donnell, J. H., Von Dreele, R. B., Chan, M. K., & Toby, B. H. (2018). A scripting interface for GSAS-II. *Applied Crystallography*, *51*(4), 1244-1250.
191. Von Dreele, R. (2019). Protein refinement with GSAS-II. *Powder Diffraction*, *34*(S1), S32-S35.
192. Von Dreele, R. B. (2014). Small-angle scattering data analysis in GSAS-II. *Applied Crystallography*, *47*(5), 1784-1789.
193. Stevie, F. A., & Donley, C. L. (2020). Introduction to x-ray photoelectron spectroscopy. *Journal of Vacuum Science & Technology A*, *38*(6).
194. Siegbahn, K. (1981, December 8). *Electron spectroscopy for atoms, molecules and condensed matter* [Nobel lecture]. Institute of Physics, University of Uppsala, Sweden.
195. Siegbahn, K. (1982). Electron spectroscopy for atoms, molecules, and condensed matter. *Reviews of Modern Physics*, *54*(3), 709.
196. Nordling, C., Sokolowski, E., & Siegbahn, K. (1957). Precision method for obtaining absolute values of atomic binding energies. *Physical Review*, *105*(5), 1676.
197. Steinhardt, R., & Serfass, E. (1951). X-ray photoelectron spectrometer for chemical analysis. *Analytical Chemistry*, *23*(11), 1585-1590.
198. Ratner, B. D., & Castner, D. G. (2009). Electron spectroscopy for chemical analysis. *Surface analysis–the principal techniques*, *51*.
199. Werner, W. S., & Powell, C. J. (2021). Applications of the National Institute of Standards and Technology (NIST) database for the simulation of electron spectra for surface analysis for quantitative x-ray photoelectron spectroscopy of nanostructures. *Journal of Vacuum Science & Technology A*, *39*(6).
200. Tran, D. T., Prabhakaran, S., Kim, D. H., Hameed, N., Wang, H., et al. (2021). Ruthenium single atoms implanted continuous $MoS_2$-$Mo_2C$ heterostructure for high-performance and stable water splitting. *Nano Energy*, *88*, 106277.

## References


201. Ji, X., Yao, T., Liu, X., Ma, D., Han, X., & Wang, H. (2024). Atomic layer deposition of aluminum-doped zinc oxide onto $MoO_3$ nanorods toward enhanced lithium storage performance. *Scripta Materialia*, *238*, 115769.
202. Dai, J., Qi, X., Xia, L., Xue, Q., Luo, L., et al. (2023). Aqueous ammonium-ion supercapacitors with unprecedented energy density and stability enabled by oxygen vacancy-enriched $MoO_3$@C. *Advanced Functional Materials*, *33*(10), 2212440.
203. Zhang, Y., Chen, P., Wang, Q., Wang, Q., Zhu, K., et al. (2021). High-capacity and kinetically accelerated lithium storage in $MoO_3$ enabled by oxygen vacancies and heterostructure. *Advanced Energy Materials*, *11*(31), 2101712.
204. Luo, M., Liu, S., Zhu, W., Ye, G., Wang, J., et al. (2022). An electrodeposited $MoS_2$-$MoO_3$−x/$Ni_3S_2$ heterostructure electrocatalyst for efficient alkaline hydrogen evolution. *Chemical Engineering Journal*, *428*, 131055.
205. Zhao, K., Sun, W., Zhang, X., Meng, J., Zhong, M., et al. (2022). High-performance and long-cycle life of triboelectric nanogenerator using PVC/$MoS_2$ composite membranes for wind energy scavenging application. *Nano Energy*, *91*, 106649.
206. Yao, R. Q., Shi, H., Wan, W. B., Wen, Z., Lang, X. Y., et al. (2020). Flexible Co–Mo–N/Au electrodes with a hierarchical nanoporous architecture as highly efficient electrocatalysts for oxygen evolution reaction. *Advanced Materials*, *32*(10), 1907214.
207. Tan, Y., Yan, L., Huang, C., Zhang, W., Qi, H., et al. (2021). Fabrication of an $Au_{25}$-Cys-Mo electrocatalyst for efficient nitrogen reduction to ammonia under ambient conditions. *Small*, *17*(21), 2100372.
208. Rogala, M., Sokołowski, S., Ukegbu, U., Mierzwa, A., & Szoszkiewicz, R. (2021). Direct identification of surface bound $MoO_3$ on single $MoS_2$ flakes heated in dry and humid air. *Advanced Materials Interfaces*, *8*(13), 2100328.

## References


209. Seah, M. P., & Dench, W. A. (1979). Quantitative electron spectroscopy of surfaces: A standard data base for electron inelastic mean free paths in solids. *Surface and interface analysis*, *1*(1), 2-11.

210. Powell, C. J. (2020). Practical guide for inelastic mean free paths, effective attenuation lengths, mean escape depths, and information depths in x-ray photoelectron spectroscopy. *Journal of Vacuum Science & Technology A*, *38*(2).

211. Physical Electronics Quantes Instrument Description. www.phi.com. Accessed online on 7-13-2024.

212. Ai, A. UV-Vis Spectroscopy–Principle, Instrumentation, Applications, Advantages, and Limitation. https://www.technologynetworks.com/analysis/articles/uv-vis-spectroscopy-principle strengths-and-limitations-and-applications-349865, Accessed online on 7-13-2024。

213. Harris, D. C. (2007). *Quantitative chemical analysis* (7th ed.). W. H. Freeman and Company.

214. Diffey, B. L. (2002). Sources and measurement of ultraviolet radiation. *Methods*, *28*(1), 4-13.

215. Namioka, T. (1998). 17. Diffraction Gratings. In *Experimental Methods in the Physical Sciences* Vol. 31, 347-377.

216. Nassau, K. (2001). *The physics and chemistry of color: the fifteen causes of color* , 496。

217. Burns, R. G. (1993). *Mineralogical applications of crystal field theory* (No. 5). Cambridge university press.

218. Picollo, M., Aceto, M., & Vitorino, T. (2019). UV-Vis spectroscopy. *Physical sciences reviews*, *4*(4), 20180008.

219. Hollas, J. M. (2004). *Modern spectroscopy*. John Wiley & Sons.

220. Bacci, M., Picollo, M., Trumpy, G., Tsukada, M., & Kunzelman, D. (2007). Non-invasive identification of white pigments on 20th-century oil paintings by using fiber

optic reflectance spectroscopy. *Journal of the American Institute for Conservation*, *46*(1), 27-37.】

221. Ghayeb Zamharir, S., Karimzadeh, R., & Aboutalebi, S. H. (2018). Laser-assisted tunable optical nonlinearity in liquid-phase exfoliated $MoS_2$ dispersion. *Applied Physics A*, *124*, 1-8.
222. Eda, G., Yamaguchi, H., Voiry, D., Fujita, T., Chen, M., et al. (2011). Photoluminescence from chemically exfoliated $MoS_2$. *Nano letters*, *11*(12), 5111-5116.
223. Li, Y., Wang, H., & Peng, S. (2014). Tunable photodeposition of $MoS_2$ onto a composite of reduced graphene oxide and CdS for synergic photocatalytic hydrogen generation. *The Journal of Physical Chemistry C*, *118*(34), 19842-19848.
224. Li, B., Jiang, L., Li, X., Ran, P., Zuo, P., et al. (2017). Preparation of monolayer $MoS_2$ quantum dots using temporally shaped femtosecond laser ablation of bulk MoS2 targets in water. *Scientific reports*, *7*(1), 11182.
225. Bolar, S., Shit, S., Murmu, N. C., Samanta, P., & Kuila, T. (2021). Activation strategy of $MoS_2$ as HER electrocatalyst through doping-induced lattice strain, band gap engineering, and active crystal plane design. *ACS applied materials & interfaces*, *13*(1), 765-780.
226. Bera, S. K., Mandal, D., & Adarsh, K. V. (2021, September). Engineering exciton many-body interaction in atomically thin $MoS_2$. In *AIP Conference Proceedings* (Vol. 2369, No. 1). AIP Publishing.
227. Wang, W., Sui, N., Ni, M., Chi, X., Pan, L., et al. (2019). Studying of the biexciton characteristics in monolayer $MoS_2$. *The Journal of Physical Chemistry C*, *124*(2), 1749-1754.
228. Raja, P. M. V., & Barron, A. R. (n.d.). *Raman and surface-enhanced Raman spectroscopy*.https://chem.libretexts.org/Bookshelves/Analytical_Chemistry/Physi

cal_Methods_in_Chemistry_and_Nano_Science_(Barron)/04%3A_Chemical_Speciation/4.03%3A_Raman_Spectroscopy. Accessed online on 12-6-2024.

229. Dent, G. (1996). Modern Raman Spectroscopy A Practical Approach.
230. Hiemenz, P. C., & Rajagopalan, R. (2016). *Principles of Colloid and Surface Chemistry, revised and expanded*. CRC press.
231. Lowell, S., Shields, J. E., Thomas, M. A., & Thommes, M. (2012). *Characterization of porous solids and powders: surface area, pore size and density* (Vol. 16). Springer Science & Business Media.
232. Dukhin, A. S., & Goetz, P. J. (2010). Fundamentals of interface and colloid science. In *Studies in Interface Science,* Vol. 24, 21-89.
233. Hubbard, A. T. (2002). *Encyclopedia of surface and colloid science* (Vol. 1). CRC press.
234. Park, J. K. (Ed.). (2012). *Principles and applications of lithium secondary batteries*. John Wiley & Sons.
235. Cai, M. (Ed.). (2011). *Rock mechanics: achievements and ambitions*. CRC Press.
236. W John Thomas, F., & Crittenden, B. (1998). *Adsorption technology and design*. Butterworth-Heinemann.
237. Ambroz, F., Macdonald, T. J., Martis, V., & Parkin, I. P. (2018). Evaluation of the BET Theory for the Characterization of Meso and Microporous MOFs. *Small methods*, *2*(11), 1800173.
238. Thommes, M., Kaneko, K., Neimark, A. V., Olivier, J. P., Rodriguez-Reinoso, F., et al. (2015). Physisorption of gases, with special reference to the evaluation of surface area and pore size distribution (IUPAC Technical Report). *Pure and applied chemistry*, *87*(9-10), 1051-1069.
239. Thermo Fisher Scientific Inc. Electron Microscopy Solutions. https://www.fei.com/products/sem/quanta-sem/ Accessed online on 28-4-2018.

## References


240. Laboratory Testing Inc. Material testing- SEM analysis. https://www.labtesting.com/services/materialstesting/metallurgical-testing/sem-analysis/. Accessed online on 3-5-2018.
241. A Caen group company. Inorganic Scintillator Detectors. https://caensys.com/inorganic_sd/. Accessed online on 22-7-2018.
242. Zhang, R., & Ulery, B. D. (2018). Synthetic vaccine characterization and design. *Journal of Bionanoscience*, *12*(1), 1-11.
243. Davies, T. E., Li, H., Bessette, S., Gauvin, R., Patience, G. S., et al. (2022). Experimental methods in chemical engineering: Scanning electron microscopy and X-ray ultra-microscopy—SEM and XuM. *The Canadian Journal of Chemical Engineering*, *100*(11), 3145-3159.
244. Mohammed, A., & Abdullah, A. (2018, November). Scanning electron microscopy (SEM): A review. In *Proceedings of the 2018 international conference on hydraulics and pneumatics—HERVEX, Băile Govora, Romania,* Vol. 2018, 7-9.
245. Scott, V. D., & Love, G. (1983). *Quantitative electron-probe microanalysis* (Ellis Horwood Series in Physics). Ellis Horwood.
246. Rades, S., Hodoroaba, V. D., Salge, T., Wirth, T., Lobera, M. P., et al. (2014). High-resolution imaging with SEM/T-SEM, EDX and SAM as a combined methodical approach for morphological and elemental analyses of single engineered nanoparticles. *RSC advances*, *4*(91), 49577-49587.
247. Guo, J., Zhang, K., Sun, Y., Zong, Y., Guo, Z., et al. (2018). Enhanced hydrogen evolution of $MoS_2$/RGO: vanadium, nitrogen dopants triggered new active sites and expanded interlayer. *Inorganic Chemistry Frontiers*, *5*(9), 2092-2099.
248. Zheng, S., Zheng, L., Zhu, Z., Chen, J., Kang, J., et al. (2018). $MoS_2$ nanosheet arrays rooted on hollow rGO spheres as bifunctional hydrogen evolution catalyst and supercapacitor electrode. *Nano-micro letters*, *10*, 1-11.

## References


249. Liu, X., Zhao, L., Lai, H., Wei, Y., Yang, G., et al. (2017). Graphene decorated $MoS_2$ for eosin Y-sensitized hydrogen evolution from water under visible light. *RSC advances*, *7*(74), 46738-46744.

250. Kumar, S., Sahoo, P. K., & Satpati, A. K. (2017). Electrochemical and SECM investigation of $MoS_2$/GO and $MoS_2$/rGO nanocomposite materials for HER electrocatalysis. *ACS omega*, *2*(11), 7532-7545.

251. Chen, Y., Liu, H., Li, X., Tang, S., Gu, C., et al. (2021). Development of RGO@$MoS_2$@Ag ternary nanocomposites with tunable geometry structure for recyclable SERS detection. *Sensors and Actuators B: Chemical*, *339*, 129856.

252. Zhang, Z., Lv, X., Chen, Y., Zhang, P., Sui, M., et al. (2019). $NiS_2$@$MoS_2$ nanospheres anchored on reduced graphene oxide: A novel ternary heterostructure with enhanced electromagnetic absorption property. *Nanomaterials, 9*(2), 292.

253. Wang, P., Song, X., Zhu, X., Qiu, J., Yang, S., et al. (2023). *Study on Influencing Factors of Hippocampal Injury in Closed Head Impact Experiments of Rats Using Orthogonal Experimental Design Method* (No. 2023-01-0001). SAE Technical Paper.

254. Dewilde, P. (2022, September). An introduction to orthogonal filtering and its many applications. In *2022 Signal Processing: Algorithms, Architectures, Arrangements, and Applications (SPA)*, 9-14

255. Chen, Z., Li, G., Gao, C., Tan, Y., Liu, J., et al. (2021). Prediction of freezing of gait in Parkinson's disease using a random forest model based on an orthogonal experimental design: a pilot study. *Frontiers in human neuroscience*, *15*, 636414.

256. Jones, B., Shinde, S. M., & Montgomery, D. C. (2015). Alternatives to resolution III regular fractional factorial designs for 9–14 factors in 16 runs. *Applied Stochastic Models in Business and Industry*, *31*(1), 50-58.

## References


257. International Workshop on Intelligent Statistical Quality Control. (2010). *Frontiers in statistical quality control 9*. H. J. Lenz, P. T. Wilrich, & W. Schmid (Eds.). Physica-Verlag.

258. Cong, M., Zhang, S., Sun, D., & Zhou, K. (2021). Optimization of preparation of foamed concrete based on orthogonal experiment and range analysis. *Frontiers in Materials*, *8*, 778173.

259. Shang, G., Liu, S., Wang, Q., & Cai, Z. (2023). Orthogonal experiment on underwater rock breaking by gas–liquid two-phase jet. *Marine Georesources & Geotechnology*, *41*(6), 710-720.

260. Feng, J., Yin, G., Tuo, H., & Niu, Z. (2021). Parameter optimization and regression analysis for multi-index of hybrid fiber-reinforced recycled coarse aggregate concrete using orthogonal experimental design. *Construction and building materials*, *267*, 121013.

261. Saleem, H., Haneef, M., & Abbasi, H. Y. (2018). Synthesis route of reduced graphene oxide via thermal reduction of chemically exfoliated graphene oxide. *Materials Chemistry and Physics*, *204*, 1-7.

262. Díez-Pascual, A. M., Sainz-Urruela, C., Vallés, C., Vera-Lopez, S., & San Andrés, M. P. (2020). Tailorable synthesis of highly oxidized graphene oxides via an environmentally-friendly electrochemical process. *Nanomaterials*, *10*(2), 239.

263. Kjeldby, S. B., Evenstad, O. M., Cooil, S. P., & Wells, J. W. (2017). Probing dimensionality using a simplified 4-probe method. *Journal of Physics: Condensed Matter*, *29*(39), 394008.

264. Gaspari, F. (2018). 2.4 Thin films. In I. Dincer (Ed.), *Comprehensive energy systems*, Vol. 2, 88–116.

265. Das, N. S., Jana, R., Roy, A., & Chowdhury, A. (2023). $MoS_2$-functionalized conductive carbon heterostructure embedded with ferroelectric polymers for bipolar memristive applications. *Semiconductor Science and Technology*, *38*(6), 065003.

## References


266. Thangaraj, N., John, N. J., & Gnana Sambandam, C. (2023). An improved method of synthesis of graphene oxide (GO) and reduced graphene oxide (rGO) nanocomposites. *International Journal of Current Research and Review, 15*(5), 26–32.

267. Fang, S., Huang, D., Lv, R., Bai, Y., Huang, Z. H., et al. (2017). Three-dimensional reduced graphene oxide powder for efficient microwave absorption in the S-band (2–4 GHz). *Rsc Advances*, *7*(41), 25773-25779.

268. YoungáChung, D., ChuláHam, H., & JongáYoo, S. (2014). Edge-exposed $MoS_2$ nano-assembled structures as efficient electrocatalysts for hydrogen evolution reaction. *Nanoscale*, *6*(4), 2131-2136.

269. Son, E., Lee, S., Seo, J., Kim, U., Kim, S. H., et al. (2023). Engineering the local atomic configuration in 2H TMDs for efficient electrocatalytic hydrogen evolution. *ACS nano*, *17*(11), 10817-10826.

270. Piacentini, A., Daus, A., Wang, Z., Lemme, M. C., & Neumaier, D. (2023). Potential of transition metal dichalcogenide transistors for flexible electronics applications. *Advanced Electronic Materials*, *9*(8), 2300181.

271. Liu, J., Wang, J., Wei, B., Xue, Y., Ma, L., et al. (2023). Unveiling the Effect of Organic Sulfur Sources on Synthesized $MoS_2$ Phases and Electrocatalytic Hydrogen Evolution Performances. *Inorganic Chemistry*, *62*(24), 9749-9757.

272. Kumar, K., Jamnuch, S., Majidi, L., Misal, S., Ahmadiparidari, A., et al. (2023). Active states during the reduction of $CO_2$ by a $MoS_2$ electrocatalyst. *The Journal of Physical Chemistry Letters*, *14*(13), 3222-3229.

273. Askari, M. B., Salarizadeh, P., Veisi, P., Samiei, E., Saeidfirozeh, H., et al. (2023). Transition-metal dichalcogenides in electrochemical batteries and solar cells. Micromachines, 14(3), 691.

274. Van Nguyen, T., Tekalgne, M., Nguyen, T. P., Van Le, Q., Ahn, S. H., et al. (2023). Electrocatalysts based on MoS2 and $WS_2$ for hydrogen evolution reaction: An overview. *Battery Energy*, *2*(3), 20220057.

## References


275. Chong, P., Zhou, Z., Wang, K., Zhai, W., Li, Y., et al. (2022). The stabilizing of 1T-$MoS_2$ for all-solid-state lithium-ion batteries. *Batteries*, *9*(1), 26.

276. Wang, Z., Gu, C., Jiang, S., Sun, T., & Wang, Z. (2023). The study of phase transition of $MoS_2$ regulated by $H^+$. *Journal of Physics: Condensed Matter*, *35*(32), 325401.

277. Liu, Y., Li, Q., Zhu, Y., Chen, X., Xue, F., et al. (2023). One-step synthesis of $MoS_2$/NiS heterostructures with a stable 1T phase for an efficient hydrogen evolution reaction. *Dalton Transactions*, *52*(25), 8530-8535.

278. Baheri, Y. T., Maleki, M., Karimian, H., Javadpoor, J., & Masoudpanah, S. M. (2023). Well-distributed 1T/2H $MoS_2$ nanocrystals in the N-doped nanoporous carbon framework by direct pyrolysis. *Scientific Reports*, *13*(1), 7492.

279. Hanslin, S. Ø., Jónsson, H., & Akola, J. (2023). Is the doped $MoS_2$ basal plane an efficient hydrogen evolution catalyst? Calculations of voltage-dependent activation energy. *Physical Chemistry Chemical Physics*, *25*(22), 15162-15172.

280. Wang, W., Zhao, H., Du, Y., Yang, Y., Li, S., et al. (2021). The controlled synthesis of V-doped $MoS_2$-$Ni_xS_y$ hollow nanospheres and their electrocatalytic performance in hydrogen evolution reaction. *Sustainable Energy & Fuels*, *5*(3), 698-703.

281. Jameel, M. H., Sufi bin Roslan, M., Bin Mayzan, M. Z. H., Agam, M. A. B., Zaki, Z. I., et al. (2023). Investigation of structural, electronic and optical properties of two-dimensional $MoS_2$-doped-$V_2O_5$ composites for photocatalytic application: a density functional theory study. *Royal Society open science*, *10*(7), 230503.

282. Sharma, M. D., Mahala, C., Modak, B., Pande, S., & Basu, M. (2021). Doping of $MoS_2$ by “Cu” and “V”: an efficient strategy for the enhancement of hydrogen evolution activity. *Langmuir*, *37*(16), 4847-4858.

283. Bolar, S., Shit, S., Murmu, N. C., Samanta, P., & Kuila, T. (2021). Activation strategy of $MoS_2$ as HER electrocatalyst through doping-induced lattice strain, band gap engineering, and active crystal plane design. *ACS applied materials & interfaces*, *13*(1), 765-780.

## References


284. Bolar, S., Shit, S., Kumar, J. S., Murmu, N. C., Ganesh, R. S., et al. (2019). Optimization of active surface area of flower like $MoS_2$ using V-doping towards enhanced hydrogen evolution reaction in acidic and basic medium. *Applied Catalysis B: Environmental*, *254*, 432-442.

285. Singh, A. K., Prasad, J., Azad, U. P., Singh, A. K., Prakash, R., et al. (2019). Vanadium doped few-layer ultrathin $MoS_2$ nanosheets on reduced graphene oxide for high-performance hydrogen evolution reaction. *RSC advances*, *9*(39), 22232-22239.

286. Rheem, Y., Park, S. H., Han, Y., Lee, K. H., Choi, S. M., et al. (2019). Electrospun cobalt-doped $MoS_2$ Nanofibers for electrocatalytic hydrogen evolution. *Journal of The Electrochemical Society*, *166*(13), F996.

287. Peng, J., Yu, X., Meng, Y., Tan, H., Song, P., et al. (2020). Oxygen doped $MoS_2$ quantum dots for efficient electrocatalytic hydrogen generation. *The Journal of Chemical Physics*, *152*(13).

288. Urbanová, V., Lazar, P., Antonatos, N., Sofer, Z., Otyepka, M., et al. (2020). Positive and negative effects of dopants toward electrocatalytic activity of $MoS_2$ and $WS_2$: experiments and theory. *ACS Applied Materials & Interfaces*, *12*(18), 20383-20392.

289. Mao, Y., Fang, Y., Yuan, K., & Huang, F. (2022). Effect of vanadium doping on the thermoelectric properties of $MoS_2$. *Journal of Alloys and Compounds*, *903*, 163921.

290. Rahman, R., Samanta, D., Pathak, A., & Nath, T. K. (2021). Tuning of structural and optical properties with enhanced catalytic activity in chemically synthesized Co-doped $MoS_2$ nanosheets. *RSC advances*, *11*(3), 1303-1319.

291. Kuru, C. (2020). Controlled vanadium doping of $MoS_2$ thin films through co-sputtering and thermal sulfurization. *Cumhuriyet Science Journal*, *41*(1), 305-310.

292. Singh, A. K., Prasad, J., Azad, U. P., Singh, A. K., Prakash, R., et al. (2019). Vanadium doped few-layer ultrathin $MoS_2$ nanosheets on reduced graphene oxide

for high-performance hydrogen evolution reaction. *RSC advances*, *9*(39), 22232-22239.

293. Quilty, C. D., Housel, L. M., Bock, D. C., Dunkin, M. R., Wang, L., et al. (2019). Ex situ and operando XRD and XAS analysis of $MoS_2$: a lithiation study of bulk and nanosheet materials. *ACS Applied Energy Materials*, *2*(10), 7635-7646.

294. Leelavathi, R., Vivekanandan, K., Hariharan, V., & Abirami, R. (2023). Identifying the Suitability of $MoS_2$ Nanoparticles by Two Different Methods for Photo Catalytic Applications. *International Journal of Nanoscience*, *22*(02), 2350006.

295. Cao, Y., Zhang, Y., Chen, H., Qin, S., Zhang, L., et al. (2022). $Cu_{12}Sb_4S_{13}$ Quantum Dots/Few-Layered $Ti_3C_2$ Nanosheets with Enhanced $K^+$ Diffusion Dynamics for Efficient Potassium Ion Storage. *Advanced Functional Materials*, *32*(6), 2108574.

296. Nasu, A., Sakuda, A., Kimura, T., Deguchi, M., Tsuchimoto, A., et al (2022). Iron Sulfide $Na_2FeS_2$ as Positive Electrode Material with High Capacity and Reversibility Derived from Anion–Cation Redox in All-Solid-State Sodium Batteries. *Small*, *18*(42), 2203383.

297. Tran, D. T., Prabhakaran, S., Kim, D. H., Hameed, N., Wang, H., et al. (2021). Ruthenium single atoms implanted continuous $MoS_2$-$Mo_2C$ heterostructure for high-performance and stable water splitting. *Nano Energy,* 88, 106277.

298. Chai, Y., Kong, Y., Lin, M., Lin, W., Shen, J., et al. (2023). Metal to non-metal sites of metallic sulfides switching products from CO to $CH_4$ for photocatalytic $CO_2$ reduction. *Nature Communications*, *14*(1), 6168.

299. Nasu, A., Inaoka, T., Tsuji, F., Motohashi, K., Sakuda, A., et al. (2022). Formation of passivate interphases by $Na_3BS_3$-glass solid electrolytes in all-solid-state sodium-metal batteries. *ACS Applied Materials & Interfaces*, *14*(21), 24480-24485.

300. Castner, D. G., Hinds, K., & Grainger, D. W. (1996). X-ray photoelectron spectroscopy sulfur 2p study of organic thiol and disulfide binding interactions with gold surfaces. *Langmuir*, *12*(21), 5083-5086.

## References


301. Zhang, Y., Peng, C., Zhang, Y., Yang, S., Zeng, Z., et al. (2022). In-situ crosslinked $Zn^{2+}$-conducting polymer complex interphase with synergistic anion shielding and cation regulation for high-rate and dendrite-free zinc metal anodes. *Chemical Engineering Journal*, *448*, 137653.
302. Yang, J., Cao, C., Li, Z., Wang, P., Li, B., et al. (2023). Adsorption-catalysis synergy within pyrrolic-N-rich carbon nanosheets: Propelling electrochemical kinetics and shielding polysulfides for lithium-sulfur batteries. *Chemical Engineering Journal*, *476*, 146532.
303. Song, Y. X., Shi, Y., Wan, J., Lang, S. Y., Hu, X. C., et al. (2019). Direct tracking of the polysulfide shuttling and interfacial evolution in all-solid-state lithium–sulfur batteries: a degradation mechanism study. *Energy & Environmental Science*, *12*(8), 2496-2506.
304. Xia, J., Zhang, X., Yang, Y., Wang, X., & Yao, J. (2021). Electrospinning fabrication of flexible, foldable, and twistable $Sb_2S_3/TiO_2$/C nanofiber anode for lithium ion batteries. *Chemical Engineering Journal*, *413*, 127400.
305. Quan, L., Qin, F. X., Lu, H. T., Estevez, D., Wang, Y. F., et al. (2021). Sequencing dual dopants for an electromagnetic tunable graphene. *Chemical Engineering Journal*, *413*, 127421.
306. Wang, X., Zhang, Y., Si, H., Zhang, Q., Wu, J., et al. (2020). Single-atom vacancy defect to trigger high-efficiency hydrogen evolution of $MoS_2$. *Journal of the American Chemical Society*, *142*(9), 4298-4308.
307. Thakur, R., Hoffman, M., VahidMohammadi, A., Smith, J., Chi, M., et al. (2020). Multilayered two-dimensional $V_2CT_x$ MXene for methane dehydroaromatization. *ChemCatChem*, *12*(14), 3639-3643.
308. Chen, K., Zhang, G., Xiao, L., Li, P., Li, W., et al. (2021). Polyaniline Encapsulated Amorphous $V_2O_5$ Nanowire-Modified Multi-Functional Separators for Lithium–Sulfur Batteries. *Small Methods*, *5*(3), 2001056.

## References


309. Biesinger, M. C., Lau, L. W., Gerson, A. R., & Smart, R. S. C. (2010). Resolving surface chemical states in XPS analysis of first row transition metals, oxides and hydroxides: Sc, Ti, V, Cu and Zn. *Applied surface science*, *257*(3), 887-898.

310. Wu, S., Ding, Y., Hu, L., Zhang, X., Huang, Y., & Chen, S. (2020). Amorphous $V_2O_5$ as high performance cathode for aqueous zinc ion battery. *Materials Letters*, *277*, 128268.

311. Du, M., Miao, Z., Li, H., Zhang, F., Sang, Y., et al. (2021). Oxygen-vacancy and phosphate coordination triggered strain engineering of vanadium oxide for high-performance aqueous zinc ion storage. *Nano Energy*, *89*, 106477.

312. Mendialdua, J., Casanova, R., & Barbaux, Y. J. J. O. E. S. (1995). XPS studies of $V_2O_5$, $V_6O_{13}$, $VO_2$ and $V_2O_3$. *Journal of Electron Spectroscopy and Related Phenomena*, *71*(3), 249-261.

313. Xu, C., Mu, J., Zhou, T., Tian, S., Gao, P., et al. (2022). Surface Redox Pseudocapacitance Boosting Vanadium Nitride for High-Power and Ultra-Stable Potassium-Ion Capacitors. *Advanced Functional Materials*, *32*(38), 2206501.

314. Yuan, J., Qiu, M., Chen, J. X., Hu, X., Liu, Y., et al. (2022). High mass loading 3D-printed sodium-ion hybrid capacitors. *Advanced Functional Materials*, *32*(30), 2203732.

315. Manikandan, R., Raj, C. J., Rajesh, M., Kim, B. C., Sim, J. Y., et al. (2018). Electrochemical behaviour of lithium, sodium and potassium ion electrolytes in a $Na_{0.33}V_2O_5$ symmetric pseudocapacitor with high performance and high cyclic stability. *ChemElectroChem*, 5(1), 101-111.

316. Franceschini, F., Payo, M. R., Schouteden, K., Ustarroz, J., Locquet, J. P., et al. (2023). MBE Grown Vanadium Oxide Thin Films for Enhanced Non-Enzymatic Glucose Sensing. *Advanced Functional Materials*, *33*(43), 2304037.

## References


317. Yao, Y., Ao, K., Lv, P., & Wei, Q. (2019). $MoS_2$ coexisting in 1T and 2H phases synthesized by common hydrothermal method for hydrogen evolution reaction. *Nanomaterials*, *9*(6), 844.

318. Chang, K., Hai, X., Pang, H., Zhang, H., Shi, L., et al. (2016). Targeted Synthesis of 2H-and 1T-Phase $MoS_2$ Monolayers for Catalytic Hydrogen Evolution. *Advanced Materials (Deerfield Beach, Fla.)*, *28*(45), 10033-10041.

319. Liu, T., Fang, C., Yu, B., You, Y., Niu, H., et al. (2020). Vanadium-doping in interlayer-expanded $MoS_2$ nanosheets for the efficient electrocatalytic hydrogen evolution reaction. *Inorganic Chemistry Frontiers*, *7*(13), 2497-2505.

320. Liu, Q., Fang, Q., Chu, W., Wan, Y., Li, X., et al. (2017). Electron-doped 1T-$MoS_2$ via interface engineering for enhanced electrocatalytic hydrogen evolution. *Chemistry of Materials*, *29*(11), 4738-4744.

321. Li, X., Lv, X., Li, N., Wu, J., Zheng, Y. Z., et al. (2019). One-step hydrothermal synthesis of high-percentage 1T-phase $MoS_2$ quantum dots for remarkably enhanced visible-light-driven photocatalytic $H_2$ evolution. *Applied Catalysis B: Environmental*, *243*, 76-85.

322. Tang, Y. J., Wang, Y., Wang, X. L., Li, S. L., Huang, W., et al. (2016). Molybdenum disulfide/nitrogen-doped reduced graphene oxide nanocomposite with enlarged interlayer spacing for electrocatalytic hydrogen evolution. *Advanced Energy Materials*, *6*(12), 1600116.

323. Cotton, F. A., Wilkinson, G., Murillo, C. A., & Bochmann, M. (1999). *Advanced inorganic chemistry*. John Wiley & Sons.

324. Lu, J., Zeng, Y., Ma, X., Wang, H., Gao, L., et al. (2019). Cobalt nanoparticles embedded into N-doped carbon from metal organic frameworks as highly active electrocatalyst for oxygen evolution reaction. *Polymers*, *11*(5), 828.

325. Ren, X., Ma, Q., Fan, H., Pang, L., Zhang, Y., et al. (2015). A Se-doped $MoS_2$ nanosheet for improved hydrogen evolution reaction. *Chemical Communications*, *51*(88), 15997-16000.

## References


326. Mann, J., Ma, Q., Odenthal, P. M., Isarraraz, M., Le, D., et al. (2014). 2-Dimensional transition metal dichalcogenides with tunable direct band gaps: $MoS_{2(1-x)}Se_{2x}$ monolayers. *Advanced Materials*, *26*(9), 1399-1404.
327. Munkhbayar, G., Nomin-Erdene, E., & Davaasambuu, J. (2023). Thermal Annealing Effects on the Raman and Photoluminescence Properties of Mono and Few-Layer $MoS_2$ Films. *Key Engineering Materials*, *943*, 173-178.
328. Zeng, M., & Li, Y. (2015). Recent advances in heterogeneous electrocatalysts for the hydrogen evolution reaction. *Journal of Materials Chemistry A*, *3*(29), 14942-14962.
329. Tang, Y. J., Wang, Y., Wang, X. L., Li, S. L., Huang, W., et al. (2016). Molybdenum disulfide/nitrogen-doped reduced graphene oxide nanocomposite with enlarged interlayer spacing for electrocatalytic hydrogen evolution. *Advanced Energy Materials*, *6*(12), 1600116.
330. Xie, J., Zhang, H., Li, S., Wang, R., Sun, X., et al. (2013). Defect-rich $MoS_2$ ultrathin nanosheets with additional active edge sites for enhanced electrocatalytic hydrogen evolution. *Advanced materials*, *25*(40), 5807-5813.
331. Peyrovi, M. H., & Abolhassanzadeh Parizi, M. (2022). The Modification of the BET Surface Area by Considering the Excluded Area of Adsorbed Molecules. *Physical Chemistry Research*, *10*(2), 173-177.
332. Wang, Y., Chen, Z., & Hu, L. (2023). Determining the geometric surface area of mesoporous materials. *The Journal of Physical Chemistry C*, *127*(9), 4799-4807.
333. Bui, M., Nagapudi, K., & Chakravarty, P. (2022). Determination of BET Specific Surface Area of Hydrate-Anhydrate Systems Susceptible to Phase Transformation Using Inverse Gas Chromatography. *AAPS PharmSciTech*, *23*(7), 237.
334. Gibson, N., Kuchenbecker, P., Rasmussen, K., Hodoroaba, V. D., & Rauscher, H. (2020). Volume-specific surface area by gas adsorption analysis with the BET method. In *Characterization of Nanoparticles*, 265-294.

## References


335. Isa, A. H., Abdulrahman, F. W., & Aliyu, H. D. (2014). BET Surface Area Determination of Calcium Oxide from Adamawa Chalk Mineral Using Water Adsorption Method, for Use as Catalyst. *Chemistry and Materials Research*, *6*(1), 87-92.

336. Liu, C., & Wang, X. J. (2016). Room temperature synthesis of $Bi_4O_5I_2$ and $Bi_5O_7I$ ultrathin nanosheets with a high visible light photocatalytic performance. *Dalton Transactions*, *45*(18), 7720-7727.

337. Mafa, P. J., Swana, U. S., Liu, D., Gui, J., Mamba, B. B., et al. (2021). Synthesis of $Bi_5O_7I$-$MoO_3$ photocatalyst via simultaneous calcination of BiOI and MoS2 for visible light degradation of ibuprofen. *Colloids and Surfaces A: Physicochemical and Engineering Aspects*, *612*, 126004.

338. Ghanashyam, G., & Jeong, H. K. (2022). Size Effects of $MoS_2$ on Hydrogen and Oxygen Evolution Reaction. *Journal of Electrochemical Science and Technology*, *13*(1), 120-127.

339. Bai, M., Li, W., Yang, H., Dong, W., Wang, Q., et al. (2022). Morphology-controlled synthesis of $MoS_2$ using citric acid as a complexing agent and self-assembly inducer for high electrochemical performance. *RSC advances*, *12*(44), 28463-28472.

340. Chen, R., Pei, Y., Kang, Y., Liu, J., Xia, Y., et al. (2022). A high-speed photodetector fabricated with tungsten-doped $MoS_2$ by ion implantation. *Advanced Electronic Materials*, *8*(9), 2200281.

341. Li, S., Luo, Z., Wang, S., & Cheng, H. (2023). Atomic structure and HER performance of doped $MoS_2$: A mini-review. *Electrochemistry Communications*, *155*, 107563.

342. Wang, H., Ouyang, L., Zou, G., Sun, C., Hu, J., Xiao, X., et al. (2018). Optimizing $MoS_2$ edges by alloying isovalent W for robust hydrogen evolution activity. *Acs Catalysis*, *8*(10), 9529-9536.

## References


343. Cai, J., Xia, Y., Gang, R., He, S., & Komarneni, S. (2022). Activation of $MoS_2$ via tungsten doping for efficient photocatalytic oxidation of gaseous mercury. *Applied Catalysis B: Environmental*, *314*, 121486.

344. Liang, Z., Wang, M., Liu, S., Hassan, M., Zhang, X., et al. (2024). One-pot hydrothermal synthesis of self-assembled $MoS_2/WS_2$ nanoflowers for chemiresistive room-temperature $NO_2$ sensors. *Sensors and Actuators B: Chemical*, *403*, 135215.

345. Wu, K., Zhang, Q., Zheng, Y., Yuan, J., Yu, Q., et al. (2024). Effect of W Modification on $MoS_2$ Surface Edge in the Ethanolysis of Lignin into Platform Chemicals. *Chem & Bio Engineering*, *1*(8), 725-736.

346. Ji, L., Yan, P., Zhu, C., Ma, C., Wu, W., et al. (2019). One-pot synthesis of porous 1T-phase $MoS_2$ integrated with single-atom Cu doping for enhancing electrocatalytic hydrogen evolution reaction. *Applied Catalysis B: Environmental*, *251*, 87-93.

347. Sun, G., Li, F., Wu, T., Cong, L., Sun, L., et al. (2019). $O_2$ adsorption associated with sulfur vacancies on $MoS_2$ microspheres. *Inorganic chemistry*, *58*(3), 2169-2176.

348. Hussain, S., Vikraman, D., Sarfraz, M., Faizan, M., Patil, S. A., et al. (2023). Design of $XS_2$ (X= W or Mo)-Decorated $VS_2$ hybrid nano-architectures with abundant active edge sites for high-rate asymmetric supercapacitors and hydrogen evolution reactions. *Small*, *19*(8), 2205881.

349. He, J. N., Liang, Y. Q., Mao, J., Zhang, X. M., Yang, X. J., et al. (2016). 3D Tungsten-doped $MoS_2$ nanostructure: a low-cost, facile prepared catalyst for hydrogen evolution reaction. *Journal of The Electrochemical Society*, *163*(5), H299.

350. Nipane, A., Karmakar, D., Kaushik, N., Karande, S., & Lodha, S. (2016). Few-layer $MoS_2$ p-type devices enabled by selective doping using low energy phosphorus implantation. *ACS nano*, *10*(2), 2128-2137.

## References


351. Gant, P., Huang, P., de Lara, D. P., Guo, D., Frisenda, R., et al. (2019). A strain tunable single-layer $MoS_2$ photodetector. *Materials Today*, *27*, 8-13.

352. Fei, L., Lei, S., Zhang, W. B., Lu, W., Lin, Z., et al. (2016). Direct TEM observations of growth mechanisms of two-dimensional $MoS_2$ flakes. *Nature communications*, *7*(1), 12206.

353. Hussain, S., Rabani, I., Vikraman, D., Feroze, A., Ali, M., et al. (2021). $MoS_2$@$X_2C$ (X= Mo or W) hybrids for enhanced supercapacitor and hydrogen evolution performances. *Chemical Engineering Journal*, *421*, 127843.

354. Rong, J., Ye, Y., Cao, J., Liu, X., Fan, H., Y et al. (2022). Restructuring electronic structure via W doped 1T $MoS_2$ for enhancing hydrogen evolution reaction. *Applied Surface Science*, *579*, 152216.

355. Xu, Q., Zhang, Y., Zheng, Y., Liu, Y., Tian, Z., et al. (2021). Synergistic effects of tungsten doping and sulfur vacancies in $MoS_2$ on enhancement of hydrogen evolution. *The Journal of Physical Chemistry C*, *125*(21), 11369-11379.

356. Liu, W., Luo, C., Zhang, S., Zhang, B., Ma, J., et al. (2021). Cobalt-doping of molybdenum disulfide for enhanced catalytic polysulfide conversion in lithium–sulfur batteries. *ACS nano*, *15*(4), 7491-7499.

357. Raza, A., Ikram, M., Aqeel, M., Imran, M., Ul-Hamid, A., et al. (2020). Enhanced industrial dye degradation using Co doped in chemically exfoliated $MoS_2$ nanosheets. *Applied Nanoscience*, *10*, 1535-1544.

358. Li, Z., Li, C., Chen, J., Xing, X., Wang, Y., et al. (2022). Confined synthesis of $MoS_2$ with rich co-doped edges for enhanced hydrogen evolution performance. *Journal of Energy Chemistry*, *70*, 18-26.

359. Pan, M., Zhang, X., Pan, C., Wang, J., & Pan, B. (2023). Identification of Co–O–Mo active centers on Co-doped $MoS_2$ electrocatalyst. *ACS Applied Materials & Interfaces*, *15*(15), 19695-19704.

360. Xiong, Q., Zhang, X., Wang, H., Liu, G., Wang, G., et al. (2018). One-step synthesis of cobalt-doped $MoS_2$ nanosheets as bifunctional electrocatalysts for overall water

## References

splitting under both acidic and alkaline conditions. *Chemical Communications*, *54*(31), 3859-3862.

361. Pan, J., Song, C., Wang, X., Yuan, X., Fang, Y., et al. (2017). Intermediate bands of $MoS_2$ enabled by Co doping for enhanced hydrogen evolution. *Inorganic Chemistry Frontiers*, *4*(11), 1895-1899.
362. Zhang, N., Gan, S., Wu, T., Ma, W., Han, D., et al. (2015). Growth control of $MoS_2$ nanosheets on carbon cloth for maximum active edges exposed: an excellent hydrogen evolution 3D cathode. *ACS applied materials & interfaces*, *7*(22), 12193-12202.
363. Li, A. Y., Shen, H. X., & Wang, X. C. (2022). Improved optical and electronic properties of single-layer $MoS_2$ by Co doping for promising intermediate-band materials. *Key Engineering Materials*, *905*, 96-102.
364. Raza, A., Ikram, M., Aqeel, M., Imran, M., Ul-Hamid, A., et al. (2020). Enhanced industrial dye degradation using Co doped in chemically exfoliated $MoS_2$ nanosheets. *Applied Nanoscience*, *10*, 1535-1544.
365. Xiang, Z., Zhang, Z., Xu, X., Zhang, Q., Wang, Q., et al. (2015). Room-temperature ferromagnetism in Co doped $MoS_2$ sheets. *Physical Chemistry Chemical Physics*, *17*(24), 15822-15828.
366. Li, Y., Wang, S., Hu, Y., Zhou, X., Zhang, M., et al. (2022). Highly dispersed Pt nanoparticles on 2D $MoS_2$ nanosheets for efficient and stable hydrogen evolution reaction. *Journal of Materials Chemistry A*, *10*(10), 5273-5279.